



Norwegian University of
Science and Technology

Fabrication of Multiferroic Tunnel Junctions on (111)-oriented SrTiO₃

Kristoffer Kjærnes

Master of Science in Electronics

Submission date: August 2016

Supervisor: Thomas Tybell, IET

Co-supervisor: Torstein Bolstad, IET

Norwegian University of Science and Technology
Department of Electronics and Telecommunications

Problem Description

Magnetic tunnel junctions (MTJ) and ferroelectric tunnel junctions (FTJ) are subject to large research efforts for use in memory applications, especially random access memories due to supreme speed and energy efficiency compared to DRAM, with magnetic and ferroelectric RAM, respectively. The two concepts may be joined in the same device with ferromagnetic electrodes separated by a thin ferroelectric barrier, sometimes referred to as an artificial multiferroic tunnel junction (MFTJ). MFTJs are promising for memory applications where the two degrees of freedom can utilize both tunnel magnetoresistance (TMR) and tunnel electroresistance (TER) at the same time in the same memory cell. In this work, focus will be devoted to the establishment of a MFTJ model system on (111)-oriented SrTiO₃ substrates, for the study of ferroelectric and ferromagnetic coexistence in such devices. Development of schemes for good electrical contacts to the MFTJs will be emphasized. Lastly, an electrical measurement setup will be established for TMR and TER measurements.

Abstract

The phenomenon of quantum mechanical electron tunneling is widely used in device technology, of which magnetic tunnel junctions (MTJ) have been important for many years and ferroelectric tunnel junctions (FTJ) are becoming increasingly important. MTJs consist of two ferromagnetic electrodes separated by a thin insulating barrier material while FTJs have a thin ferroelectric insulator separating two metallic electrodes. The probability for tunneling through these junctions depend on the relative orientation of the magnetic electrodes in MTJs, or the direction of polarization relative to the tunneling electrons in FTJs. Two stable states are usually obtained in each type of junction, which gives rise to different electrical resistance for the two states. These effects are known as the tunnel magnetoresistance (TMR) in MTJs and tunnel electroresistance (TER) in FTJs.

MTJs and FTJs are subject to large research efforts, particularly for use in memory applications. Furthermore, the two concepts may be joined in the same device with ferromagnetic electrodes separated by a thin ferroelectric barrier. These junctions are sometimes referred to as artificial multiferroic tunnel junctions (MFTJ), because they represent a device which has multiple ferroic orders, but where none of the constituent materials are more than singly ferroic. An increasing amount of research is devoted to MFTJs, as they are promising for memory applications where the two degrees of freedom can utilize both TMR and TER at the same time in the same memory cell. Effectively, this can give four distinct electrical resistance states, which can be used to hold two bits of information. Moreover, a third possibility opens by considering non-nollinear magnetic alignments of the magnetic electrodes, which may give rise to additional resistance states and another information bit. Consequently, a substantial increase of memory density can be achieved if the memory cell size is kept equal to former technologies.

Here, two model systems for MFTJs on (111)-oriented SrTiO_3 (STO) substrates are designed and fabricated for the study of ferroelectric and ferromagnetic coexistence. Epitaxial structures of ferromagnetic, half-metallic $\text{La}_{0.7}\text{Sr}_{0.3}\text{MnO}_3$ (LSMO) followed by ferroelectric BaTiO_3 (BTO), grown on (111)-oriented STO substrates, are utilized as bottom electrode and insulating barrier materials, respectively. Sputter deposited $\text{Ni}_{0.81}\text{Fe}_{0.19}$ (permalloy) and epitaxial LSMO with a sputtered Pt capping and contacting layer, are used as ferromagnetic top electrodes for asymmetric permalloy MFTJs and all-oxide epitaxial MFTJs, respectively. The fabrication is done by electron beam lithography (EBL) and overlay exposure to define precise micron scale MFTJs.

Room temperature wedge-wedge bonding with gold and aluminium wire to either Au or Al bond pads are reported with highly reproducible results.

Evidence for TMR with multiple resistance states between the totally parallel and antiparallel magnetic alignments as well as TER with resistive switching are presented. The TMR results indicate intermediate magnetic alignments which

are stable and switchable without using multiple directions of the applied magnetic field. Furthermore, the TER results imply the presence of simultaneous ferroelectric switching.

Investigations on scripting the Quantum Design VersaLab Electrical Transport Option (ETO) with Visual Basic programming is performed in order to do more specific electrical characterization of the fabricated MFTJs. Promising low-current measurements of differential resistance and capacitance versus DC-current are reported, by utilizing AC lock-in data from measurements directly.

Sammendrag

Kvantemekanisk elektron-tunnelering er et fenomen som er mye brukt innen komponentteknologi, hvorav magnetiske tunneloverganger (MTJ) har vært viktige i mange år og ferroelektriske tunneloverganger (FTJ) blir stadig viktigere. MTJer består av to ferromagnetiske elektroder separert av et tynt isolerende barriere-materiale, mens FTJer har en tynn ferroelektrisk tunnelbarriere som separerer to normale metalliske elektroder. Sannsynligheten for at elektroner kan tunneler gjennom disse tynne overgangene avhenger av den relative orienteringen mellom de magnetiske elektrodene i MTJer, eller retningen på polarisasjonen relativt til retningen elektronene tunnelerer med i FTJer. To stabile tilstander eksisterer som regel i hver type overgang, og dette gir opphav til forskjellig elektrisk motstand for de to innbyrdes tilstandene. Disse effektene kalles tunnelerende magneto-motstand (TMR) i MTJer og tunnelerende elektro-motstand (TER) i FTJer.

MTJer og FTJer er begge hete temaer innen forskning, spesielt med tanke på bruk innen minneteknologi. De to konseptene kan implementeres i samme enhet med ferromagnetiske elektroder separert av en tynn ferroelektrisk isolator. Disse enhetene kalles av og til syntetiske multiferroiske tunneloverganger (MFTJ), fordi de representerer en enhet som inkorporerer flere ferroiske ordensparametre samtidig, selv om ingen av materialene som utgjør strukturen har mer enn én enkelt ferroisk ordensparameter hver. Forskning på dette området er i vekst, siden slike enheter er lovende for fremtidig minneteknologi der begge frihetsgradene kan utnyttes simultant for å muliggjøre både TMR og TER til samme tid og i samme minnecelle. Totalt sett kan dette gi fire distinkte motstands nivåer, som kan brukes til å holde på to bit informasjon. Videre er en tredje mulighet å utnytte ikke-sammenfallende magnetiske innretninger av de magnetiske elektrodene, for å tilby enda en frihetsgrad med tilhørende distinkte motstands nivåer. Dette kan da gi en tredje bit informasjon for totalt en tre-biters minnecelle. Konsekvensen av disse mulighetene er at en betydelig økning i minnekapasitet kan være mulig dersom størrelsen på hver minnecelle holdes uendret eller minskes i forhold til eksisterende teknologi.

I dette arbeidet vil to modellsystemer for MFTJer på (111)-orienterte SrTiO_3 -substrater (STO) designes og fabrikkeres, for å studere sameksistensen av ferroelektrisitet og ferromagnetisme. Epitaksielle strukturer av ferromagnetisk og halvmetallisk $\text{La}_{0.7}\text{Sr}_{0.3}\text{MnO}_3$ (LSMO) etterfulgt av ferroelektrisk BaTiO_3 (BTO), grodd på (111)-orienterte STO-substrat, utnyttes henholdsvis som bunnelektrode og isolerende tunnelbarrierere. $\text{Ni}_{0.81}\text{Fe}_{0.19}$ (permalloy) deponert ved hjelp av sputring, samt epitaksiell LSMO med sputrede Pt terminerings- og kontakt-ringslag, er henholdsvis brukt som ferromagnetiske toppelektroder for asymmetriske permalloy MFTJer og hel-oksidd epitaksielle MFTJer. Fabrikasjonen er gjort ved hjelp av elektronstråle-litografi (EBL) og flerlags eksponering for å definere MFTJer på mikroskala nivå.

Elektrisk kontaktering ble gjort ved romtemperatur med gull- og alumini-

umsleder til enten Au eller Al kontaktflater. En kile-formet kontakteringsnål ble benyttet (wedge-wedge bonding) og svært reproduerbare resultater ble oppnådd.

Bevis for TMR med flere distinkte motstandsnivåer mellom helt parallelle og helt anti-parallelle magnetiske innretninger, samt TER med resistiv svitsjing blir presentert. Resultatene for TMR indikerer flere mellomliggende magnetiske innretninger som er stabile og kontrollerbare uten å rotere det påtrykte magnetiske feltet vekk fra parallell/anti-parallel hovedretning. I tillegg impliserer resultatene for TER at ferroelektrisk svitsjing er tilstede i enheten samtidig.

Undersøkelser for å kontrollere målesystemet, et Quantum Design VersaLab-system og en Electrical Transport Option (ETO), med Visual Basic-programmering, er gjort for å muliggjøre mer spesifikke elektriske målinger på de fabrikkerte MF-TJene. Lovende lav-strømmålinger av differensiell motstand og kapasitans versus DC strøm rapporteres. Disse blir regnet ut ved hjelp av kretsteknisk analyse og baseres på data fra AC lock-in-teknikken som benyttes av ETO.

Preface

This master thesis has been conducted at the Department of Electronics and Telecommunications (IET), NTNU, during the spring semester of 2016. It is the final fulfillment of a MSc degree in Nanoelectronics and Photonics from the integrated five-year study program of Electronics. I consider myself lucky to have been part of the Oxide Electronics Group at the department throughout the final year. This research group includes wonderful dedicated people who create a stimulating working environment for all involved, also their MSc students. Fortunately, I have the pleasure of continuing to be a part of the group as a PhD candidate from September.

The master thesis has been a continuation of the initial work done during the autumn project in the fall of 2015 [1]. Fabrication was done at the NTNU NanoLab and measurements at the laboratories of the department. I must admit that I am now greatly looking forward to a few weeks break. It has been a fantastic journey in practical and theoretical learning over the past ten to eleven months, but also a vast amount of work.

Acknowledgments

Firstly, my supervisors professor Thomas Tybell and PhD candidate Torstein Bolstad deserve sincere thanks for all help, support and enthusiasm throughout the year. You have guided me along the way and pushed me in interesting directions, yet loosely enough so that I have been able to form my own project. I also thank Associate Professor Erik Folven, Professor Jostein Grepstad, and the rest of the PhD candidates in the group for being most helpful whenever I have had questions. Tore Landsem at the department's machine shop has been very supportive in creating brass shadow masks for the initial phases of the work, and later for making a very nice PCB stand for the wire-bonder tool. Gaurav Sharma also deserve thanks for interesting discussions and input with regard to wire-bonding and issues with the VersaLab system.

The fabrication part of the thesis has been done at NTNU Nanolab, and the Research Council of Norway is acknowledged for the support to the Norwegian Micro- and Nano-fabrication Facility, NorFab. I would like to express my sincere thanks to all the engineers at NanoLab, Espen Rogstad and Mark Chiappa in particular, for being so helpful and forthcoming whenever I had any questions or issues.

I would like to give my greatest thanks to my wonderful parents and sisters who always stand by me and support me in whatever I do.

Finally, I must honor my dearest friend and loving girlfriend Karianne Ellefsen for always being so supportive and motivating me during all these long hours.

Kristoffer Kjærnes
Trondheim, July 31, 2016

Contents

Problem Description	iii
Abstract	v
Sammendrag (Norwegian Abstract)	vii
Preface	ix
List of Figures	xvii
List of Tables	xix
List of Abbreviations	xxii
1 Introduction	1
1.1 Document Structure	3
2 State of the Art	5
2.1 Oxide Interfaces and Electronics	5
2.2 Tunnel Junctions and Applications	8
2.2.1 Magnetic Tunnel Junctions	8
2.2.2 Ferroelectric Tunnel Junctions	9
2.2.3 Multiferroic Tunnel Junctions	13
2.2.4 Future Prospects	17
2.3 Summary and Focus of this Thesis	18
3 Theory	21
3.1 Electrodynamics of Continuous Media	21
3.2 Multiferroic Materials	23
3.2.1 Coupling of Order Parameters	23
3.2.2 Heterostructures of Ferrioc Materials	24
3.3 Electron Tunneling	25
3.3.1 Magnetic tunnel junctions	26

3.3.2	Ferroelectric tunnel junctions	28
3.3.3	Multiferroic tunnel junctions	30
3.3.4	Direct Tunneling and Brinkman’s Model	31
3.3.5	Fowler-Nordheim Tunneling	32
3.3.6	Thermionic Emission/Injection	33
3.3.7	Other Conduction Mechanisms	33
3.3.8	Electrical Characteristics of Ferroelectric Barriers	34
4	Materials and Methods	39
4.1	Model System	39
4.1.1	Strontium Titanate	40
4.1.2	Lanthanum Strontium Manganite	41
4.1.3	Barium Titanate	43
4.1.4	Permalloy	45
4.1.5	Passivation and Electrical Contacts	46
4.2	Experimental Methods	46
4.2.1	Electron Beam Lithography	46
4.2.2	Plasma Ashing and Descumming	48
4.2.3	Physical Deposition Techniques	48
4.2.4	Profile Measurements	51
4.2.5	Scanning Electron Microscopy	52
4.2.6	Atomic Force Microscopy	52
4.2.7	Wire-bonding	53
4.2.8	Vibrating Sample Magnetometry	53
4.2.9	Electrical Transport Measurements	54
4.2.10	Four-point-probe and Four-wire Measurements	57
4.3	Data Analysis	58
5	Sample Design and Layout	61
5.1	Considerations for the Sample Layout	61
5.1.1	Junction Area, Shape and Uniformity	62
5.1.2	Ohmic Contacts	64
5.1.3	Bond Pad Adhesion	65
5.1.4	Measurement Layout	66
5.1.5	Circuit Capacitance	66
5.2	The Sample Design	66
5.2.1	Physical Design and Layout	67
5.3	Circuit Analysis	69
5.3.1	The Tunnel Junction as a Circuit Element	70
5.3.2	The Complete Circuit	73

6	Sample Fabrication	77
6.1	Electron Beam Lithography	78
6.1.1	Spin-coating	79
6.1.2	Exposure dose and development time	80
6.1.3	Proximity effects	82
6.1.4	Descumming	83
6.2	The Fabrication Process	84
6.2.1	Deposition Rates	84
6.2.2	Etch Rates	85
6.2.3	Stage 1 – Top Electrode Deposition	88
6.2.4	Stage 1-1 – Top Electrode Etch (O-MFTJ only)	91
6.2.5	Stage 2 – Bottom Electrode Contact Formation	95
6.2.6	Stage 3 – Insulation Layer Deposition	96
6.2.7	Stage 4 – Deposition of Contact Pads	98
6.2.8	The alternative fabrication approach	101
6.3	Wire-bonding	102
6.4	Sample Fabrication Summary	106
7	Electrical Characterization	111
7.1	Initial TMR and TER Measurements	111
7.2	Scripting the Electrical Transport Option	114
7.2.1	Added Functionality	115
7.2.2	Data File Organization	116
7.2.3	Differential Resistance by Scripting	116
7.2.4	Challenges and Remaining Work	118
7.2.5	ETO Scripting Summary	119
7.3	Resistance versus Temperature	119
7.3.1	LSMO in-plane Magnetoresistance	119
7.3.2	Assessing the Pt/LSMO Contact Resistance	121
7.3.3	Evaluation of Contact Layout and Interface Area	124
7.4	Current-Voltage Measurements	125
7.4.1	Numerical Derivatives of IV-curves	128
7.5	Differential Resistance versus DC Current	130
7.5.1	Taking Advantage of AC Lock-in Data	133
7.6	TMR and TER Measurements	138
7.7	Validity of the Measurements	139
8	Discussion	141
8.1	Sample Design and Layout	141
8.2	Fabrication	142
8.3	Electrical Characterization	144
8.4	Future Work	146
9	Conclusion	149

Bibliography	151
Appendix	167
A Measurements	167
A.1 Contact Resistance	167
A.2 Current-voltage Curves	169
A.3 Differential Resistance and Conductance	169
A.3.1 Calculations for AC lock-in Measurements	169
A.4 Magnetic Measurements	173
B Fabrication	175
C Substrate Symmetries	179
D Program Scripts	181
D.1 MultiVu Sequence	181
D.2 WinWrap Basic	185
D.3 Matlab	201

List of Figures

2.1	TMR and tunnel conductance at room temperature for various MTJs.	9
2.2	Record TMR for a LSMO/STO/LSMO MTJ.	10
2.3	Metal-ferroelectric-metal tunnel junction prototype and IV characteristics.	11
2.4	Methods for revealing ferroelectric switching and TER in FTJs. . .	12
2.5	Example of state of the art TER and memristive behavior in a FTJ.	13
2.6	Example of state of the art TER and composite barrier in a FTJ. .	14
2.7	First experimental realization of a MFTJ.	14
2.8	First artificial MFTJ showing four resistance states at room temperature.	16
2.9	Artificial MFTJ showing eight resistance states, i.e a 3-bit memory cell.	17
3.1	Coupling parameters between polarization, magnetization and strain.	24
3.2	Quantum mechanical tunneling.	25
3.3	Electron tunneling through an insulating barrier.	26
3.4	Tunnel magnetoresistance.	27
3.5	Ferroelectric tunnel junction.	29
3.6	Various tunnel junctions shown schematically.	31
3.7	Trapezoidal tunnel barrier potential and different tunneling mechanisms.	35
3.8	Electron transport across ultrathin ferroelectrics.	36
4.1	Qualitative sketches of the asymmetric permalloy MFTJ and the all-oxide MFTJ.	40
4.2	Ideal cubic perovskite SrTiO ₃	41
4.3	The hexagonal LSMO crystal structure and its projection along the hexagonal $\langle 001 \rangle$ axis.	42
4.4	Cubic and tetragonal representations of perovskite BaTiO ₃	44
4.5	BEAMER flow diagram for bulk/sleeve separation and proximity effect correction.	49
4.6	Etch rate determination by step profile measurements.	51

4.7	Realistic circuit diagram of a four-point-probe measurement. . . .	58
4.8	ETO vertical puck PCB with schematic representations of proper and improper 4-wire measurements.	59
5.1	Ohmic versus rectifying contacts for electrical measurements. . . .	65
5.2	Cross section view of the final MFTJs.	68
5.3	Top-down overview of the final 15 μm MFTJ.	69
5.4	3D model with a cross sectional cut of the final MFTJs.	70
5.5	Parallel RC-circuit and its equivalent circuit symbol representing a tunnel junction.	71
5.6	Circuit diagram for the MFTJs with alternating current excitation.	73
5.7	Circuit diagram for the MFTJs with direct current excitation. . . .	74
6.1	PMMA exposure dose test.	81
6.2	PMMA test pattern and sidewall profile from exposure in 100 kV EBL system with 1000 $\mu\text{C cm}^{-2}$ dose.	82
6.3	PMMA exposure proximity effects.	83
6.4	Step edge etch profile for titanium as imaged by SEM.	87
6.5	MFTJ fabrication stage 1 – top electrode deposition.	89
6.6	Developed structures from fabrication stage 1.	90
6.7	Top electrode profiles and SEM images after fabrication stage 1. . .	91
6.8	All-oxide MFTJ fabrication stage 1.1 – Ar sputter etch to define free-standing LSMO/BTO.	92
6.9	SEM micrographs of etched top electrodes for the all-oxide MFTJs.	93
6.10	O-MFTJ top electrode profiles and AFM images after fabrication stage 1-1.	94
6.11	MFTJ fabrication stage 2 – bottom electrode etch and deposition.	95
6.12	MFTJ fabrication stage 3 – insulation layer deposition.	97
6.13	SEM micrographs of the insulation layer surface after stage 2. . . .	98
6.14	MFTJ fabrication stage 4 – electrical contact deposition.	99
6.15	SEM micrographs of top contact layer surface.	100
6.16	Test sample for wire-bonding on small pads.	105
6.17	Finished sample with MFTJs of different size aligned in a grid. . .	109
6.18	MFTJs numbered for identification.	110
7.1	Initial evidence for TMR and TER from autumn work sample P51006.	113
7.2	$R_{\text{LSMO}}(T)$ for sample P60212.	120
7.3	Magnetoresistance versus temperature for sample P60212.	121
7.4	$R_{\text{LSMO}}(T)$ in zero magnetic field for sample P60212 with and without contact resistances.	122
7.5	2nd and 3rd harmonics for sample P60212 with and without contact resistances.	123
7.6	IV-curves for samples P60403 and P60501 for $I_{\text{dc}} = \pm 10 \text{ nA}$	125

7.7	IV-curves for samples P60403 and P60501 for $I_{dc} = \pm 50 \mu\text{A}$	126
7.8	Differential resistance and conductance versus V_{dc} for sample P60501, current sweep both ways between $\pm 10 \text{ nA}$	129
7.9	Differential resistance and conductance versus V_{dc} for samples P60403 and P60501, current sweep from $+50 \mu\text{A}$ to $-50 \mu\text{A}$	130
7.10	Measured dV/dI versus I_{dc} for samples P60403 and P60501.	131
7.11	Converted dI/dV versus V_{dc} for samples P60403 and P60501 based on dV/dI data.	132
7.12	dV/dI versus I_{dc} for samples P60403 and P60501 based on in-phase and quadrature voltage data.	136
7.13	Capacitance versus I_{dc} for samples P60403 and P60501 based on in-phase and quadrature voltage data.	137
A.1	Relative share of measured resistance ascribed to contact resistance in sample P60212.	168
A.2	IV-curves for samples P60403 and P60501 for $I_{dc} = \pm 200 \text{ nA}$	169
A.3	Differential resistance and conductance versus V_{dc} for samples P60403 and P60501, current sweep from $+10 \text{ nA}$ to -10 nA	171
A.4	Differential resistance and conductance versus V_{dc} for samples P60403 and P60501, current sweep from $+200 \text{ nA}$ to -200 nA	172
A.5	Saturation magnetization measurements on sample P60214.	173
A.6	Magnetization versus magnetic field versus temperature measurements on sample P60214.	174
B.1	Titanium step profile after sputter-etching in the AJA system.	175
B.2	MFTJ fabrication stage 2 – insulator deposition and etching by PECVD and ICP-RIE.	176
B.3	Signs of boiling or dissolving PMMA during e-beam evaporation.	177
B.4	EBL mask overview, final sample fabrication.	178
C.1	Sample orientation and important crystal directions.	179
C.2	STO substrate symmetries.	180

List of Tables

2.1	List of existing reports on tunnel electroresistance and magnetoresistance with BaTiO ₃ barriers.	19
3.1	Electromagnetic quantities and their units.	22
5.1	Diameter, area and capacitance of the MFTJs.	75
6.1	Deposition rates and parameter details for sputtering of various materials in the AJA system.	84
6.2	Expected etch rates by argon sputter etching.	85
6.3	Overview of test samples used for fabrication process development.	86
6.4	Measured etch rates by argon sputter etching.	86
6.5	Wire-bonding parameters for aluminium wire to aluminium test pads.	103
6.6	Wire-bonding parameters for aluminium wire to gold and aluminium pads on oxide samples.	104
6.7	Wire-bonding parameters for gold wire to aluminium and gold pads on oxide samples.	104
6.8	Overview of final fabricated samples.	107
6.9	Overview of top electrode diameter on final fabricated samples.	107
6.10	Fabrication process flow for the final samples.	108
6.11	List of known faulty MFTJs on final samples.	110
7.1	Measured TMR effects from sample P51006.	112

List of Abbreviations

AFM	Atomic Force Microscopy
BTO	BaTiO ₃
CMR	Colossal Magnetoresistance
CMRR	Common-Mode Rejection Ratio
DFT	Density Functional Theory
DI	De-ionized water
DSP	Digital Signal Processor
EBL	Electron Beam Lithography
ETO	Electrical Transport Option
FTJ	Ferroelectric Tunnel Junction
ICP-RIE	Inductively Coupled Plasma Reactive Ion Etching
IPA	Isopropyl alcohol
LCMO	La _{0.5} Ca _{0.5} MnO ₃
LSMO	La _{0.7} Sr _{0.3} MnO ₃
MeRAM	Magnetoelectric Random Access Memory
MFTJ	Multiferroic Tunnel Junction
MTJ	Magnetic Tunnel Junction
PEC	Proximity effect correction
PECVD	Plasma Enhanced Chemical Vapor Deposition
Permalloy	Ni _{0.81} Fe _{0.19}

PFM	Piezoresponse-Force Microscopy
PLD	Pulsed Laser Deposition
PMMA	Poly(methyl methacrylate), $(C_5O_2H_8)_n$
ReRAM	Resistive Random Access Memory
SEM	Scanning Electron Microscopy
SRO	$SrRuO_3$
STO	$SrTiO_3$
TER	Tunnel Electroresistance
TMR	Tunnel Magnetoresistance
VSM	Vibrating Sample Magnetometer
WWB	WinWrap [®] Basic

Chapter 1

Introduction

In the second half of the last century the world has seen a monumental technological revolution, especially within the field of solid-state electronics. In accordance with the naming of earlier times in history, the present time is sometimes referred to as the «silicon age», or «the information age», due to the enormous influence silicon semiconductor science has had on our society. Today however, the semiconductor industry is faced with fundamental problems of quantum mechanical limitations in miniaturization [2]. To continue the increase of device performance, some research fields show a shift of focus towards the incorporation of more functional properties into electronic devices, making them more multifunctional. A promising technology currently under development and subject to strong benefits from miniaturization, is multi-state resistive memory. This technology aims to combine the best properties of magnetic and ferroelectric memories into the same device.

Multiferroic materials are currently subject to large research efforts for enabling multifunctional device technology. A multiferroic material typically exhibit electric and magnetic ordering simultaneously and in the same phase [3, 4, 5]. In principle, this can advance the control of magnetism with electric fields, or electric polarization with magnetic fields [6]. Furthermore, with or without the presence of a magnetoelectric coupling between the electric and magnetic orders, the two different order parameters bring about two degrees of freedom which can be highly useful in memory technology [7].

The tunnel magnetoresistance (TMR) effect is the phenomenon of spin dependent transport of electrons through a thin insulating barrier [8, 9, 10]. A TMR device consists of two ferromagnetic electrodes separated by a thin insulating tunnel barrier, a structure known as a magnetic tunnel junction (MTJ). Two different resistance states are found for a current tunneling through the MTJ when the electrodes are aligned parallel or antiparallel. The tunnel electroresistance (TER) effect is an analogous phenomenon with electrons tunneling across a ferroelectric insulating barrier between two metal electrodes [11, 12, 13]. Such a

structure is called a ferroelectric tunnel junction (FTJ). Depending on the ferroelectric polarization direction relative to the direction of tunneling, two different resistance states occur. Consequently, TMR provides for non-volatile magnetic memory, while TER can provide non-volatile electric memory.

A combination of TMR and TER in the same device is one of many possibilities with multiferroic materials, and the combination can lead to four or more distinct resistance states [13, 14, 15]. The combined device is hence called a multiferroic tunnel junction (MFTJ). Four or more resistance states means the possibility for two or more bits per memory cell, which is desirable for increased storage density and more cost effective devices. Different materials with separate ferroic orders may just as well, or even better, be used to compose an overall multiferroic device [16]. A number of advantages follow from using a composition of materials that have separate ferroic orders instead of one single-phase multiferroic material. There are more materials to choose from, and the magnitudes of the effects one wants to exploit are often larger [4]. Also, the interfaces between different materials are themselves major sources for useful functional properties [2]. Moreover, the use of different materials provides better freedom of device design and enables the engineering of specific functional properties or a materials-by-design approach [2, 6, 17, 18].

Complex transition-metal oxides have been, and still are, under heavy investigation for the use as multiferroic materials or systems in the past few decades [19, 20, 21]. This is motivated by the wide range of order parameters and variety of tunable physical properties that are found for example in the perovskite family of materials [19]. The mixed-valence manganites are a group of magnetic oxides that have received particularly much attention, because of their remarkable relationship between structure, electronic and magnetic properties [22]. One of the striking properties is that they show a very large negative magnetoresistance, called colossal magnetoresistance (CMR), close to the ferromagnetic to paramagnetic transition temperature, which is associated with a metal-insulator transition [22, 23]. Moreover, they are termed «half-metallic ferromagnets», owing to a very large spin-polarization at the Fermi level [19]. What this means is that the material is metallic for electrons with a preferred (majority) spin direction, while it is nearly insulating for electrons with the opposite (minority) spin direction.

One specific solid solution of a mixed-valence manganite is $\text{La}_{0.7}\text{Sr}_{0.3}\text{MnO}_3$ (LSMO), which is a ferromagnetic half-metal below about 360 K [19]. For this reason LSMO has been used extensively as electrode material in (001)-oriented epitaxial MTJs, and more recently MFTJs, to enable very large TMR effects [24, 25, 26, 27, 28]. Yet, no studies exist where the tunneling properties of (111)-oriented films have been investigated, due to difficulties in growing high-quality oxide interfaces with this orientation [17]. Previous work in our group have provided ways to fill this gap, and we are now able to grow (111)-LSMO/SrTiO₃ heterostructures routinely with atomic layer precision [29, 30].

Recently, Hallsteinsen et al. [31] studied the magnetic anisotropy of thin

LSMO films on (111)-oriented SrTiO_3 (STO). No macroscopic easy or hard axes were observed, thus giving a uniform in-plane magnetic anisotropy. However, on a local level a 6-fold magnetic easy-axis was found along the $\langle 1\bar{1}0 \rangle$ and $\langle 11\bar{2} \rangle$ in-plane directions [31]. Hence, it is of interest to study how the local magnetic domain reorientation along these different easy-axes may give rise to intermediate resistive states during magnetization switching. Moreover, $\text{Ni}_{0.81}\text{Fe}_{0.19}$ (Permalloy) and LSMO(111) has already been verified to work in a MTJ structure [1], while LSMO(111) grown on ferroelectric BaTiO_3 (BTO) show much larger coercive fields than structures with BTO grown on LSMO(111).¹ Hence, both permalloy/BTO/LSMO(111) and LSMO/BTO/LSMO(111) structures are anticipated to show promising results in MFTJs.

In this work, two types of multiferroic tunnel junctions were fabricated for simultaneous electrical characterization of TMR and TER in (111)-oriented junctions. Both junction types used BTO as ferroelectric insulating tunnel barrier and LSMO as the ferromagnetic bottom electrode. The first type utilized permalloy as the ferromagnetic top electrode, and effectively gave an asymmetric MFTJ. The second type used an epitaxial LSMO top electrode, and thus represented an all-oxide MFTJ. The electrical measurements were performed with a Quantum Design VersaLab system equipped with an Electrical Transport Option (ETO). For more versatile measurements, the ETO module was programmed using the WinWrap[®]Basic scripting language. A part of the work was associated with finding out how the ETO measurement modes can be controlled by scripting, and if possible, the development of measurement scripts for TMR, TER and temperature dependent combinations of the two.

1.1 Document Structure

The thesis is split into a total of 9 chapters. To provide a deeper insight into the early and current state of the research field, following first is a more thorough introduction to oxide electronics and (multi)ferroic tunnel junctions in Chapter 2. Thereafter a presentation of the most relevant theory is given in Chapter 3, followed by detailed descriptions of the model system and experimental methods in Chapter 4. Since the experimental work consists of three main phases, results and discussions are presented in three separate chapters 5, 6 and 7, for the design and layout, fabrication, and measurement parts, respectively. Considerations and results are discussed locally in each chapter, and a final discussion of common trends and the overall project is given in Chapter 8. Suggestions for future work is also included here. Finally, some conclusive remarks are presented in Chapter 9.

¹Results from unpublished parallel work by PhD candidate Torstein Bolstad.

Chapter 2

State of the Art

In this chapter, a brief literary review is presented. The goal is to give an introduction to the research field's state of affairs. This includes what has already been achieved, where the recent research is focused, and some researchers' thoughts on what might reveal itself in the future. Hopefully, the reader will have a notion of how the current work fits into the bigger picture at the end of the chapter.

2.1 Oxide Interfaces and Electronics

Conventional electronic devices like transistors, solid-state lasers and solar cells rely strongly on interfacial phenomena [2], and as Nobel laureate Herbert Kroemer stated; "Often, it may be said that *the interface is the device*" [2, 32]. In ordinary semiconductors like silicon, the interface effects give rise to many interesting phenomena both from a fundamental and applications point of view, while the bulk material is rather uninteresting as the electrons behave close to free particles there. In transition-metal oxides, however, both bulk and interfaces provide arenas for interesting phenomena. Regularly spaced ions, especially the oxygen ions, interact with the electrons, and the electrons interact among themselves, in ways that make them deviate from free-particle behavior [2].

Over the past two decades research in the growth and synthesis of transition-metal oxide materials and interfaces have flourished, due to the many remarkable physical properties that they exhibit [17]. Especially the interfaces between these material systems are interesting, because in many of them the electrons are strongly correlated. This means that any single electron's motion is crucially dependent on the many neighboring electrons' movements [2, 17]. Strongly correlated electrons can provide interesting and useful phenomena like magnetism with high Curie temperatures, high-temperature superconductivity, metal-insulator transitions, multiferroicity, and colossal magnetoresistance [2, 17]. However, it has been difficult to realize these systems in practice, due to a strong dependency

on near perfect crystalline quality of the parent material. With an increasing amount of experience in how to fabricate high quality interfaces during the two last decades, the challenges are gradually being resolved [2, 17].

Oxide interfaces typically possess higher areal densities of carriers and shorter electron confinement lengths than is found in the ordinary semiconductor interfaces [17]. In addition the parent materials often have nearly ionic bonds, at least much less covalent bonds than ordinary semiconductors [2, 17]. These properties imply that there must be large gradients in the electrochemical potential, which may drive unwanted reconstructions in the chemical or structural phases [17]. On the other hand, gaining decisive control over such reconstructions will provide exciting opportunities. This challenge is considered equally important as was the problem of passivating semiconductor surfaces in the 1940s [17].

The opportunities may be realized by gaining control over less common crystal orientations enabling interfaces across the (110) or (111)-planes for example, by using carefully selected substrates to control the epitaxial strain, or by studying how interfaces between an oxide and non-oxide compound behave [17]. The two first methods are used for the material systems in the present work, as will become clear later. Recently, coworkers in our research group have made great progress in controlling growth along the [111]-direction of SrTiO_3 substrates, with abrupt (111)-planar interfaces as the ultimate goal [29, 30, 31]. Achieving single termination across such interfaces is difficult due to the strong polarity of the crystal plane, which for example is ± 4 on $\text{SrTiO}_3(111)$ terminated by Ti^{4+} or SrO_3^{4-} , respectively [30]. It is emphasized that substantial gain is within reach by overcoming these difficulties and enabling such control. For example, it is pointed out that intriguing systems as artificial topological insulators may be fabricated if reliable growth along these directions is made possible [17].

So how can oxide materials and their interfaces be utilized for novel electronic devices? One remarkable potential device is the *Mottronic* device which is thought to be possible by taking advantage of metal-insulator transitions in Mott insulators [17]. By changing the temperature or applied electric field over oxides exhibiting this property, a sharp on-off transition can be useful for transistor devices or resistive random access memories (ReRAM) [17, 33, 34].

Spintronic devices are already becoming largely explored in oxide materials as well as conventional semiconductors [19, 35]. Spintronics is a field that brings together many different disciplines with the goal of actively manipulating the spin degrees of freedom in solid-state systems [35]. Oxides are particularly interesting in spintronics owing to their supreme spin polarization. Furthermore, since transition-metal oxides provide many ferroic degrees of freedom, they have the possibility of providing multifunctional devices that add more functionality to the spintronic platform [19]. During the mid 1990s, research in room-temperature MTJs expanded when it became clear that highly sensitive magnetic-field sensors, magnetic read heads and non-volatile magnetic memory could be made possible for applications at normal temperatures [35]. Over the last two decades, these concepts have found commercial use especially within the storage industry as

read-heads in hard disk drives or active memory cells in MRAM [36]. Applied spintronics is currently more relevant than ever, as the company Everspin recently announced that they will deliver 256 Mb and 1 Gb MRAM chips this year, based on MTJs with spin-transfer torque for writing [37]. According to Everspin, these devices operate at the speeds of DRAM and have write speeds five orders of magnitude larger than NAND flash memory. These merits may enable a major shift in the way mainstream dynamic and solid-state memories work over the coming years.

Multiferroics can be viewed as a family of materials in the field of spintronics [19]. Owing to their inherent multifunctional nature with two or more simultaneous ferroic orders [3, 21], multiferroics are naturally promising for enabling more functionality in electronic devices that are subject to a continuing miniaturization [19]. By taking advantage of multiple ferroic orders and the potential coupling between them, very interesting applications can be proposed. For memory applications again, the magnetoelectric coupling between magnetic and electric orders in multiferroic materials should enable a FeRAM written by a magnetic field, or more interestingly a MRAM written by an electric field [19]. The latter was suggested as a magnetoelectric random access memory (MeRAM) with the multiferroic material BiFeO_3 [7]. This should be possible by indirectly flipping the free layer of a MTJ through the direct coupling between the anti-ferromagnetic and ferroelectric orders of BiFeO_3 [7]. Recent reports, however, have shown prototypes of MeRAMs using the conventional MgO insulating barrier and CoFeB-based ferromagnets with different voltage controlled switching schemes [38, 39, 40]. If these are successful, they will even rival the MRAMs noted above, primarily in terms of energy efficiency, but also on operating speed. Still, as will become clear later, multiferroic materials and devices show promise for even better MeRAMs, if their ferroic orders can be made sufficiently robust at normal temperatures and small scale. Again, this is where transition-metal oxides are significant.

Another emerging field in nanoscience has been coined *Nanoferronics* and lies at the heart of oxide interfaces, spintronics, multiferroics, nanoscale ferroelectricity, and correlated-electron systems [18]. Nanoferronics represent devices made from materials with ordered phases and phase transitions like ferromagnetism, ferroelectricity, ferroelasticity or ferrotoroidicity, and the potential couplings between them. Envisioned applications are logic devices with built-in memory, non-volatile switches for programmable logic architectures, or even new forms of computational schemes with more than two logic states [18]. At the present time, great efforts are laid down in order to find the best suited material systems for utilizing useful electronic devices that take advantage of these order parameters. Various tunnel junctions are especially promising candidates, as they are simple two-terminal devices with the possibility of changing logic state by varying the magnitude or polarity of the applied signal [18].

2.2 Tunnel Junctions and Applications

Tunnel junctions are an important family of devices in modern electronics. There are several groups of tunnel junctions; superconducting [41], magnetic, ferroelectric, ohmic [42] and multiferroic to name the most important ones. To restrict the scope of this part, only tunnel junctions for TMR and TER applications will be considered here, meaning magnetic, ferroelectric and multiferroic tunnel junctions. More details on how these work will be given in the next chapter. In the following, these types of tunnel junctions will be reviewed briefly and in sequence with some history and important contributions on the way towards the current situation.

2.2.1 Magnetic Tunnel Junctions

Research on MTJs was initiated by Julliere [8] in his well known work from 1975, but what later became known as TMR was not larger than 14 % at temperatures below 4.2 K for the particular system studied. Following that was 20 years of less scientific interest before Moodera et al. [9] presented large TMR effects at room temperature in 1995. In the meantime, the GMR effect had become superior to TMR by utilizing superlattices of ferromagnetic and normal metals [43]. Hence, GMR was indeed used by IBM for read-heads in hard-disk drives from 1997 [44]. However, as noted above, interest in TMR quickly gained pace after 1995 and eventually surpassed the merits of GMR [45, 46]. As the technology matured and became better than GMR, Seagate developed and introduced TMR to the market as read-heads for improved storage density in their hard-disk drives from 2002 to about 2006 [47, 48]. In parallel, corresponding research in highly spin-polarized transition-metal oxides increased, especially the mixed-valence manganites like LSMO [24, 25, 49, 50]. The reason for this was mainly the realization that large TMR ratios should follow from the use of highly spin-polarized ferromagnetic electrodes, as was clear from the inspection of Julliere's formula [8, 51, 52].

The study published by Moodera et al. [9] in 1995 sparked a considerable increase of TMR research, specifically aimed at room temperature applications. The key findings are reprinted in Figure 2.1 with magnetoresistance ratios versus magnetic field on the left, and tunnel conductance as a function of applied bias on the right. They reported TMR ratios of 11.8 %, 20 % and 24 % at 295 K, 77 K and 4.2 K, respectively. Moreover, they discussed the fact that TMR decreases significantly for junction biases above 0.1 V without being able to propose a reason for this [9]. The conductance versus junction bias on the right, shows the typical electric field dependency of the tunneling resistance. Parabolic dependence indicates direct tunneling, while other dependencies may indicate Fowler-Nordheim or inelastic thermal tunneling effects [51].

Following the above mentioned initial studies of TMR with the mixed-valence manganite LSMO [24, 25, 49, 50], Bowen et al. [26] could in 2003 report a record TMR ratio of 1850 % for LSMO/STO/LSMO MTJs at 4 K. The TMR decreased

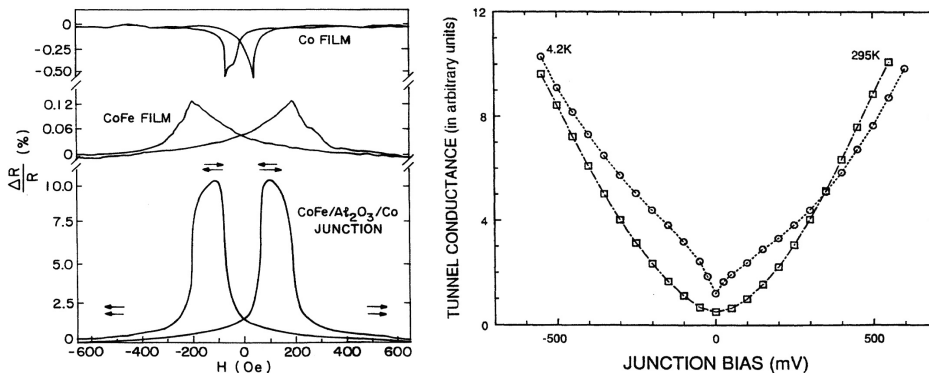


Figure 2.1: TMR and tunnel conductance at room temperature for various MTJs. Reprinted from reference [9]. **Left:** TMR ratio vs magnetic field in the film plane for a CoFe/Al₂O₃/Co MTJ at 295 K. In addition, the two upper curves show the varying film resistance (anisotropic magnetoresistance) for the two electrode materials as functions of magnetic field. **Right:** Tunnel conductance as function of applied DC bias for a CoFe/Al₂O₃/NiFe MTJ at 4.2 K and 295 K and zero magnetic field.

with increasing temperature, but were still 30% at 250 K. At the low temperature, the LSMO spin-polarization corresponded to 95% from the Julliere formula [26]. Figure 2.2 shows these results.

As far as the author is aware, Bowen et al. [26] has the publication with the largest TMR ratio recorded to date. Even though it is not comparable to the best TMR ratios at room temperature achieved by more conventional materials (e.g. [36, 48]), or the fact that LSMO cannot become a useful material for normal temperatures due to its loss of magnetism around 350 K [53], it stands as an example and may suggest that there might exist similar material systems that outperform existing devices at higher temperatures.

2.2.2 Ferroelectric Tunnel Junctions

FTJs were actually proposed by Esaki et al. [11] in 1971, before Julliere's paper on MTJs, but due to difficulties in fabricating high-quality ferroelectric thin films experiments with FTJs had to wait more than 30 years [18, 51, 54]. Moreover, it was believed that the lower thickness limit for ferroelectricity in thin films was relatively large at 10-100 nm, which would be too thick for tunneling phenomena to be dominating or possible at all [54]. However, Tybell et al. [55] showed in 1999 that ferroelectricity was indeed possible in ultrathin films of Pb(Zr_{0.2}Ti_{0.8})O₃ down to a thickness of 4 nm. This observation and corresponding theoretical predictions lead to a renewed interest in the field, and Rodriguez Contreras et al. [12] were the first group to report resistive switching in a FTJ in 2003.

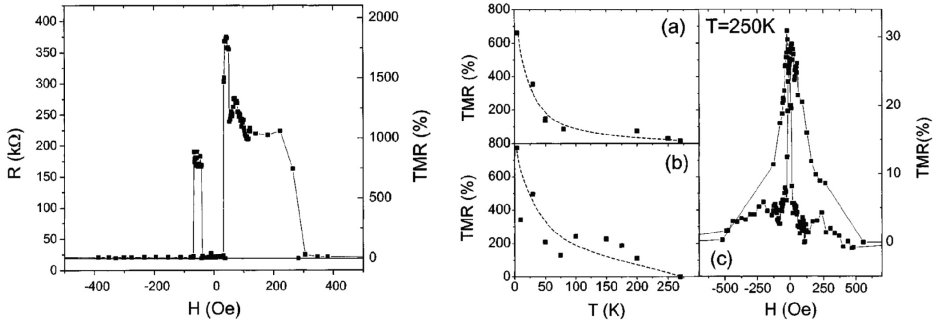


Figure 2.2: Record TMR for a LSMO/STO/LSMO MTJ. Reprinted from reference [26]. **Left:** Resistance and TMR vs magnetic field for a $5.6 \mu\text{m} \times 5.6 \mu\text{m}$ MTJ at 4.2 K. **Right:** Temperature dependence of the TMR measured with $V_{\text{dc}} = 10$ mV for two junctions: $2 \mu\text{m} \times 6 \mu\text{m}$ (a) and $1.4 \mu\text{m} \times 4.2 \mu\text{m}$ (b). TMR vs magnetic field at 250 K and $V_{\text{dc}} = 10$ mV (c).

Rodriguez Contreras et al. [12] fabricated asymmetric FTJs consisting of Pt and SrRuO₃ electrodes separated by a 6 nm thick Pb(Zr_{0.52}Ti_{0.48})O₃ ferroelectric barrier. The junction area was $200 \mu\text{m}^2$. The device structure and measured IV-characteristics can be seen in Figure 2.3. Resistive switching is readily apparent in the IV-characteristics as an abrupt voltage decrease or increase at $V_{\text{switch}}^+ = 0.86$ V and $V_{\text{switch}}^- = -0.54$ V, respectively, for an incremental increase of the applied current. The curves are noted with numbers from 1 to 8 for the direction of current sweep. At points 3 and 7, the low and high resistance states are stable after switching has occurred, and the arrows note that both an increasing and decreasing current will follow the same IV-curve thereafter. The high and low resistance corresponding to the two distinct IV-curves at the origin were 4.3 k Ω and 1.1 k Ω , respectively. Important to note, however, is the fact that the authors could not conclude, only argue for the likelihood, that ferroelectric switching was the reason for the resistive switching.

The experimental findings were soon followed by theoretical considerations, notably the ones by Zhuravlev et al. [56] and Kohlstedt et al. [54], and various experimental studies. To assess the ferroelectric contribution to resistive switching, two groups used measurement systems for ferroelectric capacitors with success [57, 58], followed by three reports using piezoresponse-force microscopy (PFM) [59, 60, 61]. The latter seems to have become the preferred method in subsequent studies, since it gives direct evidence for tunnel electroresistance from polarization switching in the barrier [51]. These two methods are shown in Figure 2.4 with the ferroelectric capacitor measurement systems on the left and piezoresponse-force on the right. Ferroelectric hysteresis curves with polarization versus electric field (up left) is calculated from the IV-characteristics taken at high and low excitation frequencies (down left). The total current (black line, down left) is the sum of ferroelectric displacement current caused by the switching

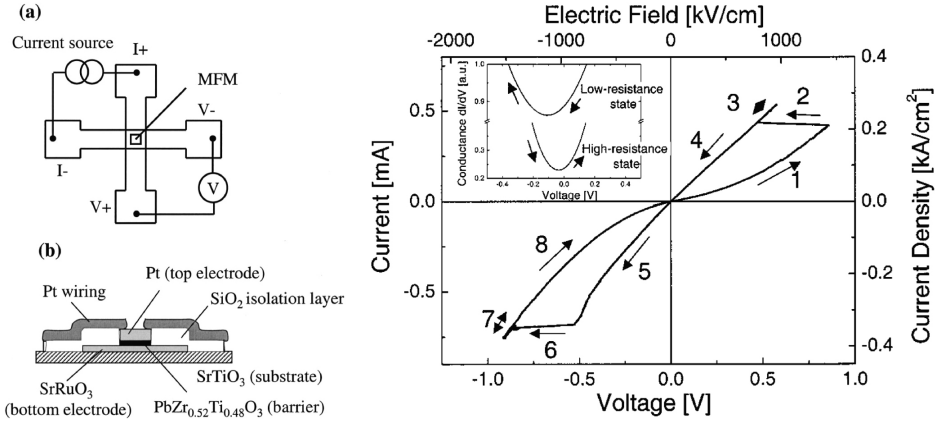


Figure 2.3: Metal-ferroelectric-metal tunnel junction prototype and IV characteristics. **Left:** The FTJ cross-strip geometry as seen from above including measurement schematics in (a), and the FTJ cross section in (b). **Right:** The corresponding IV-characteristics from a DC current-sweep (10 minutes for one cycle). The inset shows the differential conductance calculated from the high- and low-resistance IV-curves. Compiled from reference [12].

of the spontaneous polarization, junction leakage current, and dielectric displacement current [58]. At low-frequency excitation both displacement currents can be neglected. Thus, by taking the difference between the high- and low-frequency excitations, the displacement current (primarily ferroelectric) can be found and integrated to get the polarization charge (top left) [58]. Piezoresponse-force microscopy data is shown on the right side. Opposite poling voltages have been applied to the different areas of the film and the resulting piezoresponse phase angle (top right) and resistance (middle right) are subsequently mapped. The resistance modulation resulting from the opposite poling voltages is also shown after a lateral scan (down right) [60].

In the following years up until now a number of publications have been made, some of which will be listed in the summary below. To end the part on FTJs, two publications will be used. The first is a report by Wen et al. [62] on FTJs with one semiconducting (Nb:SrTiO_3) and one metallic (Pt) electrode. The hysteretic dependence of resistance and the on/off conductance ratio as functions of poling voltage are shown in Figure 2.5. The large difference in polarization charge shielding length of the semiconducting and metallic electrodes resulted in an off/on ratio of about 10^4 . Moreover, the device behave as a memristor with exponential resistance increase as function of negative poling voltage. This is still the record holder for largest on/off resistance ratio in FTJs, as far as the author is aware. The second report is by Wang et al. [63], who fabricated FTJs consisting of composite $\text{BaTiO}_3/\text{SrTiO}_3$ barriers with metallic Au/Ti and SrRuO_3 electrodes. The essentials of this study can be seen in Figure 2.6. The idea of using a

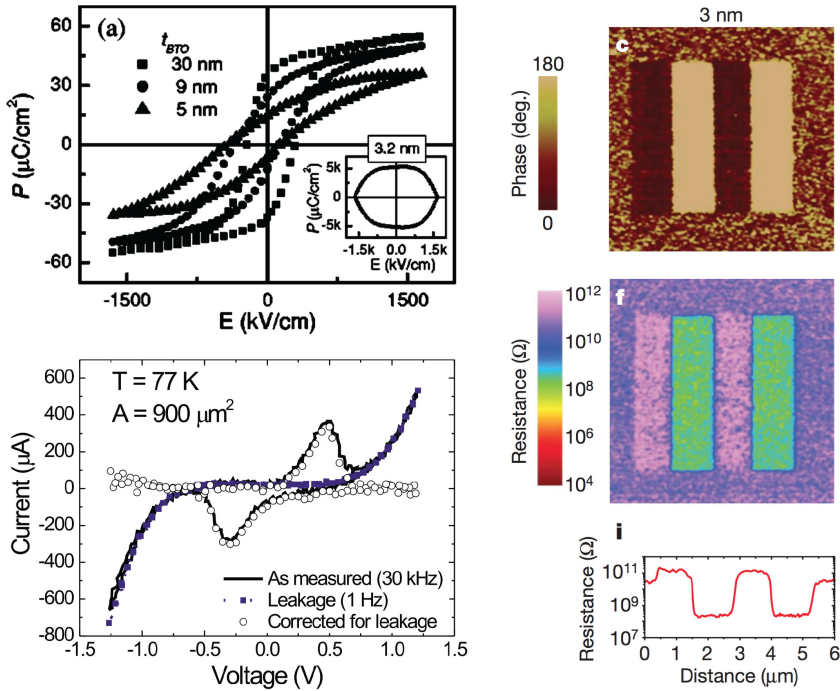


Figure 2.4: Methods for revealing ferroelectric switching and TER in FTJs with BaTiO₃ barriers (different substrates/electrodes). **Left:** Top; polarization vs electric field (from [57]) giving ferroelectric hysteresis. Bottom; IV-characteristics taken at two different sweep frequencies to reveal the ferroelectric displacement current (from [58]). **Right:** Piezoresponse-force phase map (top), conductive-tip atomic force microscopy resistance map (middle), and lateral resistance scan (bottom) taken from [60].

composite barrier was to limit the relatively large leakage current that has been problematic for device applications with BaTiO₃ barriers [63]. The left part of the figure shows how the composite barrier (solid band profiles) compare to a regular single barrier profile (dotted band profiles) for the two polarization directions. All devices had a nominal thickness of 10 unit cells (≈ 4 nm) with x unit cells of BTO and $10 - x$ unit cells of STO. The middle part (a-d) shows IV-curves for the on and off states for a varying BTO thickness, and the rightmost part (e-f) shows the hysteretic resistance dependence and piezoresponse force phase/amplitude as functions of poling voltage. In e) a single barrier (BTO only) is also shown for comparison, both curves were read at -1.1 V. The maximum off/on ratio was about 10^3 for a 6 unit cells BTO + 4 unit cells STO barrier. The authors conclude that their new approach deal with two known FTJ issues; the large leakage current for thin barriers and the small tunneling current for thicker barriers [63].

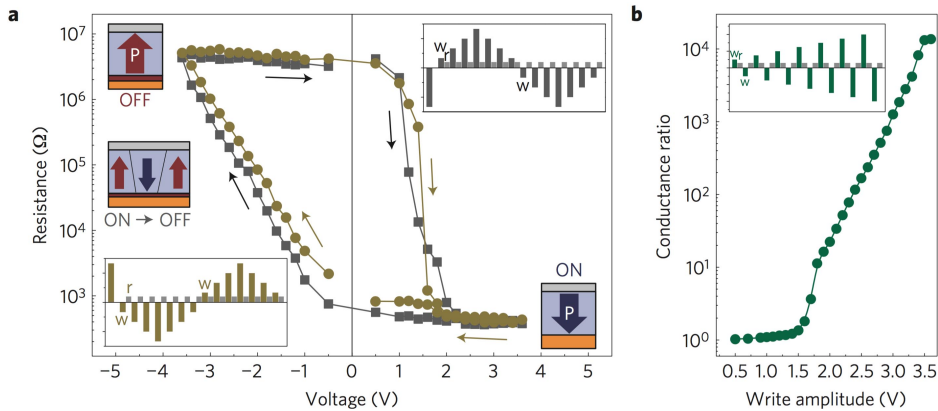


Figure 2.5: Example of state of the art TER and memristive behavior in a FTJ, from reference [62]. **(a):** Resistance hysteresis loop with dark squares (green circles) measured using the pulse train shown in the bottom-left (top-right) inset. The device is preset to the ON (OFF) state by a positive (negative) 3.6 V pulse. The domain evolution is shown schematically in the bottom-right, top-left and middle-left insets for the ON, OFF and intermediate (ON \rightarrow OFF) states, respectively. The pulse trains are composed of write pulses (w) following a triangular profile between +3.6 and -3.6 V and read pulses (r) of +0.1 V following each write pulse. **(b):** Conductance ratio as a function of write amplitude. The measurement starts from an unpolarized state. At a certain write amplitude, a pair of write pulses with opposite polarity is applied, as illustrated in the inset. The data points are the ratio between tunneling currents collected by +0.1 V read (r) pulses after the positive and negative write (w) pulses.

2.2.3 Multiferroic Tunnel Junctions

A natural consequence of the quickly developing knowledge on MTJs and FTJs at the beginning of the new millennium was a combination of the two concepts. Tsymbal and Kohlstedt [13] discussed some of the possibilities with this type of structures along with their presentation of the dominating physics in FTJs. There are in principle two types of MFTJs; those composed of a single-phase multiferroic material and a ferromagnetic electrode, or the artificial ones where a ferroelectric insulator is sandwiched between two ferromagnetic electrodes. The first is similar to a pure spin-filter [51], but where the ferromagnetic insulator is also ferroelectric. The second is effectively a MTJ with a ferroelectric barrier, or similarly a FTJ with ferromagnetic electrodes. Artificial MFTJs are advantageous in this respect, due to the very limited amount of true multiferroic materials [4, 15].

The first group to experiment with MFTJs were Gajek et al. [14] in 2007. They reported on a MFTJ with a single-phase multiferroic tunnel barrier, 2 nm thick $\text{La}_{0.1}\text{Bi}_{0.9}\text{MnO}_3$, showing simultaneous ferroelectric and ferromagnetic order below 90 K which was found as the ferromagnetic Curie temperature [14]. The electrodes were Au and half-metallic ferromagnetic $\text{La}_{2/3}\text{Sr}_{1/3}\text{MnO}_3$, result-

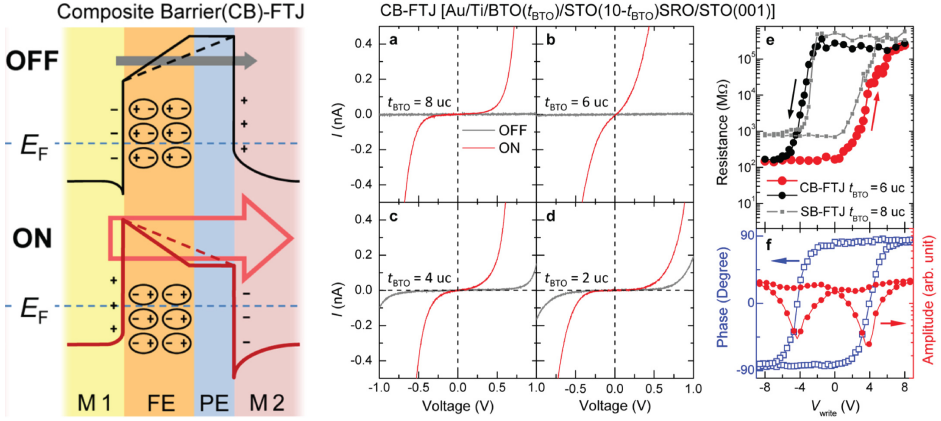


Figure 2.6: Example of state of the art TER and composite barrier in a FTJ, from reference [63].

ing in a spin-filter type MFTJ as noted above. The main results are given in Figure 2.7 with resistance versus magnetic and electric fields on the left, and the corresponding TER and TMR as functions of junction bias voltage on the right. By utilizing both parallel/antiparallel magnetic states as well as opposite

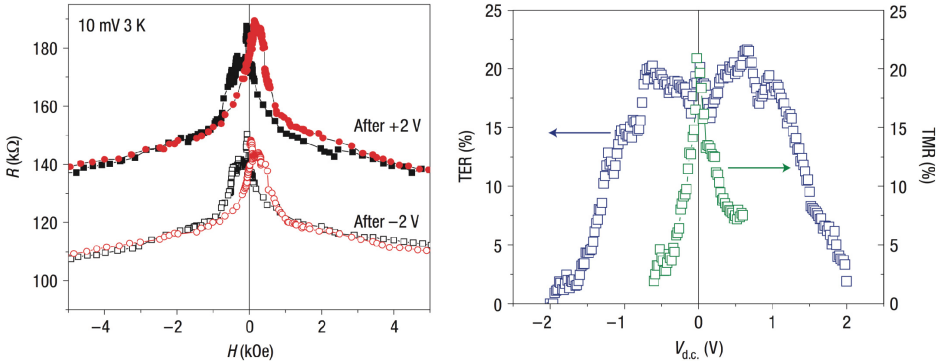


Figure 2.7: First experimental realization of a MFTJ, compiled from Gajek et al. [14]. **Left:** Tunnel magnetoresistance curves for opposite ferroelectric polarizations taken at a junction bias of 10 mV and below 4 K. **Right:** TER and TMR as functions of junction voltage bias.

polarization directions in the barrier, four distinct resistance states are shown on the left side. In effect this represents the first realization of a four-state memory device, though at very low temperatures. The authors conclude by remarking that these results may open the way towards novel reconfigurable logic spintronics architectures, and to electrically controlled readout in quantum-computing

schemes using the spin-filter effect [14].

Later, in 2009, Velev et al. [15] showed by theoretical first-principles calculations that this should indeed be possible in structures consisting of ferromagnetic electrodes with a ferroelectric barrier. They used density functional theory (DFT) and an all-perovskite epitaxial oxide structure with 6 unit cells BTO as ferroelectric barrier, and SrRuO₃ (SRO) as electrodes. SRO is ferromagnetic below about 160 K [15] and they modeled the BTO/SRO interfaces with BaO termination on one side and TiO₂ termination on the other side to get an asymmetric FTJ setup for enhancing the TER [54]. Importantly, they show that four distinct resistance states are produced by the simultaneous presence of TMR and TER. For each of the parallel/antiparallel magnetic states there exist two polarization states (towards each electrode) or vice versa [15].

Following this first experimental realization and theoretical prediction, a number of studies have been published. In 2010, Garcia et al. [64] reported on the observation of ferroelectric control of spin-polarization in a MFTJ with different ferromagnetic electrodes. They emphasize the role of the interfacial magnetoelectric coupling on controlling the effective spin-polarization of the ferromagnetic electrodes, by means of the ferroelectric polarization. They reported a 450% change of TMR for the two opposite ferroelectric polarization directions at low temperature, 4.2 K [64]. Valencia et al. [65] followed up with a similar study in 2011 where they emphasized the an interfacial multiferroic character in the normally ferroelectric BTO barrier at room temperature.

More interestingly, in 2011 Yin et al. [27] published a study showing coexistence of TMR and TER at room temperature in an all-oxide artificial MFTJ. They fabricated MFTJs with a Ba_{0.95}Sr_{0.05}TiO₃ ferroelectric barrier separating two LSMO ferromagnetic electrodes. The junction layout and four-state resistance plot versus magnetic field and poling voltage can be seen in Figure 2.8. Four distinct resistance states are clearly present even though the TMR and TER ratios are very small. This means a precise measurement method is necessary to detect the different states, which is not beneficial for practical use. Moreover, the magnetic order will vanish in LSMO at about 350 K [27], easily reached in electronic devices, meaning a loss of stored information. Nevertheless, this report presents an important and very definite proof of concept for a 2-bit micron scale memory cell, based on resistive readout and the combination of electric and magnetic writing.

In 2012, Pantel et al. [66] continued the earlier reports on interfacial magnetoelectric coupling [64, 65], when they presented a reversible and remanent inversion of spin-polarization by switching the ferroelectric polarization of the barrier in a MFTJ [66]. In 2014, Liu et al. [67] found coexistence of four resistance states and exchange bias in a MFTJ consisting of an antiferromagnetic and ferroelectric BiFeO₃ barrier and La_{0.6}Sr_{0.4}MnO₃ ferromagnetic electrodes.

Recently, Yau et al. [68] reported on a study of the same model system as one of those considered in this work, however, the (001)-oriented equivalent and with a much thicker bottom electrode (60 nm). They prepared MFTJs with NiFe

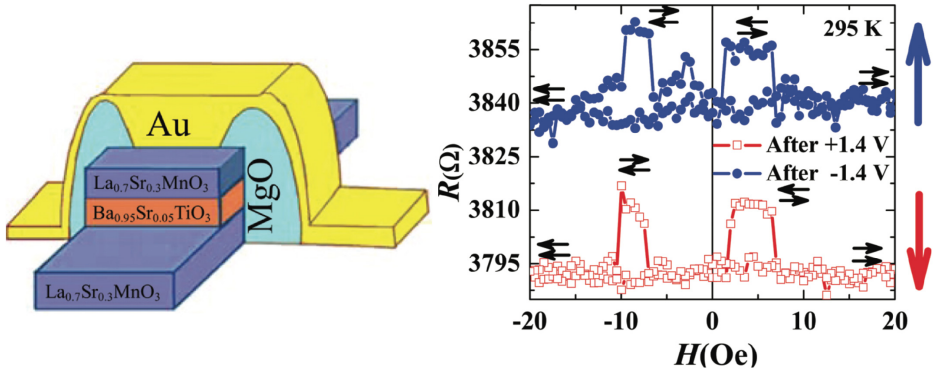


Figure 2.8: First artificial MFTJ showing four resistance states at room temperature, compiled from Yin et al. [27]. **Left:** Device structure showing a $10\ \mu\text{m} \times 20\ \mu\text{m}$ top electrode/barrier with 3.5 nm barrier thickness and longer rectangular bottom electrode. **Right:** TMR curves taken after opposite junction poling voltages. Magnetic field is in-plane and along the longitudinal direction of the bottom electrode. Positive voltage is with respect to the top electrode. Small but clear TMR and TER effects are evident.

and LSMO ferromagnetic electrodes and 5 nm thick BTO as ferroelectric barrier material. Four resistance states were indeed found with a resistance ratio of 16 for opposite ferroelectric polarizations and corresponding TMR effects of +0.3% and -0.15%, respectively.

Yin et al. [28] moved even further by taking advantage of magnetocrystalline anisotropy as a third degree of freedom in artificial MFTJs. They presented a MFTJ revealing 8 distinct and reproducible non-volatile resistance states, effectively working as a 3-bit memory cell. The MFTJ consisted of LSMO ferromagnetic electrodes and a BTO ferroelectric barrier. The junction structure is shown on the left side in Figure 2.9, with a top electrode/barrier dimension of $15\ \mu\text{m} \times 15\ \mu\text{m}$ and bottom electrode dimension $750\ \mu\text{m} \times 30\ \mu\text{m}$. The magnetic field was applied in-plane and the [001]-direction was along the longitudinal direction of the bottom electrode. On the right side the resistance hysteresis curves are shown and all eight resistance states at zero magnetic field have been denoted in accordance with an octonary notation. These were modified from the original publication in order to correspond with the summary presented in the reprinted table in the bottom part of Figure 2.9. To reach each of the eight resistance states, one needs to apply either positive or negative poling voltage and a corresponding magnetic field direction/magnitude after negative saturation with parallel alignment of the electrodes. Resistance states $\underline{0}$ and $\underline{4}$ are the parallel magnetic alignments along [110] for negative and positive poling voltages, respectively. From there, states $\underline{2}$ and $\underline{3}$ (or $\underline{6}$ and $\underline{7}$) can be reached by applying a positive magnetic field of 60 Oe and 90 Oe along [110] and returning to zero field, respectively. Hence, state $\underline{2}$ ($\underline{6}$) is an intermediate state (90° rotation of the soft

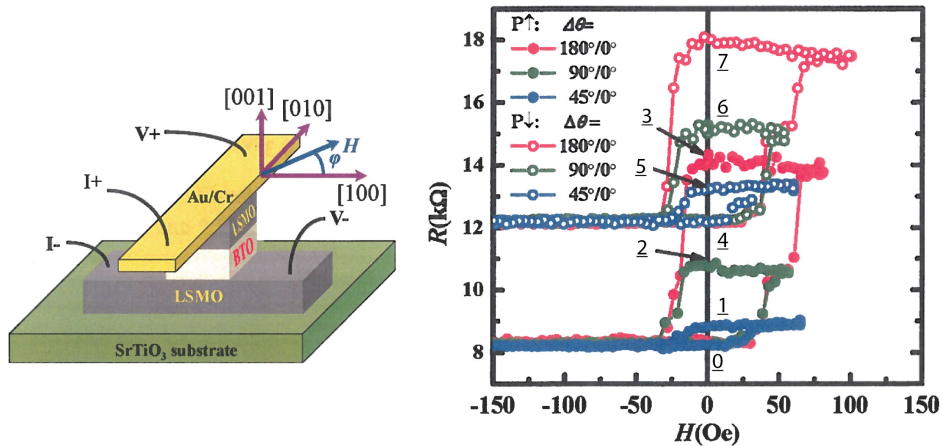


Table 1. Schematic illustrations of the encoding states (binary and octonary) for the MFTJ at different magnetoelectric states with ferroelectric polarization upward (P_{Up}) or downward (P_{Down}) and relative orientation between \vec{M}_{top} and \vec{M}_{bottom} $\Delta\theta = 0^\circ, 45^\circ, 90^\circ,$ or 180° . The combination of electric and magnetic fields to achieve any state from an arbitrary state is also displayed.

$\Delta\theta =$		0°	45°	90°	180°
$P_{Up} (-1.5V)$	Binary	000	001	010	011
	Octonary	0	1	2	3
	Magnetic field [Oe]	$-600_{[110]}$	$-600_{[010]} + 65_{[010]}$	$-600_{[110]} + 60_{[110]}$	$-600_{[110]} + 90_{[110]}$
$P_{Down} (+1.5V)$	Binary	100	101	110	111
	Octonary	4	5	6	7
	Magnetic field [Oe]	$-600_{[110]}$	$-600_{[010]} + 65_{[010]}$	$-600_{[110]} + 60_{[110]}$	$-600_{[110]} + 90_{[110]}$

Figure 2.9: Artificial MFTJ showing eight resistance states, i.e a 3-bit memory cell at 80 K and 10 mV read voltage, compiled from Yin et al. [28]. **Left:** Device structure showing a $15\ \mu\text{m} \times 15\ \mu\text{m}$ top electrode/barrier with 3 nm barrier thickness and $750\ \mu\text{m} \times 30\ \mu\text{m}$ bottom electrode. **Right:** "Single-sided" TMR curves taken for opposite junction poling voltages. The magnetic field is swept from negative saturation towards the positive flip-field of the soft magnetic layer and then reversed to give hysteresis resistance curves. The denoted resistance states ($\underline{0}, \underline{1}, \dots$) have been modified here to correspond to the ones noted in the table. **Bottom:** Table listing the magnetic field directions/magnitudes and polarization poling voltages to reach each resistance state.

magnet) on the way to antiparallel state $\underline{3}$ ($\underline{7}$). To reach state $\underline{1}$ or $\underline{5}$, however, the magnetic field must be applied along $[100]$ instead to get a quarter rotation (45°) of the soft magnet relative to the hard magnet. Although two magnetic field directions are necessary and temperatures above 200 K destroy the TMR [28], this work is a good demonstration of what is possible by using functional oxides for multifunctional devices.

2.2.4 Future Prospects

Mannhart and Schlom [2] point out that the exploration of interfacial electronic systems in complex oxides are in its infancy, and thus is a nascent field of research

in electronics. They emphasize the vast potential for applications, however, that the fundamental science must be understood before the main focus can shift towards applications. They argue that the current state of the field is reminiscent of the research on semiconductor physics in the 1950s: there is an enormous challenge lying ahead, in understanding, predicting and tailoring the interfaces between complex oxides. The tackling of this task is currently just beginning, and they believe that decades with vast and unforeseen opportunities, technologies and science will come once it is mastered [2].

Chakhalian et al. [17] note that transition-metal oxides are abundant, thus making them ideal for electronic devices at a relatively low cost. They remark that oxide heterostructures present a prodigious opportunity for realizing new phases through controlled synthesis. Theory, synthesis and measurements will all meet challenges in taking advantage of these opportunities. They conclude that the structure-property relationships which emerge from the increasing understanding, likely will be used by electrical and chemical engineers in the design of totally new electronic architectures and green-energy technologies [17].

Bibes [18] considers the gap in knowledge between bulk materials and ultra-thin films of ferroelectrics. Even though several oxide ferroelectrics exist with good bulk properties at room temperature, little is known about their thin film response to strain, domain nanostructure or dynamics. He notes in contrast, that there are very few high-temperature ferro- or ferrimagnetic oxides, which should motivate the design of hybrid interfaces between ferroic materials from various structural families. He concludes by stating, among other things, that much will have to be learned about the details of tunneling physics across ferroic insulators, in order to design more responsive devices. Furthermore, he asserts that the influence of ferroelasticity and ferrotoroidicity on charge and spin transport remain unknown, however, that a strong coupling with tunneling transport is anticipated from the expected influence of those orders on barrier height and thickness [18].

2.3 Summary and Focus of this Thesis

Memory technology is clearly one of the primary driving forces and a short-term goal for research on multiferroic devices. As the preceding sections show, research on ferroelectric, multiferroic and possibly magnetoelectric memory has increased in popularity over the past ten years. With an increasing number of researchers working towards the goal of achieving MFTJs which are reliable at room temperature and above, the field is inspiring and exciting to follow.

Table 2.1 shows a list of publications that have studied tunneling phenomena through a thin ferroelectric barrier. For keeping the most relevance to the current work, only studies with BTO barriers have been listed. The upper part lists reports that focused on the TER effect only, even though some of the model systems were actually multiferroic. The lower part lists reports with focus on both TMR and TER utilized by MFTJs. To keep a consistent presentation,

Table 2.1: List of existing reports on tunnel electroresistance and magnetoresistance with BaTiO₃ barriers. None of these are (111)-oriented. The upper half represents TER studies only, while the lower half represents studies of TER and TMR simultaneously in MFTJ structures. NGO = NdGaO₃, DSO = DyScO₃, SRO = SrRuO₃, LCMO = La_{0.5}Ca_{0.5}MnO₃.

Subs, E1, E2	d_{FE} [nm]	Dim. [μm]	A_t [μm^2]	R_{off} [Ω]	R_{on} [Ω]	Year	Ref.
NGO, LSMO, Co	2.0	0.50	0.20	10M	100k	2012	[69]
NGO, LSMO, Co	1.6	5.00	19.63	600M	1M	2012	[70]
DSO, SRO, Ag	3.0	0.02	–	7.5G	15M	2012	[71]
Nb:STO, Pt	2.9	30.00	707	5M	0.5k	2013	[62]
STO, LSMO, LCMO	3.0	15, 15	225	900k	10k	2013	[72]
STO, SRO, Ti	3.4	0.50	0.20	400G	1G	2016	[63]
NGO, LSMO, Fe	1.2	0.03	–	17M	13M	2010	[64]
NGO, LSMO, Co	1.2	–	–	3.2M	1.8M	2011	[65]
STO, LSMO, LCMO	3.0	10, 10	100	1.4M	30k	2013	[72]
STO, LSMO, LSMO	3.0	15, 15	225	18k	8k	2015	[28]
STO, LSMO, NiFe	5.0	100.00	7854	1.5M	5k	2015	[68]
STO, LSMO, LSMO	3.0	20, 20	400	10.7k	4.7k	2016	[73]

all reports are listed with the same reference for the max/min resistances, R_{off} and R_{on} . These are all given for zero magnetic field, meaning they provide information for the pure TER ratio. The lower part of the list naturally provides at least two more resistance levels as a result of the additional TMR levels, but these are excluded here. The substrate and electrode materials (E1, E2), FE tunnel barrier thickness d_{FE} , dimension (diameter if one number, square sides if two) and corresponding junction area A_t are presented.

What the current work is intending to address is the following. First, since no publications, as far as the author is aware, have been reported on tunneling

phenomena in (111)-oriented transition-metal oxides, samples will be prepared for both tunnel magneto- and electroresistance studies for this orientation here. Second, the low magnetocrystalline anisotropy and six-fold magnetic easy axis apparent in the plane of (111)-oriented LSMO thin films, make it an interesting target for the study of partially switched intermediate magnetic states between fully parallel and antiparallel alignments of magnetic electrodes in a MTJ. By pairing magnetic electrodes with a (111)-oriented epitaxial BTO ferroelectric barrier, both TER and TMR with multiple resistive states can be investigated.

The MFTJs will be fabricated in two types. The first type will have a sputtered permalloy top electrode, the other an epitaxial LSMO top electrode. The permalloy MFTJ will be asymmetric in terms of electrode crystallinity, conductivity, and spin-polarization, while the all-oxide MFTJ will be symmetric, although with a patterned top LSMO layer and uniform bottom LSMO layer. Differences in the two BTO/LSMO interfaces may still occur, and the epitaxial strain for the top and bottom electrodes may differ as the top layer is patterned, further away from the substrate, and grown on top of the intermediate BTO.

The questions that will be attempted answered are: Do TER and TMR effects exist in the (111)-orientation? If so, how large are the effects and how do they compare with known values from conventional orientations? Are intermediate non-collinear magnetic states possible, stable and switchable with or without a reorientation of the applied magnetic field? It is not expected that all these questions can be answered within the scope of this thesis, but the samples will be available for continued measurements which in due time hopefully will reveal interesting insights.

Chapter 3

Theory

In this chapter the most relevant theory is presented. The necessary theory is similar to what was presented in the autumn project [1] and is thus not reproduced in full here. However, parts of the chapter is adapted from the project thesis with only slight modifications in order to have a proper context for the additional material. The specific sections adapted with only smaller modifications are 3.2 and 3.3 up to 3.3.4 where specific tunneling mechanisms are introduced.

First, the electromagnetic quantities are stated and presented with the relevant units. Ferroic order parameters with focus on ferroelectricity and ferromagnetism were thoroughly introduced before, thus the reader is referred to the autumn project or other literature [1, 52, 74]. Next, multiferroic materials are presented briefly as this material is considered relevant for the tunneling phenomena of the MFTJ structure, presented in the final section. The section on electron tunneling first includes presentations of the tunnel junctions constituting the MFTJ, before introducing the three most important conduction mechanisms in tunnel junctions. The section ends by going through electrical characteristics of the ferroelectric tunnel barrier and typical measurement techniques.

3.1 Electrodynamics of Continuous Media

To establish the macroscopic electromagnetic field quantities, Maxwell's equations are stated. They are a refined set of four equations and two constitutive relations [52, 74, 75], based on James Clerk Maxwell's *Dynamical Theory of the*

Electromagnetic Field [76] and the works of many before him:

$$\nabla \times \mathbf{E} = -\frac{\partial \mathbf{B}}{\partial t}, \quad (3.1)$$

$$\nabla \times \mathbf{H} = \mathbf{J} + \frac{\partial \mathbf{D}}{\partial t}, \quad (3.2)$$

$$\nabla \cdot \mathbf{D} = \rho_{\text{free}}, \quad (3.3)$$

$$\nabla \cdot \mathbf{B} = 0, \quad (3.4)$$

where \mathbf{E} is the electric field strength, \mathbf{B} is the magnetic flux density, \mathbf{H} is the magnetic field strength, \mathbf{D} is the electric flux density (displacement), \mathbf{J} is the *free* current density, and ρ_{free} is the volume density of free charges.

In addition, the constitutive relations between the field strength and flux quantities are

$$\mathbf{D} = \varepsilon_0 \mathbf{E} + \mathbf{P}, \quad (3.5)$$

$$\mathbf{B} = \mu_0 (\mathbf{H} + \mathbf{M}), \quad (3.6)$$

where \mathbf{P} is the polarization density, \mathbf{M} is the magnetization density, ε_0 is the vacuum electric permittivity and μ_0 the vacuum magnetic permeability. The constitutive relations describe the properties of a medium of interest and are necessary to develop the electromagnetic wave equations from Maxwell's equations. It is noted that for the ferroelectric and ferromagnetic materials used here, the polarization and magnetization depend nonlinearly on their driving fields (\mathbf{E} and \mathbf{H}), and the equations as stated above will not be valid in these materials.

For the rest of this thesis the vector notation will be abandoned since only the scalar quantities are relevant for the present work. Moreover, the electric field strength will rather be denoted \mathcal{E} , in order not to interfere with E which is used for energy. Table 3.1 lists the relevant electromagnetic quantities and their corresponding units in the SI-system or derived units thereof. For the magnetic field and magnetization useful conversions to other typical units are included.

Table 3.1: Electromagnetic quantities and their units. Unit conversions are done according to Fickett [77]. Oe is Oersted and emu is «electromagnetic units».

Quantity	Unit (SI)	Converted unit
\mathcal{E}	V m^{-1}	–
P	$\mu\text{C cm}^{-2}$	–
H	A m^{-1}	$4\pi/10^3 \text{ Oe}$
M	A m^{-1}	10^{-3} emu/cm^3

3.2 Multiferroic Materials

Multiferroics are as the name suggests materials which exhibit two or more ferroic orders at the same time. At first, multiferroics were defined as single-phase materials which simultaneously show two, or all three, ferroic orders – ferroelectricity, ferromagnetism and ferroelasticity [3]. Such a material would have a spontaneous magnetization that can be reoriented by an applied magnetic field, a spontaneous polarization that can be reoriented by an applied electric field, and a spontaneous deformation that can be reoriented by the application of stress, all at the same time [4]. However, the ferroelastic property tends to be excluded, while the possibility for ferrotoroidicity alongside ferroelectricity and -magnetism often is included in principle [6]. Furthermore, antiferroic ordering has been included in the definition of multiferroics [6], due to the fact that very few are known to exist and that ferromagnetism and ferroelectricity might be mutually exclusive properties [4, 5]. As a consequence, multiferroic materials are today referred to as materials which show simultaneous *ferroelectric and magnetic ordering* [16].

3.2.1 Coupling of Order Parameters

Magnetoelectric coupling is a term usually found in relation to multiferroics, and it is the coupling between magnetic and electric fields in matter [78]. Such a coupling is interesting in multiferroics because it allows magnetization to be operated by an applied electric field, or polarization to be changed by an applied magnetic field [5, 6]. However, it is important to stress the fact that magnetoelectric coupling is possible *without* ferroic orders necessarily being present [6, 78]. Figure 3.1 shows the three ferroic orders (electric, magnetic, elastic) with their respective direct couplings and possible cross-couplings in a multiferroic. The magnetoelectric coupling is shown through the green arrows. Below is a list of the other interactions shown in the same figure.

Piezoelectricity is the linear coupling between an applied electric field and a change in strain (direct piezoelectric effect), or a change in polarization as a linear function of applied stress (indirect piezoelectric effect) [6]. These are marked as the black arrows between electric field (stress) and strain (polarization) in Figure 3.1.

Piezomagnetism is the equivalent of piezoelectricity for the magnetic-elastic interaction. It describes a change in strain as a linear function of applied magnetic field, or a change in magnetization as a linear function of applied stress [6]. These are marked as the black arrows between magnetic field (stress) and strain (magnetization) in Figure 3.1.

Electro- and magnetostriction are quadratic terms of the same mechanisms as piezoelectricity and piezomagnetism, respectively [6].

All the above mentioned coupling mechanisms can be expressed from the expansion of the free energy of a material, $F(\mathbf{E}, \mathbf{H})$, and so are not restricted to ferroic materials. However, multiferroic materials are liable to show such

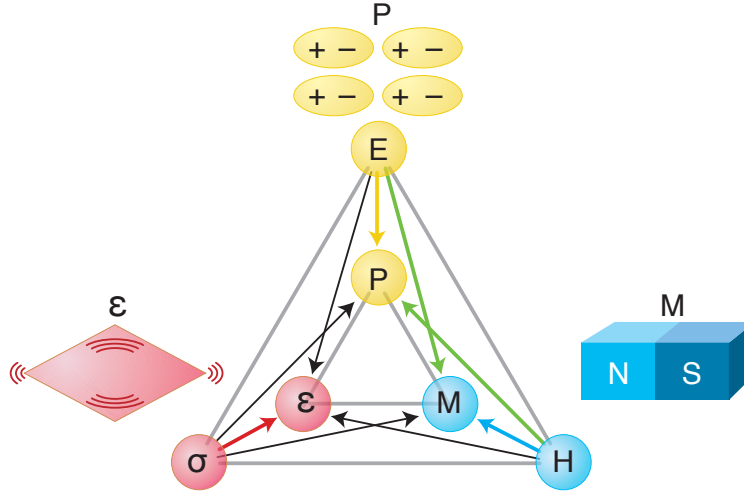


Figure 3.1: Various coupling parameters between polarization P , magnetization M and strain ε , and their control quantities the electric field E , magnetic field H and stress σ , respectively. A multiferroic with two or more of the ferroic orders may exhibit coupling between the different orders. Magnetoelectric coupling is marked by the green arrows as a direct link between electric field and magnetization or magnetic field and polarization. Similar interactions with stress/strain are marked with black arrows. Reprinted from reference [5].

interactions, due to the many necessary symmetry conditions for the various coupling factors being present already [78, 79]. The interested reader is referred to the works of Schmid [79] and Fiebig [78] for detailed information.

3.2.2 Heterostructures of Ferroic Materials

An alternative route to multiferroic *devices* is to use separate materials with their respective order parameters in composite, laminated or epitaxial multilayer structures [6]. This way of engineering new functional material structures, holds specific promise for the success in developing devices that are multiferroic as a whole, although consisting of constituent materials which are not multiferroic by themselves [16]. There are various ways this can be done and different mechanisms causing the combination of ferroic orders in such structures. In horizontal and vertical heterostructures, epitaxial strain from lattice mismatch of the constituent materials is the most promising route to multiferroic behavior, and especially a large magnetoelectric coupling [6, 16].

3.3 Electron Tunneling

The quantum mechanical concept of electron tunneling is known as an electron's ability to traverse a sufficiently thin insulating barrier (see Figure 3.2) although the barrier energy may be larger than the electron energy [54]. This is strictly forbidden in classical physics and unexpected from that point of view. It is an intriguing phenomenon which is useful for a number of applications, for instance the scanning tunneling microscope and (resonant) tunnel diodes. The full nature of electron tunneling is diverse, some of which will be introduced below, but by considering Figure 3.2 it is possible to see the basic principle. In the free electron approximation for a metal (considering only one dimension), an electron with wave function, $\Psi(x)$, is initially located to the left of the barrier. However, the wave function has an exponentially decaying amplitude in the barrier region and, for sufficiently thin barriers of width d , a non-zero amplitude to the right of the barrier. Consequently, there is a finite probability for finding the electron to the right of the barrier, although much smaller than the probability for finding it to the left. [51, 80]

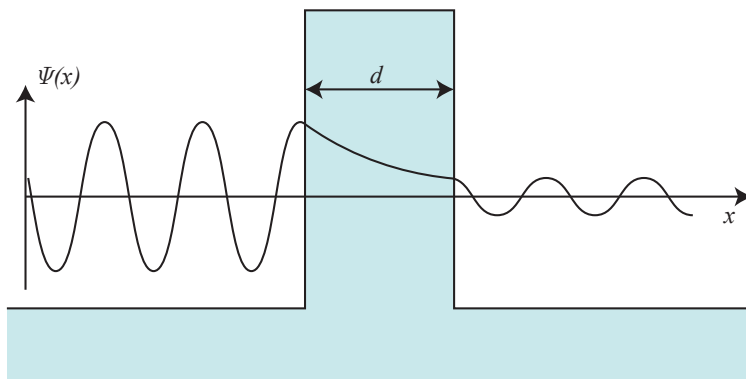


Figure 3.2: Quantum mechanical tunneling of a free electron through an insulating barrier. The electron wave function $\Psi(x)$ has an exponential decay within the barrier, but a non-zero amplitude on the other side of the barrier. Hence, there is a small probability of finding the electron on the right side of the barrier as well.

The above mentioned picture describes direct tunneling. However, there are other mechanisms strongly contributing to the electronic transport as well, in particular Fowler-Nordheim tunneling and thermionic emission/injection [81, 82]. These three concepts are introduced below, but first the concept of tunnel junctions is presented along with the relevant junction types for this thesis.

Electron tunneling is utilized in various *tunnel junctions*. The general principle of a tunnel junction can be seen as two identical conducting electrodes separated by a thin insulating barrier (Figure 3.3), typically with a thickness 1 nm to 5 nm [51]. In thermal equilibrium with zero bias applied, no net current

flows, as the probability for tunneling from one electrode to the other and vice versa are the same. By application of a small bias voltage over the junction, the tunneling probability of electrons can be altered, so that the net current is larger in one of the directions depending on bias magnitude, bias direction, and what kind of tunnel junction it is [83, 84]. Tunnel junctions come in many forms which induce a variety of tunneling effects. In the following, the relevant tunnel junctions for this work are introduced together with their respective tunneling effects.

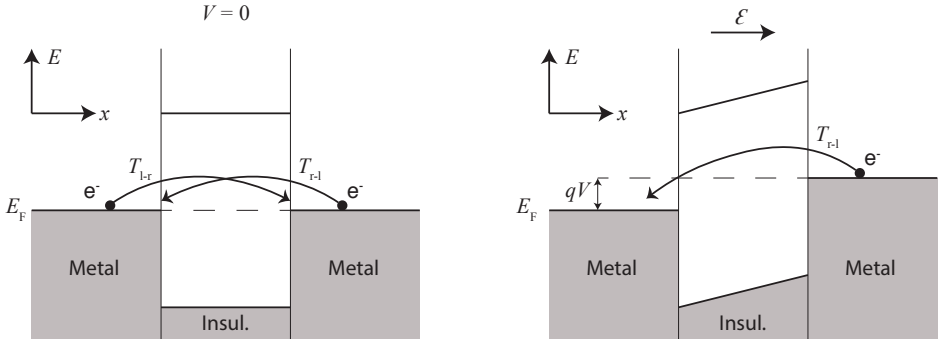


Figure 3.3: General principle of a tunnel junction, here with two identical metals separated by an insulating barrier. Energy E vs distance x on the axes. Left: no bias applied, $V = 0$, hence transmission probabilities are equal, $T_{l \rightarrow r} = T_{r \rightarrow l}$, and no net current flows. Right: a small applied bias, $V \neq 0$, establishes an electric field \mathcal{E} over the junction. This lifts the energy of one electrode relative to the other by qV , which increases the probability for tunneling in one direction, ($T_{l \rightarrow r} > T_{r \rightarrow l}$), and a net tunneling current flows. Here q is the electron charge.

3.3.1 Magnetic tunnel junctions

Magnetic tunnel junctions (MTJ) have ferromagnetic (FM) conducting electrodes which are separated by a diamagnetic dielectric tunnel barrier [51]. In a ferromagnet at the Fermi level, E_F , the density of states (DOS) for spin-up and spin-down electrons are not equal. If one assumes that the spin is conserved during tunneling, a spin-up (spin-down) electron can only tunnel from an initial spin-up (spin-down) state to a final unoccupied spin-up (spin-down) state [52]. The total tunnel current will then be the sum of currents from two parallel transport channels, spin-up and spin-down (see Figure 3.4). For a MTJ with parallel (P) or antiparallel (AP) configurations of the electrodes' magnetization, the conductances are proportional to the product of the DOS:

$$G_P \propto G_{\uparrow\uparrow} + G_{\downarrow\downarrow} \propto N_{1\uparrow}N_{2\uparrow} + N_{1\downarrow}N_{2\downarrow} , \quad (3.7)$$

$$G_{AP} \propto G_{\uparrow\downarrow} + G_{\downarrow\uparrow} \propto N_{1\uparrow}N_{2\downarrow} + N_{1\downarrow}N_{2\uparrow} . \quad (3.8)$$

Here, $N_{1\uparrow(\downarrow)}$ and $N_{2\uparrow(\downarrow)}$ are the DOS of the two ferromagnetic electrodes at the Fermi level with respect to majority spin electrons (\uparrow) and minority spin electrons (\downarrow). In Figure 3.4 the parallel and antiparallel conductances, G_P and G_{AP} , can be seen schematically. In the parallel state, there are both many available majority electrons and many corresponding states for tunneling into, while the opposite is the case for minority electrons. Hence, the majority carrier current is large and the resistance low. In the antiparallel state, there are relatively few corresponding states to tunnel into for majority carriers, while there are few available minority electrons even though the corresponding states for tunneling into are many. Consequently, the total current is low and the resistance large. This phenomenon of a difference in resistance for the parallel and antiparallel configurations has been named *tunnel magnetoresistance* effect.

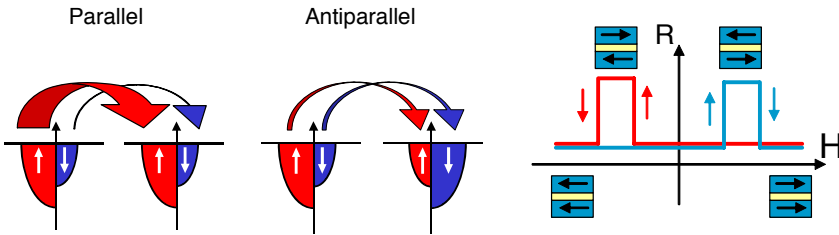


Figure 3.4: Spin-dependent tunneling schematic in a TMR structure with two identical positively spin-polarized electrodes. Left: parallel magnetization state giving a large tunnel current carried by the spin-up channel and low resistance. Middle: antiparallel magnetization giving a small total tunnel current due to an insufficient number of available states (spin-up channel) and an insufficient number of available electrons (spin-down channel) and a high resistance. Right: Two resistance states as the magnetic field is cycled, dependent on the relative magnetization direction of the electrodes. Reprinted from Bibes et al. [51].

Tunnel Magnetoresistance

The tunnel magnetoresistance (TMR) is the general phenomenon of spin dependent transport of electrons through an insulating tunnel barrier with ferromagnetic electrodes. Julliere [8] first expressed the TMR ratio as

$$\frac{\Delta G}{G} = \frac{2P_{\text{spin}}^1 P_{\text{spin}}^2}{1 + P_{\text{spin}}^1 P_{\text{spin}}^2}, \quad (3.9)$$

where P_{spin}^1 and P_{spin}^2 is the spin polarization of the electrodes. With the spin conservation hypothesis as above, the spin polarization is given by

$$P_{\text{spin}}^i = \frac{N_{i\uparrow} - N_{i\downarrow}}{N_{i\uparrow} + N_{i\downarrow}}. \quad (3.10)$$

Hence, the equations 3.7, 3.8 and 3.9 are linked through equation 3.10, and the TMR effect is usually found in one of the equivalent forms:

$$TMR = \frac{2P_{\text{spin}}^1 P_{\text{spin}}^2}{1 + P_{\text{spin}}^1 P_{\text{spin}}^2} = \frac{G_{\text{P}} - G_{\text{AP}}}{G_{\text{P}}} = \frac{R_{\text{AP}} - R_{\text{P}}}{R_{\text{AP}}}, \quad (3.11)$$

where R_{P} and R_{AP} are the resistances of the MTJ in a parallel or antiparallel configuration, respectively. [51, 52]

To the right in Figure 3.4, the two resistance states are shown for an ideal MTJ with identical FM electrodes. By cycling the applied magnetic field from positive to negative or negative to positive, two equivalent orientations of parallel and antiparallel MTJ configurations occur. These correspond to the high (R_{AP}) and low (R_{P}) resistance states of the MTJ.

A further inspection of Jullière's model (eq. 3.9 and 3.10) shows that high TMR values can be achieved if the electrodes are completely spin-polarized ($P_{\text{spin}}^i = \pm 1$). This is almost the case in half-metallic ferromagnets, which are behaving metallic for majority electrons and next to insulating for minority electrons [51]. Furthermore, the TMR effect may be positive (normal) or negative (inverse) depending on the signs of the spin-polarizations [52].

Jullière's model is often not sufficient to consistently explain observations from TMR experiments [52]. The model is simple, especially with regard to the barrier material which is not a part of the equation (eq. 3.9). A realistic barrier material may modify the decay length of the electron wave functions as compared to a vacuum barrier in the model [52]. Furthermore, the crystalline structure of the barrier, its physical properties (electronic, magnetic, ferroic etc.), and the chemical bonding between the insulator and electrodes will strongly influence the transmission properties for the tunneling of electrons [51]. Nevertheless, the model is useful as a figure of merit for comparing different types of MJTs.

3.3.2 Ferroelectric tunnel junctions

Ferroelectric tunnel junctions (FTJ) have conducting electrodes that are, in general, normal metals separated by a ferroelectric tunnel barrier [13, 54]. In a FTJ the tunnel current will depend on the direction of polarization in the ferroelectric barrier. There are mainly three mechanisms (see Figure 3.5) identified which affect the transmission probability of a FTJ [13]:

1. Electrostatic potential: an incomplete screening of the ferroelectric bound charge leads to an electrostatic potential profile that superimposes the contact potential of the FTJ.
2. Interface effect: depending on the barrier and electrode materials, interfacial displacements of ions may occur and influence the atomic orbitals at the interface. This can lead to different transmission probabilities for the opposite polarizations.

3. Strain effect: The piezoelectric effect inherent in the ferroelectric barrier causes strain in the barrier upon application of a bias voltage. Furthermore, the opposite polarizations can have different stable strain states, which makes the barrier width and attenuation change upon polarization reversal.

Figure 3.5 shows an energy diagram for a FTJ ($\text{SrRuO}_3/\text{BaTiO}_3/\text{SrRuO}_3$) and sums up the different contributions listed above. The essential characteristic of a FTJ is that the resistance has a large difference between opposite polarization directions, which leads to resistive switching and the *tunnel electroresistance* effect.

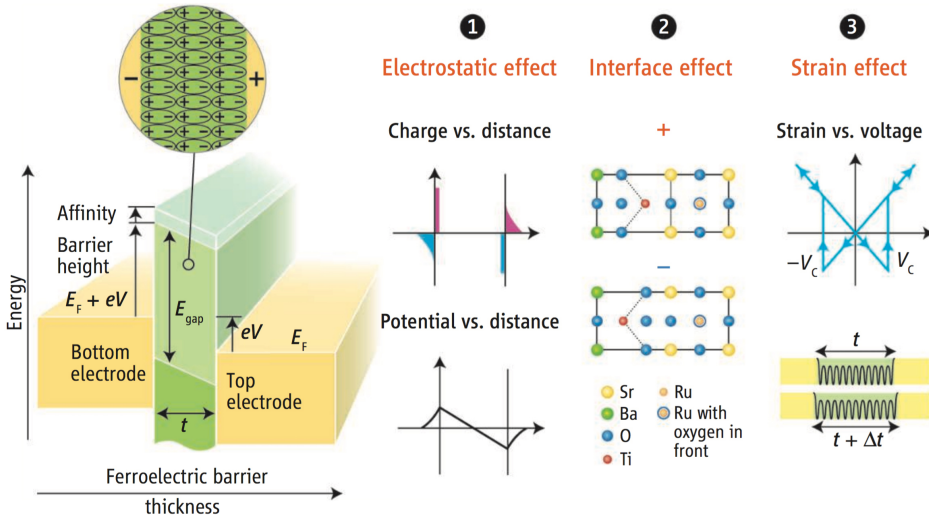


Figure 3.5: Ferroelectric tunnel junction consisting of two normal metal electrodes separated by a ferroelectric barrier. An applied bias (V) from the top to bottom electrodes polarizes the ferroelectric towards the bottom electrode, as shown by the electric dipoles in the barrier (inset). Screening charges develop at the interfaces which gives an electrostatic potential profile over the junction (1). Interfacial effects (2) may occur as ionic displacements affect atomic orbitals and transmission probability. Finally, the piezoelectric effect of the ferroelectric can strain the barrier differently in the opposite polarization directions, which can give additional strain effects (3) on the transmission probability. Reprinted from [13].

Tunnel Electroresistance

The tunnel electroresistance (TER) effect is the general phenomenon of polarization dependent transport of electrons through an insulating ferroelectric tunnel barrier with metallic electrodes [15, 56, 61, 72]. The mathematical definition varies in literature [15, 56, 61], however, several authors [60, 68, 72] use the

definition analogous to the TMR effect,

$$TER = \frac{R_{\leftarrow} - R_{\rightarrow}}{\min(R_{\leftarrow}, R_{\rightarrow})}, \quad (3.12)$$

where R_{\leftarrow} and R_{\rightarrow} corresponds to the resistances of the left and right (or up/down) polarization configurations of the FTJ.

It should be noted that a FTJ with asymmetric electrodes (different materials for top/bottom electrode) may enlarge the different effects listed above and, hence, increase the TER ratio [54, 56]. This can be favorable for applications where a large on/off ratio is desired [54].

3.3.3 Multiferroic tunnel junctions

In multiferroic tunnel junctions (MFTJ), the concepts of both MTJs and FTJs are combined in the same junction. By using ferromagnetic electrodes separated by a ferroelectric tunnel barrier [64, 68, 72], a total device with multiferroic behavior is achieved [15]. Gajek et al. [14] reported on a MFTJ with a *multiferroic barrier*, however, in this text only the MFTJ composed of materials with separate ferroic orders is considered.

In 2007 Gajek et al. [14] reported on an experimental observation of four resistance states in their multiferroic barrier MFTJ. However, they could not conclude with decisive certainty that the ferroelectricity of the barrier caused the hysteresis in the device's I-V characteristic, despite several indications for it [14]. Later, Velev et al. [15] predicted from theoretical first-principle calculations, that four separate resistance states should be possible in a MFTJ, and subsequent reports have confirmed the findings of four resistance states in MFTJs [64, 68, 72].

Consequently, the essential characteristic of MFTJs is that the transport properties of the tunneling electrons can be varied by two degrees of freedom; polarization direction in the barrier and magnetization direction in the electrodes. For each of the polarization directions, there are both one antiparallel and one parallel magnetic configuration of the electrodes. This leads to four distinct resistance states.

Tunnel Electromagnetoresistance

To the knowledge of the author, *tunnel electromagnetoresistance* (TEMR) is not an established term in the research field, however, Garcia et al. [64] coined the term to «quantify the sensitivity of the TMR effect with ferroelectric polarization». They defined the TEMR effect as

$$TEMR = \frac{TMR_{P_{\leftarrow}} - TMR_{P_{\rightarrow}}}{TMR_{P_{\rightarrow}}}, \quad (3.13)$$

where $TMR_{P_{\leftarrow}}$ and $TMR_{P_{\rightarrow}}$ are the TMR effects observed with polarization direction left and right (or up/down), respectively. The essential issue is of course

to achieve a TER effect which separates the two TMR effects sufficiently well, so that it is easy to distinguish all four resistances from an electronic circuit point of view.

To sum up, all three tunnel junction structures described above are shown schematically in Figure 3.6. The MTJ is shown to the left, with two ferromagnets (FM) separated by a dielectric diamagnetic insulator (I). One magnet is soft (small coercive field) and the other hard (larger coercive field), in order to enable antiparallel configuration. A FTJ is shown in the middle, with two metals (M) separated by a ferroelectric (FE) barrier which can be polarized towards left or right. Lastly, a MFTJ is shown to the right as a combination of the MTJ and FTJ. In general, the ferromagnetic electrodes may be different materials to enhance the TER effect. The MFTJ is the most relevant structure to consider for the rest of this text.

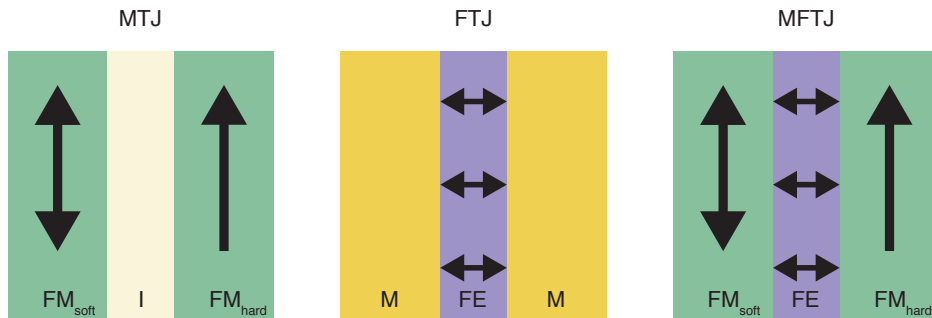


Figure 3.6: Various tunnel junctions. **Left:** a magnetic tunnel junction (MTJ), with two ferromagnets (FM) separated by a dielectric diamagnetic insulator (I). The soft and hard magnets are easy and hard to switch, respectively, in order to enable an antiparallel configuration. **Middle:** a ferroelectric tunnel junction (FTJ), with two metals (M) separated by a ferroelectric (FE) barrier which can be polarized towards left or right. **Right:** a multiferroic tunnel junction (MFTJ) as a combination of the MTJ and FTJ. In general, the FM electrodes may be different materials to enhance the TER effect.

3.3.4 Direct Tunneling and Brinkman's Model

The above introduction to electron tunneling shows a naive, conceptual and idealistic presentation of direct tunneling through a symmetric metal-insulator-metal junction (fig. 3.3). In a more realistic model, more parameters describing the tunnel barrier material and electrodes are necessary. Brinkman, Dynes and Rowell calculated the voltage-dependent tunneling conductance of trapezoidal potential barriers for low voltages [85]. They used two models, one was the WKB approximation, the other a model with perfectly sharp boundaries between the metal electrodes and insulator. The key findings were that at low biases the differential

tunneling conductance is roughly parabolic in shape, and unless the electrode materials are equal the lowest conductance point will be shifted slightly off from zero bias [85]. Their work has later been used by many researchers, particularly lately in many of the papers dealing with FTJs or MFTJs that were listed earlier (tbl. 2.1), and is often referred to as Brinkman's model or Brinkman's equation [12, 68]. The model describes what is further referred to as direct tunneling (DT).

Brinkman et al. [85] were building on important works by others before them, and the models are relatively complex. Gruverman et al. [61] took advantage of the WKB approximation model and simplified it further. They considered a trapezoidal potential barrier where the profile depends on the direction of ferroelectric polarization (see e.g. fig. 3.7). The barrier has width d and potential steps at the interfaces ϕ_1 and ϕ_2 , giving a varying potential energy across the barrier with a bias voltage V present, as $\phi(x, V) = \phi_1 + eV/2 + x(\phi_2 - eV - \phi_1)/d$. Further they assumed that the voltage was relatively low, i.e. $eV/2 < \phi_{1,2}$, and that the barrier width was not too small, so that $d[(2m/\hbar^2)\phi_{1,2}]^{1/2} \gg 1$. Thus, they obtained an analytic expression for the current density

$$J_{\text{DT}} \cong C \frac{\exp \left\{ \alpha(V) \left[\left(\phi_2 - \frac{eV}{2} \right)^{3/2} - \left(\phi_1 + \frac{eV}{2} \right)^{3/2} \right] \right\}}{\alpha^2(V) \left[\left(\phi_2 - \frac{eV}{2} \right)^{1/2} - \left(\phi_1 + \frac{eV}{2} \right)^{1/2} \right]^2} \times \sinh \left\{ \frac{3eV}{4} \alpha(V) \left[\left(\phi_2 - \frac{eV}{2} \right)^{1/2} - \left(\phi_1 + \frac{eV}{2} \right)^{1/2} \right] \right\}, \quad (3.14)$$

where $C = -\frac{4em}{9\pi^2\hbar^3}$, $\alpha(V) \equiv \frac{4d\sqrt{2m}}{3\hbar(\phi_1 + eV - \phi_2)}$, and e, m is the electron charge and effective tunneling mass. With this model, they fitted experimental data obtained by scanning probe microscopy techniques on BTO barriers with very good precision [61].

3.3.5 Fowler-Nordheim Tunneling

In 1928 Fowler and Nordheim [86] pursued the problem of describing electric field induced emission of electrons from bulk metal surfaces into the vacuum. They used a triangular energy barrier to describe the material's Fermi energy, electron affinity and a linearly decreasing energy barrier out into the vacuum due to an electric field gradient. With this scheme they find the coefficients for electron emission, or tunneling, into the vacuum from a cold metal, i.e. at normal temperatures where the thermal energy is negligible to the problem [86]. Thus, their work has later been a major cornerstone in the area of (cold) field electron emission and is generally known as Fowler-Nordheim tunneling (FNT) [81, 82].

Pantel and Alexe [81] notes that FNT also occur for rectangular or trapezoidal energy barriers once a sufficiently large electric field \mathcal{E} is applied so that the barrier shape becomes triangular. Furthermore, FNT is basically the same phenomenon

as DT, but in the high voltage regime rather than the low voltage regime for DT. They present the current density from FNT as

$$J_{\text{FNT}} = \frac{e^3 m_e}{8\pi h m \phi_B} \mathcal{E}^2 \exp \left[-\frac{8\pi\sqrt{2m}}{3he} \frac{\phi_B^{3/2}}{\mathcal{E}} \right], \quad (3.15)$$

where m_e is the free electron mass, m the same effective tunneling mass as for DT above, and ϕ_B is the FNT barrier height, i.e. $\phi_{B,1}$ and $\phi_{B,2}$ for $V > 0$ and $V < 0$, respectively (see fig. 3.7 (a),(b)). The latter barrier heights refer to the above DT barrier heights as $\phi_{B,i} = \phi_i \pm \Delta\phi_i$ [81].

3.3.6 Thermionic Emission/Injection

Thermionic emission or injection (TI) describes the emission of electrons into the vacuum from a heated material [83, 86] or thermal injection of electrons into another material across a potential barrier [81]. The essence is the same, e.g. transport of electrons over some potential barrier, facilitated by sufficient thermal energy (see fig. 3.8 on the left). Thermionic injection is similar to Schottky injection and the terms seem to be interchanged [84, 87]. Pantel and Alexe [81] took the Schottky effect of image force lowering into account for the following thermionic injection current density. For sufficiently high voltages, i.e. $V > 100$ mV at room temperature or approximately $3k_B T/e$, they found

$$J_{\text{TI}} = AT^2 \exp \left[-\frac{1}{k_B T} \left(\phi_B - \sqrt{\frac{e^3 \mathcal{E}}{4\pi\epsilon_0 \epsilon_{ifl}}} \right) \right], \quad (3.16)$$

where ϕ_B is the potential barrier, A is the effective Richardson constant, and ϵ_{ifl} the relative permittivity of the dielectric responsible for image force lowering. At low temperatures they approximate the current by an ohmic relation [81].

It should be noted here that the work of Fowler and Nordheim [86] also includes thermionic emission from bulk metals whenever the temperature contribution is large enough. They show that a more advanced model takes the form of thermionic emission at high temperatures and the form of their triangular approximation for cold field emission at low temperatures. Indeed, they argue that there is no phenomenological difference between electrons emitted by thermal emission and purely field emitted electrons at low temperatures, a distinction previous papers by others had tried to make [86].

3.3.7 Other Conduction Mechanisms

There are other types of conduction mechanisms known to occur in ferroelectric capacitors with a larger thickness than FTJs. Dawber et al. [87] discuss the Poole-Frenkel effect, space-charge-limited currents, and grains or grain boundaries as possible mechanisms. Any details are not included here since the above

mentioned mechanisms are likely dominating in FTJs. However, the reported leakage currents present along surface step-edges in ultrathin BTO FTJs [63] may be a related feature of grain boundary conduction paths in polycrystalline thicker films.

3.3.8 Electrical Characteristics of Ferroelectric Barriers

Here, electrical characteristics and typical measurement techniques for ferroelectric barriers are presented. This is of relevance for MFTJs due to being combined FTJs and MTJs. Although possible couplings between the ferroelectric barrier and ferromagnetic electrodes are certainly important, this will not be considered here as it is less known. In Chapter 2 a few studies on the ferroelectric control of spin-polarization were included as examples of coupling, while the other MFTJ reports focused more on how the TMR is shifted with the on/off states of the TER. In this work, the TMR effect is rather considered on its own as presented above for MTJs, while two (or more) TMR curves may be shifted and modulated in resistance magnitude by the TER effect of the ferroelectric barrier.

Current-voltage measurements

An important characterization technique is measurement of the leakage current. This is usually done by measuring the voltage (current) at a specified current (voltage) level, giving a current-voltage relationship (IV-curve). Due to ferroelectric relaxation it is important that the measurement is done sufficiently slow so that the current flowing is the true leakage current and not to a large degree relaxation current [87]. Thus, the IV-curve should be DC current versus DC voltage, i.e. measured with a sufficiently slow sweep rate to be considered steady-state for each measurement point.

The three analytical expressions for DT, FNT, and TI given above, were utilized by Pantel and Alexe [81] to calculate the respective contributions to the total tunnel current in FTJs with BTO barriers of varying thickness. Their results have been compiled in Figure 3.7. In (a) the applied potential setup V to ground, polarization P , depolarization field $\mathcal{E}_{\text{depol}}$ and polarization charges \pm towards each of the metal electrodes are shown. Note also the different charge shielding lengths due to asymmetric metal electrodes. In (b) the trapezoidal potential barrier with all parameters used in the above equations are seen for both polarization directions. On the right side, the various contributions to the total current density for different BTO barrier thicknesses from the above mentioned conduction mechanisms are shown. Solid and dashed lines correspond to opposite polarizations. For increasing BTO thicknesses the contribution from DT goes from dominating to negligible. This is also true for FNT, but to a less extent. TI, although changing with thickness too, is much less thickness dependent due to the nature of electrons overcoming the barrier instead of tunneling through it, and thus goes from negligible to dominating in the total current density. TI of

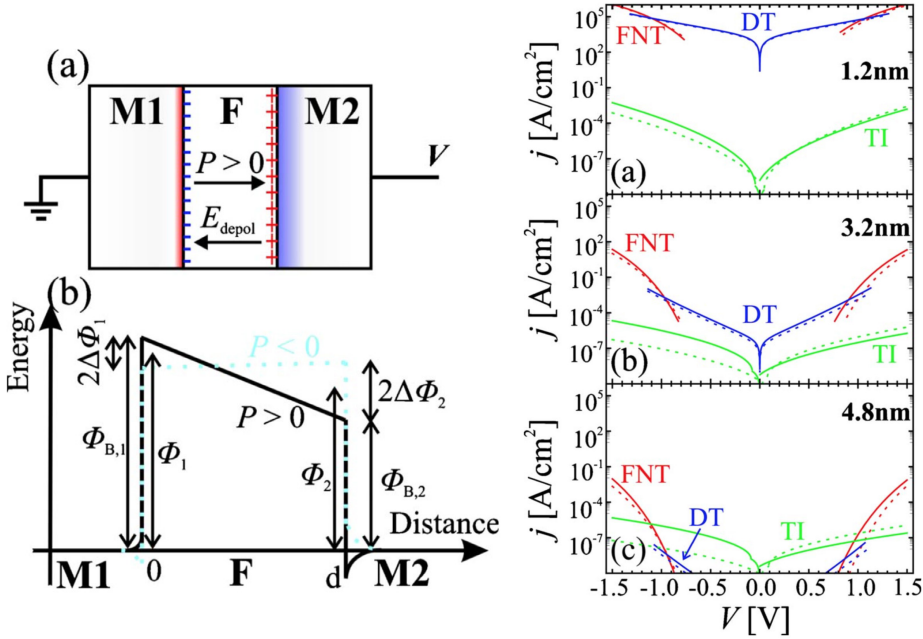


Figure 3.7: Trapezoidal tunnel barrier potential and different tunneling mechanisms. Device setup (a), tunnel barrier dependent on polarization direction (b) and resulting current density contributions from DT, FNT and TI for increasing ultrathin BTO barrier thickness (right). Compiled from Pantel and Alexe [81].

course needs a certain temperature in order to be relevant at all, while DT and FNT ideally are not temperature dependent.

Streetman and Banerjee [84] emphasize that the overall physics of DT and FNT is similar in tunneling across insulators, but with some of the details different. One thing they note is that DT involves tunneling directly through the thin insulator without the need for the electrons to go via the insulator conduction band, while with FNT the electrons tunnel through the first part of the insulation barrier and emerge in the conduction band of the insulator where they «hop» along to the opposite electrode [84]. This is readily illustrated in Figure 3.8 on the left side.

Figure 3.8 sums up the three different potential barriers seen by the different conduction mechanism on the left side. In the middle, the total current density, $J_{\text{tot}} = J_{\text{DT}} + J_{\text{FNT}} + J_{\text{TI}}$, as calculated by Pantel and Alexe [81] is shown for different ultrathin BTO barriers. On the right the TER (ER) in terms of changing current density for opposite polarization versus voltage bias is plotted as the theoretical BTO thickness is changed. The investigation of the different conduction mechanisms' contribution to the total current density is very useful, because it

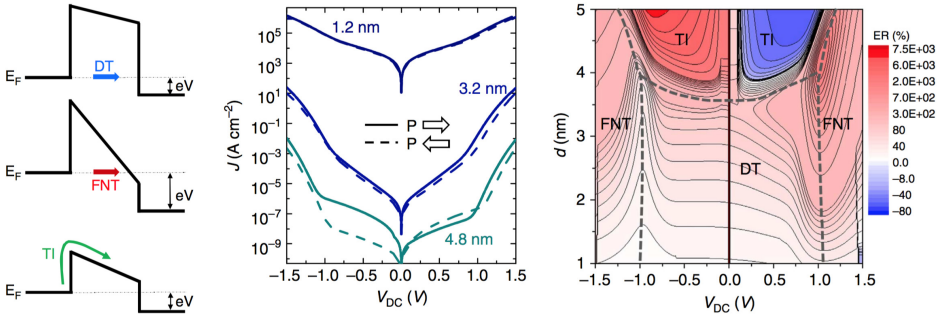


Figure 3.8: Electron transport across ultrathin ferroelectrics. The conceptual barrier profiles and conduction mechanisms for DT, FNT and TI (left), the combined total current densities for increasing ultrathin BTO barrier thickness (middle), and corresponding electroresistance from the dominating conduction mechanism versus bias voltage and barrier thickness (right). Compiled from Garcia and Bibes [82], who had reprinted the center and right parts from Pantel and Alexe [81].

gives an intuitive feeling for which mechanisms are at play in a certain FTJ by plotting the measured IV-curve with a logarithmic current axis. Moreover, the largest electroresistance is found for the thickest barriers in the TI dominated regime, though at the expense of a strong decrease in the read current at low voltage bias [81].

As Garcia and Bibes [82] point out, the experimental frontiers between the different conduction mechanisms are hard to define since they depend on so many various parameters (eq. 3.14, 3.15, 3.16). Nonetheless, the signatures of each mechanism are clear (fig. 3.7, 3.8), and since TI is a thermally activated process, it should lead to strong variations with temperature while DT and FNT should not [82]. At low temperatures then, the DT and FNT should be relatively easy to recognize by the slope of the current versus voltage diagrams, while the TI part can be assessed by comparing IV-curves taken at different temperatures.

Differential measurements

Differential measurement techniques are useful for studying nonlinear quantities, particularly electron tunneling effects which are so strongly depending on the electron energy, as seen above. Differential conductance is the derivative of the IV-curve, i.e. dI/dV or dG , and sometimes referred to as *electron energy spectroscopy*, *tunneling spectroscopy* or a *density of states* measurement when used to study quantum effects [88]. There are in principle two ways to perform such a measurement, either by derivation of the IV-curve or by use of a small sinusoidal AC excitation superimposed on a slowly varying DC bias. The latter is typically done by use of AC lock-in amplifiers [88].

The AC excitation can be a sinusoidal current or voltage, and the DC off-

set can be a DC current or DC voltage, so in general both differential resistance, dV/dI , and differential conductance, dI/dV , can be measured as functions of DC current or DC voltage by this technique. These four combinations are also possible for differentiated IV-curves of course, and the chosen representation depends on what one wants to emphasize.

Dawber et al. [87] point out that an impedance analyzer can be used to measure the real and imaginary parts of the impedance by use of a small-amplitude AC signal superimposed on a DC bias voltage. They refer to automated systems that are commercially available and that the dielectric permittivity of the sample can be studied this way by measurements of capacitance versus voltage (CV-curve). Furthermore, they note that ferroelectric samples display a characteristic «butterfly loop» in the CV-curves, since the capacitance is different for increasing and decreasing bias voltage. By varying the frequency of the AC signal, *impedance spectroscopy* can be performed to analyze the time scales at which processes happen in the sample [87]. Later it will be shown that the differential AC lock-in method can be used to measure the capacitance here, although not as capacitance-voltage, but capacitance-current (CI-curve) due to the specific type of sourcemeter available.

When analyzing CV (or CI) data one must be very careful, because there are more possible sources for the dependence of capacitance on applied voltage. Ferroelectric films can be compared to metal-semiconductor-metal systems [87] in the sense that the depletion width in the semiconductor is dependent on applied electric field, while the depletion width or screening length at ferroelectric capacitor interfaces also can have this property. In addition, the ferroelectric's dielectric constant is known to have a nonlinear response and thus can be expected to be expressed in the CV-curve [87]. For FTJs this argument seems to be even more important, since the electric field dependent polarization in the barrier can influence both the actual junction thickness through piezo-strain and the effective tunneling thickness through increased or decreased screening lengths in the electrodes [13, 54]. Therefore, the junction capacitance's dependence on electric field \mathcal{E} can be expected to come from both the material permittivity ε and effective barrier thickness d as

$$\frac{C(\mathcal{E})}{A} = \frac{\varepsilon(\mathcal{E})}{d(\mathcal{E})}. \quad (3.17)$$

Consequently, it will be wise to follow the advice of Dawber et al. [87] not to make any conclusions on the origin of the voltage dependent capacitance from such measurements alone. Nevertheless, a CV or CI measurement is in itself interesting in order to evaluate the junction capacitance.

Ferroelectric hysteresis curves

Ferroelectric polarization versus voltage or electric field follow a hysteresis curve [1]. The ferroelectric hysteresis curve can be measured by integration of charge or

current. The polarization is not measured directly, but the total switched charge Q is used to calculate the remanent polarization P_r after an applied electric field pulse \mathcal{E}_a as [87]

$$Q = 2P_r A + \sigma \mathcal{E}_a t , \quad (3.18)$$

where A is the electrode area, σ is the leakage conductivity of the capacitor and t is the pulse width. For a FTJ where the conductivity can be very large this is difficult, and PFM measurements are generally used instead as was seen in Chapter 2.

Chapter 4

Materials and Methods

Here the model system for realizing both types of MFTJ is introduced and described in more detail. The experimental techniques that were used are presented and explained briefly together with some typical parameters that were used. However, specific process parameters are given in Chapter 6 together with the fabrication process. The measurement systems used for magnetic and electrical characterization are presented briefly, with most focus on the electrical measurement setup. Data analysis was conducted with MatLab, and the most relevant information from that part is also included briefly. Much of the material in this chapter is adapted from the autumn project [1], but has been revised and extended where necessary.

4.1 Model System

The MFTJs were realized using a model system consisting of a (111)-oriented SrTiO_3 (STO) substrate with epitaxial $\text{La}_{0.7}\text{Sr}_{0.3}\text{MnO}_3$ (LSMO) and BaTiO_3 (BTO) as bottom ferromagnet and ferroelectric insulating layer, respectively. Two types of top ferromagnets were used: sputter deposited $\text{Ni}_{0.81}\text{Fe}_{0.19}$ (permalloy) and epitaxial LSMO, which were defined by lift-off and dry-etching, respectively. Both top electrodes were covered with platinum for electrical contact, and to prevent oxidation of the permalloy. Conceptual sketches of the two qualitative MFTJ structures are seen in Figure 4.1. From here on, the permalloy MFTJ is referred to as P-MFTJ (permalloy) and the all-oxide MFTJ as O-MFTJ (oxide). Below is a presentation of the different materials used for the model system. The final sample structure is presented and discussed in Chapter 5.

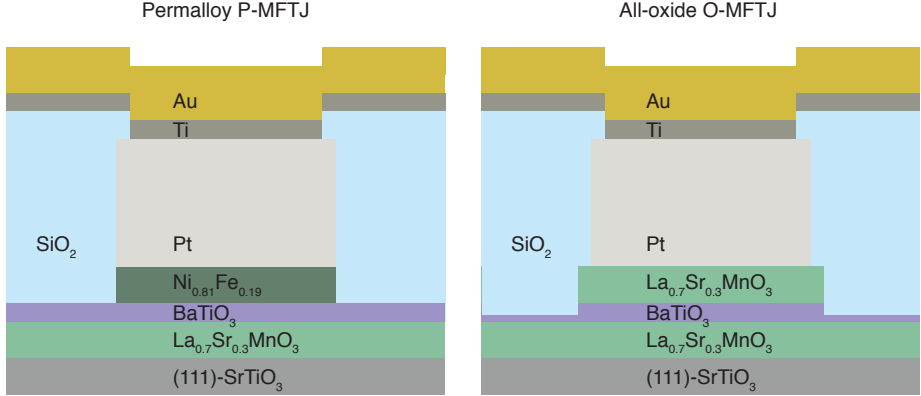


Figure 4.1: Qualitative sketches of the asymmetric permalloy MFTJ and the all-oxide MFTJ. P-MFTJ on the left and O-MFTJ on the right.

4.1.1 Strontium Titanate

Strontium Titanate SrTiO_3 (STO), with (111)-surface orientation, has been used as substrate for all samples in this work. STO is a dielectric and diamagnetic perovskite with ideal cubic symmetry, and the lattice constant is $a_{\text{STO}} = 3.905 \text{ \AA}$ at room temperature [20, 89]. The cubic unit cell centered around the octahedral A-site in which Sr resides can be seen on the left side in Figure 4.2. The right side shows the (111)-plane of STO which exhibits hexagonal symmetry of TiO_6 -octahedra and Sr-atoms. Here, the light blue (111)-plane crosses through the octahedrally coordinated Ti-atoms. (111)-layers of Sr-atoms and TiO_6 -octahedra, respectively, are intertwined and ABC-stacked along the body diagonal [111]-direction. The planes of SrO_3 , seen as the deep blue (oxygen) and green (strontium), may as well be considered cubic close packed (ccp) layers [90].

STO is much used as wafer material in oxide electronics research due to its good controllability of surface flatness and specific cation termination for (001)-oriented surfaces. A well defined surface termination enables abrupt interfaces to epitaxial films deposited on the substrate. Moreover, STO has a relatively low thermal expansion coefficient of $10.4 \cdot 10^{-6} \text{ K}^{-1}$, and the lattice constant is close to those of LSMO and BTO, thus making it suitable as a stable substrate for epitaxial growth of these materials [89].

However, a well defined surface termination is not necessarily true for (111)-oriented planes, as the termination of such planes are harder to control. This can be seen by considering Figure 4.2. Ideal (111)-oriented STO surfaces are terminated by planes of either SrO_3^{4-} or Ti^{4+} , which make the surfaces very polar with surface charge ± 4 per unit cell [30]. Hence, the surface easily reconstructs to form more stable facets or reacts with other substances. By comparison,

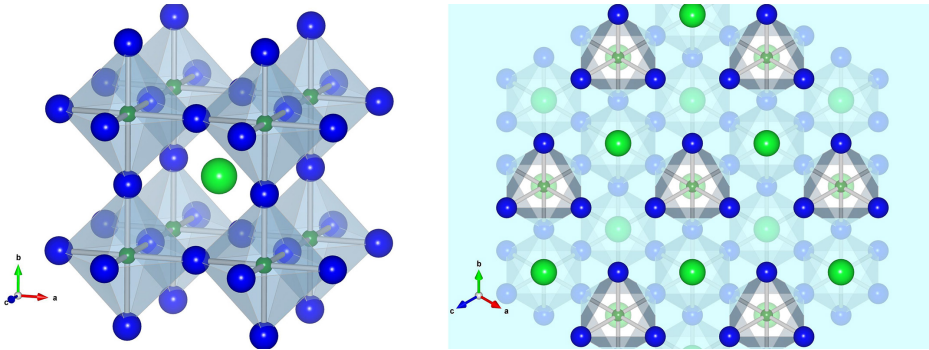


Figure 4.2: Ideal cubic perovskite SrTiO_3 , where Ti (dark green) is captured inside the oxygen (blue) octahedra while Sr (light green) resides centered between eight of the octahedra. **Left:** the unit cell centered around the A-site cation, Sr. **Right:** shows the crystal structure projected along the $[111]$ -axis, where respective ABC-stacking of the TiO_6 octahedra and Sr-atoms is visible.

the (001)-oriented surface is non-polar, and consequently more stable, with either BaO or TiO_2 as terminating layers [30]. Nevertheless, the polarity of the (111)-orientation is very interesting in terms of investigating novel interface effects [17], as noted before. Moreover, the recent success in well controlled growth on STO(111) [29, 31], makes it possible to take advantage of this particular orientation in this work.

4.1.2 Lanthanum Strontium Manganite

Lanthanum Strontium Manganite, $\text{La}_{0.7}\text{Sr}_{0.3}\text{MnO}_3$ (LSMO), is one of the *mixed valence manganites* [20]. The general chemical formula for manganese oxides is $\text{RE}_{1-x}\text{A}_x\text{MnO}_3$, where RE is one of the trivalent rare earth lanthanide series ions, and A is one of the divalent alkaline earth ions [20].

In this work a solid solution of 70% La and 30% Sr ions ($x = 0.3$) have been used, which gives the formula unit $\text{La}_{0.7}\text{Sr}_{0.3}\text{MnO}_3$. The abbreviated name LSMO refers to this particular solid solution throughout the text if not stated otherwise. It should be noted that the term *solid solution* is interchangeable with *extrinsic doping* of a parent crystal. However, as the doping concentration is increased above 0.1-1%, it is common practice to refer to the material as a solid solution instead [90, ch. 2.3]. Furthermore, the LSMO is a *substitutional* solid solution, as the parent La ion is substituted with Sr in 30% of the crystal's A-sites.

LSMO crystallizes in a distorted perovskite structure with the large La and Sr ions at the A-sites with 12-fold oxygen coordination, and the smaller Mn ions at the octahedral B-sites [20]. A neutral manganese atom has the electron configuration $[\text{Ar}]3d^54s^2$, where the 3d orbital is incomplete [90]. When ionized,

the manganese ions first lose their $4s^2$ electrons, then the $3d$ electrons. As a result, Mn^{3+} is $3d^4$ and Mn^{4+} is $3d^3$. Due to the octahedral crystal field surrounding the manganese ions, a splitting of the 5-fold degenerate $3d$ orbital occurs, and according to Hund's first rule Mn^{4+} has one electron in each t_{2g} orbital and no electrons in either of the e_g orbitals, while Mn^{3+} has one electron in each t_{2g} orbital and one electron in one of the e_g orbitals. Hence, the manganese ions are all high spin (HS), with total spin $S = 2$ and $S = 1.5$ for Mn^{3+} and Mn^{4+} , respectively. [20]

For $x = 0.3$, the perovskite crystal structure is distorted into a rhombohedral structure for the entire temperature range from 0 K-500 K, with a phase transition at about $T_C = 370$ K from a paramagnetic to ferromagnetic phase upon decreasing the temperature [20, 91, 92]. This can be represented with a hexagonal unit cell,¹ as is depicted in Figure 4.3. The hexagonal unit cell is shown on the left and a larger view of the hexagonal (001)-plane is shown on the right. Note the

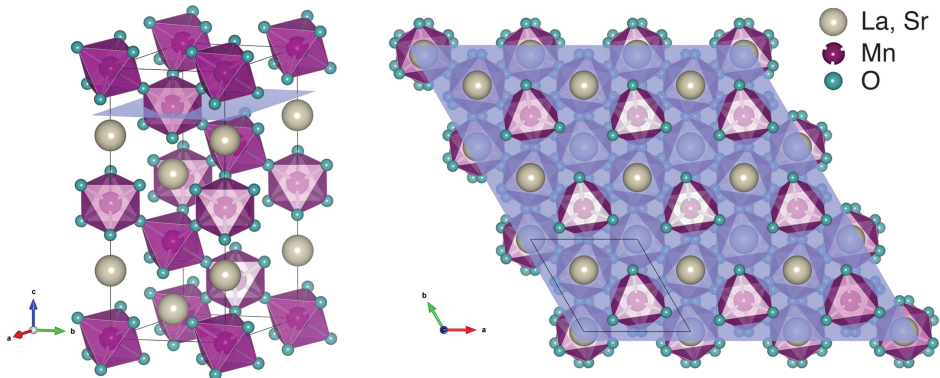


Figure 4.3: The hexagonal LSMO crystal structure (left) and its projection along the hexagonal [001]-axis (right). The purple-blue plane cuts through the plane of manganese ions between two planes of $\text{La}_{0.7}\text{Sr}_{0.3}\text{O}_3$. The structural model was received from PhD candidate Torstein Bolstad.

similarity between the LSMO hexagonal (001)-plane here and the cubic (111)-plane of STO in Figure 4.2. As for STO along its cubic [111]-direction, LSMO has alternating layers of $\text{La}_{0.7}\text{Sr}_{0.3}\text{O}_3^{3-/4-}$ and $\text{Mn}^{3+/4+}$ along the hexagonal [001]-axis. The in-plane hexagonal symmetry is the same, the only difference is the slightly twisted MnO_6 octahedra and a small difference in interatomic distance. For STO, the distance between nearest neighbor Sr ions is 5.522 Å, while for LSMO the distance between La, or Sr, ions is 5.506 Å. Thus, a good epitaxial match is found for this interface, which ideally should enable a single atomic layer interface between the materials. Still, the same issue with surface polarity

¹Springer Materials http://materials.springer.com/isp/crystallographic/docs/sd_1814188

applies for LSMO as well, with total charge ± 4 or ± 3 per unit cell depending on the local manganese valence. Hence, in practice the LSMO/STO(111) interface extends over a few atomic layers [30].

As early as in 1950, Van Santen and Jonker [93] found that the resistivity was minimized in LSMO solid solutions at $x = 0.3$. Moreover, they reported in the same paper that the peak resistivity occurs precisely at the Curie temperature [93]. In another paper published earlier the same year, they found that LSMO with $x = 0.3$ had close to the highest Curie temperature (slightly higher for $x = 0.35$) and the highest saturation magnetization [94]. The discovery of these properties subsequently led to a lot of research on LSMO [20, 91, 92]. Zener [95] proposed a theory of *double exchange* between the manganese ions of different valence, to explain both the high conductivity and simultaneous ferromagnetism. The double exchange works by having an electron traverse from a Mn^{3+} ion across and intermediate O^{2-} ion to an adjacent Mn^{4+} ion, so long as the spins of the manganese ions are oriented parallel [95]. The process includes the exchange of two electrons, hence the name double exchange. First, one electron transfers from the d orbital of Mn^{3+} to the p orbital of O^{2-} , but for this to be possible the O^{2-} must move one of its own electrons further on to the adjacent Mn^{4+} , due to the p orbital of O^{2-} being full [96]. Furthermore, an electron with the same spin direction must be passed on from the O^{2-} , as spin-pairing of complete orbitals require antiparallel spins. As a result, double exchange is only favorable for adjacent manganese ions sharing the same spin direction, and the high conductance of electrons in the crystal coincides with ferromagnetic order [96]. Consequently, the Fermi energy has nearly 100% spin polarization of the electrons, which makes the material suitable for spin filtering in various devices [20, 97]. Although the level of spin polarization reported in the literature has been varying much, it has been suggested that the spin polarization is indeed close to 100% in the mixed-valence manganites, however, only if the materials can be properly fabricated [26].

In sum, the relatively large magnetization, low resistivity, and the almost completely spin-polarized half metallic character, makes LSMO useful in this work. In addition, at low temperatures LSMO is expected to show relatively large coercivity, with the result that it can be used as a hard magnet in the MFTJs.

4.1.3 Barium Titanate

Barium Titanate, BaTiO_3 (BTO), is a distorted perovskite with tetragonal symmetry at room temperature [20, 89, 90, 98]. The unit cell parameters are $a_{\text{BTO}} = 3.989 \text{ \AA}$ and $c_{\text{BTO}} = 4.029 \text{ \AA}$ [89], while the reported Curie temperature ranges from 393 K-398 K [20, 89]. It shows a relatively large bulk remanent polarization of $P_r = 26 \mu\text{C cm}^{-2}$ [20]. However, larger polarizations have been shown for strained BTO [57, 60], and a remanent polarization has been shown at room temperature for (001)-oriented highly strained BTO-films down to 1 nm thickness [60].

Figure 4.4 shows the cubic and tetragonal unit cells of BTO. The left part shows the cubic phase, as occurs above the Curie temperature, where BTO is in the paraelectric state [20]. The tetragonal phase is shown on the right side. Here, small displacements of the O^{2-} and Ti^{4+} ions relative to the Ba^{2+} ions can be seen. In a study of powder form BTO, Kwei et al. [98] found that the oxygen anions were displaced in two different quantities relative to Ba^{2+} . At 300 K, the two oxygens above and below Ti^{4+} along the [001]-direction were displaced by approximately -2.44% , while the four lateral oxygens surrounding Ti^{4+} in the ab-plane were displaced by about -1.05% . Ti^{4+} on the other hand, was found to be displaced $+2.24\%$ relative to Ba^{2+} along the [001]-direction [98]. These displacements have been applied for the tetragonal representation in Figure 4.4. The arrows illustrate the major (red) and minor (yellow) contributions to the total electric dipole moment induced by the displaced ions.

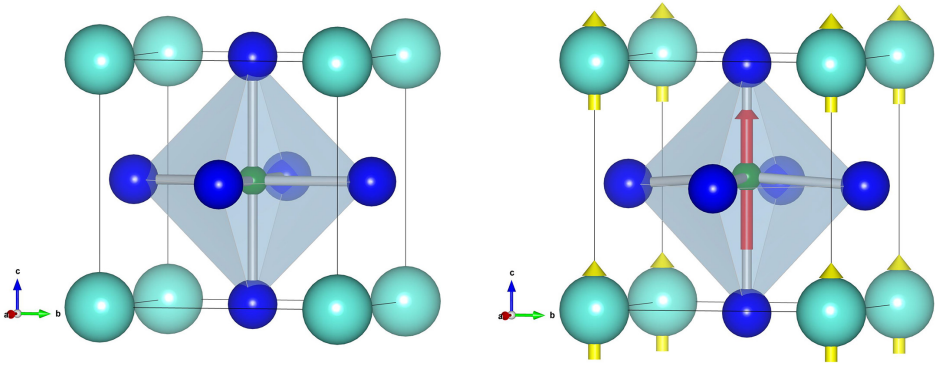


Figure 4.4: $BaTiO_3$ represented by its cubic structure above T_C (left) and its tetragonal structure at room temperature (right). Ti (dark green) is captured inside the oxygen (blue) octahedra while Ba (indigo) is at the perovskite unit cell corners. In the tetragonal phase, the red arrow represents the main contribution to the electric dipole moment from the displacement of Ti^{4+} , while the yellow arrows represent a much smaller contribution from the displacement of O^{2-} relative to Ba^{2+} . The lattice parameters were taken from Kwei et al. [98].

The small displacements of Ti^{4+} and O^{2-} , along the [001]-axis are collective for adjacent unit cells, which leads to a large dipole moment as a result of the separation of positive and negative charge centers. Regions of collectively oriented polarization vectors thus forms ferroelectric domains, which can be oriented by an applied electric field to form a macroscopic remanent polarization in the medium. Upon reversal of the applied electric field, the oppositely charged ions are forced to switch displacement direction within the unit cell as the field strength overcomes the coercive field [90].

As the temperature is lowered, bulk BTO goes through two additional phase transitions. At about 278 K it goes from the tetragonal phase to a orthorhombic

bic phase were the polarization vector changes direction from lying along [001] to [011], one of the face diagonals, in the pseudocubic unit cell. Furthermore, at about 183K it goes from the orthorhombic to rhombohedral phase, and the polarization vector changes again to the body diagonal [111]-direction of the pseudocubic unit cell [98]. The thin film structure is, however, not precisely known. Thus, assuming a tetragonal phase also for lower temperatures, the polarization vectors will lie along either of the $\langle 001 \rangle$ -directions, with an angle relative to the (111)-plane normal. Hence, the polarization may be harder to saturate than for the (001)-oriented films, and a single ferroelectric domain is less likely to occur.

In sum, the BTO is used in the MFTJs here because of its relatively large polarization, which can be maintained down to thicknesses thin enough for tunnel junctions. Moreover, it is a more environmentally friendly candidate than the much used lead zirconium titanate (PZT).

4.1.4 Permalloy

Permalloy, $\text{Ni}_{0.81}\text{Fe}_{0.19}$, here with constituent weight shares 81% Ni and 19% Fe,² has been chosen for the soft magnetic top layer in the MFTJs.

$\text{Ni}_{1-x}\text{Fe}_x$ alloys take either the body centered (bcc) or face centered (fcc) cubic crystal structures under ambient conditions, where the bcc and fcc structures are favored for iron-rich or nickel-rich alloys, respectively. Furthermore, the name permalloy usually refers to alloys with stoichiometry in the range $x \in [0.18, 0.25]$ [99]. Consequently, it can be expected that the permalloy deposited in this work takes the fcc structure, but no verification of the actual crystal structure has been done.

Permalloy has a small magneto-crystalline anisotropy and close to zero magnetostriction, but very large magnetic permeability [100]. Moreover, it has a low coercivity and significant anisotropic magnetoresistance [101]. These properties make it one of the most important soft magnets in a variety of applications, such as the cores of electric machinery and the free layers of spin-valve magnetic reading heads. The low magnetostriction is critical for industrial applications, where variable stresses in thin films would otherwise cause a ruinously large variation in magnetic properties [99]. The experimentally reported Curie temperature of bulk permalloy is 871 K for the fcc phase [102]. In the bcc phase it is 553 K, and was shown to lie above 400 K at thin film thicknesses down to 2 nm [99]. Accordingly, the fcc phase is expected to have a Curie temperature in thin films well above the bcc phase, as in bulk.

To sum up, the low coercivity, high magnetic permeability giving rise to large magnetization, and high Curie temperature, make permalloy a suitable for the easily switchable soft magnet in the P-MFTJs here. Furthermore, as the top and bottom electrodes of the P-MFTJ are different materials and one interface

²Permalloy is in general nickel-iron alloys with small amounts of manganese, carbon, molybdenum or silicon added. In this text, however, only a pure nickel-iron alloy is meant when talking of permalloy.

is epitaxial while the other is not, the asymmetric conditions that favor a large TER effect are present.

4.1.5 Passivation and Electrical Contacts

SiO_2 was used for passivation of the complex oxides and insulation to make electrical wiring and contact pads for wire-bonding without shorting the top and bottom electrodes. For the wiring and contact pads gold was used with a thin layer of titanium first, to promote adhesion to the underlying materials.

Sputtered platinum, Pt, was used to make electrical contacts to both top and bottom electrodes. For the P-MFTJs it worked mainly to prevent oxidation of the permalloy. For LSMO in both types of MFTJs' bottom electrodes, and for the top electrode in the O-MFTJs, platinum was used to achieve an ohmic contact. Abuwasib et al. [103] investigated the use of platinum for contacting metallic oxide electrodes SrRuO_3 and $\text{La}_{0.67}\text{Sr}_{0.33}\text{MnO}_3$ after different processing environments. For untreated LSMO(001) films of thickness 50 nm, they found a specific contact resistivity for Pt/LSMO of $\rho_c = 5 \times 10^{-5} \Omega \text{ cm}^2$. After reactive ion etching with BCl_3/Ar or O_2 plasma, the specific contact resistivity increased to $\rho_{c,\text{RIE}} = 1.2 \times 10^{-3} \Omega \text{ cm}^2$ or $\rho_{c,\text{O}_2} = 4.4 \times 10^{-2} \Omega \text{ cm}^2$, respectively. Importantly however, the contacts were ohmic in all cases, as opposed to identical samples with titanium instead of platinum [103]. Moreover, the Pt/LSMO contacts improved with a decreasing contact resistance for rapid thermal annealing treatments up to 700 °C. Hence, platinum seems to be a good choice for making ohmic contacts to LSMO.

The final contact pads and wiring were made from either gold (as shown in fig. 4.1) or aluminium with a thin adhesion layer of titanium underneath.

4.2 Experimental Methods

In this section, a brief explanation of the experimental techniques used for fabrication of the MFTJs is given. The systems used are presented along with essential parameters that were varied.

4.2.1 Electron Beam Lithography

Electron beam lithography (EBL) is a patterning technique similar to photolithography, however, where accelerated electrons are used to expose an electron sensitive resist material instead of photons. An Elionix ELS-G100 system has been used for EBL in this work. It is a 100 kV EBL system with a 100 MHz pattern generator. The beam current can be set to between 100 pA and 100 nA, where the beam spotsize correspondingly varies from 1.8 nm to 300 nm. Large beam currents and spotsize may be used for writing large structures, while smaller current and spotsize is necessary for small dimensions and to get better edge contrast.

EBL works by having a focused electron beam scanned over the area where a pattern is intended for a given time, corresponding to the delivery of a certain amount of electrons. The total amount of electrons delivered to an unit area is called the *area dose*, or just dose, and is usually given in units of $\mu\text{C cm}^{-2}$. The dose, D , is simply given by the beam current, I_{beam} , scanned uniformly over an area, A , during a time, t , or

$$D = \frac{I_{\text{beam}} \cdot t}{A} . \quad (4.1)$$

Depending on the resolution that is needed, the beam current can be decreased or increased for better or worse resolution, respectively. This will in turn increase or decrease the total time of the exposure, respectively, since the same area dose is needed for a complete exposure. For a small or large beam current, the beam diameter will vary correspondingly, effectively giving an upper bound for the smallest theoretically possible area that can be exposed with a given beam current. To control the beam scanning and the resulting area dose, the exposure area is divided into a grid of spots, like pixels on a screen. The pitch between neighboring spots should be about the same as the beam diameter or slightly less, to make sure a uniform exposure is achieved. To find the time the beam has to be positioned at each spot in order to deliver the designated dose, the above relation is rearranged to

$$t_{\text{spot}} = \frac{D \cdot A_{\text{spot}}}{I_{\text{beam}}} , \quad (4.2)$$

where D is the wanted dose, A_{spot} is the area of a single spot, and I_{beam} is the beam current. This parameter is used by the pattern generator for scanning the beam with correct speed so that all spots are irradiated with the correct amount of electrons. The needed dose to achieve complete exposure for an electron resist is highly dependent on the acceleration voltage. However, since the EBL system used is a dedicated 100 kV system, no more details on this matter will be given here.

BEAMER – advanced EBL patterning and dose correction

The Elionix EBL system makes use of a specialized software from GenISys called BEAMER to make exposure sessions more efficient, versatile and uniform. There are a few issues with EBL compared to conventional photolithography, which especially regards exposure time and proximity effects. BEAMER helps to minimize these issues, and there are two ways in which this tool has been used in this work. These are proximity effect correction (PEC) and a division of exposure masks into bulk and sleeve regions for faster exposure.

To correct for proximity effects, the software employs simulation models for various resist types and thicknesses on different substrate materials. When an exposure contains different kinds of geometric shapes with varying size and spacing, proximity effects strongly deteriorate the final result after development, as

structures always will be slightly exposed when the beam is exposing neighboring structures. Moreover, small and lonely structures in general need more dose than large structures to develop sufficiently.

To minimize the time needed for exposing large areas, the masks were divided in bulk and sleeve regions. After preparing the mask, BEAMER was used to extract the bulk and edge areas of the mask into two different patterns with a small overlap. For the large bulk areas a high beam current was used for fast dose delivery and larger spotsize, while for the edge areas a smaller beam current with a fine spotsize was used to get better resolution and less proximity effects. Depending on the exposure pattern, a little or very much time can be saved by employing this method. If the total area to be written is not large, the time used for switching the beam current and setting up the system can exceed the time that is saved. Moreover, the system should be given an idle time of 25 minutes or more after changing the beam current, in order to stabilize. If this is not done, the beam can have a subtle shift over time and produce small offsets of the bulk and sleeve patterns, which will result in a bad pattern that needs to be redone.

In Figure 4.5 on the left side, a BEAMER flow chart can be seen where a combination of both bulk/sleeve separation and PEC has been utilized. This flow was employed for all stages of the fabrication process, which will be presented in chapter 6. The right side shows an example of how the dose is corrected for proximity effects with the goal of giving equal development for all parts of the pattern. Warmer and colder colors correspond to more or less dosage, respectively. Also visible in the down right inset is a magnified view of the overlapping region between bulk and sleeve. The overlap used in this work was 200 nm, while the sleeve was the outermost 500 nm of any structure.

4.2.2 Plasma Ashing and Descumming

A Diener Electronics Femto plasma cleaner was used for cleaning and surface preparation of test wafers and final samples. It was also used for descumming of resist residues after development, before further processing. Oxygen and ambient air are the process gases used in this system. Unfortunately there are no definite units used for this system, only percentages of some maximum, and the exact processing pressure is unknown. For simplicity the same process parameters were always used, while the process time was varied. The parameters were 80% O₂ flow and 80% generator power. Processing time was usually either 1 or 3 minutes, but this will be specified later.

4.2.3 Physical Deposition Techniques

Electron Beam Evaporation

Electron beam evaporation (e-beam) is a method for physical vapor deposition of thin films in single or multiple layers onto a given sample substrate. An

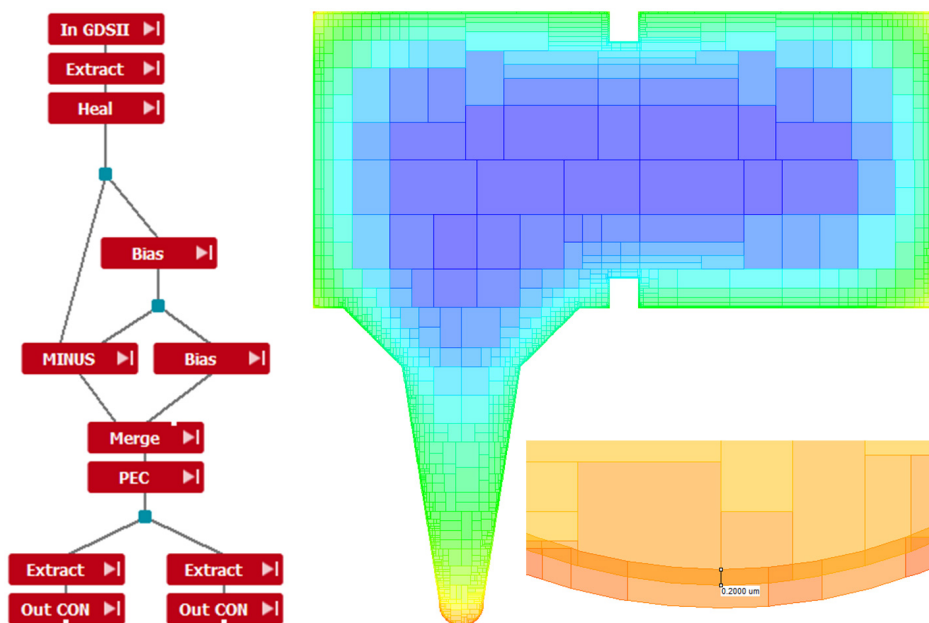


Figure 4.5: BEAMER flow diagram for bulk/sleeve separation and proximity effect correction. **Left:** BEAMER flow diagram where the mask design file is imported, healed, split in bulk and sleeve, merged into one file for PEC, and then exported in separate exposure files for bulk/sleeve with common PEC. **Right:** Example of PEC on a structure with varying dimensions. The inset down right is a magnification of the bottom circular structure, showing the bulk/sleeve overlap region.

electron beam is focused into a crucible containing the desired material, and heats the material until vaporization either from a solid or liquid phase. The evaporating material subsequently condensate all over the chamber and covers the sample, which is typically situated straight above the evaporation source. The process takes place in a high vacuum, typically below 10^{-7} Torr (1 atm = 760 Torr, 1 Torr = 1.33 mbar), so that the vaporized atoms move relatively freely. A quartz crystal oscillator calibrated for all materials in the system is used for thickness monitoring, with 0.1 \AA s^{-1} deposition rate resolution.

A Pfeiffer Vacuum Classic 500 e-beam evaporation system (Pfeiffer system) has been used for deposition of titanium, aluminium and gold for contact pads and wiring. The targeted deposition rates used were 1.0 \AA s^{-1} to 12.5 \AA s^{-1} for titanium, 5 \AA s^{-1} to 20 \AA s^{-1} for aluminium, and 5 \AA s^{-1} to 17 \AA s^{-1} for gold. The e-beam acceleration voltage is 8 kV, and typical currents used were 30 mA to 58 mA for titanium, 190 mA to 235 mA for aluminium, and 55 mA to 90 mA for gold. The chamber pressure during deposition of titanium, aluminium and gold were roughly 10^{-8} Torr, 10^{-7} Torr, and 10^{-6} Torr, respectively. The system

is reported to deposit uniform films for samples up to 50 mm size without sample rotation. Even though all samples in this work were much smaller than this, rotation with about 15 rpm was always used during deposition.

Sputter Deposition

Sputtering is a method for physical vapor deposition of thin films in single or multiple layers onto a given sample substrate. In a typical sputtering process, argon atoms are ionized by strong AC or DC electric fields to form a plasma, accelerated by another DC bias and bombarded onto the target material. The relatively heavy bombarding argon atoms eject atoms from the target surface, which are thrown towards the sample and chamber walls for condensation. The process takes place in a lower vacuum (higher pressure) than evaporation, typically below 10 mTorr, since enough gas atoms are needed for plasma generation. A quartz crystal oscillator calibrated for all materials in the system, is used for thickness monitoring with 0.1 \AA s^{-1} deposition rate resolution.

An AJA International Inc. Custom ATC-2200V sputter and evaporation system (AJA system) has been used for sputtering of permalloy, platinum, gold and SiO_2 . Moreover, dry-etching of BTO and LSMO was done with pure argon etching with the low power substrate etch available in this system. It was supposed to be used for e-beam evaporation too, but the e-beam power supply was out of order during the entire period of this work. The deposition rates were about 1.0 \AA s^{-1} for permalloy, 1.13 \AA s^{-1} for platinum, 2.0 \AA s^{-1} for gold, and 0.3 \AA s^{-1} for SiO_2 . More details are found in Chapter 6. All sputtering was done with a 3 mTorr argon pressure, after plasma striking at 30 mTorr and stepwise decrease. For permalloy, platinum and gold sputtering, a DC-generated plasma was used, and a RF-plasma was used for SiO_2 sputtering and sample etching. The AJA system is reported to deposit uniform films for samples up to 4 inches size with sample rotation on. Although all samples in this work were much smaller, rotation with about 20 rpm was always used during deposition.

Deposition Rate, Etch Rate and Selectivity

The deposition rate is the rate at which a desired material is deposited on some wafer or sample surface in a certain deposition system. Thus the relation is written [104]

$$r_d = \frac{\Delta T_d}{t_d}, \quad (4.3)$$

and is typically given in Ångströms or nanometers per minute. Here ΔT_d is the thickness of deposited material divided by the deposition time t_d .

The etch rate is the rate at which a material is removed from the wafer surface upon etching. It is given by [104]

$$r_e = \frac{\Delta T_e}{t_e}, \quad (4.4)$$

typically given in Ångströms or nanometers per minute. Here ΔT_e is the thickness difference of the etched material before and after etching, and t_e is the etch time.

The etch selectivity is the relative ratio of etch rates between two materials in the same etch process. Selectivity thus becomes [104]

$$S = \frac{r_{\text{film}}}{r_{\text{ref}}}, \quad (4.5)$$

where r_{film} is the etch rate of the film to be etched, and r_{ref} is the etch rate of some reference material under the same etching conditions. For example, the reference can be a soft or hard masking layer, or the underlying material. Usually a high etch selectivity is desired, so that only the material of interest is etched while other materials are affected as little as possible.

Whenever sample patterning is achieved by etching, an etch mask is needed. To find the etch rates of both the material one wants to etch and the etch mask material, a series of three step height measurements can be used. These step heights are shown in Figure 4.6. The initial mask thickness after deposition of

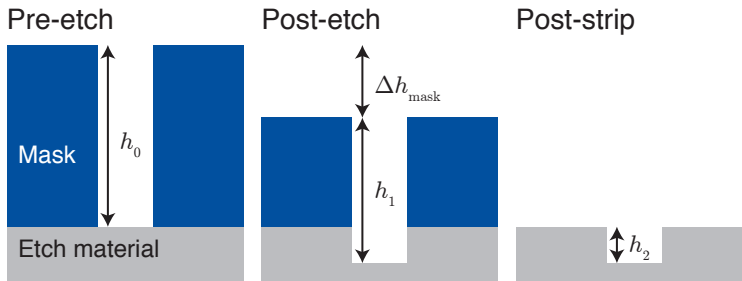


Figure 4.6: Etch rate determination by step profile measurements before etching, after etching and after removing the etch mask. Here it is illustrated for an etch process using a thick soft mask (resist), but the same principle is valid when using a thinner hard mask.

a hard mask or development of a soft mask is h_0 . After etching, h_1 represents the total height of the etched material plus what remains of the mask. When the mask has been removed, another height, h_2 , can be measured as the actual etch depth of the etched material and used to calculate the material's etch rate. To find the etch rate of the mask, a straightforward relation follows as

$$\Delta h_{\text{mask}} = h_0 - (h_1 - h_2), \quad (4.6)$$

where Δh_{mask} can be divided by the etch time to find the mask etch rate. The two rates are subsequently used to find the final selectivity.

4.2.4 Profile Measurements

Soft mask and deposited material profiles were investigated by profilometer scans from a Veeco Dektak 150 profilometer. A profilometer is used to measure surface

profiles and determine the roughness of sample surfaces. A 12.5 μm diamond tip stylus is scanned along a straight line over the sample surface and records the height differences by laser interferometry. The scan is recorded and analyzed with the Dektak software.

4.2.5 Scanning Electron Microscopy

Two scanning electron microscopes (SEM) have been used for sample characterization in this work. Both can be operated with acceleration voltages from 1 kV to 30 kV. A high-end Hitachi S-5500 S(T)EM with in-lens sample mounting and a cold-field emission electron gun was used for high resolution imaging. The S-5500 can achieve resolutions of less than a nanometer with good samples, and it is relatively fast and easy to optimize the beam for a good image. Beam currents can be selected from 1 μA to 20 μA . Here 5 kV was usually used for surface sensitive imaging, and the currents were kept low at around 2 μA to minimize charge buildup in the poorly conducting or insulating samples. Since the sample is mounted inside the electromagnetic lens environment in this instrument, magnetic materials are prohibited to prevent samples from being pulled off the stage or magnetic materials to be ripped off the sample surface. Still, it was used for imaging of LSMO samples, since LSMO is a very weak magnet at room temperature and the material was epitaxially grown on the substrates. Samples with permalloy top electrodes were not imaged in this system at all.

A JEOL JSM-6480LV with a thermal emission tungsten filament was used for medium resolution imaging and imaging of samples containing permalloy. Experienced users with good samples can achieve resolutions below about 50 nm with this microscope, however, for the purpose of its use here, a resolution of several hundred nanometers was sufficient. One of the key advantages of this instrument is its sample stage control, which enables a very quick change of working distance, tilting and rotation. This is useful for imaging large sample areas and taking overview images, or to locate smaller features from known references. The beam current can not be set explicitly, but there is a convenient software bar which controls the gun aperture for relative current control on the go.

4.2.6 Atomic Force Microscopy

A Veeco Metrology diMultimode V atomic force microscope (AFM) was used for surface and profile characterization of top electrodes and BTO/LSMO etch profiles. AFM offers topographic measurements of surfaces with accuracy down to atomic monolayers for high quality samples. It can be used in contact, tapping or ScanAsyst modes, where ScanAsyst is the simplest one to use and also the mode used here. It automatically uses a peak force mode to calculate the best parameters for the sample under measurement

4.2.7 Wire-bonding

Wire-bonding is a broad term covering the processes of thermocompressive bonding, ball bonding, wedge bonding and thermosonic bonding, where the latter three are all varieties of ultrasonic bonding. Furthermore, these processes are *cold weld* processes, meaning they weld materials without melting them [105]. The purpose of wire-bonding is to make electrical connections between small electronic circuits or samples and the outside world, for example integrated circuit dies to the leads of their protective package, or the tunnel junctions of this work to the external measurement circuit. The interconnections are done by means of cold welding thin gold or aluminium wires with a wire-bonder tool. In this work wedge bonding with gold wire has been used mostly. Wedge bonding with aluminium wire has been tested with less success, because only bond needles optimized for gold wire was available. Wedge and ball bonding methods are briefly explained below.

Wedge bonding uses ultrasonic energy, time and pressure to join two materials, typically aluminium and/or gold. Ultrasonic energy, when applied to a metal for bonding, temporarily renders the material soft and plastic. In turn, this causes the material to flow under the applied pressure, and the deformation of the wire brakes up contaminants and sweeps them aside from the weld area. A clean metallurgical bond is thus formed without the need for external heating, as heat is already generated in the bonding process [105]. The wedge tool is an asymmetric needle which feeds the wire out under its clamped wedge at an angle, before being stamped onto the bond pad. The main advantage of wedge bonding is the small area of the needle, which enables bonding to tiny pads.

Ball bonding uses the same parameters as wedge bonding, but the needle is here symmetric and feeds the wire down vertically. Only gold wire is used, and the first bond is made with a small ball at the end of the wire. The ball is made by a discharge from an electrode swiped in under the needle's end, which melts the gold to form a drop/ball at the end. The tool is subsequently lowered onto the bond pad, and the bond is formed much like the wedge bond. The second bond is essentially a wedge bond.

A TPT B05 Wedge and Ball Bonder (wire-bonder) was used for wire-bonding the samples. It offers thermosonic bonding with either a wedge or ball bonding tool. Thermosonic only means that it can bond with external heat added from a hot plate, however, this has not been used here because it could not be lowered enough to fit the measurement system's PCBs at the correct height. A PCB mounting station was specially made by Tore Landsem at the IET machine shop for this purpose, but it does not have a heater element connected. Hence, only room temperature wire bonding has been utilized here.

4.2.8 Vibrating Sample Magnetometry

A Quantum Design VersaLab physical property measurement system (VersaLab), was used with a Vibrating Sample Magnetometer (VSM) module to measure

the magnetic properties of the epitaxial samples used for the O-MFTJ. VSM measurements of the permalloy and bottom electrode epitaxial samples were done previously in the autumn project [1]. As the name indicates, the magnetic sample is oscillated in a static, or slowly varying, magnetic field, and the induced voltage in a pickup coil surrounding the vibrating sample is measured and converted to find the sample's magnetization as a function of applied magnetic field and temperature. Details on the different default measurement modes of the VSM was revised in the autumn project [1] and is not further featured here.

4.2.9 Electrical Transport Measurements

The VersaLab system was used with an Electrical Transport Option (ETO) module to measure the electrical resistance over the MFTJs as a function of applied electric and magnetic fields. The supported measurements are standard AC resistance, IV-curves and differential resistance versus DC current (dVdI). The ETO module supports two wiring configurations, 4-wire for low impedances and 2-wire for high impedances, and it has two completely independent measurement channels. The hardware consists of AC lock-in amplifiers and filter circuits to drive and measure AC signals and a DC source to superimpose DC offsets on the AC signals [106]. Details on the different default measurement modes of the ETO was revised in the autumn project [1] and only the most relevant information is presented below. In section 4.2.10 a brief introduction to the four-point-collinear and four-wire measurement techniques are given, and the sample wiring used in this work is shown there in Figure 4.8.

Four-wire mode

In the 4-wire mode the ETO sources current and reads the voltage response. The current source employs an internal feedback in order to deliver the requested current regardless of load impedance. There is no default supported way to control the current source by means of the voltage readout, i.e. a voltage controlled current source. The different measurement modes are entirely controlled by the DSP once they are initiated. The 4-wire mode is approved for measuring resistances in the range $10^{-8} \Omega$ to $10^7 \Omega$ and can source currents in the range 10 nA to 100 mA. Below the different measurement types and controllable parameters introduced.

Standard resistance measurements applies a sinusoidal AC current only and no DC offset. The AC frequency can be adjusted from about 0.4 Hz to 200 Hz and the current amplitude from 10 nA to 100 mA.

IV-curve measurement mode works by measuring the sample's voltage response to an applied triangular current waveform. The sweep direction can be selected either to go towards positive or negative currents, but always starts at zero. In addition, the sweep can be selected to stop when returning to zero (half

triangular period) or continue to the opposite polarity before stopping at zero (complete triangular period). The current sweep range can be set from 10 nA to 100 mA. The measurement contains exactly 256 data points per quarter triangular period, i.e. 1024 points for a complete cycle, regardless of the amplitude of the current sweep. The cycle frequency can be set from about 0.3 Hz to 100 Hz and is also independent of current sweep amplitude. Hence, for larger sweep amplitudes, the data points for each current setpoint are further apart and the current rate of change increases. All IV-curves presented in this thesis were performed at a special user-defined cycle frequency of 0.15 Hz.

Differential resistance mode operates by superimposing a small sinusoidal AC excitation on top of a DC current offset and measures the approximate differential resistance at each discrete DC point. Since this operation mode is a direct measure of the derivative of the IV-curve at any given DC offset, it is useful for thorough investigations of nonlinearities in a sample's IV characteristic if the AC amplitude is small enough relative to the range over which the nonlinearity extends. The dVdI mode is essentially the ordinary resistance mode with an extra DC offset that can be adjusted in steps of 1 nA, however, the DC offset cannot be smaller than the AC amplitude. dVdI can be started at zero or both maximum offset polarities and swept in discrete steps through a complete cycle or down to quarters of a cycle.

Two-wire mode

In the 2-wire mode the ETO applies a voltage and measures the current with a nanoammeter. The voltage source employs an internal feedback in order to deliver the requested voltage regardless of load impedance. 2-wire mode uses only wiring pads I+ and V- and there is no way to know the exact junction voltage, only the total applied voltage to the circuit under test. The 2-wire mode is approved for measuring resistances in the range $10^6 \Omega$ to $5 \times 10^9 \Omega$ and can measure currents up to a maximum of 250 nA. The voltage bias can be set in the range 10 mV to 20 V, and all ordinary sequence mode measurements are as for the 4-wire mode, but with reference to voltage instead of current. This description is included for reference. The 2-wire mode has not been used in the thesis.

Tunnel Junction IV-curves

Standard IV measurements at the lowest cycle frequency were used to measure the MFTJs approximate DC tunneling characteristics. 4-wire measurements were conducted with the proper wiring shown at channel 1 in Figure 4.8 below. The junction voltages of interest had to be found manually by increasing the current sweep amplitude carefully. A typical IV-curve measurement script can be seen in the Appendix, Listing D.1.

Resistance versus Temperature

Longitudinal resistance measurements of the type shown on channel 2 in Figure 4.8 (both proper and improper) were done by ordinary resistance mode measurements while sweeping the temperature with and without the presence of a constant magnetic field. A series of four $R(T)$ during cooling and heating with and without a magnetic field can be found in the Appendix, Listing D.2.

Resistance versus Magnetic Field and Temperature (TMR)

dVdI-measurements were used to probe the MFTJ resistance as a function of magnetic field, $R(H)$, i.e. TMR measurements. A one-sided measurement with a single DC point per quadrant was used to measure the resistance at $|I_{\max}|$ and $I = 0$, first for positive current then for negative. The magnetic field was swept from +50 Oe to -50 Oe to +50 Oe while running a dVdI-measurement for each magnetic field step. The field sweep was repeated for increasing temperatures to measure the temperature dependence as well. Naturally, a constant current amplitude measurement over a magnetic field range which varies the junction resistance leads to varying junction voltages, but the voltage can not be controlled explicitly in the 4-wire mode. A typical measurement script for resistance as a function of magnetic field and temperature is found in the Appendix, Listing D.3.

Resistance versus Poling Voltage (TER)

dVdI-measurements were used to probe the MFTJ resistance as a function of applied poling voltage, i.e. TER measurements. To pole the junction standard IV-curve sweeps were used, and the resistance was read between subsequent poling voltages by dVdI and low amplitude IV-curves. Approximate poling voltages were applied in a triangular fashion with steps of 0.5 V from +2.5 V to -2.5 V to +2.5 V. The read current amplitude was set to coincide with approximately 10 mV and kept at a constant current level for all reads. All voltages were manually found by inspection of a reference IV-curve and entered into a sequence that can be found in the Appendix, Listing D.4.

Measurements Scripted with WinWrap[®]Basic

In addition to the sequence controlled measurements, prototype measurements were developed with scripting in WinWrap[®]Basic. It was only possible to implement dVdI and ordinary resistance mode measurements within the scope of the thesis. This work is presented in Chapter 7, and a representative example of script can be found in the Appendix, Listing D.5. Both DC current and magnetic field sweeps have been implemented. The object file holding all functions for communicating with the ETO module via CAN-bus has been extended considerably to extract more relevant information from the ETO. This file is found in the Appendix, Listing D.6.

4.2.10 Four-point-probe and Four-wire Measurements

Four-point collinear probe measurements are typically conducted on semiconductors to measure a relatively high resistivity dependent on doping level [107]. The technique involves four equally spaced probes along a straight line with sharp tips that are brought into contact with the material of interest. A known current is passed through the two outside probes and the voltage is sensed at the two inside probes. Due to specific geometrical constraints, the resistivity can be calculated according to a specific formula [107]. However, if the probes are not point sharp, instead they might be relatively large contacts, or they are not perfectly in line, rather the contacts may be placed around some specific part on a sample, the standard resistivity formula cannot be used. In this case, the setup is no longer a four-point collinear measurement, but is still useful for measuring the device resistance without interference from contact and wiring resistances. The latter is referred to as a *four-wire measurement setup* (4-wire, or Kelvin setup) [107], which will be used in the rest of this thesis.

Figure 4.7 shows a realistic circuit representation of a four-point-probe measurement setup, and it is equally well descriptive for a 4-wire setup. Given that the voltmeter has an input resistance, R_{IN} , much larger than the contact (and lead) resistances, $r_1...r_4$, only material resistance 2, between the voltage probes, will be measured. A very small current will flow through the sense leads, but as long as the device resistance under test (R_2) is not very large, it can usually be ignored. Hence, the voltage drop across the sense leads is negligible, and the measured voltage V_M is practically the same as the voltage across the resistance V_{R_2} . The result is that the measured resistance is much closer to the true device resistance than for a simple two-wire measurement [107]. The true device resistance will be more accurately measured by placing the voltage probes as close as possible to the device of interest, to exclude more of the current lead resistance.

A Common-Mode Current is also indicated, which will be an important source of error when the device or contact resistances are large and comparable to the current source and voltmeters' isolation to chassis ground, $R_{C,V}$ [107]. There are ways to suppress this influence which will not be discussed here, and the measurement systems are usually specified with a certain common-mode rejection ratio (CMRR) to describe how well they deal with this issue. The CMRR of the ETO module is reported to be larger than 100 dB. For low frequencies, this indicates that a common mode signal is canceled to 1 part per 10^5 [108]. This is a good rejection merit, but the error can still be significant if the common mode signal becomes large due to noise at the measurement frequency or a very large sample device resistance [108].

Figure 4.8 shows a schematic of the ETO vertical sample puck which enables in-plane magnetic fields. Two samples are shown connected to each measurement channel. On channel 1 a MFTJ is connected in a *proper* way with separate current and voltage probes bonded to the corresponding PCB pads for current sourcing independent of voltage readout. On channel 2 an example of a longitudinal

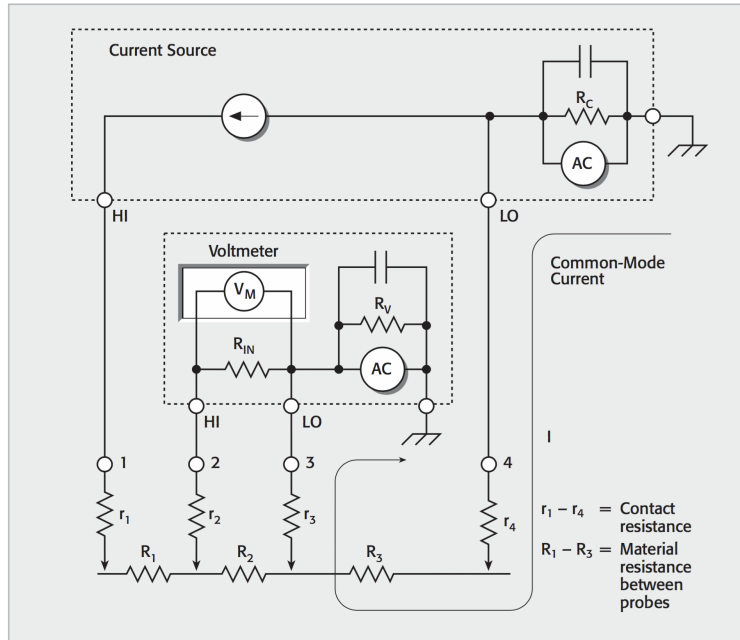


Figure 4.7: Realistic circuit diagram of a four-point collinear probe or 4-wire measurement setup. Reprinted from reference [107].

resistance measurement with *proper* and *improper* connections is shown with green and red voltage probe bonds, respectively. In an improper setup the voltage pads are directly shorted to the current pads on the PCB and the reported voltage will include the total potential drop over the lead, contact and sample resistances. A proper measurement on the same sample would report the voltage drop locally between the voltage probes located in line and within the current sourcing probes at each edge.

4.3 Data Analysis

Matlab was used to analyze and plot the relevant data. Measurement raw data was generated from two systems, the VersaLab ETO data files and the extracted profile data from AFM scans. Import functions were made for each of these, in order to enable analysis with MatLab. A thorough description of all scripts and functions will not be given here, for details the reader is referred to Appendix D. In the following paragraphs the most important parts of some of the analysis are shown.

Numerical derivatives of the current and voltage data from the IV measurements was done to assess the differential resistance and conductance as functions

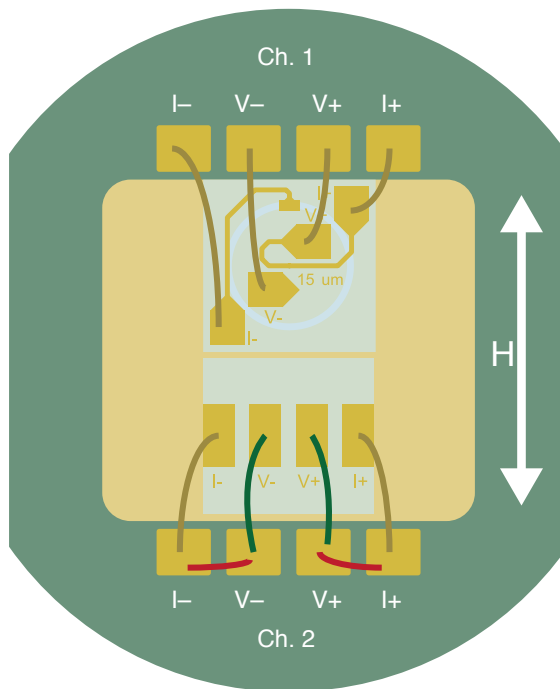


Figure 4.8: ETO vertical puck PCB with schematic representations of proper and improper 4-wire measurements. Proper measurements have all PCB bond pads bonded to the corresponding probes on the sample (Ch.1 and green on ch.2) while an improper measurement has the voltage probes shorted to the current probes so that lead and contact resistances are included in the reported voltage (red ch.2).

of junction bias. The following code lines describe the essentials of how this was done with Matlab after the data was properly imported:

Listing 4.1: Taking the numerical derivative of IV-data to find the differential conductance as a function of voltage.

```

for i = 1:2
    len = length(etoData{i}{1,6}(1:end,3-i));
    dI = diff(etoData{i}{1,5}(1:end,3-i));
    dV = diff(etoData{i}{1,6}(1:end,3-i));
    dG = smooth(dI)./smooth(dV);
    avgV = zeros(1,len-1);
    for j = 1:len-1
        avgV(1,j) = (etoData{i}{1,6}(j,3-i)+etoData{i}{1,6}(j+1,3-i))/2;
    end
end
plot(avgV,dG,'-o')

```

The differential resistance versus DC current data was converted to differential

conductance versus DC voltage for comparison with the numerical derivatives of the IV-curves. This was done simply by inverting the resistance to get the conductance, and using Ohm's law the DC current was converted to DC voltage for each resistance (or conductance) point:

Listing 4.2: Converting the differential resistance versus DC current to differential conductance as a function of DC voltage.

```
% Differential resistance measurement data
dR = R;           % unit Ohms
I_dc = cellfun(@str2double, rawData(idx:end,6)); % unit mA
I_ac = cellfun(@str2double, rawData(idx:end,7)); % unit mA
V_dc = dR.*I_dc./10^3; % unit V
dG = 1./dR;      % unit S
plot(V_dc,dG,'-o')
```

Chapter 5

Sample Design and Layout

In this chapter, the considerations for and final version of the sample layout are presented. The first section explains five main focus areas that need consideration when deciding on a final sample design. In the second section, the practical design as of the final iteration is presented, and circuit analysis based on this design is conducted in section three.

5.1 Considerations for the Sample Layout

As was discussed in the autumn project, careful consideration has to be put into designing a good sample layout [1]. Firstly, the top electrodes should be well defined with regard to size and shape. This was not the case before, as the lead attachment to the top electrodes was done manually by hand with silver paste, in order not to puncture and short the junctions with the wire-bonder. Consequently, the junction footprint became large with a corresponding increase in junction capacitance and decrease in junction resistance. Secondly, it should be strived for achieving uniform and ohmic contacts to the bottom electrodes. In the autumn project, gold was simply deposited along the sample edge to create contact with the LSMO layer. However, BTO and permalloy were deposited in between, so in principle the contact along the sample edge was just a slightly thinner version of the tunnel junction itself, apart from a naturally varying edge roughness. The contacts seemed decent from tests done with a multimeter, but no real verification was done. Moreover, a single contact at the sample edge leads to a varying series resistance from the LSMO layer depending on how far away from the sample edge the MFTJ is located. By including dedicated bottom electrode contacts in the fabrication scheme, these issues can both be addressed. Thirdly, the problem of bad adhesion between contact pads and the underlying material must be addressed. It was very clear that both permalloy and gold had appalling adhesion to the complex oxides, especially BTO. This posed a serious

difficulty for wire-bonding and has to be solved. Fourthly, a four-wire layout should be developed so that the true junction resistance can be measured without the influence of series and contact resistances. Fifthly, the wiring circuitry and contact pads should be made as small as possible to avoid the addition of unnecessary capacitance.

The above mentioned points are summed up and listed below. In turn they are further evaluated throughout the following paragraphs. With regard to these considerations and some necessary compromises, the final sample layout is presented in the next section.

Focus areas for the MFTJs:

1. Top electrode area, shape and uniformity need to be controlled precisely.
2. Uniform ohmic contacts to the top and bottom electrodes, with special focus on the latter, must be emphasized.
3. Contact pads with good adhesion to the underlying layer must be addressed for ease of wire-bonding.
4. A four-wire layout is needed for more precise measurements.
5. Wiring and contact pads should be made as small as possible to avoid unnecessary contribution of circuit capacitance.

5.1.1 Junction Area, Shape and Uniformity

For the preliminary MFTJs made in the autumn project, a simple brass shadow mask was used to define the MFTJ top electrodes [1]. Due to mechanical limitations, the diameter of these electrodes was as large as 200 μm with relatively large edge roughness and dimension tolerance. Moreover, this method is not suited for overlay deposition of insulating or conductive materials since precise alignment is difficult. Later when leads were attached, the effective top electrode area increased dramatically and arbitrarily, since the leads were glued to the approximate top electrode locations by hand with silver paste. For this reason only a small fraction of the top electrode was actually ferromagnetic, and the area was not known. To remove these issues while allowing for measurements with the VersaLab system, it is clear that multi-layered devices are needed. Thus, lithographic processing is necessary, and information on that part will follow in the next chapter. Most importantly, multi-layered devices prepared by lithography enables very precise control of dimensions, and bond pads can be placed away from the actual device. In addition, the exact shape of the tunnel junctions is given by the mask that is used and can easily be customized as wanted.

To enable practical measurements, a compromise between large and small junction area is necessary. Details will be introduced below in the part on circuit analysis, but in general smaller junctions minimize the capacitive effect and enhances the device resistance as the cross section decreases. Moreover, the junction characteristics are highly dependent on voltage bias and signal frequency.

Recently, other work in our research group has revealed quite large leakage currents in the BTO films, possibly enlarged by the presence of holes or voids in the films.¹ Leakage currents in BTO has also been reported as a serious general issue by others [63]. Smaller junction area is thus one way of limiting the leakage current and junction capacitance. However, the minimum area of prototype junctions should correspond to a resistance which is not larger than the measurement system can handle. Hence, there is a conflict between small and large device area. On one hand, smaller junction areas are what is interesting from a device point of view, to demonstrate that a technology may be interesting for commercialization. A small area is also what is interesting when it comes to enhancing the quantum effects that are investigated, as well as the possibility to observe novel functionality. On the other hand, the device resistance must be small enough so that practical measurements are possible.

It is not easy to know where this optimal range of junction area lies. However, a place to start is the existing literature, which was reviewed in Chapter 2. In Table 2.1 existing studies of FTJs and MFTJs with BTO barriers were listed. There is apparently no clear correlation from the existing data between junction resistance and junction area. Most of the existing reports show off-resistances in the megaohm range, but there are exceptions both well above and below (giga- and kilo-range). This may be a manifestation of varying degrees of leakage current paths in the junctions, the different electrode materials' influence on the effective tunnel barrier height, or it may be related to different junction biases and contact resistances involved in the resistance readings. A combination of these points as well as different operating temperatures are probable causes for the strongly differing resistance-area products. Resistance is inversely proportional to the area of the current path, so the resistance-area product, RA , of the tunnel junctions should in principle be more or less constant for similar devices with only a varying area. For a few of the listed reports this relationship seems to be indicated, but there are too many different electrode materials and other parameters involved to ascertain any clear correlation based on the available studies.

There is, however, a publication by Yin et al. [72] that seems particularly interesting in relation to the current work, because they used a model system that is relatively similar to the ones that are studied here. It was also listed in tbl 2.1 both under FTJs and MFTJs. They fabricated (001)-oriented LSMO/BTO/LSMO both with and without an intermediate $\text{La}_{0.5}\text{Ca}_{0.5}\text{MnO}_3$ (LCMO) layer at one of the interfaces between BTO and LSMO. The BTO thickness was kept at 3 nm while the LCMO interlayer was varied from none to five unit cells (0 to 2 nm). Hence, the tunnel barrier thickness was in the same range as here. The junction areas they used ranged from $5\ \mu\text{m} \times 5\ \mu\text{m}$ to $70\ \mu\text{m} \times 70\ \mu\text{m}$, and they report resistances in the range from 1 k Ω to about 1 M Ω [72]. To the knowledge of the author, there are no reports on TER with (111)-oriented BTO, but it is assumed here that the resistivity will be in a similar range. Hence, the

¹Private communication with PhD candidate Torstein Bolstad and Professor Thomas Tybell.

lower micron scale seems plausible as a target feature size range for this work. This scale should be sufficiently small to isolate the TMR and TER effects well, if they exist, while hopefully maintaining resistances within measurable upper limits.

5.1.2 Ohmic Contacts

Ohmic contacts are important in order to get precise measurements. As we will see, this is true whether one does ordinary 2-wire measurements where the contact and lead resistances are included, or 4-wire measurements where contact and lead resistances are supposed to be excluded. Additionally, with 2-wire measurements, the contact resistances must be small compared to the device resistance, in order not to have a detrimental impact on the measurement results. For 4-wire measurements, the contact resistances can be accepted while being relatively large, since they do not alter the measurement. However, if the contacts are rectifying in some way or another (non-ohmic), there is a problem, especially when measuring small voltage magnitudes or with alternating signal polarity.

A rectifying contact will need some voltage bias in order to conduct in the forward biased regime, which will result in a correspondingly lower reported read-out voltage. Even worse, in the reverse biased regime it might not conduct at all for the voltage range of interest. This is modeled in Figure 5.1 with a finite, but ohmic, contact resistance R_c in a), and a rectifying Schottky diode with threshold voltage V_t in b). The voltage probe is modeled as an ideal capacitor, C_{probe} , since the external measurement electronics should have a very high input impedance for the voltage probes. The voltage probe pad and wiring, or capacitor, still needs charging and discharging, and hence, a rectifying contact will alter the probe voltage more or less depending on its properties relative to the signal range, as can be seen in c) and d): For a positive sample voltage, V_+ , the probe voltage will charge up to the level where the rectifying contact is no longer conducting, yielding $V_{\text{probe}} = V_+ - V_t$. On the other hand, for a negative sample voltage, V_- , the rectifying contact will not conduct and the probe voltage remains unchanged. Depending on the direction of rectification, the above description may be reversed, but the result is the same. A shaded contact resistance, R_{leak} , is included in b)-d) as a possible large parallel resistance which may enable DC and very low frequency AC measurements. In this case, the rectifying contact is leaking sufficiently to enable slowly changing measurements, and the problem, in principle, reduces to the case shown in a). In any case, the issue is clear. Ideally one should have ohmic contacts, and they should be as small as possible so that the voltage probe time constant, $\tau_{\text{probe}} = R_c C_{\text{probe}}$, does not become comparable to the period of the applied signal that is measured.

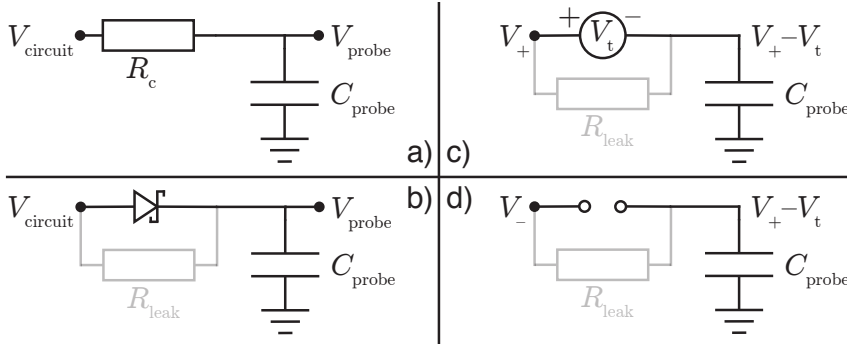


Figure 5.1: Ohmic versus rectifying contacts for electrical measurements. V_{circuit} , V_{probe} and C_{probe} are the true sample voltage, the measured sample voltage, and the voltage probe wiring and pad capacitance, respectively. **a)**: A proper ohmic contact to the circuit of interest. Ideally the contact resistance, R_c , should be very small. **b)**: A non-ideal contact with rectifying behavior, here modeled as a Schottky rectifier. **c)**: The rectifying contact in forward bias mode, where the measured sample voltage will be lower than the true sample voltage by the (threshold) voltage drop of the rectifier. **d)**: The rectifying contact in reverse bias mode, where the measured sample voltage will be unchanged from what it was before (here shown with c) as before). **b,c,d)**: A shaded contact resistance, R_{leak} , is modeled in parallel to allow the possibility for a leaking rectifier. In this case, the leakage results in the same principle as shown in a), but with a very large contact resistance.

5.1.3 Bond Pad Adhesion

Wire-bonding for electrical connections to the samples prepared in the autumn project proved to be one of the most time consuming challenges [1]. In brief, the problem was that gold deposited directly on BTO, or with the permalloy layer in between, had next to no adhesion at all. Thus when bonds were attempted, the metal was simply ripped off the surface along with the wire. The solution, which was far from optimal, was a rather violent aluminium wire wedge-bond on the same location till the aluminium attached to the oxide material stack itself. With a large gold pad in contact with the aluminum wire, seemingly good contacts were achieved, but the bonding process was time consuming and not particularly reproducible.

To promote bond pad adhesion, tests with a thin titanium interlayer between the pad material and the sample will be done. Titanium is known for its highly reactive properties and is much used as adhesion and contact layer in semiconductor fabrication [103]. However, the use of titanium in the vicinity of LSMO requires care, as it easily reacts with interfacial oxygen atoms in LSMO, which induces oxygen diffusion from the nearby region and a structural phase transition [109, 110]. This is in turn detrimental for the ferromagnetic order in LSMO [110]. Moreover, the LSMO film conductivity decreases considerably

upon titanium deposition, and the contact resistance turns non-ohmic at slightly elevated temperatures [103]. Hence, a different metal is needed for contacting LSMO, while titanium can be used for adhesion in the final deposition of bond pads. Metals that seem suitable for contacting LSMO are gold, platinum and palladium [103, 110, 111].

5.1.4 Measurement Layout

To reveal a more true device resistance from the electrical measurements, a four-wire layout will be needed. The main purpose is to remove lead and contact resistances from the reported resistance, so that the value reported is closer to the real value. If the sample resistance is very large, the difference may be negligible as long as the lead and contact resistances are minor in comparison. However, since both the final device resistance and the contact resistances to LSMO in this work are unknown, it is better to fabricate the samples with dedicated probes for current bias and voltage sensing. Moreover, the MFTJ devices show highly nonlinear current-voltage characteristics, which means that resistance contributions from the external circuit will have a variable impact on the junction bias depending on the applied signal magnitude. Hence, by probing the local voltage over the junction, these issues are effectively omitted. Technical details on how four-wire measurements are done and sources of error associated with them, were discussed in section 4.2.10. How the four-wire layout is implemented in practice will be presented in the next section.

5.1.5 Circuit Capacitance

Quantum Design specifies a circuit capacitance of approximately 375 pF for the ETO module and wiring, which is not possible to control in the experimental design here. Still, the sample layout can be made to contribute with as little capacitance as possible. It is mainly the top electrode contact pads including their wiring back to the actual device that will contribute, since these will have capacitive coupling to the blanket film LSMO layer that acts as bottom electrode. As will be presented in more detail below, the contact pads can be made small enough to have negligible impact on the total capacitance from the junction area itself and the ETO capacitance.

5.2 The Sample Design

The following presentation is the design of the final samples that were fabricated at the end of the experimental work. There have been several revisions along the way, but the early ones will not be explained here as they have been rejected from various reasons. Important issues that have been tested and verified, however, are addressed with the respective results in the next chapter. To give the reader an

intuitive understanding of all circuit symbols presented later, the MFTJ design and physical layout will be presented first. A justification of the various chosen device dimensions will be given along with the circuit analysis in the next section. It is noted that the following presentation describes the P-MFTJ structure, but the O-MFTJ structure is completely analogous as conceptually shown previously in Figure 4.1.

5.2.1 Physical Design and Layout

It was decided from the considerations in the preceding section to fabricate devices with diameters of 1, 3, 5, 10 and 15 micrometers, to cover a range of junction areas while at the same time have relatively small devices. Circular top electrodes were preferred to avoid shape anisotropy effects, in order to probe the possibility for partial switching of the LSMO layer along the in-plane magnetic easy-axes. To insulate the active parts of the device from the measurement circuit, SiO_2 was used. Titanium was used as an adhesion layer for the gold contact pads and wiring. All materials and thicknesses can be seen from a cross sectional view in Figure 5.2. To fit all the relevant information in the same figure, correct proportions and scales were abandoned. However, a top-down overview of the complete MFTJ layout with correct proportions, can be seen in Figure 5.3.

Figure 5.2 shows Pt used as contact material for the top and bottom electrodes. For the permalloy top electrodes, Pt also functioned as a capping layer to prevent oxidation. It was planned to use gold for this purpose, however, the e-beam evaporator part of the AJA system was down during the entire fabrication period. To save fabrication time and prevent the sample from exposure to atmosphere in the middle of a process stage, sputtered platinum was used instead.² Gold seems to have been the preferred material for contacting LSMO by other groups [27, 68, 72, 73], and it was used in the preliminary work as well [1]. However, platinum and gold are both noble metals, and platinum, like gold, does not have a deteriorating effect on the magnetic order of LSMO [109, 110]. Moreover, the study of ohmic Pt/LSMO contacts by Abuwasib et al. [103] shows excellent specific contact resistivity. Thus, to create electrical contacts to the LSMO bottom electrode, a physical sputter etch through the BTO/LSMO layers and subsequent platinum deposition was used. It was anticipated that ohmic contacts would develop over the cross-sectional interface of LSMO with Pt in the etched holes.

Figure 5.3 shows a top-down overview of the final layout for a 15 μm MFTJ. It shows the Au/Ti contact pads with wiring on top. The contact pads are ordered in this diagonal way to enable a 90° rotation of the sample while maintaining easy access for wire-bonding without crossing wires. Underneath is the light blue insulating SiO_2 layer with via holes to the top electrode in the figure center, and the bottom electrode at both V- and I-. The small circle in the V- pad

²Gold sputter targets were not available.

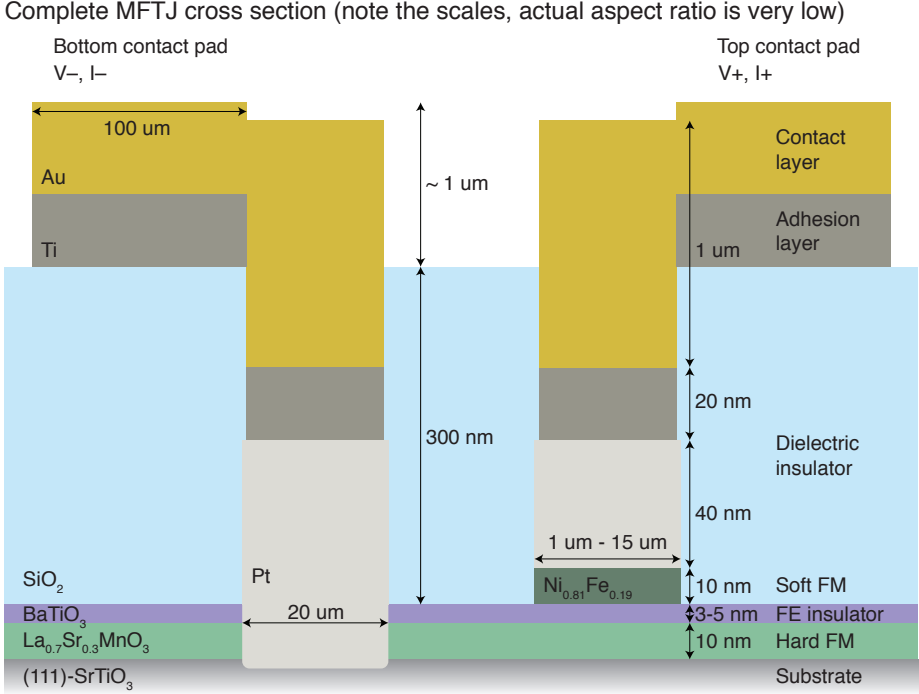


Figure 5.2: Cross section view of the final MFTJs. Here shown is the permalloy/BTO/LSMO MFTJ. The all-oxide LSMO/BTO/LSMO MFTJ is similar, but the BTO layer is partly etched together with the LSMO top electrode. To fit all relevant information into the same figure, scales and proportions have been altered.

and the large ring connected to the I- wiring are two separate bottom electrode Pt/LSMO contacts. The ring was chosen to give an as uniform as possible radial electric field in the bottom electrode, since LSMO has about three orders of magnitude higher resistivity than platinum. At room temperature the resistivities are $\rho_{\text{LSMO}} \approx 3 \text{ m}\Omega \text{ cm}$ [112] and $\rho_{\text{Pt}} = 10.5 \mu\Omega \text{ cm}$ [83], respectively. The separate V- circular contact was made to probe the potential in the bottom electrode LSMO layer separate from the current driving I- contact. At the positive probe side, it was chosen not to separate the V+ and I+ leads due to limited space on the top electrodes, so these two pads are directly connected through the gold wiring. Strictly speaking therefore, the four-wire layout is not a true four-point geometry, since the V+ and I+ pads are not completely separate. Yet, this geometry is similar to the one used by a number of other groups [12, 24, 27, 28, 72, 73], also known as the cross-strip geometry, shown earlier in figures 2.8 and 2.9. The main difference is that the bottom electrode is here a large uniform disc instead of a single strip under the device.

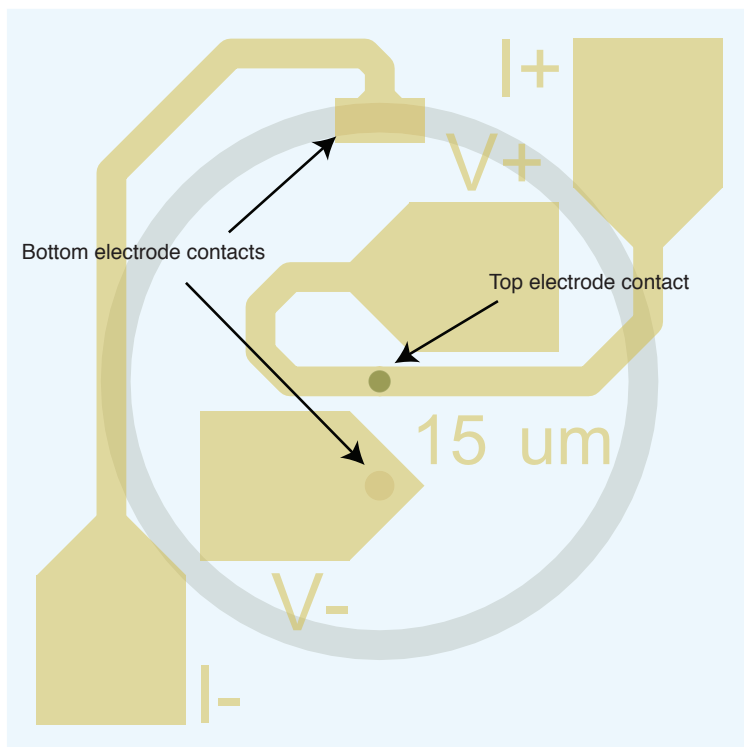


Figure 5.3: Top-down overview of the final $15\ \mu\text{m}$ MFTJ. All dimensions are to scale; the total area of each MFTJ including wiring and pads (blue square) is $500\ \mu\text{m} \times 500\ \mu\text{m}$, and the contact pads are $100\ \mu\text{m} \times 100\ \mu\text{m}$ along the square sides. The wiring paths are $20\ \mu\text{m}$ wide.

In Figure 5.4 a 3D model of a complete $15\ \mu\text{m}$ MFTJ is shown with the missing slice revealing the cross section structure. The cross section shows the same information as was seen in Figure 5.2, while the top surface replicates what was seen in Figure 5.3. The dimensions along the upwards direction are strongly deviating from real values for illustrative purposes. On the final fabricated samples, many of these structures were patterned next to each other in a grid covering an area of $3\ \text{mm} \times 3\ \text{mm}$.

5.3 Circuit Analysis

With the physical layout in mind, the circuit analysis can be presented and the choices of specific parameters justified. First, the isolated MFTJ is analyzed in terms of its resistive and capacitive nature from a circuit element point of view.

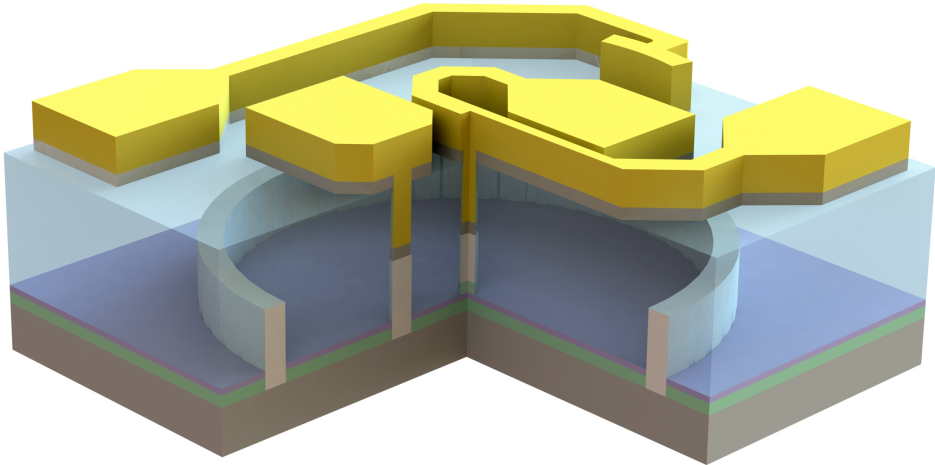


Figure 5.4: 3D model with a cross sectional cut of the final MFTJs. Here the $15\ \mu\text{m}$ junction is shown with the permalloy top electrode. The dimensions in the height direction are greatly exaggerated for illustrative purposes. Hence, the scales and aspect ratios are far from realistic.

Second, the complete circuit is analyzed with wiring, contact pads and external source.

5.3.1 The Tunnel Junction as a Circuit Element

In essence, tunnel junctions are capacitors where the insulating dielectric has been reduced to a thickness where a substantial leakage current can flow, mediated by direct tunneling or other tunneling phenomena as was introduced in Chapter 3. The geometry of interest here is the standard parallel plate capacitor, where the electrodes of the MFTJs are the parallel capacitor plates separated by the thin, leaking ferroelectric insulator. From a macroscopic circuit analysis point of view, this can be evaluated as a parallel RC-circuit, as is shown in Figure 5.5. Note that single electron tunneling is not of interest here, only macroscopic currents where classical laws apply are considered. Also shown on the right side is the equivalent circuit symbol often used to represent tunnel junctions [52]. The tunnel junction resistance and capacitance are denoted R_t and C_t , respectively. Both these properties are highly dependent on the applied electric field, however, the following analysis will assume that they are normal constants. The validity of the analysis and its limitations will be discussed below.

Ordinary circuit analysis [113] gives an equivalent junction impedance, the

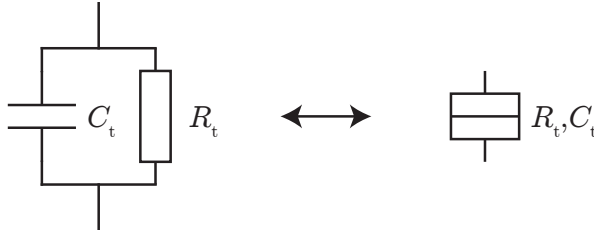


Figure 5.5: Parallel RC-circuit representing a tunnel junction (left), and the equivalent circuit symbol (right).

parallel impedance of the capacitor and resistor, as

$$Z_t(i\omega) = \frac{1}{\frac{1}{R_t} + i\omega C_t} = \frac{R_t}{1 + i\omega R_t C_t} = \frac{R_t}{1 + i\omega \tau_t}, \quad (5.1)$$

where $\tau_t = R_t C_t$ is the tunnel junction time constant. The junction impedance is further developed into real and imaginary parts

$$\begin{aligned} Z_t(i\omega) &= \frac{R_t(1 - i\omega R_t C_t)}{(1 + i\omega R_t C_t)(1 - i\omega R_t C_t)} = \frac{R_t}{1 + (\omega R_t C_t)^2} - i \frac{\omega R_t^2 C_t}{1 + (\omega R_t C_t)^2} \\ \Rightarrow \Re\{Z_t\} &= \frac{R_t}{1 + (\omega R_t C_t)^2}, \quad \Im\{Z_t\} = \frac{-\omega R_t^2 C_t}{1 + (\omega R_t C_t)^2}. \end{aligned} \quad (5.2)$$

Following from equation 5.1, the amplitude response is

$$|Z_t(i\omega)| = \sqrt{Z_t Z_t^*} = \frac{R_t}{\sqrt{1 + (\omega \tau_t)^2}} = \frac{R_t}{\sqrt{1 + \left(\frac{\omega}{\omega_c}\right)^2}}, \quad (5.3)$$

where $\omega_c = 2\pi f_c = 1/R_t C_t$ represents the junction's cutoff frequency. Correspondingly the phase response follows from equation 5.2 as

$$\begin{aligned} \theta(i\omega) &= \angle Z_t(0) + \angle Z_t(i\omega) = \arctan\left(\frac{0}{R_t}\right) - \arctan\left(\frac{\omega R_t^2 C_t}{R_t}\right) \\ \theta(i\omega) &= -\arctan(\omega R_t C_t) = -\arctan(\omega/\omega_c). \end{aligned} \quad (5.4)$$

Hence, by considering either the circuit in Figure 5.5, equation 5.2, or equations 5.3 and 5.4, the tunnel junction will be purely resistive for DC excitations, or whenever $\omega \ll 1/R_t C_t$. For AC excitations where $\omega \geq 1/R_t C_t$, the junction will behave more and more like a pure capacitor for increasing frequency, and the resistance will ultimately go to zero. The range of frequencies in between will give a device impedance that resembles a load with considerable capacitive signature. It is important to stress that this description is only valid for macroscopic currents

where electrons can be said to tunnel continuously. Moreover, for AC excitations, the signal amplitude must be so small that the voltage bias never exceeds the linear low-bias regime where the resistance starts to depend nonlinearly on the electric field. If the electric field dependence is taken into account, both the resistance and capacitance will rather be $R_t(\mathcal{E})$ and $C_t(\mathcal{E})$, more complicated functions of the electric field strength, \mathcal{E} . Consequently, the impedance and its amplitude and phase responses will depend on both frequency and the amplitudes of DC and AC components of the junction voltage.

In other words, one must be very careful when analyzing electrical measurements of MFTJs, especially AC measurements. It seems clear that DC measurements is a simple way to characterize the junction resistance and its electric field dependence. This can be done with a current source where the current is slowly ramped, either continuously or in discrete steps, and the junction voltage recorded correspondingly. With an AC measurement on the other hand, one could characterize both resistance and capacitance since the measured signal will hold information on both the real and imaginary parts of the impedance. In this case, special care must be taken with regard to the AC signal amplitude of the above mentioned reasons. An AC measurement is typically done by utilizing a lock-in amplifier, of which a much better signal to noise ratio is a major advantage over DC measurements [108]. The VersaLab ETO module uses this technique, and it will be revisited in more detail in Chapter 7. In the following circuit diagrams, a current source will be used, since the 4-wire mode of the ETO only offer control of the applied current, while the voltage response is read back.

To end this section, an interesting observation should be mentioned. Consider the tunnel junction as a disc-shaped structure, where the disc thickness is the junction thickness, or more precisely the tunnel barrier thickness, d_{BTO} . The junction area is thus the area of one of the disc's sides, A_t . The junction resistance is given by the disc dimensions and the volume resistivity of the separating layer, i.e

$$R_t = \frac{\rho_{\text{BTO}} d_{\text{BTO}}}{A_t} ,$$

since the junction area is the current path's cross section, and the thickness is the length of the current path related to this particular resistance. It scales inversely with the junction area and proportionally with the thickness. Conversely, the junction capacitance scales with the same quantities in the opposite way, as

$$C_t = \frac{\varepsilon_0 \varepsilon_{\text{BTO}} A_t}{d_{\text{BTO}}} .$$

Here ε_0 and ε_{BTO} are the vacuum permittivity and relative permittivity of BTO, respectively. As a result, the junction time constant becomes

$$\tau_{\text{junction}} = R_t C_t = \rho_{\text{BTO}} \cdot \varepsilon_0 \varepsilon_{\text{BTO}} , \quad (5.5)$$

for a given bias level. Naturally, the same limitations with regard to electric field dependence as discussed above also apply here. Thus, in principle the junction

time constant should be independent of junction area for the same junction thickness. This means that the range of selected junction areas can be expected to behave more or less similarly as a load in the measurement circuit. There are of course other things influencing this simple picture. For example, grain boundaries [87], atomic surface steps [63], or local voids/holes in the film working as low resistance current paths, can have a strong impact. Nevertheless, it should be kept in mind when analyzing measurement data.

5.3.2 The Complete Circuit

Based on the physical design presented earlier, Figure 5.6 shows the complete circuit diagram for an alternating current excitation (AC). Here, the bottom electrode LSMO-layer and gold wiring resistances have been neglected and are shown as ideal conductors (wires). Going clockwise from the current source, $i(t)$,

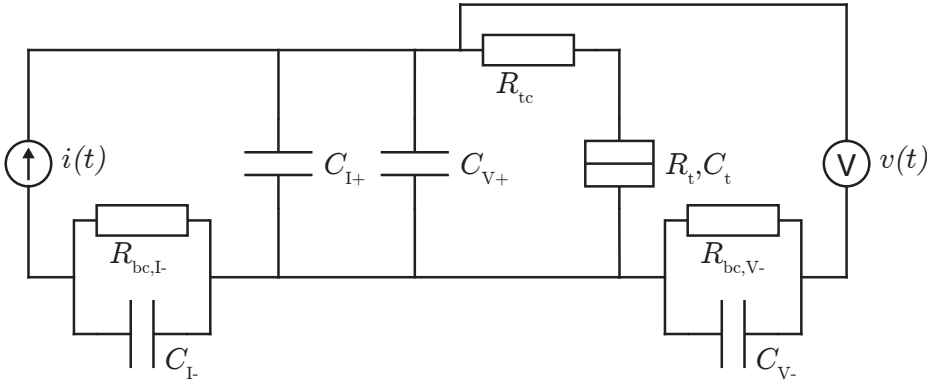


Figure 5.6: Circuit diagram for the MFTJs with alternating current excitation. $i(t)$ is some time-varying current with or without a DC component and $v(t)$ is the measured voltage.

the source is connected to the I+ pad, which will have a capacitance, C_{I+} , to the LSMO ground layer. The parallel V+ pad is correspondingly represented with its capacitance, C_{V+} . Voltage readout is modeled as a voltmeter, $v(t)$, connected to the gold wiring before the Au/Ti/Pt/NiFe or Au/Ti/Pt/LSMO top contact resistance, R_{tc} . The actual tunnel junction is modeled with its tunnel resistance and capacitance, R_t, C_t . At the interfaces between the negative pads I-/V- and the LSMO, parallel RC-circuits are inserted to account for the possibility that the Pt/LSMO contact resistance may be large. Since the I- and V- pads have different interface dimensions to the LSMO layer (fig. 5.3), these bottom contact resistances are differentiated as $R_{bc,I-}$ and $R_{bc,V-}$, respectively. Due to the uniform LSMO ground plane, both I- and V- pads will have capacitive couplings to this plane if the contact resistances are large. It has not been included here,

but if these contacts are rectifying or in some way non-ohmic, the issues with rectifying contacts introduced before will be detrimental.

Figure 5.7 presents the direct current excitation (DC) equivalent circuit. In this case the circuit reduces to a very simple system, where all capacitances no longer have an impact. They will charge to their equilibrium states during an initial phase after the driving current, I_{DC} , has made a change, and then remain unnoticed. Hence, this diagram is suitable for DC measurements, or AC measurements with a sufficiently low frequency. It will also be a good approximation to

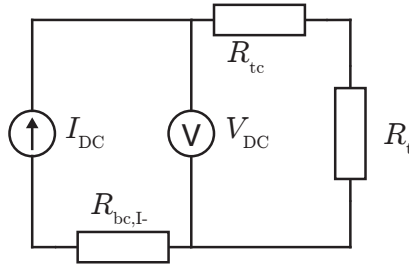


Figure 5.7: Circuit diagram for the MFTJs with direct current excitation. I_{DC} is an applied DC current and V_{DC} is the measured DC voltage.

the case where a relatively large DC component is present in an AC measurement with small amplitude. The differential resistance, dVdI-measurement, mode of the VersaLab ETO module will be such a case whenever the AC amplitude is much less than the DC offset. The voltage, V_{DC} , now reports the potential difference between its probes without the lead and contact resistances. However, since the V+ pad is directly connected to the I+ pad, the top contact resistance, R_{tc} , is still included in the potential drop reported. As noted above, this is probably much less than the tunnel resistance and can likely be ignored. The contact resistance at the negative current lead will still be present, but it will not be included in the voltage readout as the negative voltage lead is independent.

Table 5.1 lists the selected MFTJ diameters with the corresponding junction areas and capacitances for 3 nm and 5 nm thick ferroelectric layers. In addition, the total capacitance of the I+ and V+ pads, or equally I- and V- in the case of large bottom contact resistances, are included for comparison. The values are based on calculations described below.

To demonstrate the calculations, the last row of Table 5.1 is used, i.e the 15 μm electrode. The junction area, corresponding to the current path cross section, is

$$A_{15\mu\text{m}} = \pi r_{15\mu\text{m}}^2 = \pi \left(\frac{15\mu\text{m}}{2} \right)^2 \approx 177\mu\text{m}^2 = 177 \cdot 10^{-12}\text{m}^2.$$

The relative permittivity of BTO in our thin films is unknown, however, Nakagawara et al. [114] made measurements on multilayers of alternating BTO/STO

Table 5.1: Diameter, area and capacitance of the MFTJs with 3 nm and 5 nm ferroelectric barriers. The capacitance of the top electrode contact pads $C_{I+,V+}$ calculated with $d_{\text{SiO}_2} = 200$ nm, is included for reference. Relative permittivities used are $\varepsilon_{\text{SiO}_2} = 3.9$ and $\varepsilon_{\text{BTO}} = 300$. For reference, the wiring capacitance in the ETO module is reported to be approximately $C_{\text{ETO}} = 375$ pF.

Diam. [μm]	Area [μm^2]	$C_{3\text{nm}}$ [pF]	$C_{5\text{nm}}$ [pF]	$C_{I+,V+}$ [pF]
1	0.79	0.70	0.42	4.32
3	7.07	6.26	3.76	4.32
5	19.63	17.39	10.43	4.32
10	78.54	69.54	41.72	4.32
15	176.71	156.47	93.88	4.32

on Nb:STO(111) with a varying thickness periodicity from 0.45/0.45 nm to 10/10 nm. They found an almost linear increase from the thickest to the thinnest periodicity with $\varepsilon_{10/10} = 334$ to $\varepsilon_{0.45/0.45} = 594$, respectively [114]. Bulk values are typically larger than 1000 for the tetragonal phase [90], reportedly 3000 along the *a*-axis and 800 along the *c*-axis in the tetragonal phase [89]. To make some qualitative calculations here, however, the parameter is set to $\varepsilon_{\text{BTO}} = 300$ even though it may be smaller or larger. The capacitance of the 3 nm thick junction is then

$$C_{15\mu\text{m}} = \frac{\varepsilon_0 \varepsilon_{\text{BTO}} A_{15\mu\text{m}}}{d_{\text{BTO}}} = \frac{8.85 \cdot 10^{-12} \cdot 300 \cdot 177 \cdot 10^{-12}}{3 \cdot 10^{-9}} \text{F} \approx 156 \text{ pF} .$$

Correspondingly, the contact pad capacitance is found by using $\varepsilon_{\text{SiO}_2} = 3.9$ [104]. A minimum thickness constraint was set to 200 nm to ensure a sufficiently thick insulating layer. In practice, the SiO_2 thickness was aimed at 250 nm to 300 nm. The minimum practical contact pad area was believed to be $100 \mu\text{m} \times 100 \mu\text{m}$, as will be shown in Chapter 6. The wiring contributes to a slightly larger capacitance, but is neglected here for simplicity. Hence, the contact pad capacitance

$$\begin{aligned} C_{I+,V+} &= C_{I+} + C_{V+} = \frac{\varepsilon_0 \varepsilon_{\text{SiO}_2} 2.5 A_{I+}}{d_{\text{SiO}_2}} \\ &= \frac{8.85 \cdot 10^{-12} \cdot 3.9 \cdot 2.5 \cdot 10000 \cdot 10^{-12}}{200 \cdot 10^{-9}} \text{F} \approx 4.3 \text{ pF} . \end{aligned}$$

The factor 2.5 counts that there are 1.25 units of $100 \mu\text{m} \times 100 \mu\text{m}$ (square plus one fourth, see fig. 5.3) per pad and two pads in parallel.

Looking at Table 5.1 again, some trends are clear. For the large MFTJs, their capacitance is dominating the contact pad capacitance as wanted. For the small MFTJs the opposite is still the case. In comparison, the wiring capacitance in the ETO module is reported³ to be approximately $C_{\text{ETO}} = 375$ pF, which

³The ETO manual does not say anything regarding this. It has been stated in several presentations during 2014-2015, made available for customers by Quantum Design.

unfortunately is far larger than wanted. Hence, the major capacitive contribution in fact comes from the wiring and circuitry between the sample and the ETO sourcemeter.

To get a feeling for the circuit time constant from the 15 μm tunnel junction including the ETO capacitance and the I+ and V+ pads, a test resistance of 1 M Ω can be used. By neglecting all contact resistances and placing the ETO capacitance in parallel with the contact pads' capacitance, this gives

$$\tau_{\text{circuit}} \approx R_t(C_{\text{ETO}} + C_{\text{I+,V+}} + C_t) \approx 1 \text{ M}\Omega \cdot 535 \text{ pF} = 0.535 \text{ ms} . \quad (5.6)$$

The circuit's cutoff frequency is thus

$$f_{\text{c,circuit}} = \frac{1}{2\pi\tau_{\text{circuit}}} \approx \frac{1}{2\pi \cdot 0.535 \text{ ms}} \approx 300 \text{ Hz} . \quad (5.7)$$

This means that if the junction resistance is instead 10 k Ω or 100 M Ω , the cutoff frequency will rather be 30 kHz or 3 Hz, respectively. Clearly, for AC measurements this difference may be drastic. Moreover, it illustrates the detrimental influence of circuit capacitance when the junction resistance gets large.

Finally, by considering equations 5.5 and 5.6 together, the issue with circuit capacitance is even more clear. It seems possible that varying the junction size will not change the load impedance seen by the measurement circuit. However, the contact pads and ETO wiring represent a constant capacitance for all device sizes. The first two terms in equation 5.6 thus grow with decreasing junction size, even though the last term may remain constant. Consequently, the circuit time constant will grow when the devices shrink, leaving the total circuit impedance more and more capacitive. This will be a serious problem for AC measurements if the device resistances come out too large.

Chapter 6

Sample Fabrication

To meet the requirements for improved reproducibility and performance of the devices, a better fabrication process for the MFTJs was found necessary. A more advanced fabrication scheme has been developed based on the design presented in the preceding chapter, which consists of four main stages. Each stage is associated with a new lithography layer and corresponding process steps. The detailed steps required to finish each stage will be explained later. The main stages for fabrication of P-MFTJs are as follows:

1. Top electrode deposition (fig. 6.5).
2. Bottom electrode etch and deposition (fig. 6.11)
3. Insulation layer deposition (fig. 6.12).
4. Electrical contact pad deposition (fig. 6.14).

In addition, for the O-MFTJs, an intermediate stage 1-1, between 1 and 2, is needed to define free-standing LSMO/BTO top electrodes (fig. 6.8).

Two fabrication approaches were initially proposed, where the main difference lies in stages 2 and 3 for how to define the bottom electrodes and deposit the insulation layer. The approach that was not implemented suggests Plasma Enhanced Chemical Vapor Deposition (PECVD) for SiO_2 deposition, and subsequent dry-etching of the top and bottom electrode openings with Inductively Coupled Plasma Reactive Ion Etching (ICP-RIE). The second approach, which was selected as the preferred method here, uses radio-frequency sputter deposition and lift-off of SiO_2 . Initially, both approaches required three (four) stages, however, over the course of developing the process it has become clear that the selected approach requires four (five) stages, as listed above, to work properly. The alternative fabrication process is described briefly below for reference, and the specific choice of fabrication approach, pros and cons, will be discussed in Chapter 8.

In this chapter, following first is a presentation of the lithography part of each fabrication stage. The second section introduces the fabrication process in

detail. Process specific parameters for etching and deposition are presented first, before an introduction to each fabrication stage is given. For each fabrication stage representative results are given and discussed along the way. The third section deals with wire-bonding, where the development of proper bond pads and testing to achieve reproducible bonding are given much attention. Finally, the entire fabrication process is summarized with the most important information for each step of the process. Fabrication specifications for the final samples are also included here. In all sections, selected results after optimizing each process step are included, and themes are discussed within their respective scopes.

6.1 Electron Beam Lithography

In all stages of the fabrication a lithography step is needed, and in this work electron beam lithography (EBL) has been used. In the following, a presentation of the complete EBL process is given.

The resist used here is the acrylic polymer *Poly(methyl methacrylate)*, or PMMA, chemical formula $(C_5O_2H_8)_n$. More specifically it is referred to as 950PMMA A9, a solution of 9% PMMA resin with molecular weight 950 000 amu in the relatively safe Anisole solvent ($CH_3OC_6H_5$). This solution has a viscosity suitable for resist thicknesses of a few microns. PMMA is commonly used as a high resolution positive resist for direct write e-beam processes, or x-ray and deep UV photolithographic processes [115]. PMMA is easy to work with and is not suspected to affect the functional oxides. It can be stripped by acetone, while exposure de-links the polymer chains so that the much lighter chains can be developed by a mixture of isopropanol and water. Below, the EBL process is summarized in ten steps plus a resist removal step. In all steps involving either baking or plasma cleaning, the samples were placed on a 2-inch Si wafer to ease the handling and prevent resist residues from contaminating the bake plates.

1. **Cleaning:** Ultrasonic acetone bath for 5 minutes, followed by immersion in isopropyl alcohol (IPA), and subsequent drying with N_2 gas flow.
2. **Dehydration-bake:** $180^\circ C$ for 2 minutes, evaporate remaining solvents and moisture.
3. **Ashing:** O_2 plasma ashing for surface preparation and removal of remaining organic contaminants. This step was done in the Diener plasma cleaner with 80% O_2 flow and 80% generator power for 3 minutes.
4. **Spin-coat:** Resist was dispensed manually by a pipette, followed by spin-up after 10 seconds. Spinner recipe: fast acceleration of 3000 rpm/s to final speed 3000 rpm. 2 minutes total spin time. Resist thickness about $1.5 \mu m$.
5. **Soft-bake:** 3 minutes at $180^\circ C$ to evaporate most solvents in the resist.
6. **Exposure:** Direct write exposure with e-beam acceleration voltage 100 kV and high dose. $1000 \mu C cm^{-2}$ as base dose.
7. **Develop:** Immersion in a solution of de-ionized water (DI) and IPA with DI:IPA ratio 1:9. In practice, 10 ml DI water to 90 ml IPA was used with

- sample immersion for 10 to 20 seconds. The development was terminated by immersion in pure DI water for 30 seconds, before blow-dry with N₂ gas.
8. **Post-bake:** 100°C for 3 minutes. A post development bake was used to evaporate remaining moisture and solvents. To protect the developed PMMA from deformation, the temperature was lower than for soft-bake.
 9. **Inspection:** Inspection with an optical microscope to verify the exposure and development before further processing.
 10. **Descumming:** A brief O₂ plasma ashing step to remove small particles and resist residues in corners or along edges. The Diener plasma cleaner was used with 80% O₂ flow and 80% generator power for 1 minute.¹
 11. **Resist strip:** To remove the developed resist, an ultrasonic bath with acetone was used for 5 to 10 minutes. This step applies whether the resist is used for lift-off, etch mask or just need to be removed due to failure in the preceding steps.

The following paragraphs describes the optimization of the most important EBL steps in more detail.

6.1.1 Spin-coating

Initially it was aimed for resist thicknesses of about 2 μm after spin-coat and soft-bake. This was achieved on Si test samples at 1500 rpm for 90 seconds. However, due to the relatively high viscosity of 950PMMA A9, it was not possible for the smaller STO samples where edge beads became dominant. Hence, to get a useful area with uniform resist thickness, a higher spinner speed was necessary.

Tests were done with varying resist droplet size and varying spinner recipes. For large droplets, low spin speeds did not manage to throw away enough resist, while for small droplets the film did not become uniform or did not cover the whole sample. Hence, intermediate size droplets seemed preferential overall. Spinner recipes with various resist distribution and throw-off steps before the main uniform spin step, was also tested. These methods did not seem to be easily reproduced and gave varying uniformity and thickness from run to run. Thus, a simple recipe with quick acceleration of 3000 rpm/s to final speed 3000 rpm, was found to give the best results. To stabilize the edge beads, the spin was held for 2 minutes, more than double of what the PMMA datasheet suggests. On STO samples measuring approximately 5 mm × 5 mm, the edge beads extended about 1 mm from each edge and a little more in each corner. Hence, the uniform area measured about 3 mm × 3 mm, and the thickness was very reproducible at about 1.5 μm as read by a reflectometer.

For simplicity, this spinner recipe was used for all fabrication stages except the final contact pad deposition (stage 4). For stage 4, the same spin-coat and

¹One should be careful when descumming PMMA with an oxygen plasma, as PMMA etches fast. The PMMA thickness here was typically 1.5 μm, so a minute of descumming was ok.

soft-bake routine was repeated twice for each sample, giving a total of about 3 μm resist thickness with the same or slightly larger uniform area.

6.1.2 Exposure dose and development time

With the spin-coat recipe established, tests were done to find a good base dose, developer solution and development time. The initial tests used a base dose of $1000 \mu\text{C cm}^{-2}$, as recommended by an experienced engineer at NTNU NanoLab.² A few initial tests were done with the developer MIBK:IPA 1:3 as specified by the PMMA datasheet, however, these results were poor and a developer of DI water blended in IPA with ratio 1:9 was used instead. It has been known for a while that DI:IPA developers may perform superior to the MIBK:IPA developers in terms of both sensitivity and contrast [116]. The specific choice of DI:IPA ratio 1:9 was based upon earlier experience by engineers and researchers at NTNU NanoLab, and a developer time of 10 to 30 seconds was anticipated to work well.

A dose test with doses ranging from $600 \mu\text{C cm}^{-2}$ to $1800 \mu\text{C cm}^{-2}$ with intervals of $400 \mu\text{C cm}^{-2}$ was exposed on a SiO_2/Si test sample. This was developed in DI:IPA 1:9 for 10 seconds followed by immersion in pure DI water for 30 seconds to terminate development. N_2 gas flow was used for drying. The result can be seen in Figure 6.1, which clearly show that $1000 \mu\text{C cm}^{-2}$ is enough to get a good development. From optical images it was not possible to distinguish any dose-dependent dimension difference between the fully developed structures. Interestingly though, the proximity effect from exposing large areas with a uniform dose is very clear from these optical images. Higher dose gives more and more distinct color gradients in the reflections from nearby un-exposed resist, while for the lowest dose this is hardly visible at all. It is not known if the color gradient is due to partial development which gives uneven resist thickness, or if it is purely due to gradients in the level of de-linked resist material. The dose test sample was developed for another 10 seconds to see if the $600 \mu\text{C cm}^{-2}$ would develop fully. There were no noticeable difference apart from a slightly different periodicity in the reflected colors from the $600 \mu\text{C cm}^{-2}$ dose mark, indicating a further development, yet still without completion. BTO/LSMO/STO samples were prepared and developed along with the dose test sample, and they showed full development at the same dose and developer time. Hence, $1000 \mu\text{C cm}^{-2}$ was indeed set as the base dose for the rest of the work, while 10 seconds was set as the reference for development time. The true base dose is likely lower, but for the purpose of this work with critical dimension as large as $1 \mu\text{m}$, it was not necessary or worth the time consumption to optimize this part any further.

The sidewall profile of developed PMMA was investigated with SEM on a cross section sample. This was done in the initial phase where the resist thickness was $2 \mu\text{m}$, and the result can be seen in Figure 6.2. A test pattern with various

²The author has later seen base dose recommendations ranging from $500 \mu\text{C cm}^{-2}$ to $800 \mu\text{C cm}^{-2}$ for PMMA exposed by 100 kV EBL systems.

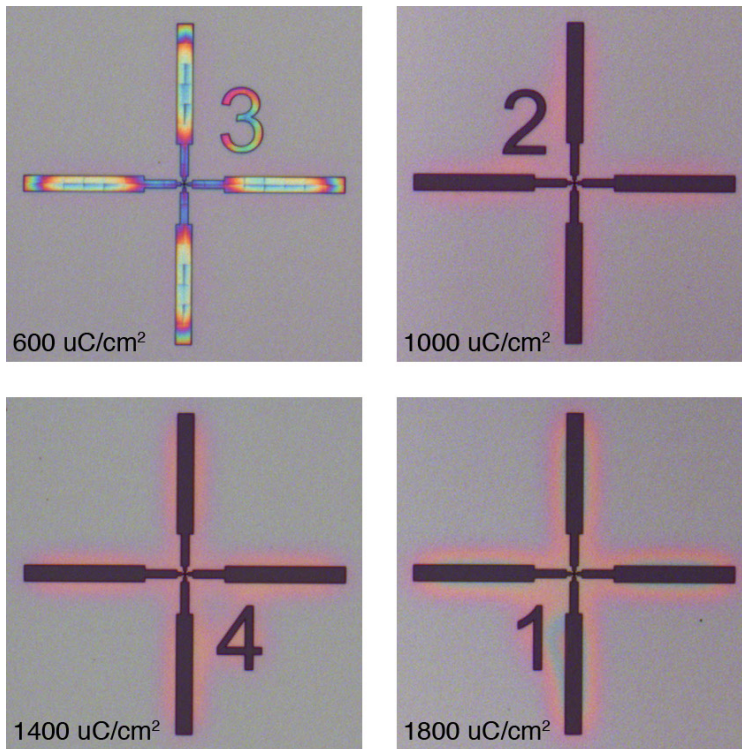


Figure 6.1: PMMA exposure dose test on SiO_2/Si . Note the clearly visible proximity effect around the marks. These marks are $400\ \mu\text{m}$ from end to end and $20\ \mu\text{m}$ wide at the outermost arms.

structures and dimensions was used (bottom), and full development was seen down to $1\ \mu\text{m}$ linewidths (up right). The test sample was a silicon wafer covered with $92\ \text{nm}\ \text{SiO}_2$, which can be seen by looking carefully at the foot of the resist in the upper two images. The dose was $1000\ \mu\text{C}\ \text{cm}^{-2}$, and no PEC was applied. The development time was 90 seconds in DI:IPA developer, which indicates that this dose was too low for $2\ \mu\text{m}$ resist thickness. Nearly vertical sidewalls are clearly apparent (up left and right), which is typically found for $100\ \text{kV}$ EBL systems. There is a very slight indication for an undercut, but not considerable. However, a considerable broadening of the linewidth is clear, with $190\ \text{nm}$ to $350\ \text{nm}$ for the $1\ \mu\text{m}$ lines. This was similar for the larger structures and is considered a limit related to the particular beam current ($10\ \text{nA}$), resist thickness, and acceleration voltage used for this test. No further optimization of linewidths was done, except PEC which is described below, as this error was not seen as particularly relevant for the purpose of this work.

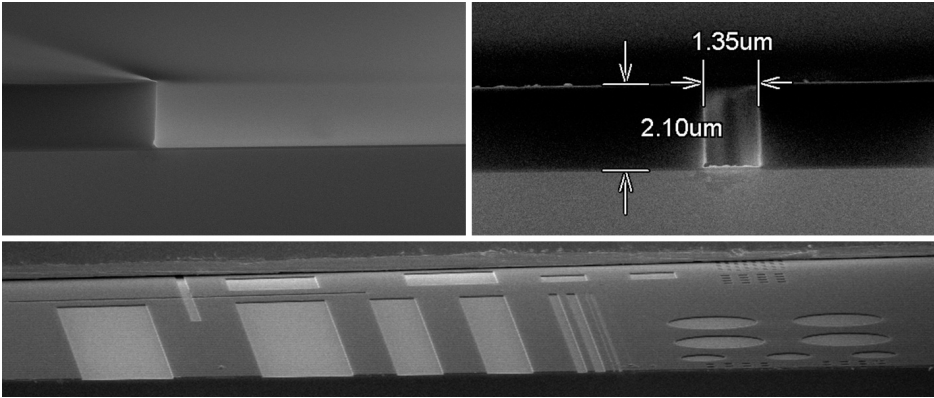


Figure 6.2: PMMA test pattern and sidewall profile after exposure with $1000 \mu\text{C cm}^{-2}$ at 100 kV and 10 nA beam current. The test pattern (bottom) included structures and dimensions suitable for optimizing exposure and development to the current process. The broadest linewidth was $100 \mu\text{m}$. Nearly vertical sidewalls are clearly seen (up left) and full development was found for structures of dimension down to $1 \mu\text{m}$, although with considerable broadening (up right).

6.1.3 Proximity effects

As is evident from Figure 6.1, proximity effects are important to consider when doing EBL. This is especially true when different sized structures are patterned in the same exposure. The BEAMER software was utilized to help with proximity effect correction, as described previously in section 4.2.1.

Figure 6.3 shows an example of exposure being done with and without PEC. The resist thickness was $3 \mu\text{m}$ and base dose $1500 \mu\text{C cm}^{-2}$ to account for the double thickness. On the left side PEC was not used and the pattern was uniformly exposed. In the lower left corner the mask was overlapping so that the corner square was doubly exposed. The narrow inner corners of the arrowheads and letters were not fully developed due to less total exposure. Furthermore, the parts of the letter patterns which are closest to the large arrows, show a clear indication for the range of proximity effects. The letter ends close enough to the arrows are fully developed, while the ends slightly further away are not. Also note the minus signs which were small enough to require a higher dose to develop fully at all. By comparison, the right side shows a more complex pattern exposed with PEC after healing the mask from overlapping structures. The range of dose correction was from about 60% to about 180% of the base dose for bulk and edge/corner parts, respectively. Everything is fully developed and there is no sign of deformed structures. It should be noted that what appear as diffuse smoke or fog in the images are reflections from the sample's rough backside, which are out of focus. The right image was taken at lower magnification which gives a better depth of focus so it is more easily seen.

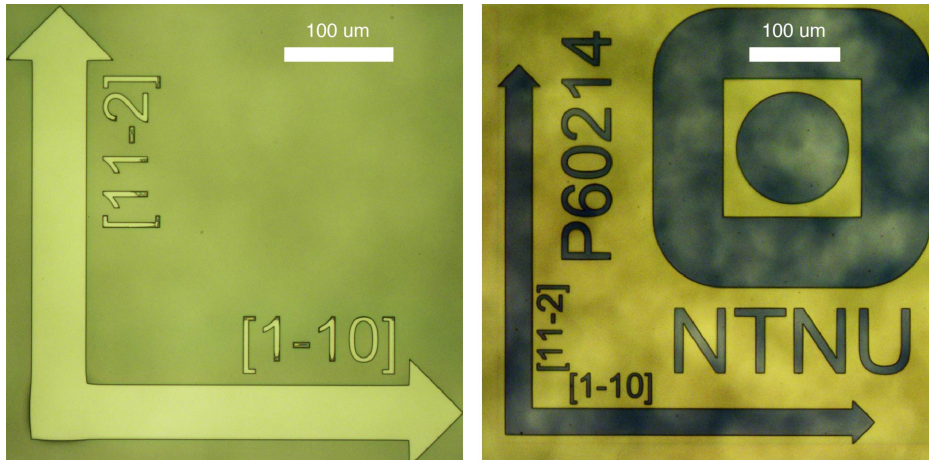


Figure 6.3: PMMA exposure proximity effects on BTO/LSMO/STO (left) and $\text{SiO}_2/\text{LSMO}/\text{BTO}/\text{LSMO}/\text{STO}$ (right). Both samples were exposed with base dose $1500 \mu\text{C cm}^{-2}$, due to a double layer of resist ($3 \mu\text{m}$), and developed for 15 seconds. **Left:** The pattern was exposed with uniform dose and no PEC. In the down left corner, the mask was overlapping so that the square in the corner was exposed twice. The narrow corners of the arrowheads and the smaller letters were not fully developed. **Right:** The pattern was exposed with PEC, giving a non-uniform dose depending on structure size, shape and distance to nearby structures. In addition, the mask was healed from overlapping structures before doing the PEC. All parts of the pattern was fully developed without any noticeable distortions.

6.1.4 Descumming

Descumming of resist residues or other organic contaminants after development is considered important for good lift-off or dry-etch processing. This step has not been optimized thoroughly here. However, a few tests were done with the Diener plasma cleaner to remove residues from developed patterns that were visible with an optical microscope at high magnification. After 1 minute of plasma cleaning with 80% O_2 flow and 80% generator power, the visible traces were almost entirely gone. Hence, this was set as a reference for clearing traces that are not visible by optical inspection. It was confirmed by profilometer scans that the un-exposed pattern did not suffer from this. No clear height difference was measurable, and the edges did not seem to round off. Consequently, when the patterns showed no visual traces of resist during optical inspection after development, the processing proceeded to descumming. The descumming step was done with equal parameters for all samples and all stages, regardless of what the further processing in the respective stage was.

6.2 The Fabrication Process

This part describes the entire fabrication process including selected optimization results acquired for each fabrication stage. Over the course of the work, there has been a back and forth connection between the experimental process flow presented here and the design presented in the preceding chapter. What is presented and discussed here is the final result of this incremental development. First the process parameters involved in several of the main fabrication stages are presented, before the details of the fabrication stages are described along with the selected optimization results.

6.2.1 Deposition Rates

Sputter deposition rates for SiO₂, NiFe Au and Pt were found in the AJA system. The system has a quartz crystal rate monitor installed, but this is not in use while sputtering samples. Thus, the rate must be known prior to deposition. Moreover, the rate monitor is not necessarily precise, so deposition tests were done both with the rate monitor and on a test wafer for SiO₂. All sputter deposition sessions were done with 3 mTorr argon pressure unless stated otherwise. The plasma were struck at 50 W in 30 mTorr pressure before reducing the pressure and ramping to the desired power level by 1 W s⁻¹. When reaching the target power level, all targets were pre-sputtered for about one minute before opening the shutter for deposition. Table 6.1 sums up the sputter deposition rates that have been found.

Table 6.1: Deposition rates and parameter details for sputtering of various materials in the AJA system at 3 mTorr argon pressure. The RF sputtering shows applied/reflected power in the power column, respectively. *Gold sputtering was done at 6 mTorr argon pressure due to a difficulty with sustaining the plasma at lower pressure. This turned out to be a broken target, and platinum was used instead.

Target	Type	Power [W]	Voltage [V]	Time [s]	Thickness [Å]	Rate [Å min ⁻¹]
SiO ₂	Monitor	RF 300/4	815	120	23	11.5
SiO ₂	Wafer	RF 300/4	815	3600	1070	17.8
Au*	Monitor	DC 50	375	60	59	59.0
Au*	Monitor	DC 100	375	60	123	123.0
NiFe	Monitor	DC 215	408	60	63	63.0
Pt	Monitor	DC 100	377	120	136	68.0

For SiO₂ deposition, a clean 2-inch silicon wafer was used to check the deposition rate more precisely. After depositing for one hour, the thickness was measured by a reflectometer as stated in Table 6.1, with uniformity within a few Ångströms.

6.2.2 Etch Rates

Sputter etching rates for SiO₂, BTO/LSMO/STO, PMMA and Ti were found in the AJA system. The system has a substrate RF sputtering feature, which is intended for native oxide removal and surface activation prior to deposition, or for increasing film density of a material while depositing. It is limited to a maximum power of 50 W and the acceleration voltage cannot be controlled manually. Nevertheless, it is useful for etching through the thin ferroelectric barrier here, in order to reach the underlying LSMO bottom electrode for electrical contacts, as well as top electrode definition in the O-MFTJs.

As a starting reference, the silicon test wafer with SiO₂ deposited on top was etched for 6 minutes at 50 W, which gave an acceleration voltage of 315 V after adjusting the impedance matching capacitors to 2 W reflected power. The resulting thickness change was uniformly measured to 6.1 nm, or an etch rate of approximately 10 Å min⁻¹. By using HTE Labs' tabulated sputter deposition rates for a normalized sputter power density [117], expected etch rates were found for most of the materials of interest. These are presented in Table 6.2 together with the expected etch rates in the AJA system.

Table 6.2: Expected etch rates by argon sputter etching. HTE etch rate represents the etch rates at a normalized power level 12.5 W/in² and bombardment energy 600 eV, as tabulated by HTE Labs [117]. The expected etch rates for etching in the AJA system are normalized with respect to the known etch rate for SiO₂.

Material	HTE etch rate [nm min ⁻¹]	Normalization factor	Expected etch rate AJA [Å min ⁻¹]
SiO ₂	21	1.00	10.0
BaTiO ₃	10	0.48	4.8
SrTiO ₃	10	0.48	4.8
Ti	24	1.14	11.4
NiFe	33	1.57	15.7
Au	96	4.57	45.7
Pt	61	2.90	29.0

Test samples were made for the development of the fabrication process. These are summarized with the relevant material data in Table 6.3. Four samples were scribed and cleaved from the silicon test wafer, one of which was additionally coated with titanium. To compare the etch rates of each material involved in the final etch process, the test samples were etched simultaneously for one hour in the AJA system. Sample stage rotation was on and the argon pressure was kept at 3 mTorr. The maximum power of 50 W was used, which gave an acceleration voltage of 330 V after adjusting the impedance matching capacitors to 0 W reflected power. Profilometer measurements were done before etching (h_0 , pre-etch), after etching (h_1 , post-etch), and after stripping the resist (h_2 , post-strip). This was

Table 6.3: Overview of test samples used for fabrication process development. S and E means deposition by sputtering or e-beam evaporation, respectively, while PLD means pulsed laser deposition.

Sample	Materials	Substrate	Thickness	Deposition
T1	Ti/SiO ₂	Si (001)	100 nm/92 nm	E/S
T2	SiO ₂	Si (001)	92 nm	S
T3	SiO ₂	Si (001)	92 nm	S
T4	SiO ₂	Si (001)	92 nm	S
T5	BTO/LSMO	STO (111)	5 nm/10 nm	PLD
P60206	BTO/LSMO	STO (111)	3 nm/10 nm	PLD
P60503	BTO/LSMO	STO (111)	10 nm/10 nm	PLD

done to measure the step height differences resulting from the etch process, as was illustrated earlier in Figure 4.6. The profile step-heights and resulting etch rates are summarized in Table 6.4. The PMMA etch rate was determined from the height difference formula, equation 4.6. This parameter is stated in Table 6.4 for the samples that were uniform enough to be considered.

Table 6.4: Measured etch rates by argon sputter etching in the AJA system. The samples were etched simultaneously at 50 W sputter power for 60 minutes. * The Ti etch rate was surprisingly low, and the height differences too close to the profilometer sensitivity, which lead to a difficulty in resolving a well defined number. However, 30 nm is in the upper range of step-heights from the data, which should be fine for the use of Ti as an etch stop. † Sample T5 etched through all materials BTO/LSMO/STO, which are expected to have essentially the same etch rate. Also, due to a very thick and nonuniform resist, h_0, h_1 could not be resolved. ‡ The PMMA etch rate is an upper average to get a worst-case parameter since it is used as etch mask.

Sample	Material	h_0 [μm]	h_1 [μm]	h_2 [nm]	Δh_{PMMA} [nm]	r_e [$\text{\AA} \text{min}^{-1}$]
T1	Ti	2.00	1.87	*30	160	*5.0
T2	SiO ₂	1.98	1.87	74	184	12.3
T3	SiO ₂	2.00	1.91	73	163	12.2
T5	†BTO	–	–	32	–	5.3
	PMMA				184	‡30.7

The measured etch rates shown in Table 6.4 corresponds well with the expected etch rates from Table 6.2, however, with one exception. Titanium shows a surprisingly low etch rate of less than half of what was expected. For the role of Ti here, this is a positive thing, since its purpose is to work as an etch stop for

protecting the underlying structures from being etched.³ Thus, a low etch rate is wanted, and it means the titanium layer can be made thinner than expected. It should be noted that the stated value for the etch depth and etch rate for titanium (tbl. 6.4) is a worst-case value based on the highest steps from the data. This was chosen in regard to the use of titanium as an etch stop, which requires a sufficiently thick layer to prevent etching through. One of the profile measurements for the titanium etch pattern can be found in the appendix, Figure B.1. For PMMA the higher estimate was also used to determine the etch rate, since it works as a soft masking layer in the etch process. The resist is initially very thick compared to the needed etch depth, so it is no problem that its etch rate is about six times larger than for BTO/LSMO/STO.

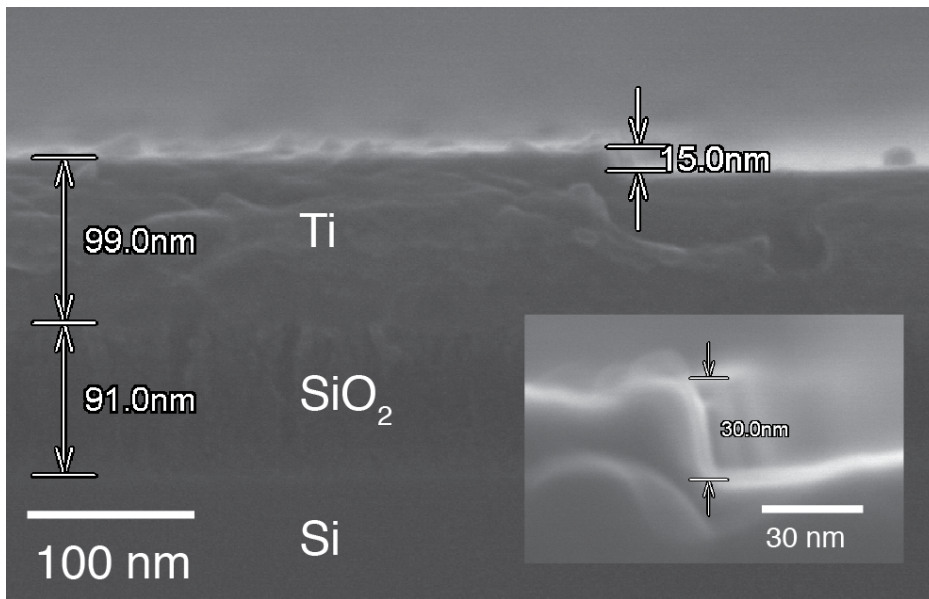


Figure 6.4: Cross sectional step edge etch profile for titanium as imaged by SEM. The sample is T1 as referred above in Table 6.3, with Ti/SiO₂ on Si. The inset shows another step edge profile on the same sample, and all measured steps were lying within these two limits.

To confirm the etch rate of titanium, a cross section of the etch test sample was investigated with SEM. Figure 6.4 shows an etch step after resist removal which measures 15 nm. Another step edge (inset) shows 30 nm height difference, but most edges were between 15 nm and 20 nm. However, for the above mentioned reasons, the largest difference was used for determining the needed etch mask

³Since the fabrication was rearranged and extended with an extra round of EBL, this method has not been used in the final fabrication. Nevertheless, it is necessary knowledge if the PECVD/ICP-RIE or equivalent etching method is wanted.

thickness. As is evident from the micrograph, the surface is quite rough and a shadow of a structure standing up can be vaguely seen out of focus behind. It is believed that the Ti atoms redeposit on the surface and mask sidewalls while etching, thus contributing to a lower etch rate at the expense of more roughness. This does not seem to be a problem for the particular process, as the sidewalls will be SiO₂ in the final processing and extra adhesion for the subsequent metalization will only be beneficial. Additionally, the micrograph reveals the thicknesses of the deposited SiO₂ and Ti layers, which correspond very well with the thicknesses measured by the reflectometer and e-beam evaporation thickness monitor, respectively.

6.2.3 Stage 1 – Top Electrode Deposition

Figure 6.5 shows the process flow for stage 1 of the fabrication process. Step a) shows a plain epitaxial⁴ sample ready for processing after cleaning, plasma-ashing and baking. The EBL process is shown through steps b) to d), where all details are found above (EBL process steps 1-10). Step e) shows the metal deposition performed with the AJA system. Both permalloy and platinum were sputtered, the deposition rates and power were 1.0 Å s⁻¹/215 W and 1.13 Å s⁻¹/100 W, respectively. The nominal aimed thicknesses were 10 nm permalloy and 40 nm platinum. In step f) the final sample with top electrodes is shown after a completed lift-off (EBL step 11). For O-MFTJs only platinum was deposited with the same rate and nominal thickness 50 nm.

A representative view of properly developed structures is shown in Figure 6.6. Up left is the main alignment mark placed in the lower left corner of the sample. The end of the uniform resist area is starting there, as the edge bead starts to become visible. Up right is the central part of the alignment mark where the 20 μm cross changes to 1 μm width and squares separated by 500 nm in the center. The lower half shows a compilation of the five different sized top electrodes and their measured dimensions in the optical microscope at 100x magnification. It is easily seen that dimensions smaller than about 5 μm are hard to inspect precisely with the optical microscope. Yet, by manipulating the focus carefully it was possible to see resist residues if present for all but the smallest electrode. Moreover, with PEC in the exposure the smallest structures usually developed slightly faster than the large bulk regions, so it was never a problem with underdevelopment of the structures that could not be inspected visually.

The resulting structures after completed lift-off in stage 1 are depicted in Figure 6.7 together with their height profiles. The top electrodes were scanned by AFM, and the profiles were extracted from the AFM-data. It is clear that structures smaller than 5 μm in diameter were not successful. The measured step height for the 1 μm electrode was about 4 nm, or only 8 % of the nominal thickness. The 3 μm electrode was better with a height about 44 nm, or 88 % of

⁴PhD candidate Torstein Bolstad, co-supervisor of this work, was responsible for the epitaxial growth as part of his doctoral studies.

Stage 1; top electrode deposition

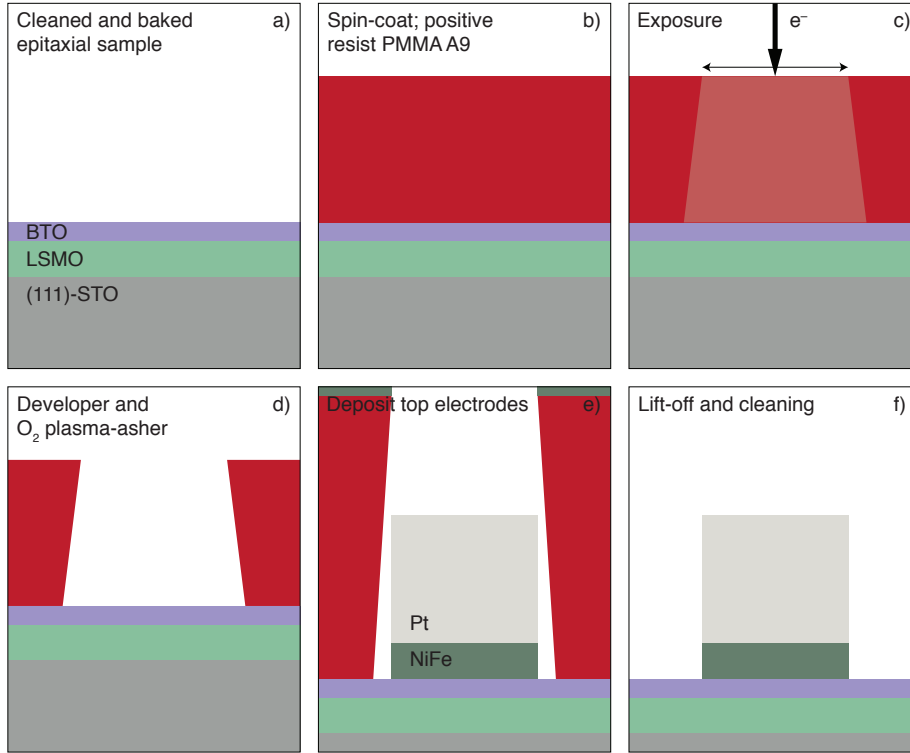


Figure 6.5: MFTJ fabrication stage 1 (not to scale). Steps a) to f) show the most important processing steps for top electrode deposition by EBL and sputtering.

the nominal thickness. For the larger top electrodes the nominal thickness was reached, but the trend with narrowing towards the top is present for them as well. The SEM micrographs show the same trend by the difference in reflected brightness and lower contrast for the small electrodes, due to less deposited metal. By considering the plots for the $5\ \mu\text{m}$ and $10\ \mu\text{m}$ electrodes, it is seen that the lateral extent of narrowing is more than $1.5\ \mu\text{m}$, possibly as much as $2\ \mu\text{m}$ if one counts the distance from totally horizontal on top to totally vertical on the sides. This can be explained by the off-axis sputter head placement in the AJA system. Since it is a combined sputter and evaporation system, the sputter heads are placed in a circle along the chamber walls pointing at an angle in and up towards the center where the substrate holder is located. Hence, some shadow effect must be expected when depositing on patterned samples, which is clearly visible here. The author is not aware of the exact off-axis angle, however, an estimation can be attempted based on the data. The resist thickness was $1.5\ \mu\text{m}$ for stages 1

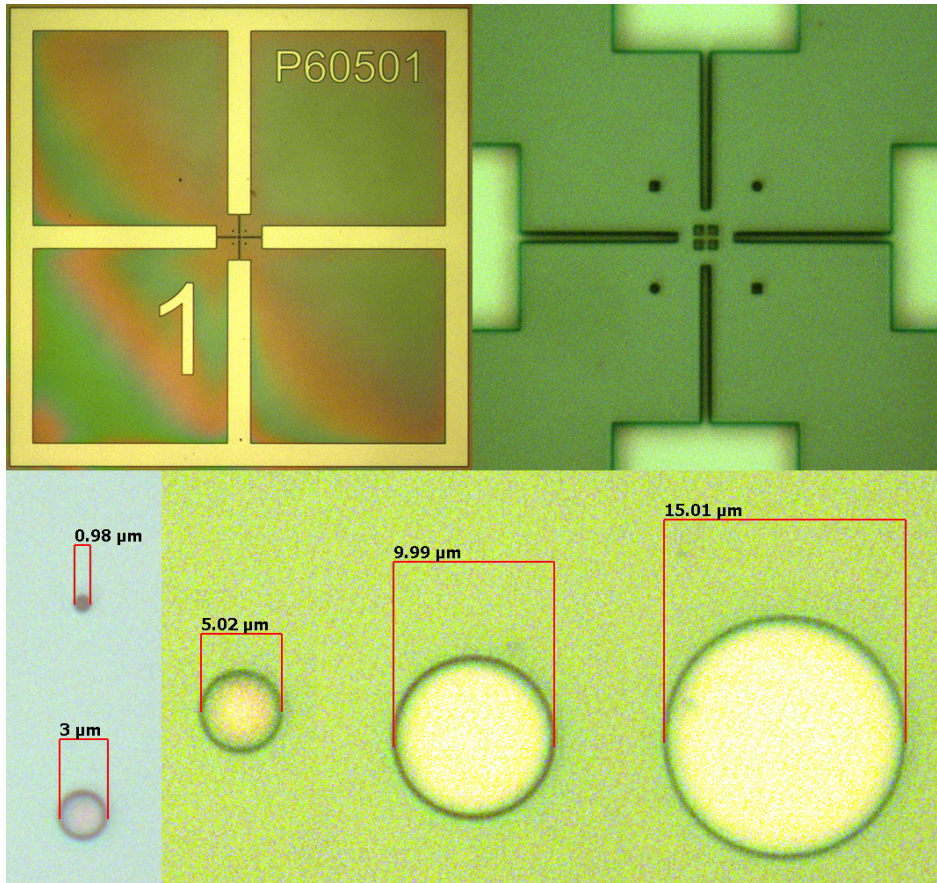


Figure 6.6: Developed structures from fabrication stage 1, here represented by sample P60501. The main alignment mark (up left), where the non-uniform edge bead is visible in the lower left corner. The central parts of the alignment mark (up right) with critical dimension $1\ \mu\text{m}$. The lower half shows a compilation of all top electrode sizes and their dimensions measured with an optical microscope.

to 3. Hence, the off-axis angle, i.e the incident angle relative to the substrate normal, should be in the range $\theta \in [45^\circ, 53^\circ]$ ($[\arctan(1.5/1.5), \arctan(2.0/1.5)]$), and probably closer to the higher value. This seems to be much, but it sounds reasonable based on how the chamber is designed. At any rate, the result is that structures with diameters less than about $2\ \mu\text{m}$ are totally hidden by shadow from the resist sidewall. Consequently, only a little material that is reflected down into the hole is deposited, as is clearly seen for the smallest structures. Thus, for the P-MFTJs it can be expected that devices smaller than $5\ \mu\text{m}$ will show non-existent or much lower TMR effect, due to a missing or much thinner

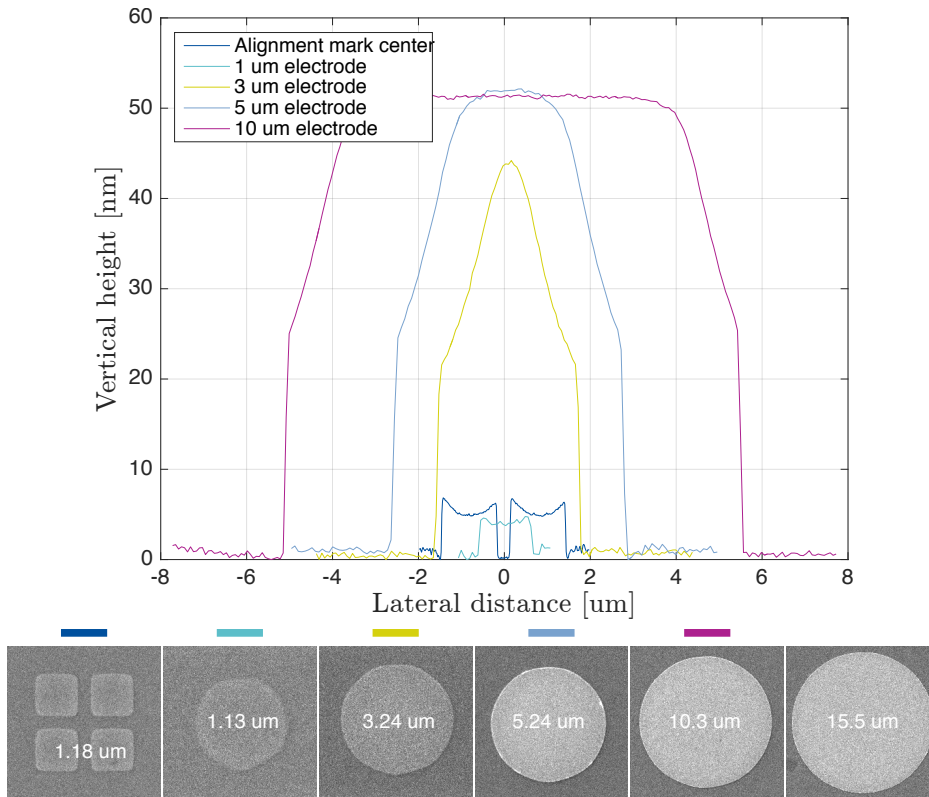


Figure 6.7: Top electrode profiles extracted from AFM scans (upper), and SEM images of the same electrodes (lower, not to scale), after fabrication stage 1. The SEM images are labeled with the corresponding colors for their respective profile plots. The diameter (width for alignment mark center) as measured with the SEM is stated in white letters. Nominal deposition thickness was 50 nm in total.

permalloy layer. The problem may exist for the larger structures too, but for them at least parts of the top electrode will have the nominal thickness. For the O-MFTJs none of the device sizes should in principle be limited by this issue, since only an ohmic contact is needed from the platinum layer.

6.2.4 Stage 1-1 – Top Electrode Etch (O-MFTJ only)

An extra process stage is necessary for the O-MFTJs in order to define top electrodes from the upper LSMO layer. The extra stage is done between the ordinary stages 1 and 2. A process flow diagram can be seen in Figure 6.8. Steps a) to d) show the EBL process, however, a "negative" mask needs to be written in the positive resist, since everything except the active junction areas

Stage 1-1; top electrode etch

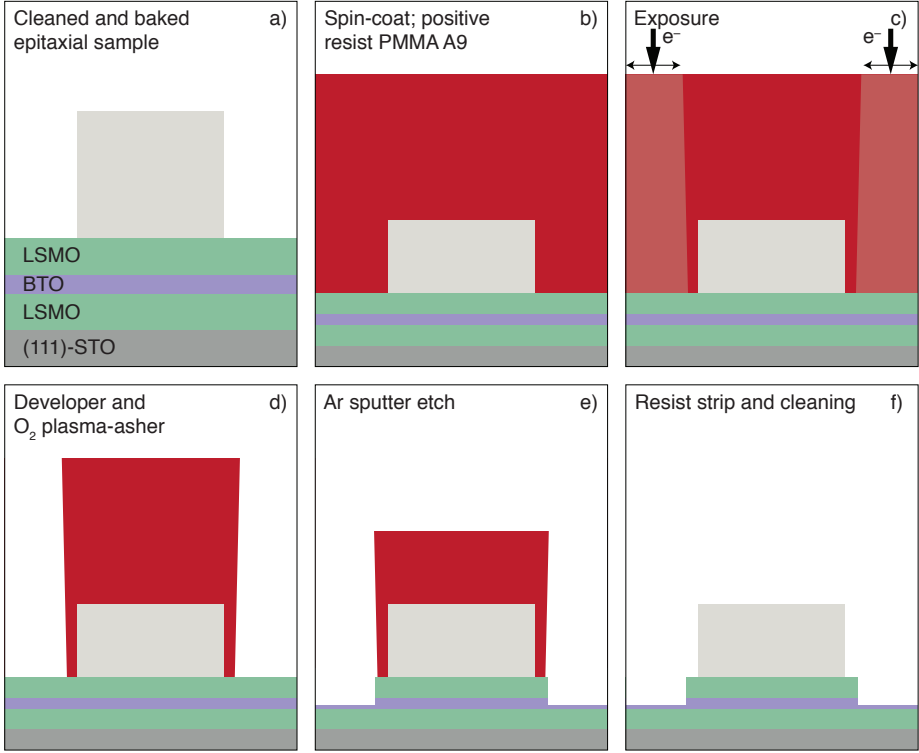


Figure 6.8: All-oxide MFTJ fabrication stage 1.1 – Ar sputter etch to define free-standing LSMO/BTO. Steps a) to f) show the essential process steps required to make free-standing top electrodes from LSMO/BTO on the underlying LSMO layer.

need exposure. Consequently, the area to be exposed is relatively large. This is time consuming, but by utilizing BEAMER with bulk/sleeve separation a rapid dose deliverance is achieved, and the exposure time can be kept within reasonable time limits for prototyping. Bulk regions are exposed with high beam currents, while the edges are exposed with small beam currents for better precision. The platinum top electrode contacts deposited in stage 1 were intentionally made $1\ \mu\text{m}$ (200 nm for the $1\ \mu\text{m}$ electrodes) smaller in diameter than for the cousin P-MFTJs, to allow some slack in the overlay exposure alignment, deviation from nominal dimensions, and to prevent platinum residues to short over the edge. In step e) the physical sputter etch with Ar ions is shown. The nominal etch depth targeted was 12 nm, in order to etch through the upper LSMO layer and into the BTO without etching any of the bottom layer LSMO. Etching was done with the AJA system's RF substrate etcher at maximum power 50 W, resulting in an

acceleration voltage of about 330 V. In f) the sample is shown after completing the resist strip. Further processing of O-MFTJs followed the same procedure as for the P-MFTJs.

The results after etching were investigated with both SEM and AFM. Representative SEM images can be seen in Figure 6.9. On the left is a close up

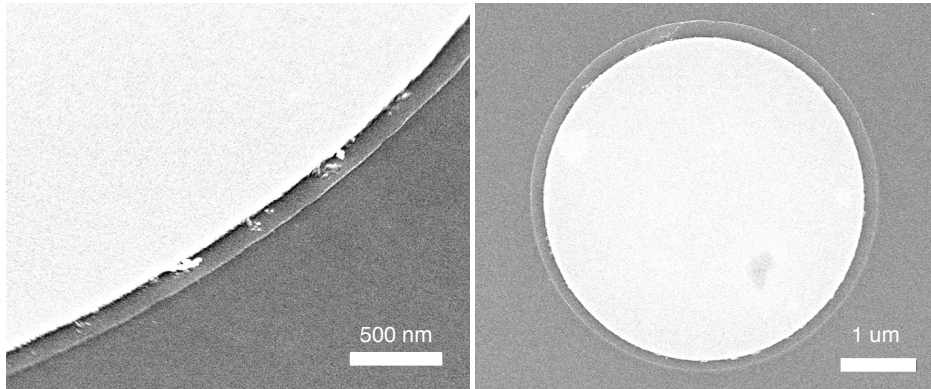


Figure 6.9: SEM micrographs of etched top electrodes for the O-MFTJs. On the left is a close up view from 40° , and on the right is an overview of a $5\ \mu\text{m}$ structure. Platinum is seen in bright white, the oxides in grey.

micrograph showing the edge of the platinum top contact and the LSMO/BTO top electrode from a 40° angle. Some edge roughness from stage 1 and platinum residues are seen, but does not interfere with the top electrode edge. The right micrograph shows a $5\ \mu\text{m}$ top electrode with a $4\ \mu\text{m}$ platinum contact. Due to the opposite exposures, i.e. exposure "around" the device for etching and "inside" the device for lift-off, the platinum contact ended up slightly larger (about $4.27\ \mu\text{m}$) and the etched top electrode slightly smaller (about $4.7\ \mu\text{m}$) than their respective nominal values. A slight alignment error is also visible, however, both these issues were compensated by having the platinum contact smaller than the final top electrode dimension. Similar results were found for all device sizes.

Results from AFM scans of the O-MFTJs after top electrode etch are found in Figure 6.10. The profile data are extracted from the corresponding AFM-data imaged in the lower part of the figure. The profiles confirm the same shadowing trend that was seen above for the stage 1 deposition. Moreover, the $2\ \mu\text{m}$ nominal diameter platinum contact on the $3\ \mu\text{m}$ electrode shows a quite horizontal top surface, indicating that it was totally hidden in the resist sidewall shadow. Only about $20\ \text{nm}$ of platinum, or about 40% of the nominal thickness, reached the bottom of the hole. The flat top surface is very clearly visible in the colored AFM image down left. The AFM images all show a clear red terrace which corresponds to the LSMO/BTO top electrode surface. The same step is visible in the plot data for the two smallest electrodes, and it was found to be $11.7\ \text{nm}$ on average,

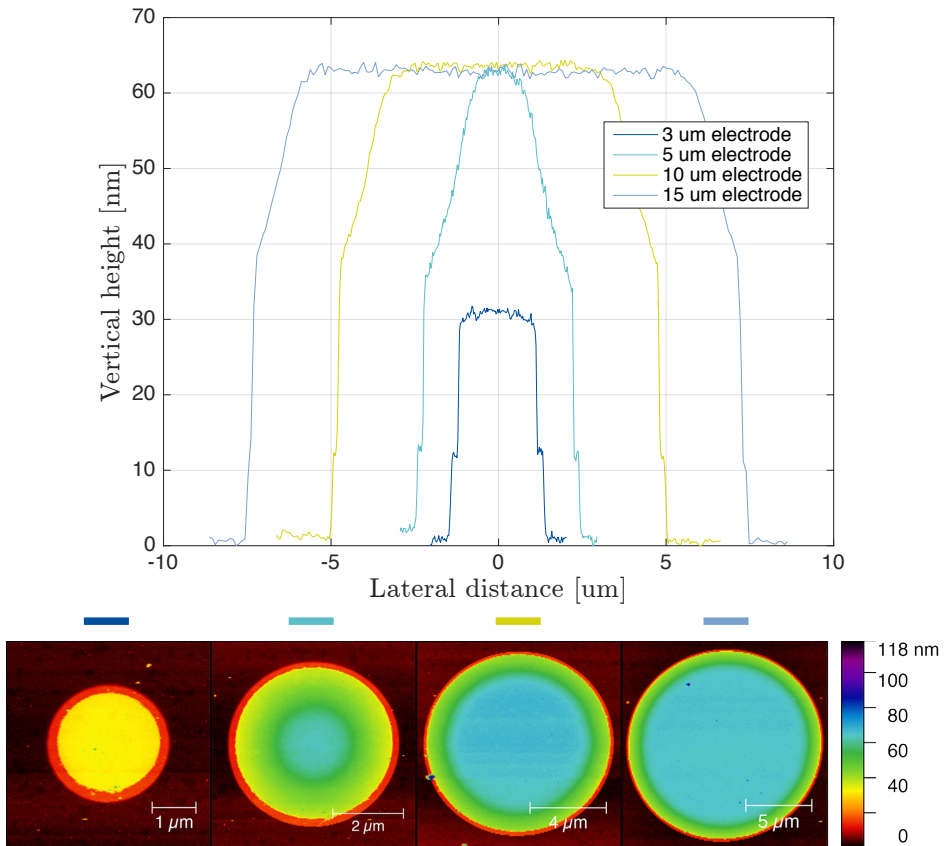


Figure 6.10: O-MFTJ top electrode profiles and AFM images after fabrication stage 1-1. Nominal deposition thickness was 50 nm Pt in stage 1 and 12 nm LSMO/BTO etch in stage 1-1. The average measured etch step height was 11.7 nm. It was not possible to locate any of the 1 μm electrodes for AFM-scan in this session.

which corresponds very well with the nominal etch depth. For the device sizes larger than 3 μm, the shadow effect is even more clearly seen from the AFM images. Since rotation was always used when depositing, the thickness profile became uniform around the contacts. The shadow effect can easily be visualized by thinking one is looking down the axial direction of a cylindrical object. By tilting it slightly away from you, more and more of the bottom is hidden from sight. However, because of the circular shape, the lateral maximum width of the bottom part that is still visible very slowly decreases as you tilt. Thus, due to the rotation roughly half of the area subject to shading is always receiving material, and the point at which the shade effect becomes visible in the plots, is roughly halfway up the structure, increasing gradually as the size of the hole increases

relative to the resist thickness. In any case, all O-MFTJ device sizes are expected to work even though the thickness of the top contact is not at its nominal value.

6.2.5 Stage 2 – Bottom Electrode Contact Formation

Electrical contacts to the bottom electrode LSMO layer were made by etching through the oxide materials stack and depositing platinum. Figure 6.11 shows the process flow for stage 2 of the fabrication process. Steps a)-c) describe the

Stage 2; etching and deposition of bottom electrodes

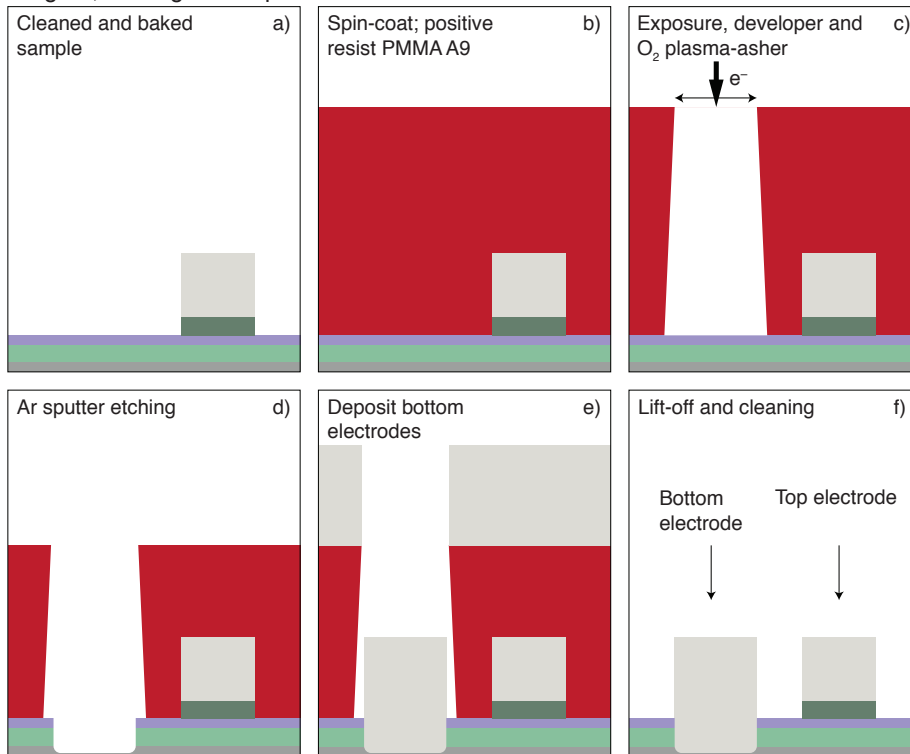


Figure 6.11: MFTJ fabrication stage 2 (not to scale). Steps a) to f) show the most important processing steps for dry etching and deposition of bottom electrodes.

ordinary EBL process. In step d), the RF substrate etcher was used at maximum power, 50 W, which gave an acceleration voltage of about 330 V, to etch through the BTO/LSMO layers. Step e) shows the subsequent deposition of platinum by DC sputtering, which gave electrical contacts to the LSMO bottom electrode through the thin-film cross section. Both sputter operations were done in sequence with the AJA system. The nominal etch depth was set to 15 nm to etch

completely through the LSMO for both thicknesses of the BTO layer. The platinum deposition thickness was set to 65 nm to end at the same nominal height of 50 nm above the BTO surface as the top electrodes. In step f) the sample is shown with top and bottom electrodes ready after lift-off.

It was expected to be more reproducible to etch through the LSMO layer rather than aiming for a timed etch stop at some depth into the film. If a timed etch stop had been implemented, the remaining thickness of the LSMO below the platinum electrode necessarily would have varied a little from sample to sample. It was assumed that this might cause a varying contact resistance, and was thus avoided, but it was not tested here. Both the etch rate for BTO/LSMO and deposition rate for platinum were thoroughly tested and verified before the final processing. Results for these methods have already been presented above. Profile measurements confirmed that the nominal thickness of the bottom electrode contacts was met.

6.2.6 Stage 3 – Insulation Layer Deposition

To passivate the sample parts around the active tunnel junction areas and for electrical integrity, an insulation layer was deposited. Figure 6.12 shows this procedure as stage 3 of the fabrication process. Steps a)-d) show the regular EBL process. In step c), only the areas which should not be covered by the insulator are left unexposed. Hence, this exposure is very similar to the one described for stage 1-1 above, with a "negative" mask pattern written in a positive resist. The unexposed areas were intentionally left slightly smaller in diameter than the areas of the top electrodes, to prevent subsequent short-circuiting to the bottom electrode in stage 4 when depositing the final contacting layer. As a result, the via holes left open in the SiO_2 after lift-off were smaller than their corresponding top electrodes. After development and descumming of the resist (d), the insulator was deposited by RF sputtering in the AJA-system, step e). The maximum power of 300 W was used, which gave about 100 nm deposited material per hour (see tbl. 6.1 for details). Finally, via hole openings for bottom and top contact pads are left after lift-off and cleaning as can be seen in step f).

Representative results from the insulation layer deposition and lift-off can be seen in Figure 6.13. The upper row depicts a 1 μm (a), 3 μm (b) and 5 μm (c) electrode, respectively. For the smallest electrode (a) the final via hole opening to the platinum ended up with a diameter of about 300 nm. This was smaller than intended, yet enough for making electrical contact in the final stage. For all the larger electrodes the process worked very well. It may not be easily seen, but one can see the edges of both the platinum contact and the LSMO/BTO top electrode follow through the SiO_2 and appear in its surface in images (b) and (c). The lower row of micrographs show a successful 10 μm electrode with remains of an insulator wall standing up (d), an unsuccessful 15 μm electrode where the resist was totally capped by a sealed insulator surface (e), and the corner of one of the bottom electrode contacts in (f). There were remarkably few examples of

Stage 3; insulation layer deposition and lift-off

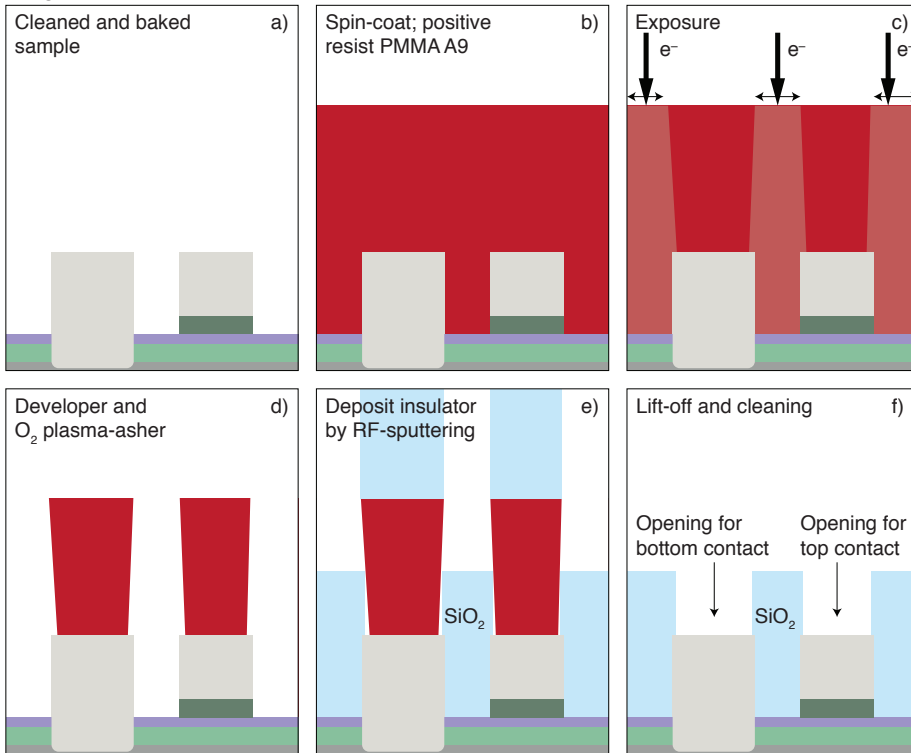


Figure 6.12: MFTJ fabrication stage 3 (not to scale). Steps a) to f) show the most important processing steps for depositing an insulation layer by RF sputtering and lift-off.

the problem seen in (e), which was indeed expected to be a possible issue with the SiO_2 lift-off process. In all the other micrographs, a relatively uneven ring can be seen in the insulator material where the platinum is first becoming covered. This is the bottom of the capping wall seen in (d) and (e), which presumably quite easily cracked when the ultrasonic excitation was applied for lift-off.

As one of the most critical parts of the entire process, it was not obvious that via holes to the smallest electrodes (a) would succeed at all. The nominal diameter of the non-exposed area for the smallest electrodes was actually set to $1\mu m$, because it was seen in the earlier tests that the remaining structure after exposure and development ended up substantially smaller (see for example fig. 6.2). This is likely caused by the proximity effect due possibly to a larger exposure dose than necessary. Nevertheless, the manual compensation enabled a successful process. It should be noted that the aspect ratio in this particular case

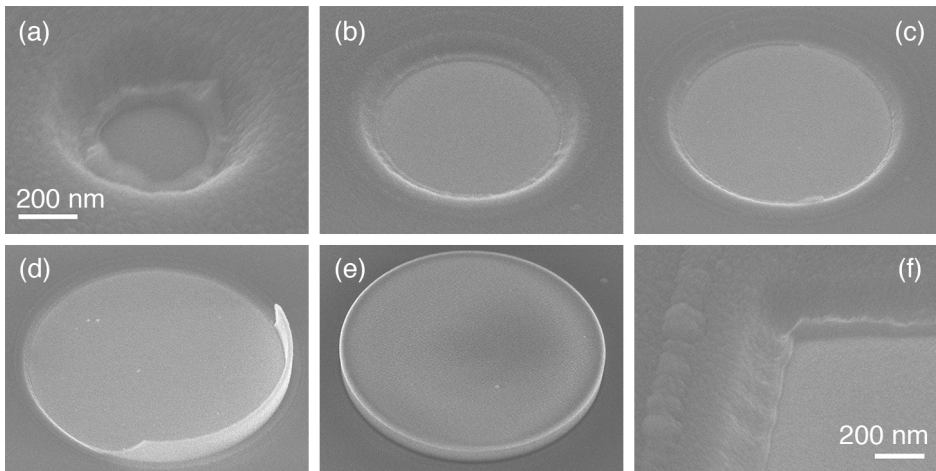


Figure 6.13: SEM micrographs of the insulation layer surface on sample P60214. The upper row shows the via holes in the SiO_2 layer down to the top electrodes; dimensions $1\ \mu\text{m}$ (a), $3\ \mu\text{m}$ (b) and $5\ \mu\text{m}$ (c). Similar results for the $10\ \mu\text{m}$ and $15\ \mu\text{m}$ electrodes. The lower micrographs show a residual insulator edge on a $10\ \mu\text{m}$ electrode (d), a $15\ \mu\text{m}$ top electrode where the SiO_2 encapsulated the PMMA completely so it could not lift off (e), and the corner of a bottom electrode via hole (f). In (b), (c) and (f) the platinum edge and LSMO etch-edge are seen in the insulator surface. All images were taken from a 40° angle.

was as large as 5:1 ($1.5\ \mu\text{m}$ resist thickness to $300\ \text{nm}$ bottom surface diameter of the PMMA), which is noteworthy considering the relatively harsh handling with stirring in developer and water, in addition to drying with pressurized nitrogen gas and subsequent descumming.

The negative consequences of the off-axis sputter head location again becomes apparent when considering images (d) and (e) in Figure 6.13. Since the sputtered material is incident at an angle, the sidewalls of the resist pattern are covered by more or less the same amount of material as the sample surface. However, judging from the curvature of the insulation from its uniform horizontal surface and down into the via holes, it looks like there has been some sort of deposition turbulence at the foot of the resist structure. The result seems to be a thinner insulator sidewall at the foot, which ultimately can crack when subjected to some outer stimuli, enabling the cap to be lifted off and removed in most cases.

6.2.7 Stage 4 – Deposition of Contact Pads

The final fabrication stage is deposition of contact pads and wiring for connections to the MFTJs top and bottom electrodes. This can be seen in Figure 6.14 as stage 4 of the fabrication process. Steps a)-d) show the ordinary EBL process, however,

with a double layer of resist to enable deposition of more material. In step e), a thin layer of titanium (20 nm) was first evaporated to enhance the adhesion of gold (1 μm) evaporated immediately after. The deposition rates were set very high in the end, as there were indications for resist boiling or dissolution due to heating during the early tests. Nominal evaporation rates were approximately 10 \AA s^{-1} and 15 \AA s^{-1} for titanium and gold, respectively. The completed sample after lift-off is seen in step f), which corresponds to the detailed structure that was shown in Figure 5.2 from the preceding chapter.

Stage 4; deposition of contact pads

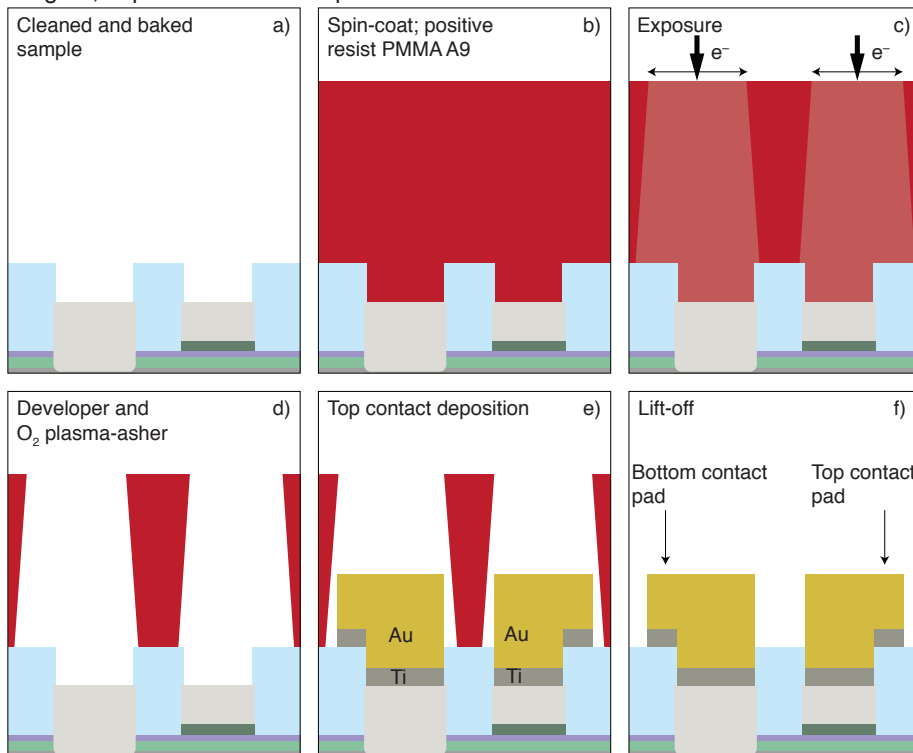


Figure 6.14: MFTJ fabrication stage 4 (not to scale). Steps a) to f) show the most important processing steps for the formation of electrical contact pads by EBL and metal evaporation.

A bundle of micrographs showing the resulting MFTJs after stage 4 are compiled and presented in Figure 6.15. The upper row depicts successful MFTJs with diameter 1 μm (a), 3 μm (b) and 5 μm (c). At first sight the typical conglomerate structure of gold nanoparticles is striking. Upon closer inspection one can still see the edges of the underlying structures following through to the conglomer-

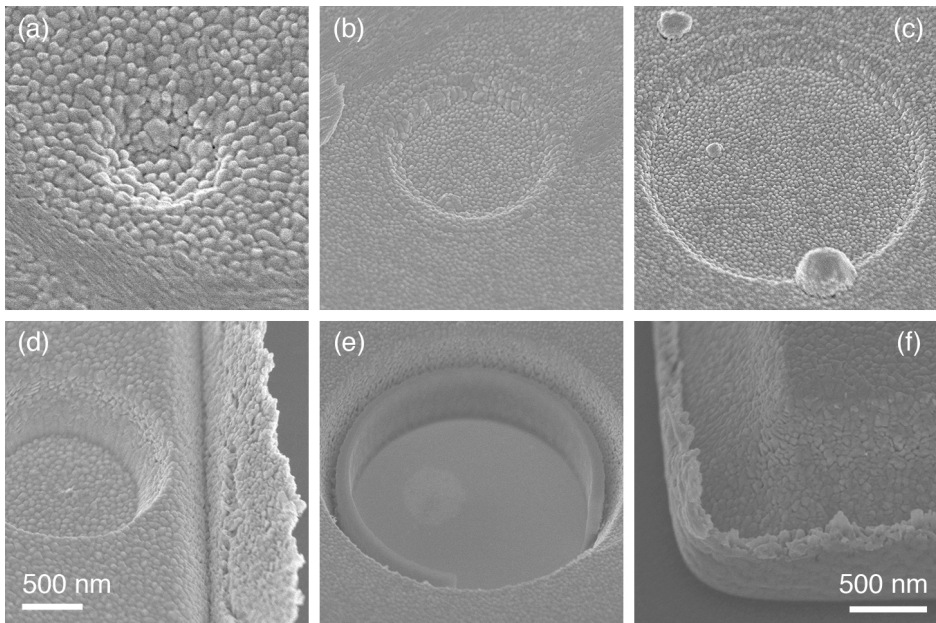


Figure 6.15: SEM micrographs of top contact layer surface on sample P60214. The upper row shows the top surface of completed and successful top electrodes; dimensions $1\ \mu\text{m}$ (a), $3\ \mu\text{m}$ (b) and $5\ \mu\text{m}$ (c). Similar results for the $10\ \mu\text{m}$ and $15\ \mu\text{m}$ electrodes as well as the bottom electrode contacts. The lower micrographs show an example of a crater most likely from droplets of PMMA (d), a $5\ \mu\text{m}$ top electrode that were unsuccessful (e), and the corner of a bond-pad (f). Note the clear edge roughness in (d) and (f) and the residues/droplets in (c), both of which were very typical for all the samples.

ate surface. Also visible are some examples of gold particulate contamination, especially in (b) and (c). The lower row shows a typical crater and substantial edge roughness after lift-off (d), an unsuccessful $5\ \mu\text{m}$ electrode (e), and the corner of a contact pad with the typical edge roughness and curvature (f). The craters and gold particles (d) were seen all over the sample and may be due to the high deposition rate that was used. No sparking was seen during evaporation, but the particles were small and the gold was in fact moving rather violently in the crucible, indicating too much heating. It was necessary to deposit at high rates in order to limit radiative heating of the PMMA. Titanium and gold both have high melting temperatures, so there is substantial heat radiation inside the chamber during e-beam evaporation. PMMA starts plastic deformation already at about $120\ ^\circ\text{C}$ [115], so it is possible that the radiation heated the resist way past this and to the point of melting or even boiling. Figure B.3 in the Appendix shows an optical image of sample P60212 that was finished with a stage 4 depo-

sition of Al/Ti $1\ \mu\text{m}/20\ \text{nm}$, deposited at low rates about $1\ \text{\AA s}^{-1}$ to $2\ \text{\AA s}^{-1}$ and $5\ \text{\AA s}^{-1}$ to $7\ \text{\AA s}^{-1}$ for titanium and aluminium, respectively. Since aluminium has a much lower melting point than titanium, it is likely that the problem was caused mainly by radiation from the titanium source. There was no time to test this thoroughly. After all, the signs of boiling or dissolving PMMA was no longer seen after high deposition rates were introduced. The end result was considered good enough, and the gold particles is not considered a problem. Images (d) and (f) show another characteristic feature, namely the extensive edge roughness and the gradually decreasing structure size with increasing deposition thickness. Both are likely caused by the nearly vertical resist sidewalls. The edge roughness is typical for lift-off processes where there is an insufficient undercut profile. The structure edge profile can be explained by material buildup on the resist edge, which gradually increases the amount of material hanging out over the opening in the resist, effectively making an undercut profile. The same phenomenon is seen in image (e). There, one of the unsuccessful electrodes from stage 3 has had a glass cap that worked as a mask for the top layer deposition. During stage 4, however, the glass must have cracked and led to lift-off of the entire cap and top layer, leaving the junction disconnected from its positive contact pads. The deposited gold around the electrode shows the same side profile as in (d) and (f), which again indicates material buildup over the edge on top of the cap, slowly covering more of the area around it as material is deposited.

6.2.8 The alternative fabrication approach

An alternative process for stages 2 and 3 has been sketched, which uses PECVD and ICP-RIE for deposition and etching, respectively. This approach has not been tested, but the intended process flow can be seen in the Appendix, Figure B.2. In step a), the same initial structure from stage 1 is seen, however, with titanium or aluminium on top to work as an etch stop material in later steps. Step b) shows a uniform deposition of SiO_2 by PECVD, although it may be deposited by RF sputtering as above too. Steps c)-e) are the same EBL process steps as before. In step f) SiO_2 and BTO/LSMO is etched by ICP-RIE, while the top electrode structure is protected by a sufficiently thick etch barrier. A brief Ar sputter-etch is used in step g) to remove native oxides that grow in atmospheric conditions between process systems. Gold is subsequently deposited by evaporation to give an ohmic contact to the LSMO layer and prevent further oxidation of the titanium etch mask. The AJA system is used both for the brief sputter-etch and gold evaporation. Finally, step h) shows the insulated sample with contact openings after lift-off and cleaning. The final contacts may now be evaporated in the third stage. It should be noted that a different resist than PMMA is probably necessary to withstand etching with ICP-RIE.

6.3 Wire-bonding

Wire-bonding with both aluminium and gold wire was tested during the development of the fabrication process. There were mainly three problems; evaluating the need for an additional adhesion layer, finding a sufficient pad thickness, and deciding a practical bond pad size which was not too small to use, yet small enough to limit capacitance and restrict the physical extent. Implicitly, by solving those problems, a highly reproducible wire-bonding process was also expected. At the beginning, aluminium wire was the only option that seemed reasonable, since bonding with gold wire in general needs a heated sample (thermosonic bonding) to work well [105, 118, 119, 120]. Heating of the sample holder and PCB was not an option due to limitations in height adjustment of the hot plate. However, the author received tips from another user of the wire-bonding tool, who was doing wedge bonding with gold wire at room temperature with decent success. Thus it was decided to include more testing with gold wire in the optimization process, even though it had been rejected during the autumn work [1]. Recent progress in room temperature wedge-wedge bonding with gold wire has indeed been reported, though with special gold wire alloys containing palladium [121].

Both aluminium and gold pads were investigated, and two pad thicknesses were tested, $0.5\ \mu\text{m}$ and $1\ \mu\text{m}$. Gold wire to gold pads is considered the most reliable bond, as no interface corrosion, intermetallic formation, or other bond degrading conditions can occur [120]. Aluminium wire to aluminium pads is also considered an extremely reliable bond for the same reasons [120]. Nevertheless, gold wire to aluminium pads is the most commonly used bond in industry, while aluminium wire to gold pads is not recommended due to low reliability from intermetallics formation [120, 122]. The intermetallic formation known to occur in gold-aluminium interfaces, also known as the purple-plague, has been a major cause of semiconductor device failure [123]. However, the formation of the purple plague is strongly temperature dependent and does not occur much at temperatures below $150\ ^\circ\text{C}$. Moreover, it needs sufficient time to develop in considerable amounts, and the majority type of intermetallic compound will depend on which of the materials gold and aluminium there is a larger richness of [123, 124]. As a result, all four combinations of wire and pad materials noted above are considered safe in the context of the present work. After wire-bonding, the sample environment temperatures will never exceed $400\ \text{K}$, or approximately $127\ ^\circ\text{C}$, and long-term reliability issues are not a concern due to the short-term time frame of the study.

In the first test two SiO_2/Si samples were prepared. One was coated with $0.5\ \mu\text{m}$ aluminium only, the other with $20\ \text{nm}$ titanium followed by $0.5\ \mu\text{m}$ aluminium. Bond tests on these samples were done with aluminium wire. There was absolutely no doubt that the adhesion layer was needed, as none of the attempted bonds on the aluminium-only sample succeeded. Some of the first bonds attached, but none of the second bonds would stick. Metal peeling when lifting the bond needle was also commonly seen for both the initial and final bonds.

On the Al/Ti-coated sample, metal peeling was very rarely seen, and the bonds attached in most cases. It appeared to be more a problem of wire handling in the wire feed system and wedge needle rather than pad-related issues, that caused some bonds to fail. The aluminium wire often got stuck after finishing a bond and had to be re-threaded. In addition, the wire did not slide very well through the bond needle, with a sort of tugging or uneven friction, that probably contributed to peeling or non-sticking bonds too. The only available type of wedge needles was the sort that has a so-called cross-groove milled into the head. It looks like a plus sign where the wire fits in the notch along its axial direction and is slightly squeezed into the perpendicular notch upon bonding (see fig. 6.16). According to the TPT wire-bonder manual, the cross-groove needles are optimized for gold wire, while aluminium wire should be bonded with ordinary blunt head wedge needles. It is thus believed that much of the trouble experienced with aluminium wire bonding was related to the wrong type of wedge needle used.

The bond parameters that worked well on the test sample with the titanium adhesion layer are listed in Table 6.5. After inspection with an optical microscope

Table 6.5: Wire-bonding parameters for aluminium wire to aluminium test pads. Wedge bonding with 250 μm tail and 10 μm feed was used on a sample of Al/Ti/SiO₂/Si (0.5 μm /20 nm/92 nm).

Bond	U.s. power [mW]	Time [ms]	Force [g]
B1	230-250	210	30
B2	240-260	220	35

it became clear that the lowest ultrasonic power values should be used. The wedge needle penetrated through the pad material and revealed the SiO₂ surface at higher ultrasonic power, which is not desired. This indicated that it could be beneficial with thicker pads. Hence, three things were clarified from these tests. First, it was concluded that a titanium adhesion layer had to be included in the fabrication process. Second, the new experiences with aluminium wire indicated that the focus should shift towards using gold wire if possible, or wait for proper wedge needles for aluminium wire. Third, the pad thickness should be increased to see if better results can be achieved. Pad thickness is indeed reported to have a dominant effect on bond quality and overall bond-ability [118].

Sample P60503 was prepared by EBL with PEC and a bond pad pattern comprising a grid of 100 μm \times 100 μm bond pads with 25 μm pitch. Evaporation of Al/Ti and Au/Ti was done in two rounds with half of the sample covered by a cover glass, to total thicknesses 1 μm /20 nm. Deposition rates were high, with 11 \AA s^{-1} , 16 \AA s^{-1} , and 15 \AA s^{-1} for Ti, Au and Al, respectively, to avoid heating as discussed above. The selected pad size was based on measurements of bond footprints with an optical microscope and the wedge needle head size of about 70 μm \times 70 μm . Further tests of wire-bonding with both aluminium and gold

wire was done on this sample, which had followed other samples in the process of insulation layer deposition. Hence, the underlying materials were the same as for the final fabricated samples.

With aluminium wire relatively good and reproducible bonding was achieved with the parameters presented in Table 6.6. These parameters also worked well on

Table 6.6: Wire-bonding parameters for aluminium wire to gold and aluminium pads on oxide samples. Wedge bonding with 250 μm tail and 10 μm feed was used on a sample of (Al or Au)/Ti/SiO₂/BTO/LSMO/STO (1 μm /20 nm/293 nm).

Bond	U.s. power [mW]	Time [ms]	Force [g]
B1	230	210	32-35
B2	240-250	220	40

the silicon test sample introduced above (tbl. 6.5). There were some day-to-day differences which can be seen as the ranges in ultrasonic power and push force. The last parameters that were used, however, were the higher ultrasonic power and the lower push force. The parameters worked well on both pad materials, no changes had to be done when changing from gold to aluminium pads or vice versa.

With gold wire even better results were achieved, surprisingly considering the ambient temperature of about 19 °C, both on gold and aluminium pads. The working bond parameters used for gold wire are listed in Table 6.7 where the upper half are the parameters for aluminium pads and the lower for gold pads. On aluminium pads the gold wire worked relatively well. Moreover, the

Table 6.7: Wire-bonding parameters for gold wire to aluminium and gold pads on oxide samples. Wedge bonding with 110 μm tail and 10 μm feed was used on a sample of (Al or Au)/Ti/SiO₂/BTO/LSMO/STO (1 μm /20 nm/293 nm). Parameters for aluminium pads at the top and gold pads at the bottom.

Bond	U.s. power [mW]	Time [ms]	Force [g]
B1	260	220	45
B2	260	220	45
B1	240	400	45
B2	260	400	50

gold-aluminium bonds were less harmful to the pads than aluminium-aluminium bonds. The latter is likely due to the cross-groove in the wedge needle, which is not ideal for aluminium wire as noted above. On the gold pads at first the same parameters as for aluminium pads were used and worked decently, but there was quite often problems with achieving good adhesion between the gold pad and the gold wire. By increasing the time dramatically, it was thought that more

local heat generation at the bond interface could possibly help the formation of bonds. It cannot be concluded that this actually happens of course, but the bonds started to form each time, and the bond quality was apparently good. However, the main benefit from using gold wire instead of aluminium wire is that the handling of the wire in the bonder tool, or simply the user experience, is profoundly improved. The gold wire glides very well through both the feed system and the wedge needle. It very rarely sticks and has to be re-threaded, as compared to the aluminium wire. In addition, bond formation was easier when there was already gold residues from an earlier bond on the pad, which is a benefit when the bond pads are small.

SEM micrographs of gold wire bonded to gold and aluminium pads on sample P60503 can be seen in Figure 6.16. The upper row of images represents the gold pads and the lower row are aluminium pads. On the left side, close up images of

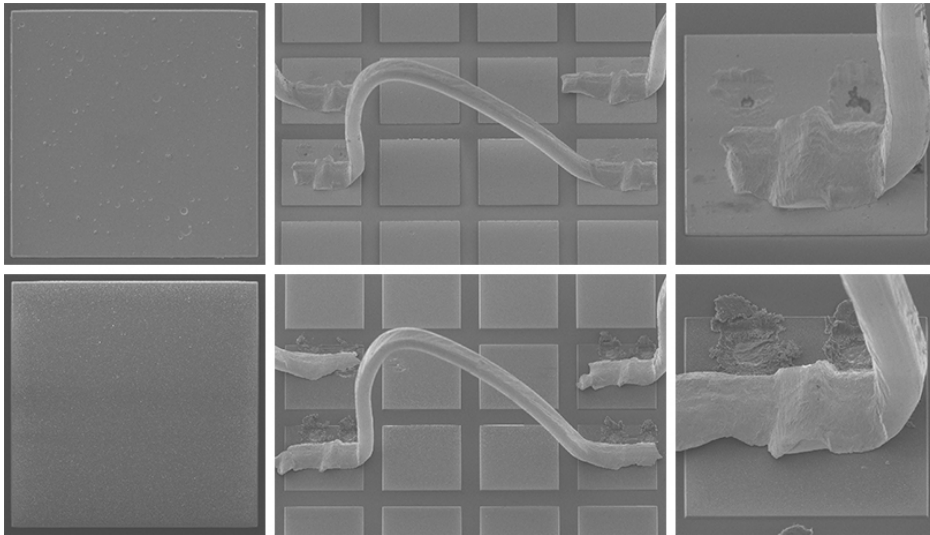


Figure 6.16: Test sample for wire-bonding on small pads. The pads are $100\ \mu\text{m} \times 100\ \mu\text{m}$, the upper row is Au/Ti and the lower row is Al/Ti, with thicknesses $1\ \mu\text{m}/20\ \text{nm}$. Sample P60503 with underlying materials $\text{SiO}_2/\text{BTO}/\text{LSMO}/\text{STO}$. Gold wire with $25\ \mu\text{m}$ diameter was used on both gold and aluminium pads.

the pads and their surfaces are seen. By careful inspection it is possible to see the typical craters and contaminant particles in the gold, that was discussed in the preceding section. The aluminium pads did not show craters or particulate contaminants, however, a distinct surface roughness was present. It is believed that both issues are caused by the high deposition rates, but none of them are considered problematic for wire-bonding. The central micrographs show two complete bonds and neighboring initial and final bonds. On the right side close up images of initial bonds on gold and aluminium pads are shown, respectively.

Both bond types worked well, but the bonds on gold pads look relatively much better. By considering the wire deformation and marks in the pad from the wedge needle, it seems that the aluminium is too hard to let the needle deform the wire sufficiently and give a proper bond. This can be argued for both gold and aluminium pads, although it seems to be a greater problem on the aluminium pads. This problem was later helped a bit when it was realized that the wedge needle had been mounted 90° off in the tests shown here, but it did not make any difference on the bond parameters. In addition, after correcting the needle direction, the sample stage was adjusted very carefully to a more correct height so the marks from the wedge needle were uniform in all four corners around the cross-groove.

The tests on sample P60503 answered all the initial problems that were assessed. With a titanium adhesion layer, $1\ \mu\text{m}$ thick bond pads of either gold or aluminium, and with size down to $100\ \mu\text{m} \times 100\ \mu\text{m}$, good and reproducible wire-bonding could be achieved. All final samples were subsequently bonded with gold wire and great reproducibility, though some times with the need for a few attempts in order to have more material stick to the pad.

6.4 Sample Fabrication Summary

Table 6.8 presents the final fabricated samples along with the materials constituting the active MFTJ region and their respective thickness and deposition method. Sample P60212 was the first completed sample and was processed along with the development of the fabrication process. The test sample P60206 was used alongside the fabrication of P60212 for corrective measures. A major change was done during fabrication as a result of the tests done on P60206. It became evident that a titanium layer was imperative for the adhesion of contact pads to make wire-bonding possible, as was discussed in the preceding section. Consequently, another EBL stage was added for the final processing of P60212. The other three samples were subsequently fabricated simultaneously with the corrected process flow that was presented above.

Table 6.9 lists the final diameters as measured versus targeted values for the top electrode contacts deposited in stage 1. The differences relative to the target value are listed as well. These results are representative for all exposures, since the EBL process was similar for all stages with the minor exception for the final contact pads deposition. The absolute overshoot in diameter grows as the junction size increase while the relative difference goes down. This implies that it is caused by the proximity effect and possibly an overcompensating PEC. The difference from targeted values is not critically large, and the overlaps between the different layers takes these offsets readily into account as has been seen above.

An overview of all process stages performed on the final samples are found in Table 6.10. The rearrangement of process stages is clear when comparing sample P60212 with the other three. As discussed above, stage 3 and 4 was

Table 6.8: Overview of final fabricated samples. S and PLD means deposition by sputtering or pulsed laser deposition, respectively. Only the materials actively contributing to the tunnel junctions are listed. All samples have STO(111) substrates. [†]P60212 was the first sample to finish processing and led to changes in the sample layout and fabrication process. The other three samples were fabricated simultaneously and with the updated layout and process flow.

Sample	Materials	Thickness [nm]	Technique
P60212 [†]	NiFe/BTO/LSMO	10/3/10	S/PLD/PLD
P60214	LSMO/BTO/LSMO	10/3/10	PLD/PLD/PLD
P60403	NiFe/BTO/LSMO	10/3/10	S/PLD/PLD
P60501	NiFe/BTO/LSMO	10/5/10	S/PLD/PLD

Table 6.9: Overview of top electrode contacts (stage 1) diameter on final fabricated samples. Targeted diameters, resulting diameter measured, and the difference relative to the target value are listed for each sample. The measurements were taken with the JEOL SEM at 5 kV, all dimensions are in [μm] and the relative differences in percent.

Target	P60403		P60501		Target	P60214	
	Meas	Diff %	Meas	Diff %		Meas	Diff %
1.0	1.15	15.00	1.17	17.00	0.8	1.04	30.00
3.0	3.18	6.00	3.24	8.00	2.0	2.22	11.00
5.0	5.24	4.80	5.27	5.40	4.0	4.26	6.50
10.0	10.30	3.00	10.40	4.00	9.0	9.31	3.44
15.0	15.50	3.33	15.40	2.67	14.0	14.40	2.86

originally combined, however, after it was found necessary to do these separately, it was simpler and better to prepare the bottom electrodes in stage 2 and deposit the insulator on top in stage 3. Other points to note are the generally larger development times of the three last samples, compared to sample P60212, and the especially long development time of sample P60212 in stage 3. The latter was due to the lack of PEC since the BEAMER license was temporarily expired. For sample P60212 the PEC calculation was done with Si substrate simulation, while for the other three samples GaAs substrate simulation was used. The difference between these simulation settings was mainly that the GaAs simulation had larger extremes both for bulk and sleeve regions, which made the bulk regions slightly underexposed compared to the rest. Hence, a longer development was needed to develop the bulk regions fully. Unless simulation files for STO substrates are acquired for BEAMER, the recommendation from the experiences here is to use the SiO_2/Si simulation files for STO substrates. The final row states which wire-bonding parameters that were used for each of the final samples.

The result of the final corrected fabrication process as described above can be

Table 6.10: Fabrication process flow for the final samples. In all stages the standard EBL process flow (steps 1-10) was used unless stated otherwise. For P60212 PEC with Si substrate simulation was used, while for the other samples GaAs substrate simulation was used. [†]The BEAMER license was temporarily unavailable, so without PEC extended development was necessary to develop the smallest electrodes fully.

Stage	P60212		P60214		P60403/P60501	
1	Developed	10 s, sputtered 10 nm NiFe, 10 nm Pt, evapor. 30 nm Ti.	Developed	20 s, sputtered 50 nm Pt.	Developed	20 s, sputtered 10 nm NiFe + 40 nm Pt.
1-1	–		Developed	20 s, etched 11.7 nm LSMO/BTO.	–	
2	Developed	10 s, sputtered 264 nm SiO ₂ .	Developed	20 s, etched 15 nm BTO/LSMO, sputtered 65 nm Pt.	Developed	30 s, etched 15 nm BTO/LSMO, sputtered 65 nm Pt.
3	Developed	60 s [†] , etched 15 nm BTO/LSMO, sputtered 30 nm Pt.	Developed	25 s, sputtered 293 nm SiO ₂ .	Developed	20 s, sputtered 293 nm SiO ₂ .
4	Double	PMMA (3 μm), developed 15 s, evapor. 20 nm Ti + 1 μm Al.	Double	PMMA (3 μm), developed 15 s, evapor. 20 nm Ti + 1 μm Au.	Double	PMMA (3 μm), developed 15 s, evapor. 20 nm Ti + 1 μm Au.
Wire- bonding	Au-Al	parameters from Table 6.7	Au-Au	parameters from Table 6.7	Au-Au	parameters from Table 6.7

seen in Figure 6.17. It shows a SEM micrograph of one of the final samples on the left and a closer view of one of the MFTJs on the right. The corresponding EBL mask can be found in the Appendix, Figure B.4. A total area of 3 mm × 3 mm was utilized on each sample, where the corners were used for alignment marks and extra bond pads for training bonds before attempting the real bonds to the MFTJs. The alignment marks have been covered by materials from the various depositions. A total of 24 MFTJs were thus fitted on each sample. There are four 1 μm junctions, and five of each of the 3 μm, 5 μm, 10 μm and 15 μm junctions. On the right an overview image of one of the 10 μm junctions is seen from an 40°

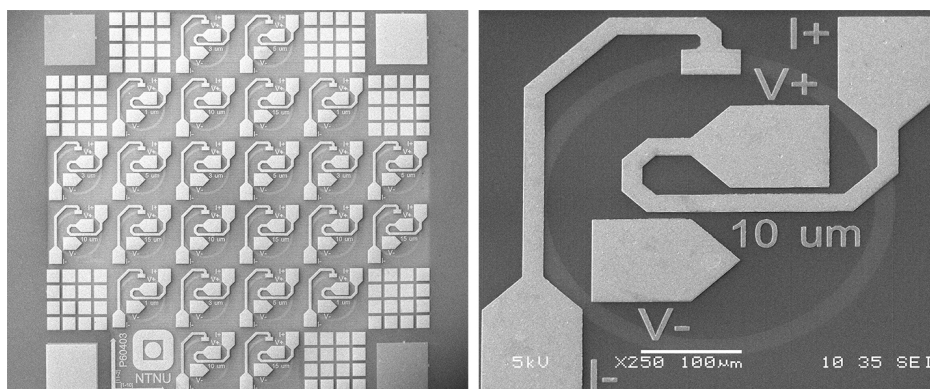


Figure 6.17: Finished sample with MFTJs of different size aligned in a grid (left). Close up of a $10\ \mu\text{m}$ device (right, taken from a 40° angle).

angle. The platinum ring contacting the bottom electrode can be vaguely seen underneath the insulating layer. By careful inspection one should also be able to see the contours of the top electrode in the center of the image, and the bottom electrode voltage probe in the V- pad.

All MFTJs from the final sample fabrication were checked by SEM to reveal any unsuccessful electrodes or other irregularities. The MFTJs were numbered along with the pattern shown in Figure 6.18. Top electrodes, bottom electrode contacts, and bottom electrode voltage probe contacts were checked. P-MFTJ samples P60403 and P60501 did not show any irregularities at all, but there was a single bottom electrode voltage probe on sample P60403 that looked slightly different from all the other. O-MFTJ sample P60214 had a few irregularities, some of which have been depicted already. A total of three top electrodes and two bottom electrode voltage probes did not lift off the insulation cap in stage 3. A total of four MFTJs were thus unsuccessful, since one of them had both a faulty top electrode and bottom probe. Table 6.11 lists all known faulty MFTJs for the final samples. Naturally, no attempt should be done on measuring the electrical characteristics of these junctions.

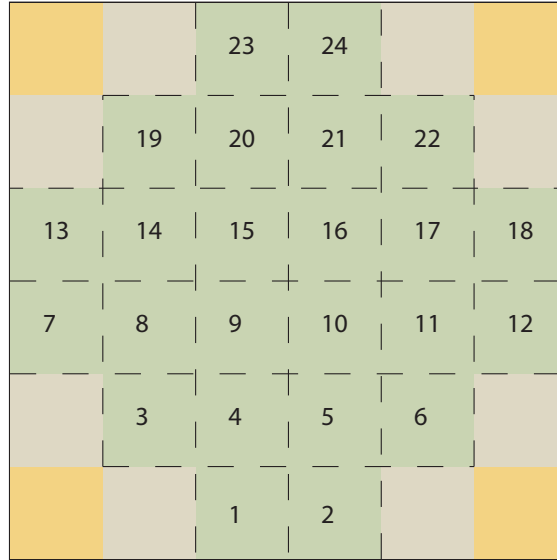


Figure 6.18: MFTJs numbered for identification. $1\ \mu\text{m}$ junctions: 3, 6, 19 and 22. $3\ \mu\text{m}$ junctions: 4, 13, 15, 17 and 23. $5\ \mu\text{m}$ junctions: 5, 14, 16, 18 and 24. $10\ \mu\text{m}$ junctions: 1, 7, 9, 11 and 20. $15\ \mu\text{m}$ junctions: 2, 8, 10, 12 and 21.

Table 6.11: List of known faulty MFTJs on the final samples. MFTJs are numbered according to the scheme in Figure 6.18.

Sample	Faulty MFTJ	Comment
P60212	–	Not checked/different layout.
P60214	2, 18, 19, 21	Top electrodes 2, 18 and 21. Bottom voltage probes 18 and 19.
P60403	–	Bottom voltage probe 24 may have an issue.
P60501	–	Everything fine.

Chapter 7

Electrical Characterization

In this chapter the performed electrical measurements are presented. First, data from TMR and TER measurements on a sample from the autumn project taken in the initial phase of the thesis are presented. Second, the work on how to take control of the ETO by scripting in Visual Basic are laid out. Third, measurements of the contact resistances achieved from the fabrication process are introduced. Current-voltage (IV) and differential resistance versus DC current offset (dVdI) measurements are presented in the fourth and fifth sections below. In the last part on the dVdI measurements, an interesting analytical approach based on AC lock-in data from the ETO is included. TMR and TER measurements on the new samples are discussed in section six, before the chapter is completed with remarks on the validity of various measurements.

7.1 Initial TMR and TER Measurements

Due to the late arrival of a new vertical sample holder for the ETO, it was not possible to perform electrical measurements with an in-plane magnetic field during the autumn work [1]. Sample P51006 prepared earlier was thus measured at the beginning of this thesis. The material structure was permalloy/BTO/LSMO with thicknesses 10 nm/5 nm/10 nm, but the magnetic part of the top electrode was relatively small, 200 μm in diameter compared to an effective top electrode of 1 mm^2 to 2 mm^2 after manual lead attachment by silver paste.

TMR measurements were conducted by finding an appropriate AC current amplitude and DC current offset from inspection of an IV-curve. A dVdI measurement was used as described in section 4.2.9 with AC amplitude 200 nA and DC offset $\pm 1 \mu\text{A}$ while the magnetic field was swept from +100 Oe to -100 Oe to +100 Oe. The current offset corresponded to a DC voltage of approximately 10 mV.

TER measurements were also done as described in section 4.2.9, with a sequen-

tial change of poling voltage from +2.5 V to -2.5 V to +2.5 V while performing a dVdI measurement at low current corresponding to about 10 mV between each poling sweep.

These measurements are presented in Figure 7.1 with TMR data on top and TER data below. The TMR data show some very interesting features. When sweeping the magnetic field from positive to negative (blue), two intermediate states (2 and 3) appear while the permalloy electrode is coerced towards the opposite magnetization and antiparallel alignment (5). Furthermore, on aligning parallel again after switching of the LSMO the end resistive state is halfway between the positive parallel (1) and antiparallel (5) states. Upon returning from negative saturation towards positive, the permalloy switches into another intermediate state (4) before reaching the antiparallel state (5) for positive magnetic field. When coercing the LSMO layer towards the positive parallel alignment, first two intermediate states are again entered (3 and 2). Thus, a total of five distinct resistive states are seen for this junction.

The maximum TMR effects were calculated according to equation 3.11 as

$$TMR_{\text{pos}} = \frac{R_5 - R_1}{R_5} = \frac{2.955 - 3.023}{2.955} \approx -2.3\% , \quad (7.1)$$

$$TMR_{\text{neg}} = \frac{R_5 - R_3}{R_5} = \frac{2.955 - 2.992}{2.995} \approx -1.3\% . \quad (7.2)$$

The same measurements were done five times and the results were consistent with intermediate states and magnitudes. Moreover, the measurements were done as function of temperature with 20 K steps from 50 K to 150 K. These results are listed in Table 7.1 for both positive and negative current offset. The five averaged

Table 7.1: Measured TMR effects from sample P51006 in percent. The upper row shows the average values from five consecutive measurements. The lower rows show the temperature dependency. The sample had been heated to room temperature for other measurements in the meantime.

Temp [K]	TMR_{pos}		TMR_{neg}	
	+1 μA	-1 μA	+1 μA	-1 μA
avg.5, 50	-2.09	-1.74	-0.98	-0.79
50	-1.44	-1.66	-0.81	-0.64
70	-1.90	-2.09	-0.48	-0.42
90	-0.87	-0.85	-0.75	-0.73
110	-	-	-	-
130	-0.35	-0.38	-0.53	-0.38
150	-0.30	-0.28	-0.23	-0.23

measurements show a slightly larger TMR than the first of the temperature sweep series measurements at 50 K, but the sample was heated and other tests performed

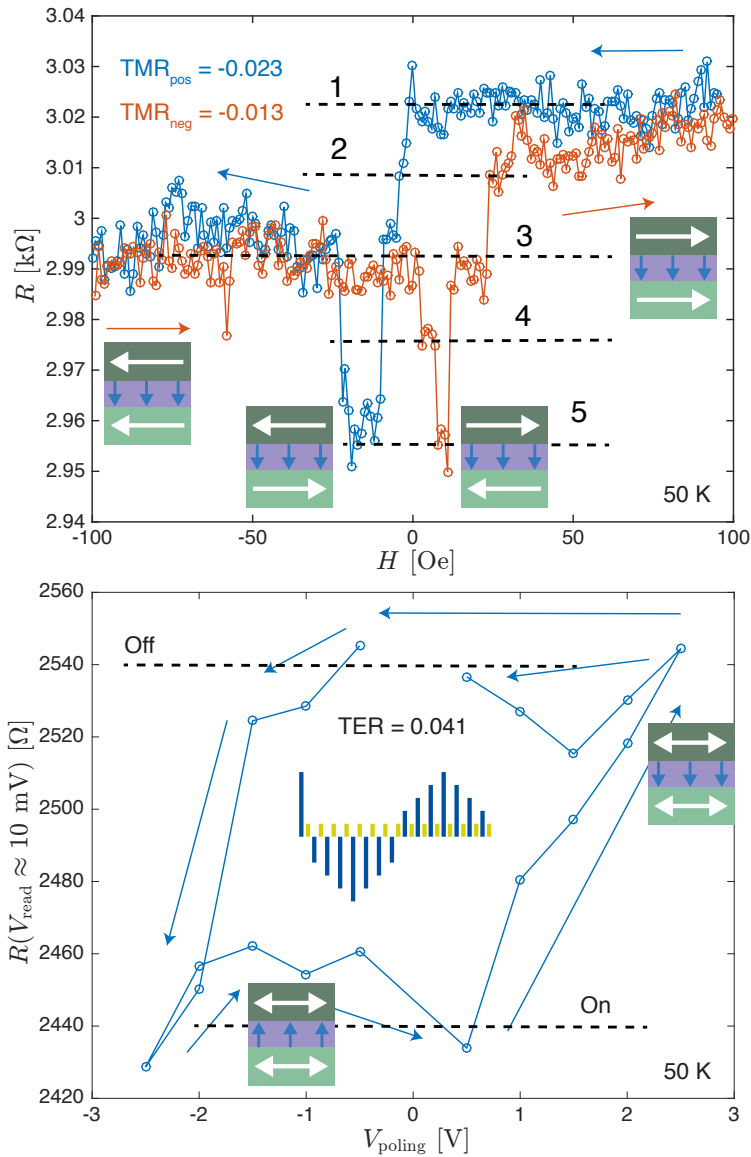


Figure 7.1: Initial evidence for TMR and TER in sample P51006 prepared during the autumn project [1] and measured during the initial phase of the thesis. Arrows indicate sweep/poling direction and insets show the MFTJ magnetization and polarization directions. Dashed lines are guides to the eye. $H \parallel (11\bar{2})$.

in the meantime. The TMR lasted to a temperature of 150 K, and the effects

were usually bigger for the positive test current, i.e. electrons tunneling from LSMO towards permalloy.

The difference in resistance for parallel states in the negative (3) or positive (1) magnetic field regime is unexpected. Tests were done with increased negative magnetic field between sweep directions, both 1000 Oe and 10 000 Oe, but the resistance did not change. Hence, both electrodes were fully saturated at ± 100 Oe, as expected from previous studies [1]. The first indication for switching happens at a few Oersteds after crossing the origin in both sweep directions. The sputtered permalloy films were found to have low coercive fields slightly below ± 2 Oe [1], and is thus responsible for the first part of the resistive switching here. The intermediate steps are believed to be caused by partial reorientation of domains in the LSMO, stepwise along the in-plane easy axes. There are a total of twelve easy axes separated by 30° , which can be seen in the Appendix, figures C.2 and C.1. Hallsteinsen et al. [31] found the switching in LSMO to develop gradually along each of the easy axes as the switching field grew from about 10 Oe to 30 Oe along the opposite direction of initial magnetization. This range seems to coincide very well with the range from fully antiparallel to fully parallel states here.

The TER measurements were subsequently done and are seen at the bottom in Figure 7.1. The central inset shows the poling and measuring as deep blue and yellow stripes, respectively. The poling followed the arrows starting from the upper right corner. The MFTJ insets show the tunnel barrier polarization as it is thought to behave. The curve clearly shows a resistive hysteresis behavior of the voltage or electric field. However, it does not seem to be fully saturated at these voltages, so it might be that there is a somewhat larger resistance difference for higher voltages biases.

The TER was calculated according to equation 3.12 as

$$TER = \frac{R_{\text{off}} - R_{\text{on}}}{R_{\text{on}}} = \frac{2540 - 2440}{2440} \approx 4.1 \% . \quad (7.3)$$

7.2 Scripting the Electrical Transport Option

One of the goals in this work has been to investigate how the VersaLab ETO module can be controlled more precisely and advantageous by programming instead of using standard measurement sequences. MultiVu, the core software system of VersaLab, has a built-in Visual Basic interpreter, called WinWrap[®]Basic (WWB). This makes it possible to build much more advanced and versatile measurements by using parameterized quantities, conditional or looping statements, and analyzing data directly when reported to make feedback loops.

A user programmed feedback loop could be used to convert the ETO current source to a voltage controlled current source. This would be ideal for TMR and TER measurements, since the junction characteristics are so dependent on the applied electric field (voltage). To that end, a key question is whether or not it is possible to measure the DC voltage at the voltage probes when a DC current is

sourced through the sample. The ETO hardware utilizes AC lock-in amplifiers to excite the sample with an AC current and detect the AC voltage response by phase lock-in. The AC lock-in principle and measurement data from this technique are presented below. However, the ETO also has a DC current source which superimposes a DC current on the AC signal when doing differential resistance measurements. Hence, it is reasonable to expect the ability to measure the DC voltage from this component too, although there is no sign for this possibility in the ETO documentation.

To this end, initial work has been done in trying to control the ETO's digital signal processor (DSP) by program scripts in WWB. The author has been in contact with Quantum Design (QD), mostly through LOT-QuantumDesign GmbH responsible for QD systems in Europe, to get more information and data spec on how the ETO hardware works. A list of commands that can be read and written to the DSP via CAN-bus from the MultiVu computer was acquired. This has been used to extend the prototype WWB ETO control object that has been released by QD. The object functions that control the ETO module can be found in the Appendix, Listing D.6. An example of write and read functions are shown in Listing 7.1.

Listing 7.1: Example code from the WWB ETO control object ETO.obm

```

'''' Current Drive Controls Start ''''
'''' Main index 0x6110 (ch1) 0x6210 (ch2)
'Set User Requested Frequency
Function Set_Frequency(Channel As Integer, F As Single)
    Dim Address As Long
    Address = &h6010 + Channel*&h100
    SDO.WriteSDO(ETOID, Address, 1, F)
End Function
'Read User Requested Frequency
Function Read_Req_Frequency(Channel As Integer) As Single
    Dim Address As Long
    Address = &h6010 + Channel*&h100
    Read_Req_Frequency = SDO.ReadSDO(ETOID, Address, 1, vbSingle)
End Function
'Read Actual DSP Frequency Returned by Module
Function Read_Frequency(Channel As Integer) As Single
    Dim Address As Long
    Address = &h6010 + Channel*&h100
    Read_Frequency = SDO.ReadSDO(ETOID, Address, 2, vbSingle)
End Function

```

7.2.1 Added Functionality

There are many measurement quantities available that are not reported in the ordinary sequence measurements. Most of those have been implemented in the ETO control object and made available for readout. Examples are sample peak voltage, average power, voltage standard deviation, and additional harmonic in-phase amplitudes (4th to 6th). Moreover, the ETO object can set operation mode of the DSP to control the type of measurement that should be conducted.

The only operation mode prototyped by QD so far is the (differential) resistance mode, however, the IV-mode and four more modes should be available. The IV-mode control functions have not been implemented due to time limitations. The additional operation modes are Oscilloscope, Spectrum Analyzer, van der Pauw, and Critical Current. It is not known whether all these are supported by the ETO module or only apply to other electrical characterization hardware from QD. Still, QD have mentioned in one of their replies that «...I-V and oscilloscope modes have been little tested on ETO. If the user uses the ETO option outside of our specifications, we cannot guarantee any results simply because we have not done much testing in those areas.». This may indicate that it is possible to read the voltage probes continuously as an oscilloscope, but it is not known if it only works for AC lock-in or can be used to determine a DC component as well. In addition, it might not be possible to use the oscilloscope functionality while at the same time apply DC and AC current excitations.

7.2.2 Data File Organization

Program scripts make it very easy and convenient to organize data files. There are two measurement channels that can simultaneously be connected to separate samples for sequential measurements. With sequence controlled measurements, all parameters must be set up manually for each channel, and the data files must be manually administrated with naming and graphic data presentation. In addition, the sequence data files contain measurement data in separate columns for channel one and two, which complicates data analysis later. With WWB data files, both measurement channels can use identical data file schemes, so that reading them in and analyzing data can be done coherently without the need to specify each data column for each channel in the analysis programs. Moreover, filenames, data storage paths, and data file titles can very easily be automated. A standardized data file layout has been made with the inclusion of all additional measurement quantities listed above. This can be found in code lines 73 to 159 of Listing D.5 in the Appendix.

7.2.3 Differential Resistance by Scripting

The prototype differential resistance script provided by QD has been extended and modified to test the additional implemented functionality for this measurement mode. Two pieces of the code used to control the ETO current source can be seen in listings 7.2 and 7.3.

By default, the AC current amplitude can not be set smaller than 10 nA in sequence controlled measurements. With scripting, however, this limitation can be omitted, and the lowest attempted amplitude was 1 pA. This did not work, but it was found that the AC current amplitude is discretized with steps of approximately 1.65 pA. The smallest AC amplitude that could be applied and controlled by the multiplying DAC in the ETO was 6.6 pA for channel one

and 8.26 pA for channel two, about three orders of magnitude lower than the recommended lower limit. As will become clear later, the reasons for testing this is that for very large impedances the current must be low enough in order not to induce a large voltage drop.

One should be very cautious when operating so close to the hardware limit. For example, quantization errors increase in relative size as the amplitude decrease towards the discretization limit. Correspondingly, for the DC current setpoint a discretization step of 3.24 pA was found. It was no problem to control the applied DC current in steps of 5 pA, although the relative error between requested setpoint and actual applied current can be large. For example, a setpoint of 5 pA can not be represented by the DAC, which will give its lowest possible value of 3.24 pA. Thus the relative error is $(5 - 3.24)/5 \cdot 100 = 35.2\%$. Since the AC amplitude usually will be quite much larger this error is not so relevant, but one should still use larger DC current steps if possible.

Listing 7.2: Example code from the WWB dVdI measurement testing script dVdI_all-data.bas

```

'*** USER INPUT NEEDED HERE ***
'Define ETO Params
  Frequency = 1.525879      'Hz. Standard lowest frequencies from QD: IV:
                          0.30517578125 dVdI: 1.52587890625 Resistance: 0.43596540178
  TotalGain = A_1X
  ACAmplitude = 0.000001    'mA
  StartDCCurrent = -0.00001 'mA
  EndDCCurrent = 0.00001   'mA
  I_Stepsize = 0.00000001  'mA
  AveragingTime = 10       'sec: averaging time must be larger than 0.5
                          sec but less than 1 minute
  CurrentRange = A_100nA   'the current range must be large enough for the
                          DC current + the AC current
  SettlingTime = 0.5      'sec

```

Listing 7.3: Code from the WWB dVdI measurement testing script dVdI_all-data.bas, showing the current source initialization and differential resistance measurement.

```

'Initialize Module parameters
  ETO.Turn_Channel_Off(1)
  ETO.Turn_Channel_Off(2)

'Initialize Measurement
  ETO.Set_Frequency(CurrentChannel, Frequency)
  ETO.Set_Ave_Time(CurrentChannel, AveragingTime)
  ETO.Set_I_Range(CurrentChannel, CurrentRange)
  ETO.Set_Total_Gain(CurrentChannel, TotalGain)
  ETO.Set_AC_Current(CurrentChannel, ACAmplitude)
  ETO.Set_DC_Current(CurrentChannel, 0.0)
  ETO.Set_Addtl_Harm(CurrentChannel, 3) '3rd...6th harmonic as 3...6
  ETO.Set_Feedback_Enable(CurrentChannel, 1)
  ETO.Set_Output_Enable(CurrentChannel, 1)
'Ramp to starting current, then initialize a measurement to get settled
  ETO.Set_DC_Current(CurrentChannel, StartDCCurrent)
  Wait(SettlingTime)
  TriggerMeasurement(CurrentChannel) 'Just to "reset" old stuff etc..
  Wait(AveragingTime+0.5)

```

```

'Start measurement
For I = StartDCCurrent To EndDCCurrent Step I_Stepsize
  ETO.Set_DC_Current(CurrentChannel, I)
  Resistance = MeasureResistance(CurrentChannel, SettlingTime,
    AveragingTime)
  MultiVu.GetTemperature(Temperature, Status)
  MultiVu.GetField(Field, Status)
  F.SetValue(TCol, Temperature)
  F.SetValue(ResCol, Resistance)
  F.SetValue(ADCVoltCol, ETO.Read_ADC_Peak_Volts(CurrentChannel))
  F.SetValue(InPhCol, ETO.Read_InPh_Volt(CurrentChannel))
  F.SetValue(QuadrCol, ETO.Read_Quadr_Volt(CurrentChannel))

```

7.2.4 Challenges and Remaining Work

It was not possible to find a DC voltage component from any of the additionally implemented measurement data. One of the interesting available candidates were «sample peak voltage», but this more or less replicated the already known «ADC peak voltage», or «voltage amplitude», as reported by standard ETO sequence measurements. Moreover, by setting either the AC frequency or AC amplitude to zero and only applying a DC current, the measurement did only report corrupted data, meaning that the lock-in did not detect properly or failed. It should be noted here that the possibility of using the reported resistance and known DC current bias in a naive conversion according to Ohm's law, could not be done. There were large differences in the measured resistance from IV-mode and differential resistance mode, indicating a strongly frequency or current sweep-time dependent change of resistance. This will be discussed in more detail below.

Due to time limitations, no real effort could be made to the implementation of IV-mode measurements from WWB scripts. In essence, the problem is that the documentation is too limited. A few setup and read streams dedicated to the IV-mode are described by the CAN-bus command list, however, succeeding in implementing this mode requires time and careful testing. This holds true also for the oscilloscope or other potentially supported measurement modes. Consequently, the IV-mode was controlled with ordinary software- and sequence-initiated measurements as described in section 4.2.9.

The initialization file containing the default measurement frequencies was modified to find the lowest possible frequency that the IV-mode would use. The lowest default frequency is 0.31 Hz, and it was found that the software would not allow frequencies lower than 0.1 Hz. Hence, no truly slow current sweep is supported by default in the IV-mode. One extra frequency of 0.15 Hz (the lowest default frequency divided by two) was added to the initialization file. Tests on both the MFTJs and a calibration resistor did not reveal any noticeable difference between these two sweep frequencies.

7.2.5 ETO Scripting Summary

In sum the ETO can be controlled conveniently by WWB scripting, though currently only for dVdI-mode measurements. Key advantages by scripting over ordinary sequences are the possibility to set up a much more sophisticated measurement scheme, very easy data file handling, and the option of controlling the current source with smaller amplitudes and offsets for prototype high impedance measurements. Experience so far supports useful DC current step sizes down to 10 pA and AC current amplitudes down to 100 pA. However, one must be aware that these are both two orders of magnitude lower than approved specification by QD, so care must be taken when using these parameters in measurements and when analyzing data based on them. Scripting mode has been used exclusively for all dVdI measurements presented below. The initial TMR and TER measurements on sample P51006 presented above were done with ordinary sequence mode dVdI.

7.3 Resistance versus Temperature

To verify that contacts to the bottom electrode LSMO layer had been achieved, standard $R(T)$ measurements were conducted on sample P60212, according to resistance versus temperature described in section 4.2.9. These measurements reveal information both of the contact formation and general temperature and field dependence of resistance in LSMO. The last part is presented first and evaluation of the contacts follow thereafter.

7.3.1 LSMO in-plane Magnetoresistance

Two bottom electrodes centered on opposite sides of the sample were bonded to the I- and I+ pads while the two bottom electrodes within and in line with the current probes were bonded to the corresponding voltage pads. The separation between current contacts on the sample was thus 2.42 mm and voltage contacts 1.42 mm (shortest distance). Each bottom electrode on this sample were rectangular $160\ \mu\text{m} \times 80\ \mu\text{m}$ with the longest side facing the current direction (see *proper* sample ch.2 in fig. 4.8). $R(T)$ was measured both in zero magnetic field (ZF) and with the maximum field (3 T) applied.

The results are plotted in Figure 7.2. The temperature sweep was done with $3\ \text{K min}^{-1}$ and there is a clear difference between the curves recorded while cooling and while heating. The difference is likely due to a temperature lag between the reported system temperature and the actual sample temperature. This is particularly easy to see by considering the measured data close to 390 K. The cooling curves have a clear change of curvature over the first 10 K to 20 K while the heating curves have an unchanging curvature in the same region. Another measurement was done when heating in zero field after the sample had been field-cooled in maximum field to order the magnetic dipoles. Interestingly, this curve

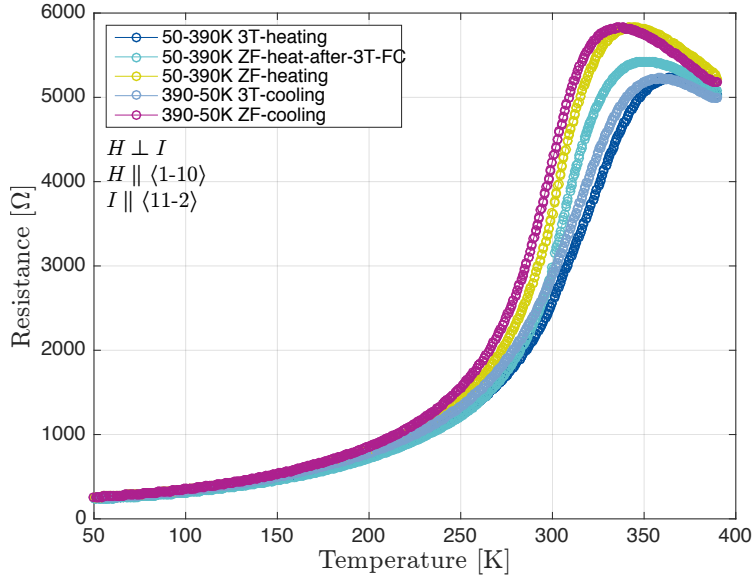


Figure 7.2: $R_{\text{LSMO}}(T)$ for sample P60212. 4-wire longitudinal bottom electrode resistance measurement. Voltage probe spacing 1.42 mm, current probe spacing 2.42 mm.

shows the lowest resistance in low temperatures, even lower than the field-cooled and field-heated curves. For higher temperatures it lies about midway between the other curves, although closer to the curves measured with a magnetic field present. This indicates that a remanent magnetization is present throughout the temperature sweep, and stable at first before decreasing more rapidly when approaching and going past room temperature. The difference at low temperatures may be due to the diamagnetic contribution from the substrate that opposes the saturation magnetization in the LSMO when a large field is continuously present. The shape of the curves are characteristic for LSMO. It resembles both the metal to insulator transition and colossal magnetoresistance (CMR) that LSMO is known for [125, 126].

To remove most of the temperature lag in the measured data, the cooling and heating curves were averaged at each temperature. With an averaged $R(T)$ curve each for zero and maximum magnetic field, the CMR was calculated similarly to TMR (eq. 3.11, and GMR) as defined by Julliere [8],

$$\text{CMR} = \frac{R(T, H = 0) - R(T, H = 30 \text{ kOe})}{R(T, H = 0)}, \quad (7.4)$$

and expressed in percent. The result can be seen in Figure 7.3 and corresponds very well with the CMR found by Raa [112] when doing van der Pauw measurements. The magnetoresistance peaks at about 320 K with a maximum of 32.5%.

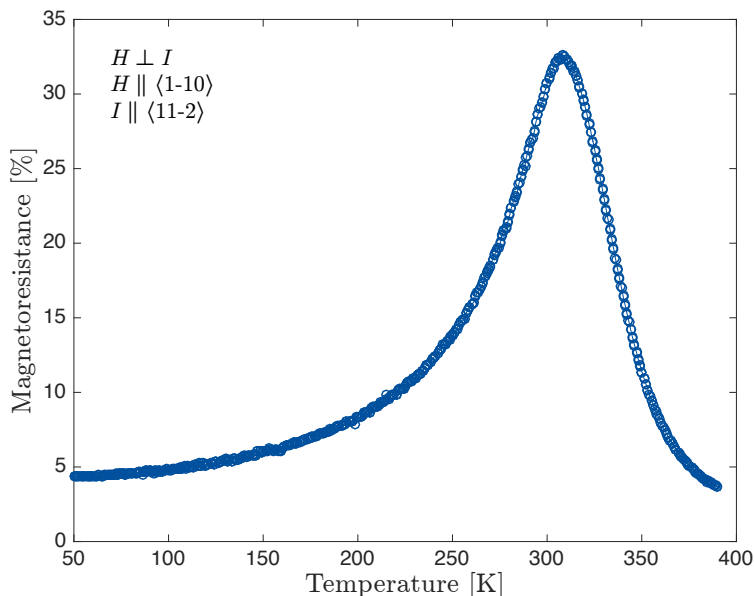


Figure 7.3: Magnetoresistance versus temperature for sample P60212. Heating and cooling curves from fig. 7.2 have been averaged to calculate the magnetoresistance.

It should be noted that no attempt was done to calculate the LSMO resistivity from these data. The current and voltage probes are in line and well defined on the sample, however, they also penetrate the LSMO film and are very large compared to point contacts that are necessary for four-point collinear probes (sec. 4.2.10) or van der Pauw measurements [127, 128].

7.3.2 Assessing the Pt/LSMO Contact Resistance

Apparently the bottom electrode contacts were working fine, but how large are the contact resistances? To partially answer that question, the voltage leads were shorted directly to the current pads on the PCB (*improper* 4-wire, fig. 4.8). Due to an unknown error with the VersaLab system, only the zero field measurements could be finished.¹ Thus, only the ZF resistance curves can be compared.

The plots of the proper and improper 4-wire measurements and the difference between them (measured difference) as functions of temperature are shown in Figure 7.4. The measured difference is large, and at low temperatures the proper curve value is only about 8% of the improper. One must keep in mind that some resistance increase is expected for the improper measurement. Since the cur-

¹During field-cooling at 3 T the temperature of the superconducting magnet increased to a value too high, and the magnet quenched. The error always occurred when cooling at slow rate and is still not fully resolved.

rent probes are further apart than the voltage probes, more of the LSMO sheet resistance is now included in the measurement. If only the length of the current path is considered, the LSMO resistance part of the improper measurement should be $2.42 \text{ mm}/1.42 \text{ mm} \approx 1.7$ times larger than for the proper measurement. This increase has been added to the values of the proper curve and re-plotted ($R_{V-V+, \text{proper}}$ adjusted), and the difference between the improper and adjusted measurements (adjusted difference) has been plotted accordingly. The adjusted difference is a better approximation to the contact resistance, but it can not be taken as a specific contact resistance still.

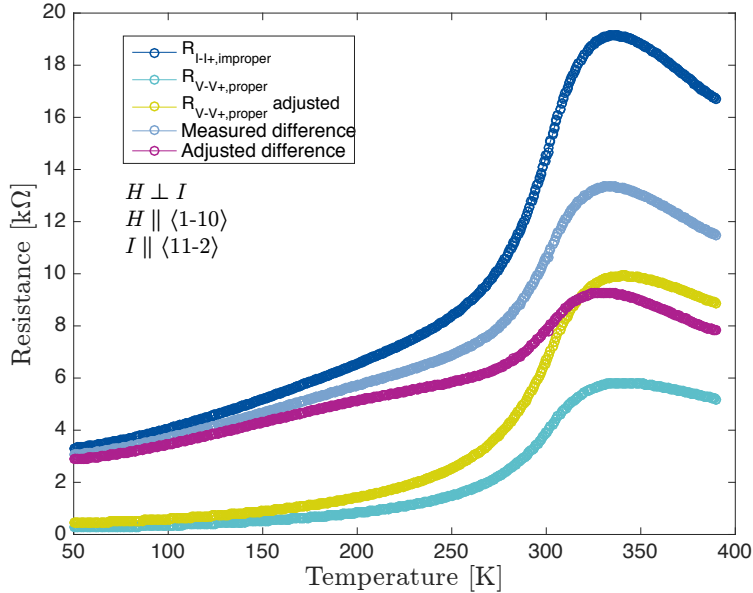


Figure 7.4: $R_{\text{LSMO}}(T)$ in zero magnetic field for sample P60212 with and without contact resistances. 4-wire longitudinal bottom electrode resistance measurement with ($R_{I-I+, \text{improper}}$) and without ($R_{V-V+, \text{proper}}$) voltage probes shorted to current pads. Voltage probe spacing 1.42 mm, current probe spacing 2.42 mm. The average of heating and cooling curves are plotted. $R_{V-V+, \text{proper}}$ adjusted has been multiplied by 1.7 to account for a longer current path in the improper measurement.

The relative difference between the measurements are plotted in the Appendix, Figure A.1, by use of the same relation as for CMR above. The adjusted difference accounts for about 87% of the total resistance at 50 K, decreases monotonically to about room temperature, before it flattens out towards 47% when temperatures approach 400 K. The shape of the difference curves (fig. 7.4) indicate that the contact resistance is much less temperature dependent than the LSMO sheet resistance. Yet, some temperature dependency of the contact resistance is clearly present, as the adjusted difference is increasing with a more or

less constant rate from low temperatures to about 275 K. In the upper temperature range the temperature dependency is more similar to LSMO, but not as prominent.

An IV-curve measurement was done in the proper 4-wire setup at room temperature before the measurements shown above were conducted (fig. 7.2). The plot was perfectly straight and gave a resistance between the voltage probes of $3.53 \text{ k}\Omega$, which was also found by an AC resistance measurement performed at the same time. So the voltage probe contacts were apparently ohmic. Unfortunately, such tests were not done in the improper 4-wire setup. Since these data were not available, the second and third harmonics from the above measurements have been plotted instead in Figure 7.5. Never mind the discontinuities. Those are caused by the automatic range selection of the ETO that changes the preamplifier settings to accommodate varying signal amplitudes during a measurement. The

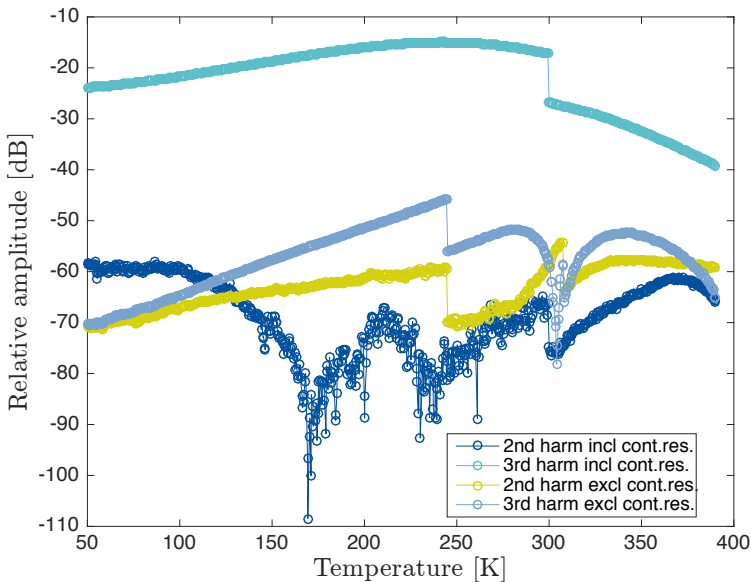


Figure 7.5: 2nd and 3rd harmonics for sample P60212 with and without contact resistances. 4-wire longitudinal bottom electrode resistance measurement with and without voltage probes shorted to current pads. Voltage probe spacing 1.42 mm, current probe spacing 2.42 mm. The harmonics for the heating curves are plotted.

harmonic contributions from the proper 4-wire measurement excluding contact resistances are almost always below -50 dB , indicating a good measurement [106]. This is also true for the second harmonic of the improper measurement, however, the third harmonic contribution is very large, indicating a nonlinearity in the sample under measurement.

Since the key difference between the two measurements is that the latter

includes the contact resistances, this result indicate non-ohmic contacts. The nonlinearity was not seen by the voltage probes in the proper measurement. This is a sign that the contacts are sufficiently leaky, according to the description in Chapter 5, to remain unnoticed for very small currents that are typically negligible for the voltage probes. On the contrary, nonlinear voltages develop over the contacts when the current amplitudes are larger and changing more rapidly, as is the case for the current sourcing probes.

The bottom electrode contacts thus indicate some nonlinearity, but the problem should not interfere with the reported values as long as proper 4-wire measurements are done. The ETO current source employs feedback to mimic an ideal current source, so there is no reason to believe that the sourced current deviates from the reported values. Hence, though nonlinear voltages develop over the current probe contacts due to varying current amplitudes, the reported current indeed flows through the device under test giving rise to whatever voltage the device accommodates. Hence, voltage probes with a proper connection will report what is close to the true device voltage.

7.3.3 Evaluation of Contact Layout and Interface Area

The device design made for sample P60212 was not a true 4-wire design, since both the bottom and top contact pads were interconnected through the top aluminium layer (see e.g. fig. B.3, similar for bottom contact pads). Hence, the design was changed to the one presented in Chapter 5 for the later fabricated samples.

The bottom electrodes of sample P60212 were rectangular with a total interface area towards the LSMO film of $2(160 + 80)\mu\text{m} \cdot 0.01\mu\text{m} = 4.8\mu\text{m}^2$. The new bottom contacts were circular with an inner diameter of $334\mu\text{m}$, giving a total interface area towards LSMO as $\pi \cdot 334\mu\text{m} \cdot 0.01\mu\text{m} \approx 10.5\mu\text{m}^2$. A more than doubled contact interface area should reduce the problems indicated above dramatically. However, the voltage probe pads were designed with contacts of diameter $20\mu\text{m}$. They were made small in order not to interfere notably with the otherwise uniform bottom electrode LSMO layer. Hence, the voltage probes' interface area is $\pi \cdot 20\mu\text{m} \cdot 0.01\mu\text{m} \approx 0.63\mu\text{m}^2$, which may be too small to function without nonlinearities. This has not been tested thoroughly due to time limitations. Still, simple tests with a multimeter at room temperature revealed polarity dependent resistances between the I- and V- pads that were very large, on the order of $0.5\text{M}\Omega$. For sample P60501 the resistance as measured with positive polarity from I- to V- was $359\text{k}\Omega$, while the opposite polarity gave $490\text{k}\Omega$. For sample P60403 the same resistances were found to be $35.8\text{k}\Omega$ and $36.2\text{k}\Omega$, additionally illustrating highly uncertain contact formation results.

7.4 Current-Voltage Measurements

It was mentioned above that WWB scripting of IV-mode measurements could not be implemented within the time-frame of this thesis, but IV measurements have been conducted with the ordinary sequence-mode method. All measurements presented here were performed at 50 K. There were additional tests done at room temperature and a few at 400 K, but those are not considered relevant here. Due to time limitations, only one MFTJ from each of the samples P60403 and P60501 have been measured. These are the 15 μm MFTJs number 21 on P60403 and 8 on P60501. As a result of the large contact resistances found in sample P60501, the bottom electrode (I-) from the nearby junction 7 was used to source current while the bottom electrode (I-) of junction 8 was used as negative voltage probe (V-). Thus, the contact resistance of the bottom electrode is included in the measurements for P60501 below.

The ETO's lowest supported current excitation amplitude in sequence mode is 10 nA, and plots of measurements with this excitation are shown in Figure 7.6. The capacitive signature that was found and discussed in the autumn project [1] is immediately present as the open loops around the origin. P60403 has a 3 nm

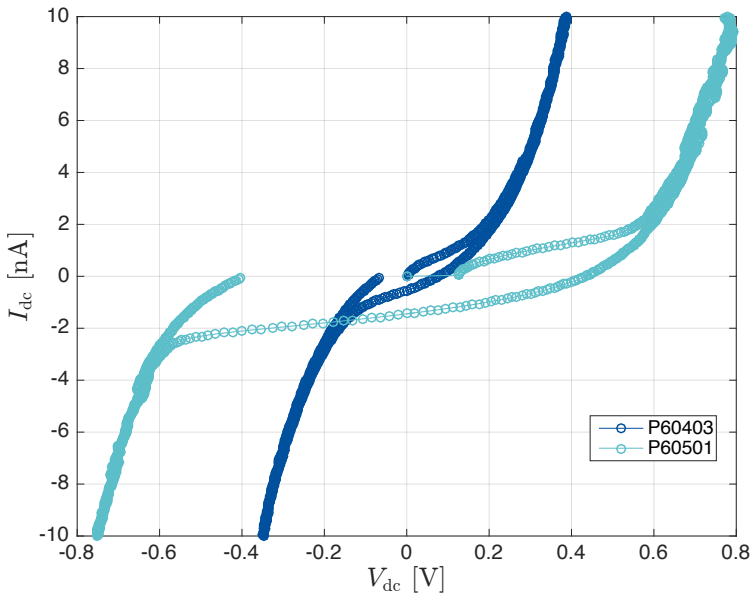


Figure 7.6: IV-curves for samples P60403 and P60501 for current excitation $I_{\text{dc}} = \pm 10$ nA. Triangular current ramp from zero to positive max to negative max to zero.

and P60501 a 5 nm BTO barrier thickness. The expected difference in tunneling resistance is clearly seen with P60501 having a threshold voltage of about ± 0.6 V, where it enters a more conductive state. The corresponding threshold voltage for

P60403 is around ± 0.2 V.

It is evident from the curves that even for the lowest supported current amplitude, substantial voltages develop across the junctions due to large tunneling resistances. For this reason, the investigation on how small currents the ETO module can be forced to source by scripting was initiated. It is well established that especially TMR [19], but also to a certain degree TER [62], is highly dependent on applied voltage over the tunnel junction. Thus ideally, the readout voltage should be in the range 10 mV to 100 mV, and stable, while doing TMR and TER measurements. As the results for 10 nA current excitation clearly show, this is impossible for the largest MFTJs here. The smaller MFTJs have not been tested, but they are expected to show increasing tunneling resistance as the junction size decrease.

IV sweeps for increasing current amplitudes were done carefully to find the current levels where the junction voltages approach typical ferroelectric switching voltages. Figure A.2 in the Appendix show IV-curves from excitation with 200 nA amplitude, and Figure 7.7 below shows the result for 40 μ A (P60403) and 50 μ A (P60501) amplitudes. The inset shows a magnified view of the box indicated, with the arrows depicting the sweep direction. This feature was seen in most IV-curves, but not for a specific range of voltages. It may be an indication

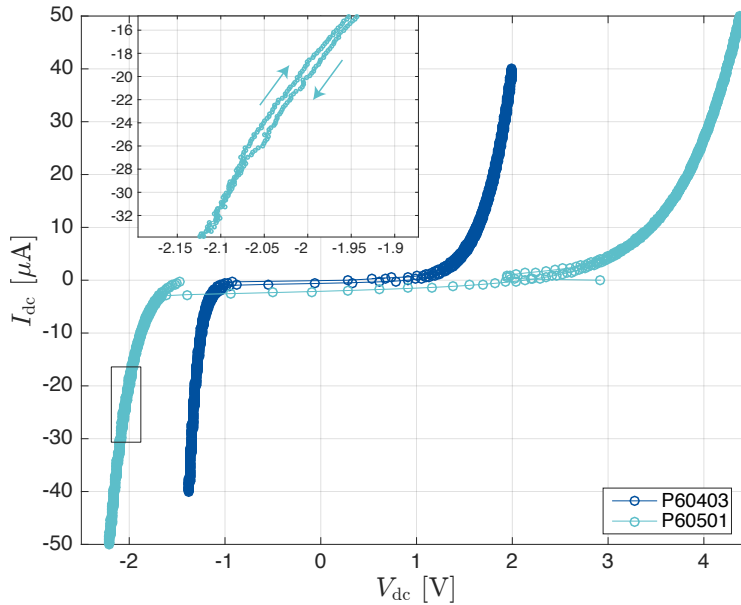


Figure 7.7: IV-curves for samples P60403 and P60501 for current excitation $I_{dc} = \pm 50 \mu\text{A}$. Triangular current ramp from zero to positive max to negative max to zero.

for stepwise ferroelectric nucleation and domain reorientation [62, 87], but it

might also be noise or other errors in the measurement. Similar signatures are visible at much lower voltages (and currents) in Figure 7.6 above, for example. There is clearly no large and distinct voltage discontinuity occurring for any current level, that can indicate ferroelectric switching. Moreover, no clear high and low resistance IV-paths are seen. The separation around the origin is due to capacitance as noted above, clearly seen as the voltage changes polarity many measurement points later than the current in both sweep directions.

Another feature of the IV-curves is that they are asymmetric. This is most easily seen for the large current amplitudes (fig. 7.7), but it can be seen also for the lowest amplitude (fig. 7.6). A plausible explanation is that the electrode materials are different, for the samples shown here permalloy on the positive bias side and LSMO on the negative. The effective energy barrier height is apparently larger for electrons tunneling from LSMO towards permalloy (positive bias) and smaller for electrons tunneling from permalloy towards LSMO (negative bias). Since there are no definite signs of ferroelectric switching, the barrier heights between BTO and the respective electrode materials is believed to be the major cause of the asymmetry.

Larger current amplitudes were also tested, up to the point that voltages both in the positive and negative regions were about ± 4 V, but they revealed nothing new or interesting features. The capacitive splitting of curves around the origin is present in all curves, but mostly notable for small current excitations where it dominates. It has been tested that this issue grows with increasing sweep rate. All IV-curves shown here were measured with a cycle frequency of approximately 0.15 Hz, meaning one complete cycle of the current sweep was finished in 6.67 s. The sweep function is automated in the ETO DSP with a fixed amount of measurement points, so for larger amplitudes the change of current between subsequent data points and the rate of change in time are larger. However, since the junction resistance drops dramatically with increasing bias, the total circuit time constant decreases rapidly. Consequently the capacitive signature is only noticed at small current amplitudes, or when the sweep rate is increased for a constant current amplitude. As noted earlier, it was not possible to implement a slower version of the current sweep within the time-frame of this work.

Finally, it is noted that the IV-curves have been plotted with linear current axes here, because single measurements for the entire current range with appropriate current step resolution could not be done. Hence, each IV-curve contains very few points at low current amplitude where the resistance is largest. Additionally, the capacitance alters the representation, so semi-logarithmic plots did not work well. However, the qualitative shape of the semi-logarithmic curves correspond well with DT and FNT at junction voltages below and above about ± 0.5 V, respectively.

7.4.1 Numerical Derivatives of IV-curves

Numerical derivatives of the current and voltage data from the IV measurements was done to assess the differential resistance and conductance as functions of junction bias. Results from current sweeps with the smallest amplitude on sample P60501 are plotted in Figure 7.8. Only the middle part of the sweeps is plotted, from ± 10 nA to ∓ 10 nA, due to the discontinuity at the beginning and end of each sweep.

Firstly, the resistances are huge, several hundreds of mega-ohms in the low-bias regime, and decrease rapidly when the junction bias builds up. Secondly, this scale of resistances result in a large circuit time constant which requires a very low sweep rate if true DC characteristics are to be found. Seen here is the capacitive voltage lag that gives rise to shifted differential curves relative to the origin. The flattest parts of the IV-curves where they change curvature are recognized by the maximum (minimum) differential resistance (conductance) points (see fig 7.6 for positive to negative sweep). Thus, for a sufficiently slow current sweep, the two shifted curves plotted here would be expected to meet approximately at the center, possibly shifted a few tens to hundreds of millivolts to one of the sides [85]. Moreover, the IV-curve would go through the origin. In the appendix, Figure A.3, corresponding plots of the data from Figure 7.6 can be seen as well, though only for one sweep direction.

The larger current amplitudes presented in Figure 7.7 above are correspondingly converted to differential data in Figure 7.9. A logarithmic y-axis have been used for both differential resistance and conductance to represent the data more informally. Only positive to negative sweep directions were done at these current levels. Due to the inherent asymmetry of the junctions discussed and seen in the plots above, the asymmetry caused by the capacitive lag is much less dominating here, although some degree of capacitive shift around the origin is expected here too.

There are two main characteristics with the large amplitude plots compared to the small amplitude plots. Firstly, the differential resistance (conductance) is much smaller (larger). The maximum resistance is here reported to be about $2\text{ M}\Omega$ as compared to about $660\text{ M}\Omega$ for the low amplitude sweep. This difference lies in the fact that the charge buildup on the junction is much more rapid in the large amplitude sweep, since the current is ramped at a much higher rate. Hence a large voltage builds up more quickly and decreases the tunnel barrier so that the seen junction conductivity increases fast. Secondly, the tunneling resistance (conductance) decreases (increases) very rapidly outside the low-bias regime, and especially for the negative bias. It is not seen here, but for P60403 the resistance is down at about $1\text{ k}\Omega$ for -2 V . For positive bias, $1\text{ k}\Omega$ is achieved just above 3 V . For sample P60501, higher current amplitudes than shown here were not tested.

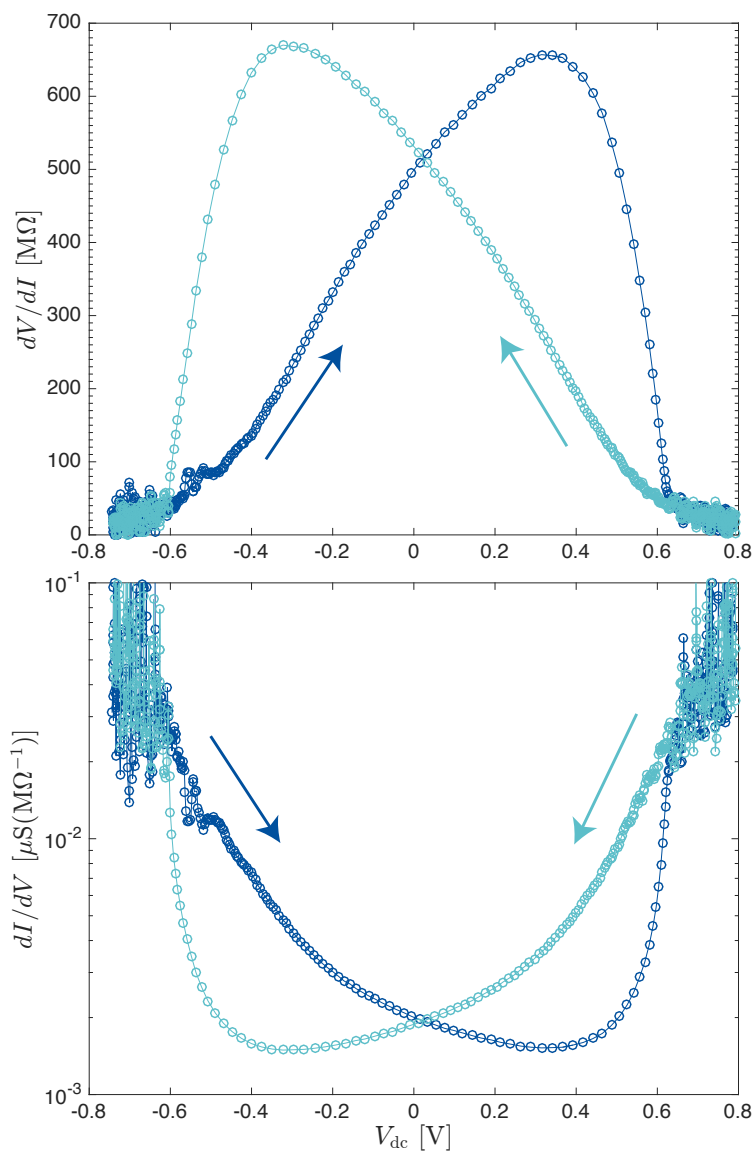


Figure 7.8: Differential resistance (upper) and conductance (lower) versus V_{dc} for sample P60501. The current sweep is here shown for both sweep directions between ± 10 nA (arrows along the sweep direction).

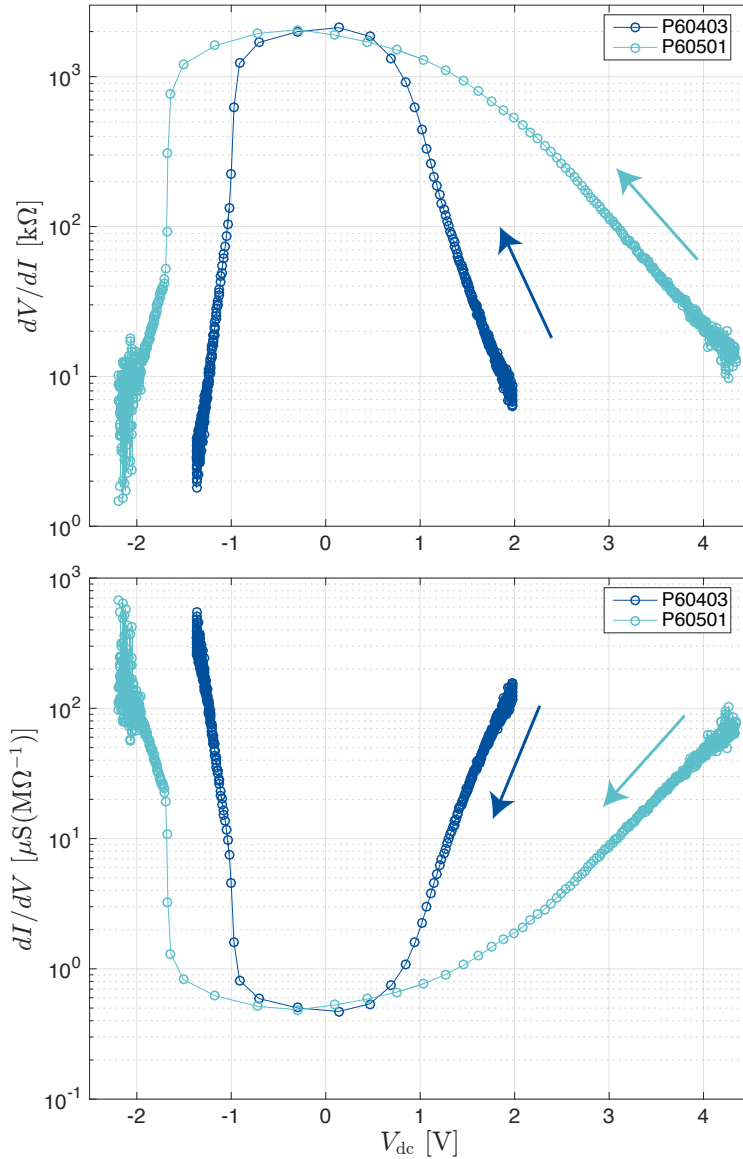


Figure 7.9: Differential resistance (upper) and conductance (lower) versus V_{dc} for samples P60403 and P60501. Both plots are based on the continuous current sweeps from $+50\ \mu\text{A}$ to $-50\ \mu\text{A}$ shown in fig. 7.7 (arrows along the sweep direction).

7.5 Differential Resistance versus DC Current

The dVdI-mode controlled by scripting was used to measure the AC differential resistance versus DC current. Due to very large tunneling resistances for low

biases and highly nonlinear IV-curves already for the lowest supported current amplitude, measurements with smaller AC amplitudes than normally accepted was tested. There are probably good reasons, some of which were pointed out above, not to go below the recommended limit. It was done anyway, and the validity of the data will be discussed later.

It was decided not to apply AC amplitudes smaller than 100 pA due to rapidly growing quantization errors with the DACs and ADCs in addition to a decreasing dynamic range in representing a sinusoidal waveform at these levels. In Figure 7.10 two measurements for each of the samples P60403 and P60501 are shown, one of which was measured with the standard lowest amplitude of 10 nA. The other two were done with 100 pA and 1 nA for P60403 and P60501, respectively. The resistances as reported by the ETO are shown. There are some very inter-

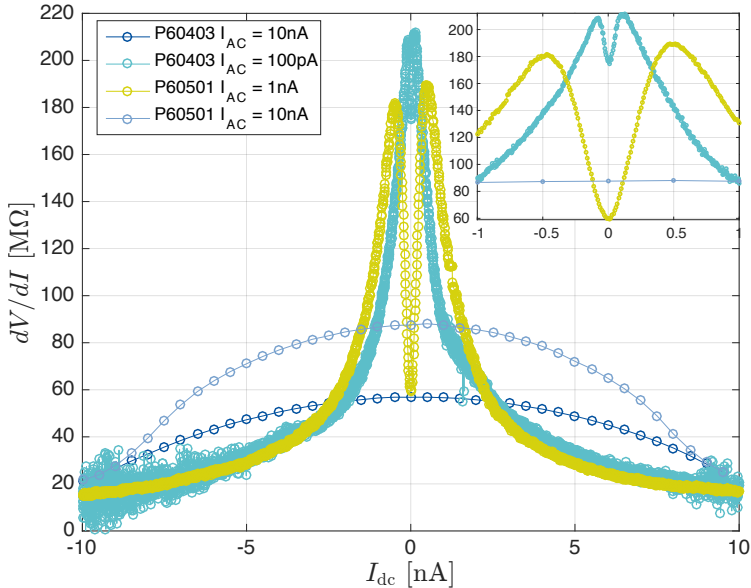


Figure 7.10: Measured dV/dI versus I_{dc} for samples P60403 and P60501. Comparison of different AC amplitudes. Inset shows more details from the very low current regime. AC frequency 1.52 Hz.

esting features seen by the small amplitude measurements that are completely washed out by the standard amplitude measurements. They are somewhat similar to the shifted curves of the numerical derivatives above, with reference to the DC current instead of voltage. Another thing to note is that the observed resistances are inversely proportional to the AC current amplitude, which was also seen for the numerical derivative resistances above. This was generally observed for higher AC amplitudes as well, where the reported resistance dropped dramatically. Tests with increased AC frequency revealed the same phenomenon

while the phase angle increased towards a purely capacitive impedance. This can be understood by evaluating the junction impedance (eq. 5.2). For larger frequencies, the real part (resistance) should go down and the imaginary part (reactive, capacitance) should go up. Moreover, as have been noted a few times, when the AC amplitude is larger more of the nonlinear IV-curve is continuously cycled. This leads to a more rapidly changing junction voltage, a lower average energy barrier, and a correspondingly lower tunneling resistance.

The differential resistance versus DC current data taken with varying AC amplitudes were converted to differential conductance versus DC voltage for comparison with the numerical derivatives of the IV-curves. The resulting data can be seen in Figure 7.11. When comparing with the numerical derivatives of the

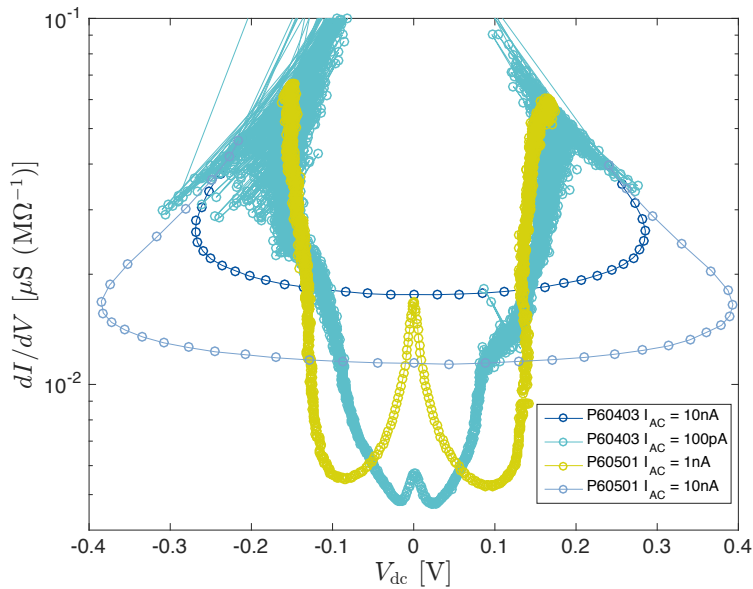


Figure 7.11: Converted dI/dV versus V_{dc} for samples P60403 and P60501 based on dV/dI data shown in Figure 7.10. AC frequency 1.52 Hz.

IV-curves, the difference is clear. The converted voltages are much smaller than the reported voltages from the IV-curves at similar conductance levels. Furthermore, there are both high and low conductance levels for the same apparent DC voltages. Thus, something is not right with this method, and it is believed that the AC resistance reported by the differential resistance measurement mode is not a good approximation to the DC resistance. For this reason, it was not possible to use the reported resistance for a continuous conversion of DC current to DC voltage while measuring, in order to implement a feedback loop for controlling the junction voltage this way.

It is important to appreciate how the $dVdI$ -mode measurements presented in

figures 7.10 and 7.11 behave. Consider the center measurement where $I_{dc} = 0$. For the 10 nA amplitude the current is continuously cycled over the entire range of DC current offsets seen in the plot, alternatively through the complete IV-curves seen in Figure 7.6. Consequently, the measurement is an effective average of the nonlinear DC resistance within the same current range. As the DC current offset is increased, the measurement will eventually span double the current range seen in the figure (e.g. -20 nA to 0 nA for $I_{dc} = -10$ nA). With the lower current amplitudes of 1 nA and 100 pA, the range of averaging for each DC offset is ten or hundred times smaller, respectively. Therefore, those measurements are reporting the nonlinear parts of the range in more detail than the blunt, relatively speaking, large amplitude of 10 nA. Nevertheless, the ETO is not approved for so small amplitudes, so the reported resistances may not be correct. Particularly the peculiar shifted resistance maximas relative to zero offset are suspicious.

A comparison with the data for phase-angle and in-phase second and third harmonic amplitudes, reveals strong similarities. The second harmonic curve is closely resembling the resistance curves while the third harmonic peaks at the center for $I_{dc} = 0$. This can be understood in terms of the shape of the IV-curve. If both positive and negative currents (voltages) are considered, it has a typical x^{odd} signature while if only one of the sides, either positive or negative, is considered, it shows a x^{even} signature. Thus, for the dVdI-mode with a DC offset and superimposed sinusoidal AC signal, the second or third harmonic contributions will vary with the DC offset. It is not known how the ETO DSP is calculating the reported resistance, but it seems there might be some corruption in the way it is done for the smallest prototype amplitude measurements made here. In the following section an alternative solution is presented to elucidate this possibility further.

7.5.1 Taking Advantage of AC Lock-in Data

The ETO module uses an AC lock-in technique [106] to excite the sample with a sinusoidal current at a reference frequency, and the voltage signal received at the voltage probes is multiplied with the reference signal by two separate lock-in amplifiers. One of the lock-ins is multiplied *in-phase* with the reference, and the other 90° out of phase, or in *quadrature* with the reference [108]. Now, this gives the ability to measure the real and imaginary contributions to an impedance directly, as will be shown next.

Consider the sinusoidal current from the ETO module, $I(t) = I_0 \cos(\omega t)$. This is the reference signal of which the phase angle is set to zero for convenience. The measured voltage signal is denoted $V(t) = V_0 \cos(\omega t + \phi)$, where ϕ is the phase relative to the reference signal (only the fundamental frequency is considered). Through a trigonometric relation, the voltage can be expanded into two terms

that are 90° out of phase,

$$\begin{aligned} V_0 \cos(\omega t + \phi) &= V_0(\cos \omega t \cos \phi - \sin \omega t \sin \phi) \\ &= V_0 \cos \phi \cos \omega t + V_0 \sin \phi \cos \left(\omega t + \frac{\pi}{2} \right) . \end{aligned} \quad (7.5)$$

The two out-of-phase components now have coefficients that are given by the voltage amplitude V_0 and the phase difference relative to the current reference. These are

$$X = V_0 \cos \phi \quad Y = V_0 \sin \phi , \quad (7.6)$$

where X is the *in-phase* and Y the *quadrature* component, respectively [108]. The voltage amplitude is the signal peak amplitude which can be measured without any knowledge of the phase relationship, as

$$V_0 = \sqrt{X^2 + Y^2} = \sqrt{V_0^2(\cos^2 \phi + \sin^2 \phi)} , \quad (7.7)$$

where the phase is removed. So the voltage amplitude V_0 is a vector entity relative to the reference signal, with in-phase and quadrature components X and Y . The phase angle is found as usual by

$$\phi = \arctan(Y/X) . \quad (7.8)$$

Details on how the lock-in amplifiers work and detect these components are not relevant here, and interested readers may consult reference [108] as a start. Most importantly, the ETO module reports all these quantities in addition to the calculated resistance. Moreover, the 2nd and 3rd harmonic in-phase magnitudes are reported. Thus, one can make use of these data to perform more specific analysis of the sample impedance.

In Chapter 5 the complete circuit diagram was laid out and the tunnel junction impedance derived. Now, any impedance can in general be evaluated by its real and imaginary parts, i.e

$$Z = A + iB . \quad (7.9)$$

The in-phase and quadrature components of the measured signal can be used to say something about the real and imaginary parts of the impedance. Using complex notation for convenience, the applied current and resulting voltage response are

$$\begin{aligned} I(t) &= I_0 e^{i\omega t} = I_0(\cos \omega t + i \sin \omega t) \\ V(t) &= V_0 e^{i(\omega t + \phi)} = V_0(\cos(\omega t + \phi) + i \sin(\omega t + \phi)) . \end{aligned} \quad (7.10)$$

The measured impedance is thus

$$Z = \frac{V_0 e^{i(\omega t + \phi)}}{I_0 e^{i\omega t}} = \frac{V_0}{I_0} e^{i(\omega t + \phi - \omega t)} = \frac{V_0}{I_0} e^{i\phi} , \quad (7.11)$$

with real and imaginary parts

$$\Re\{Z\} = \frac{V_0}{I_0} \cos \phi = \frac{X}{I_0} = A, \quad \Im\{Z\} = \frac{V_0}{I_0} \sin \phi = \frac{Y}{I_0} = B. \quad (7.12)$$

The current amplitude is known and the voltage components are measured, so the real and imaginary parts of the impedance are thus found. By knowing what the sample circuit looks like, the values of different circuit components can be calculated from the measurement data.

Consider the complete circuit diagram presented in Chapter 5 (fig. 5.6). The following calculations assume that the bottom electrode contacts are ohmic, and that the resistances of top and bottom electrode contacts are negligible. Hence, the circuit reduces to a simple system of contact pad capacitances in parallel with the tunnel junction. In addition, the ETO module wiring capacitance is included also in parallel. Effectively this gives the circuit time constant as presented in equation 5.6, with a total capacitance

$$C_{\text{tot}} = C_{\text{ETO}} + C_{\text{I+,V+}} + C_t. \quad (7.13)$$

The total circuit resistance is simply the tunnel resistance

$$R_{\text{tot}} = R_t, \quad (7.14)$$

and for convenience the total resistance and capacitance are just referred to as R, C in the calculations below. As a result, the total circuit impedance is on the same form as the junction impedance presented in equations 5.1 and 5.2, only with the total resistance and capacitance substituted for their respective junction equivalents. Thus, the real and imaginary parts of the total circuit impedance are on the form (eq. 5.2)

$$\Re\{Z_{\text{tot}}\} = \frac{R}{1 + (\omega RC)^2}, \quad \Im\{Z_{\text{tot}}\} = \frac{-\omega R^2 C}{1 + (\omega RC)^2}. \quad (7.15)$$

Comparing equations 7.15 and 7.12, we get two equations with two unknowns

$$\frac{R}{1 + (\omega RC)^2} = A, \quad \text{in-phase real parts} \quad (7.16)$$

$$\frac{-\omega R^2 C}{1 + (\omega RC)^2} = B, \quad \text{quadrature imaginary parts} \quad (7.17)$$

These can be used to find useful expressions for the resistance and capacitance. The calculations can be found in the Appendix. The resulting resistance and capacitance expressions (eqs. A.2, A.3) can now be further simplified to all known measurement parameters by using equation 7.12. Thus

$$\boxed{R_{\text{tot}} = \frac{X^2 + Y^2}{I_0 X}, \quad C_{\text{tot}} = \frac{I_0 |Y|}{\omega (X^2 + Y^2)}} \quad (7.18)$$

where the positive and negative solutions to the capacitance have been reduced to the absolute value of Y , since capacitance is a physical entity which is not meaningful if negative.

The in-phase and quadrature voltage amplitudes have been used to calculate the resistance and capacitance with the relations from equation 7.18. These are presented in Figures 7.12 and 7.13, respectively. The measurement data used for these representations are the same that were used to plot the measured differential resistance in Figure 7.10 and converted differential conductance in Figure 7.11.

There are a few interesting things to note with this method, and Figure 7.12 is considered first. Note that the resulting resistance from the standard amplitude measurements (10 nA) is more or less equivalent when using the analytical circuit model method here, as compared to the automated ETO dVdI mode method plotted earlier. For the prototype measurements with lower current amplitudes,

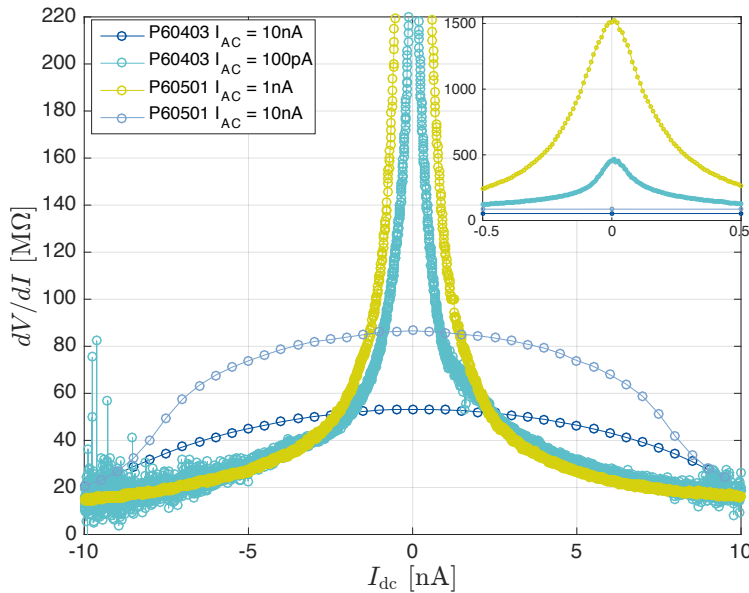


Figure 7.12: dV/dI versus I_{dc} for samples P60403 and P60501 based on in-phase and quadrature voltage data. AC frequency 1.52 Hz.

however, the difference is striking. Here the resulting resistances increase dramatically for DC current offsets less than ± 2 nA, and the trend is much more sensible with P60501 having a relatively much larger resistance than P60403. This corresponds well with the IV-curves for 10 nA sweep amplitude (fig. 7.6), where the high resistance regime is found between about ± 2 nA. Still, the question is whether the calculated resistances here are trustworthy or not. They are indeed much larger than the numerical derivate differential resistances (fig. 7.8), but as has been pointed out already, the numerical derivate curves are expected

to show larger resistances for lower current amplitude or much slower sweeps.

The circuit capacitance was calculated as well, and the resulting data are plotted in Figure 7.13. Due to very much noise in the data for the small current amplitude measurements, only the ordinary 10 nA amplitude measurements are shown here. First of all it is interesting to have the possibility to evaluate

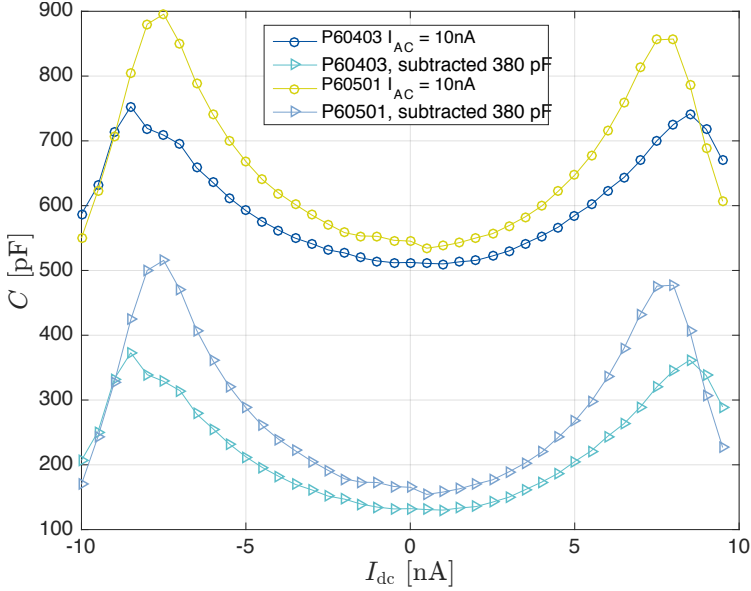


Figure 7.13: Capacitance versus I_{dc} for samples P60403 and P60501 based on in-phase and quadrature voltage data. 380 pF has been subtracted from both curves and replotted to remove the assumed magnitude of external circuit plus bond pads capacitance. AC frequency 1.52 Hz.

the MFTJ circuit capacitance in this way. Secondly, the curves show some peculiar features with peak capacitance values shifted both ways relative to the origin. Similar observations have been pointed out by Dawber et al. [87] to occur in metal-semiconductor-metal punch-through diodes, and they emphasize that these characteristics are very similar in metal-ferroelectric-metal systems [87]. This might have been the reason why the automated ETO dVdI-measurement reported similar shifts in the resistance for the prototype amplitude measurements (fig. 7.10). To better represent the junction capacitance, both curves were subtracted 380 pF which is the approximate sum of the contact pads' capacitance and ETO wiring capacitance (see eq. 7.13 and calculations ch. 5). At zero offset the capacitances are about 130 pF and 170 pF for P60403 ($d_{BTO} = 3$ nm) and P60501 ($d_{BTO} = 5$ nm), respectively. This converts to the relative permittivities

$$\text{P60501: } C \approx 170 \text{ pF} \rightarrow \epsilon \approx 543, \quad \text{P60403: } C \approx 130 \text{ pF} \rightarrow \epsilon \approx 249.$$

P60403 shows a smaller capacitance than P60501 which is opposite to what one would expect from the thickness of the insulating layer. However, since quantum mechanical tunneling is so profoundly dominating the characteristics of these capacitors, it is probably unreasonable to expect ordinary capacitor behavior. Interestingly though, the measured capacitances are not very far from the initial guesses calculated in Chapter 5. There, the BTO relative permittivity was set to 300, which seems to be a little too pessimistic for the thickest films.

On a final note, the capacitances for the small amplitude measurements were much smaller than those plotted in Figure 7.13, but the noise was dramatic. The same problem is seen for resistance at the largest DC offsets. The noise is due to a too low preamplifier setting, since the voltages were relatively small compared to the preamplifier range used. A smaller capacitance is though expected, since the measurement approaches a DC measurement with decreasing AC amplitude.

7.6 TMR and TER Measurements

TMR measurements versus DC current offset for the newly fabricated samples were scripted in WWB. These were performed by cycling the magnetic field in steps of 1 Oe from +100 Oe to -100 Oe and back while measuring the resistance at each magnetic field value. The AC amplitude was 10 nA during these combined dVdI and TMR measurements. DC current offsets from -100 nA to +100 nA with 10 nA steps were conducted. There were no signs of magnetoresistance for any DC level, but the uncertainty in the resistance was very large so it might have been hidden by the noise. Due to down-time of the VersaLab system it was not possible to do tests with lower AC amplitude after this had been implemented.

TER measurements were tested by applying IV-sweeps with opposite polarity in sequence and measuring the resistance between each triangular IV-pulse. The magnitudes of the IV-mode current pulses were manually determined by inspecting the corresponding voltage from increasing current amplitudes. Stable shifts of the measured resistance was indeed observed, however, the shifts could both increase and decrease after opposing IV-pulses. The order of increase or decrease seemed to be varying randomly between repeated identical measurement sequences. Therefore, although the data suggests some activity in the ferroelectric medium, it was not coherent or repeatable, so no successful TER effect was observed. For example, after a negative IV-pulse, the junction resistance could both increase and decrease to a stable level. Moreover, after many repeated resistance measurements, the resistance could start to increase or decrease to another stable level without any IV-pulse being applied. The latter may be a manifestation of relaxation in the BTO films that is reported to occur over relatively long times (1000s at room temperature) [87]. Consequently, the attempts for measuring TER so far did not work and no data have been included.

It is generally believed that 10 nA was a much too large AC amplitude to reveal TMR and TER, since the resulting voltage over the junctions at this level

were relatively large. The uncertainties observed in the resistance readings may have been related to current noise that induced substantial uncertainty in the reported voltages.

7.7 Validity of the Measurements

In all the different measurement approaches, various issues have been pointed out regarding too large resistances resulting in a large circuit time constant, and too rapid current sweeps or AC frequencies relative to the time constants. According to QD, the ETO is not approved for measuring resistances above approximately $10\text{ M}\Omega$ with the 4-wire current source option, due to current noise and parasitic capacitance. There is no doubt that these limitations have been dominating in the low amplitude regimes here. The 2-wire option uses a voltage source instead and calculates the current with a nano-ammeter. It is meant for high-impedance measurements. In principle this seem like a better choice, but the problem is the nano-ammeter which is not able to measure currents above 250 nA . Therefore, the 2-wire mode is useless for impedances less than approximately $1\text{ M}\Omega$. The MFTJs show rapidly falling impedances well below this once a slightly larger voltage is achieved across the junctions. Hence, it was never really an option to use the 2-wire mode. Yet, it could be interesting to use it for low bias excitation for example with voltages 10 mV to 1 V , but another limitation is that the lowest voltage that it can supply is 10 mV .

The IV-curve measurements are in general considered valid, however, the low-bias regions with very large tunneling resistances must be interpreted with care. The large circuit time constants make it inevitable with capacitive behavior in those regions, since the curves could not be recorded more slowly. The shifts of maximum (minimum) differential resistance (conductance) are thus not real.

The dVdI-mode is a powerful tool for studying details of nonlinear IV characteristics, but a major limitation is that it does not report the DC voltage component generated by the DC current offset. It seems strange that the ETO has been made without this possibility, as it appears to be essential for differential resistance or conductance measurements [88]. Furthermore, the minimum current levels that the ETO is approved for sourcing are 1 nA and 10 nA for DC and AC currents, respectively. In order to achieve low voltage biases in high impedance samples, these are too large currents. Consequently, the dVdI-mode can not be used to evaluate the MFTJ characteristics properly in the low voltage bias regime.

The AC lock-in data are useful for evaluating the sample impedance. For measurements within the nominal operating range, this seems like a promising way to measure the AC differential resistance and capacitance. The prototyped measurements with lower currents than the ETO is approved for must be validated and tested in more depth before one can consider them valid. However, both the differential resistance and capacitance measured with the low current

amplitudes seem to support general expectations.

Chapter 8

Discussion

In this chapter the general trends from each of the three preceding chapters are discussed. Specific discussions have already been presented along with the results, so the material below is aimed at being more of a summary and overall discussion. There are three sections for each of the results chapters and a final section with suggestions for future work.

8.1 Sample Design and Layout

The capacitive trends of the measurement circuit have been apparent in the analysis as well measurements presented in the last chapter. The chamber wiring and ETO hardware capacitance is considered the major and limiting contribution to the total capacitance. There is not much that can be done to counter this, although in principle a means to limit its significance is by including an impedance match on the sample, or a series inductor between the PCB and sample. In practice, however, this would require a certain area and will only be optimal for a given frequency. The contribution from the contact pads are already as small as practically possible, although not limiting as they are less than 2% of the ETO capacitance. Still, this contribution can more or less be removed by patterning the bottom electrode as well so that the capacitive coupling to the bottom electrode is removed.

In the final device design, a large ring-shaped current contact was incorporating the bottom electrode LSMO disc, and a small circular voltage contact was placed inside the LSMO disc on the opposite side of the current source contact to probe the local potential. The idea was to create a relatively uniform radial electric field in the LSMO disc and measure the average potential of this field. However there were apparent nonlinearities and a very large contact resistance seen in the small voltage probe contact from multimeter measurements. Although it is not known whether this was present also in the normal function as voltage

probe, the problem can be avoided by making the voltage probe contact interface larger. Moreover, the difference between a radial electric field through a ring-shaped current contact and an ordinary cross strip single-sided current contact is probably very small. Hence, a simpler approach is to use identical bottom electrode contacts for both I- and V- pads. This would additionally ascertain identical contact characteristics. In a design with patterned bottom electrodes, symmetric half-circular contact interfaces could be etched into the opposite edges of the circular bottom electrodes. Furthermore, if a larger contact interface area is needed without considerably increasing the size of the contacts, a castellated interface can be made. Finally, in the design used here the top contacts were not separated. However, a separation of current injection and potential readout should be sought, in order to leave out the contact resistance also on the top side.

8.2 Fabrication

The EBL process was simplified by using a standardized resist thickness and exposure dose throughout all fabrication stages. This made it possible to move on and spend time on more important parts of the process, however, there were clear indications for overexposure and structure dimensions exceeding the mask limits. Dimensions always ended up a few hundred nanometers larger than the exposed region. This trend was seen throughout all exposures and is probably a sign of overexposure or an overcompensating PEC for small structures and edges in general. It could be interesting to test a relatively much lower dose and increasing the development time to around a minute or more. Moreover, no significant undercut profile was achieved, so considerable edge roughness was present for all metal depositions regardless of deposited thickness. In addition, the standard resist thickness used, made it difficult to achieve the smallest top electrodes due to shadow effects when sputtering. To improve these points a broader spectrum of standard resist thicknesses should be selected, and two-layer copolymer resists could be used for enabling good undercut profiles. PMMA with another layer of lower molecular weight PMMA or MMA in an underlying layer can produce better undercut, if the underlying layer needs less exposure than the upper [115, 129, 130]. Hence, the proximity exposure could possibly be enough to develop a useful undercut, or dedicated side scans with lower dose could be added. More time should be spent on optimizing a more correct dosage, to prevent overexposure and increased feature sizes. Longer development times in DI:IPA combined with lower exposure dose could be the beneficial to achieve this, and other blends of DI and IPA may be better than 1:9 used here [116]. With a broader range of standardized resist thicknesses and corresponding base doses, an appropriate resist thickness and dose can be selected for the specific lift-off or dry-etch procedure wanted.

An alternative fabrication approach was initially competing with the selected one. There are a number of benefits expected to come from this approach, though

at the expense of more processing parameters and systems. First, the PECVD process is much quicker than RF sputtering for deposition of SiO_2 . Second, the EBL only needs to expose the contact hole areas, which are far smaller than the negative pattern area needed for the original stage 3. Third, etching oxides with ICP-RIE is much quicker than pure physical sputtering. Fourth, it allows the possibility to deposit gold before resist removal to produce the final bottom electrodes in the same stage, saving an extra round of EBL. Fifth, etching of contact holes in the insulator is expected to give better results than lift-off when scaling down the size of the MFTJs. When using lift-off of SiO_2 , a large resist thickness is necessary, which ultimately leads to very high aspect ratios for the free standing resist structures that are preventing insulator deposition where the contact holes should be.

On the other hand, there are benefits with the original process flow as well which ultimately lead to its selection. When considering the alternative stage 2/3 process, all options seem to be much quicker. However, there are many more process parameters that need to be optimized, and recipes must be selected wisely in order not to etch unwanted material or leave detrimental residues in the functional oxide interfaces. Furthermore, the total time consumption for the entire process may not be much less than for the selected process, since more systems are involved. The selected process flow, as presented before, was thus selected due to the simplicity of limiting the entire fabrication to the AJA system (in addition to the EBL).¹ Also, submicron feature sizes have not been a goal due to limitations in electrical characterization when areas decrease and resistances increase. Consequently, only fabrication time can be used to build a preference towards the PECVD/ICP-RIE process. Hence, in a prototype fabrication like this, such arguments were not favored.

Other alternatives could build on more active use of dry etching, either by pure sputter etching or combined with reactive ions. For fabrication of O-MFTJs, an alternative could be to initially deposit a uniform film of platinum or gold before any other treatment. In the first EBL stage, top electrodes could be defined and an etch mask metal could be deposited with the needed thickness. After lift-off, the entire sample could be dry-etched to define free-standing top electrodes, possibly with much greater precision and smaller feature size. Even though permalloy is harder to etch than gold or platinum, the same method would probably work for uniformly deposited noble-metal/permalloy films too, for P-MFTJ fabrication. Similar methods can be thought out for other parts of the fabrication as well.

One thing that intentionally was left out here is specific bottom electrode patterning. It was not done in order to save time needed for another stage of EBL. With the EBL process well established in the end, time consumption for another stage was not really that large, and thus could easily be justified. Benefits

¹In the end the Pfeiffer e-beam evaporator had to be used for evaporation, as the evaporator in the AJA system was out of order.

by doing this are several. For instance, no need for an insulation layer covering the whole sample, since the substrate is insulating. Thus bond pads could be placed directly on the substrate, and the insulation layer would only need to cover the bottom electrode between the top electrode and the etch edge. Exposure time would be reduced, and the insulation layer would not need to be as thick, since wire-bonding would not occur on top of the insulation with danger of puncture. Finally, all MFTJs on the same sample would be electrically isolated from one another, and the capacitance from bond pads would be avoided as only negligible parts of the wiring would have capacitive coupling to the bottom electrode.

With regard to wire-bonding a few remarks are needed. First of all, the bond pads need to stick properly to the sample, or else it will be nearly impossible to achieve good bonds and much time will be wasted. Secondly, there must be sufficiently thick bond pads so that the wire can be worked into the pad and made to bond with the pad material. Too thin pads also makes the wire-bonding difficult. Thirdly, an appropriate bond needle must be selected according to the wire material and thickness of the bond pads. The only available wedge needles during the course of this work was needles with a cross groove, which are optimized for gold wire only. This needle seemed to be working fine on the relatively thin bond pads on the sample ($1\ \mu\text{m}$), but did not work so well on the PCB bond pads that were very thick gold electroplated pads. It is also believed to cause the majority of the issues with aluminium wire. Moreover, certain day-to-day differences were experienced. It is difficult to say whether it had to do with sample aging or the bonder tool itself, but it is suspected to be the latter. There were times when essentially no bonds would form, even though the same parameters that had worked without problems the day before was used again. On some occasions it seemed like the ultrasonic actuator was not working, which would explain the difficulties, but it has not been verified and bonds started to work again after some changing of parameters back and forth. It is also possible that some of the differences experienced had to do with the samples being exposed to helium gas in the VersaLab system between bonding and re-bonding.

8.3 Electrical Characterization

Firstly, it is no doubt that the tunnel junction structure works well. The IV-curves reveal an overall signature that is typical for asymmetric FTJs. At small current amplitudes the tunnel resistance is very large and presumably dominated by direct tunneling. For larger current amplitudes, the junction bias increases and overcomes the potential barrier to a greater extent which effectively reduces the tunneling resistance rapidly. In fact, the tunnel resistance is dropping towards negligible values for larger biases, which implies large leakage currents. The relatively large current amplitudes used here due to hardware limitations induce junction voltages slightly too large, and the leakage current may be a contributing factor to the lack of TER and TMR at these voltage levels.

Consequently, there are two problems indicated. First, the selected junction diameters underestimated how large the low-bias tunnel resistances are. Second, the leakage current seems to be a limiting factor at typical read voltages. Thus, means to improve film quality and preventing leakage current should be evaluated. In addition, larger MFTJs can be made to lower the low-bias resistance.

The most important goal of the investigations done on WWB scripting of the ETO, was to figure out whether or not it can be used as a voltage controlled current source. So far the answer is no, but it might be some unknown possibility available in the IV- or Oscilloscope modes, if they can be properly implemented and tested. Since this was not possible, other methods were investigated instead to see if useful measurements for MFTJ characterization are feasible with the ETO module.

Measurements of longitudinal resistance in LSMO indicate relatively large contact resistances and possible nonlinearities. This was particularly seen for the voltage probes in the final design which were made relatively small. Detailed studies of specific contact resistances have not been done here, but contacts are a crucial part of the samples and should not be underestimated. Ideally, the problem of forming good ohmic contacts to LSMO buried by other materials should be solved before further work on fabrication and electrical characterization is done.

IV-mode measurements are so far the most feasible way to characterize MFTJs with the ETO. With knowledge of both the current and voltage, the differential resistance and conductance can be calculated by numerical differentiation. Still, there are major drawbacks. Only a constant and limited number of measurement points per triangular cycle is supported, and the cycle frequencies are set in software. The sweep cycle times supported are simply not slow enough for true DC characterization of the leakage current. The limited number of points per cycle gives very few points in the region of highest impedance, since the voltage is changing rapidly for incremental currents in these areas. Another known problem with IV-curves for this purpose is the noise, which makes it necessary to do very many cycles to get a good average [88]. If the IV-mode can be implemented by scripting, these limitations can possibly be omitted if they are not limited by the hardware itself.

All in all it seems to be a better choice to connect more specialized external equipment to the VersaLab in order to characterize MFTJs properly. The ETO hardware is very limited in the way it works, and it is probably not intended for this type of measurements. There are different types of external high precision solutions available from for example Keithley Instruments, and probably others. Moreover, the VersaLab can be equipped with an additional rotator module for rotation of the sample while performing electrical measurements. This can be useful for magnetotransport studies with the magnetic field along different orientations in the sample.

8.4 Future Work

- A range of PMMA/MMA or equivalent copolymer resist thicknesses should be established for lift-off of different thicknesses of material and potential nanoscale fabrication. Further standardization of complete EBL recipes could be done by carefully optimizing the different thickness schemes with appropriate dose and development times in a particular DI:IPA blend. Having a range of standard EBL processes would greatly lower the time spent on fabricating devices or additional process optimization after adjustments of device size or design.
- The problem of PMMA heating during e-beam evaporation needs attention. It can be expected that the heating declines as more metal is deposited, because more radiation will be reflected back and heat conduction in the deposited metal directs the heat away from the sample more effectively. Consequently, tests could be done with only a high deposition rate for the initial titanium layer, and a lower subsequent gold deposition rate to prevent the particle formation. In addition the cooling stage can be used to keep the sample holder at room temperature, which possibly can help maintain a lower temperature in the PMMA as well.
- The problem of contacting the LSMO layer with proper ohmic contacts needs to be addressed in a systematic way. To this end contact formation studies including measurements of specific contact resistance to LSMO from different processes and materials should be done. This is probably an entire master thesis worth of work if all aspects are taken into account. It can be done by patterning films into well defined structures along different crystal axes and varying the processes for etching and which materials are deposited. Here a simple physical Ar sputter-etch was used without any neutralizing filament, but both ICP-RIE and CAIBE techniques should also be included in such an investigation. Moreover, venting the chamber with oxygen or exposing the sample to atmosphere for some time between etching and metal deposition, may be a way to improve possible oxygen deficiency at the interface caused by the etching.
- A piezoresponse force microscopy study should be performed to evaluate whether or not stable and switchable polarization exists in the (111)-oriented BTO thin-films. Only a very weak indication for TER was observed in one of the samples from the autumn project, so it would be very useful to know more about what can be expected before more effort is put into fabricating and measuring MFTJs with this orientation.
- Further programming studies of the ETO can be done, but it is in general considered a poor use of time. If QD in the future decide to develop more prototypes for WWB scripts of the IV- and possibly oscilloscope modes, or publish proper documentation for how the ETO can be controlled, it will be easier and more worthwhile.
- In short term the 2-wire mode of the ETO should be tested on the new

samples in order to check the low voltage regime down to 10 mV. With this mode it is also easier to control the junction bias, since it is the voltage that is applied.

- In the longer term external electronics should be acquired and set up for proper electrical characterization to be possible. The ETO module is simply too limited for the purpose of studying MFTJs thoroughly. To this end LOT in Germany will be helpful. The author has already had some correspondence with an application engineer, who have come up with possible alternatives. The needs should be carefully analyzed before making a decision on what equipment to go for. Moreover, it might be that some or all of the needed instrumentation is already available in house. It is considered to be enough work included in establishing a system like this properly and doing measurements for another master thesis. In addition, the samples prepared here remains largely to be measured.
- If it is planned for fabrication of more samples, the junction sizes should be made with a wider range of diameters and the thin film quality should be improved. It can also be an idea to see if certain shapes can be used to induce more preferred easy axes in the magnets by shape anisotropy.

Chapter 9

Conclusion

In conclusion, two model systems for multiferroic tunnel junctions have been designed, fabricated and initially measured. Epitaxial structures of ferromagnetic, half-metallic LSMO followed by ferroelectric BTO, grown on (111)-oriented STO substrates, have been utilized as bottom electrode and insulating barrier materials, respectively. Sputter deposited permalloy and epitaxial LSMO with a sputtered Pt capping and contacting layer, have been used as ferromagnetic top electrodes for asymmetric permalloy MFTJs and all-oxide epitaxial MFTJs, respectively.

A MFTJ fabrication process with four or five EBL and overlay exposure stages has been established for permalloy and all-oxide MFTJs, respectively. Sputter deposition and lift-off was used for NiFe, Pt and SiO₂, e-beam evaporation and lift-off for Ti, Al and Au. Low power RF Ar-sputtering has been used for etching of the epitaxial oxides in order to define top electrodes in the all-oxide MFTJs, and for preparing electrical contacts to the bottom electrode layer. The etching has proven uniform and highly predictable, but it remains to be investigated if bombardment with ionized Ar has an impact on the behavior of the contacts due to the lack of a neutralizing filament.

Wedge-wedge bonding to 100 $\mu\text{m} \times 100 \mu\text{m}$ bond pads of either Au or Al with gold and aluminium wire at room temperature has been established. Highly reproducible results can be expected with gold wire. More suited wedge needles are anticipated to give better results with aluminium wire, possibly also with gold wire.

Further investigations on scripting the VersaLab ETO with visual basic programming, has enabled interesting low-current measurements of differential resistance and capacitance versus DC-current, by utilizing the AC lock-in data directly. Capacitance measurements can be interesting in terms of assessing the thin-film relative permittivity of BTO and possibly to track the polarization indirectly. The measurements performed by this method gave relative permittivities of 249 and 543 for BTO thicknesses 3 nm and 5 nm, respectively. The ETO

AC frequency is limited to a maximum of 200 Hz, and it is not approved for impedances larger than a few tens of mega-ohms, so careful testing and verification is needed before the method can be applied with confidence.

There appears to be no possibility for continuous DC voltage readout with the ETO, and insufficient documentation has obstructed the development of scripts for controlling the IV- and Oscilloscope modes. Gaining insight into how those modes work and how to exploit them may enable DC voltage measurements, but it is considered a dead-end until further documentation or prototype scripts are published by Quantum Design.

Electrical characterization of two 15 μm diameter permalloy MFTJs show successful overall FTJ behavior, and it is concluded that the devices are working as intended. Very high tunneling resistances, on the order of several hundred mega-ohms, were revealed for low junction biases. The resistances rapidly decrease to tens of kilo-ohms at voltages of a few volts. The capacitive nature is dominating at low biases and was strongly altering the measurements since true DC characterization could not be done. Differential resistance measurements revealed AC resistances with AC frequency 1.52 Hz that were strongly differing from the numerical derivative resistances acquired by IV-curve sweeps.

Evidence for TMR and TER have been found for a sample fabricated during the autumn project. The TMR measurements revealed three clear intermediate resistance states between the fully parallel and antiparallel magnetic alignments. Furthermore, the TER measurements revealed a stable resistance hysteresis curve as a function of junction poling voltages.

For the newly fabricated samples, no signs of ferroelectric switching have been seen, even though the MFTJs show the overall IV characteristics of FTJs. There has not been observed distinct high- and low-resistance IV-curves that are typical for resistive switching. Hence, no TER effect could be measured. Moreover, no TMR effect could be found, but this is likely due to large resistance deviations from too large current excitations relative to the tunnel resistance.

Further tests are needed to find appropriate measurement techniques for electrical characterization, and setting up specialized external electronics is seen as the natural next step towards this goal.

It is concluded that the MFTJ tunneling resistance was underestimated, and the smallest available current amplitude was still too large to enable low voltage bias measurements on the fabricated MFTJs. Considering the measurements on the older sample with much larger junction area and correspondingly smaller junction resistance, there is reason to believe that the new samples will reveal both enhanced TMR and TER once a sufficiently sophisticated measurement can be done.

Bibliography

- [1] Kristoffer Kjærnes. *Multiferroic Tunnel Junctions – Establishment of a Model System and Measurement Techniques*. Project thesis, Norwegian University of Science and Technology, 2015.
- [2] J. Mannhart and D. G. Schlom. Oxide interfaces—an opportunity for electronics. *Science*, 327(5973):1607–1611, 2010. URL <http://www.sciencemag.org/content/327/5973/1607.abstractN2>.
- [3] Hans Schmid. Multi-ferroic magnetoelectrics. *Ferroelectrics*, 162(1):317–338, 1994. ISSN 0015-0193. doi: 10.1080/00150199408245120. URL <http://dx.doi.org/10.1080/00150199408245120>.
- [4] Nicola A. Hill. Why are there so few magnetic ferroelectrics? *The Journal of Physical Chemistry B*, 104(29):6694–6709, 2000. ISSN 1520-6106. doi: 10.1021/jp000114x. URL <http://dx.doi.org/10.1021/jp000114x>.
- [5] Nicola A. Spaldin and Manfred Fiebig. The renaissance of magnetoelectric multiferroics. *Science*, 309(5733):391–392, 2005. ISSN 1095-9203 (Electronic) 0036-8075 (Linking). doi: 10.1126/science.1113357. URL <http://www.sciencemag.org/content/309/5733/391.short>.
- [6] W. Eerenstein, N. D. Mathur, and J. F. Scott. Multiferroic and magnetoelectric materials. *Nature*, 442(7104):759–65, 2006. ISSN 1476-4687 (Electronic) 0028-0836 (Linking). doi: 10.1038/nature05023. URL <http://www.ncbi.nlm.nih.gov/pubmed/16915279>.
- [7] M. Bibes and A. Barthelemy. Multiferroics: towards a magnetoelectric memory. *Nat Mater*, 7(6):425–6, 2008. ISSN 1476-1122 (Print) 1476-1122 (Linking). doi: 10.1038/nmat2189. URL <http://www.ncbi.nlm.nih.gov/pubmed/18497843>.
- [8] M. Julliere. Tunneling between ferromagnetic films. *Physics Letters A*, 54(3):225–226, 1975. ISSN 0375-9601. doi: [http://dx.doi.org/10.1016/0375-9601\(75\)90174-7](http://dx.doi.org/10.1016/0375-9601(75)90174-7). URL <http://www.sciencedirect.com/science/article/pii/0375960175901747>.

- [9] J. S. Moodera, Lisa R. Kinder, Terrilyn M. Wong, and R. Meservey. Large magnetoresistance at room temperature in ferromagnetic thin film tunnel junctions. *Physical Review Letters*, 74(16):3273–3276, 1995. URL <http://link.aps.org/doi/10.1103/PhysRevLett.74.3273>.
- [10] T. Miyazaki and N. Tezuka. Giant magnetic tunneling effect in fe/al2o3/fe junction. *Journal of Magnetism and Magnetic Materials*, 139(3):L231–L234, 1995. ISSN 0304-8853. doi: [http://dx.doi.org/10.1016/0304-8853\(95\)90001-2](http://dx.doi.org/10.1016/0304-8853(95)90001-2). URL <http://www.sciencedirect.com/science/article/pii/0304885395900012>.
- [11] L Esaki, RB Laibowitz, and PJ Stiles. Polar switch. *IBM Tech. Discl. Bull*, 13(2161):114, 1971.
- [12] J. Rodriguez Contreras, H. Kohlstedt, U. Poppe, R. Waser, C. Buchal, and N. A. Pertsev. Resistive switching in metal–ferroelectric–metal junctions. *Applied Physics Letters*, 83(22):4595–4597, 2003. doi: [doi:http://dx.doi.org/10.1063/1.1627944](http://dx.doi.org/10.1063/1.1627944). URL <http://scitation.aip.org/content/aip/journal/apl/83/22/10.1063/1.1627944>.
- [13] Evgeny Y. Tsymbal and Hermann Kohlstedt. Tunneling across a ferroelectric. *Science*, 313(5784):181–183, 2006. URL <http://www.sciencemag.org/content/313/5784/181.short>.
- [14] Martin Gajek, Manuel Bibes, Stephane Fusil, Karim Bouzehouane, Josep Fontcuberta, Agnes Barthelemy, and Albert Fert. Tunnel junctions with multiferroic barriers. *Nat Mater*, 6(4):296–302, 2007. ISSN 1476-1122. doi: http://www.nature.com/nmat/journal/v6/n4/supinfo/nmat1860_S1.html. URL <http://dx.doi.org/10.1038/nmat1860>.
- [15] Julian P. Velev, Chun-Gang Duan, J. D. Burton, Alexander Smogunov, Manish K. Niranjana, Erio Tosatti, S. S. Jaswal, and Evgeny Y. Tsymbal. Magnetic tunnel junctions with ferroelectric barriers: Prediction of four resistance states from first principles. *Nano Letters*, 9(1):427–432, 2009. ISSN 1530-6984. doi: [10.1021/nl803318d](http://dx.doi.org/10.1021/nl803318d). URL <http://dx.doi.org/10.1021/nl803318d><http://pubs.acs.org/doi/pdfplus/10.1021/nl803318d>.
- [16] R. Ramesh and N. A. Spaldin. Multiferroics: progress and prospects in thin films. *Nat Mater*, 6(1):21–9, 2007. ISSN 1476-1122 (Print) 1476-1122 (Linking). doi: [10.1038/nmat1805](http://www.ncbi.nlm.nih.gov/pubmed/17199122). URL <http://www.ncbi.nlm.nih.gov/pubmed/17199122>.
- [17] J. Chakhalian, A. J. Millis, and J. Rondinelli. Whither the oxide interface. *Nat Mater*, 11(2):92–94, 2012. ISSN 1476-1122. URL <http://dx.doi.org/10.1038/nmat3225>.

- [18] Manuel Bibes. Nanoferronics is a winning combination. *Nat Mater*, 11(5):354–357, 2012. ISSN 1476-1122. URL <http://dx.doi.org/10.1038/nmat3318>.
- [19] Manuel Bibes and A. Barthelémy. Oxide spintronics. *Electron Devices, IEEE Transactions on*, 54(5):1003–1023, 2007. ISSN 0018-9383. doi: 10.1109/TED.2007.894366. URL <http://ieeexplore.ieee.org/ielx5/16/4160089/04160091.pdf?tp=&arnumber=4160091&isnumber=4160089>.
- [20] N. Izyumskaya, Ya Alivov, and H. Morkoç. Oxides, oxides, and more oxides: High- κ oxides, ferroelectrics, ferromagnetics, and multiferroics. *Critical Reviews in Solid State and Materials Sciences*, 34(3-4):89–179, 2009. ISSN 1040-8436. doi: 10.1080/10408430903368401. URL <http://dx.doi.org/10.1080/10408430903368401>.
- [21] Shuai Dong, Jun-Ming Liu, Sang-Wook Cheong, and Zhifeng Ren. Multiferroic materials and magnetoelectric physics: symmetry, entanglement, excitation, and topology. *Advances in Physics*, 64(5-6):519–626, 2015. ISSN 0001-8732. doi: 10.1080/00018732.2015.1114338. URL <http://dx.doi.org/10.1080/00018732.2015.1114338>.
- [22] J. M. D. Coey, M. Viret, and S. von Molnár. Mixed-valence manganites. *Advances in Physics*, 48(2):167–293, 1999. ISSN 0001-8732. doi: 10.1080/000187399243455. URL <http://dx.doi.org/10.1080/000187399243455>.
- [23] A. M. Haghiri-Gosnet and J. P. Renard. Cmr manganites: physics, thin films and devices. *Journal of Physics D: Applied Physics*, 36(8):R127, 2003. ISSN 0022-3727. URL <http://stacks.iop.org/0022-3727/36/i=8/a=201>.
- [24] Yu Lu, X. W. Li, G. Q. Gong, Gang Xiao, A. Gupta, P. Lecoeur, J. Z. Sun, Y. Y. Wang, and V. P. Dravid. Large magnetotunneling effect at low magnetic fields in micrometer-scale epitaxial $\text{La}_{0.67}\text{Sr}_{0.33}\text{MnO}_3$ tunnel junctions. *Physical Review B*, 54(12):R8357–R8360, 1996. URL <http://link.aps.org/doi/10.1103/PhysRevB.54.R8357>.
- [25] J. Z. Sun, W. J. Gallagher, P. R. Duncombe, L. Krusin-Elbaum, R. A. Altman, A. Gupta, Yu Lu, G. Q. Gong, and Gang Xiao. Observation of large low-field magnetoresistance in trilayer perpendicular transport devices made using doped manganate perovskites. *Applied Physics Letters*, 69(21):3266–3268, 1996. doi: [doi:http://dx.doi.org/10.1063/1.118031](http://dx.doi.org/10.1063/1.118031). URL <http://scitation.aip.org/content/aip/journal/apl/69/21/10.1063/1.118031>.
- [26] M. Bowen, M. Bibes, A. Barthélémy, J.-P. Contour, A. Anane, Y. Lemaître, and A. Fert. Nearly total spin polarization in $\text{La}_2/3\text{Sr}_1/3\text{MnO}_3$ from tunneling experiments. *Applied Physics Letters*, 82(2):233–235, 2003. doi:

- doi:<http://dx.doi.org/10.1063/1.1534619>. URL <http://scitation.aip.org/content/aip/journal/apl/82/2/10.1063/1.1534619>.
- [27] Y. W. Yin, M. Raju, W. J. Hu, X. J. Weng, X. G. Li, and Q. Li. Coexistence of tunneling magnetoresistance and electroresistance at room temperature in $\text{La}_{0.7}\text{Sr}_{0.3}\text{MnO}_3/(\text{Ba}, \text{Sr})\text{TiO}_3/\text{La}_{0.7}\text{Sr}_{0.3}\text{MnO}_3$ multiferroic tunnel junctions. *Journal of Applied Physics*, 109(7): 07D915, 2011. doi: [doi:http://dx.doi.org/10.1063/1.3564970](http://dx.doi.org/10.1063/1.3564970). URL <http://scitation.aip.org/content/aip/journal/jap/109/7/10.1063/1.3564970><http://scitation.aip.org/docserver/fulltext/aip/journal/jap/109/7/1.3564970.pdf?expires=1453837574&id=id&accname=2120809&checksum=91AEE58F73B588792EA1852E867EC04C>.
- [28] Yue-Wei Yin, Wei-Chuan Huang, Yu-Kuai Liu, Sheng-Wei Yang, Si-Ning Dong, Jing Tao, Yi-Mei Zhu, Qi Li, and Xiao-Guang Li. Octonary resistance states in $\text{La}_{0.7}\text{Sr}_{0.3}\text{MnO}_3/\text{BaTiO}_3/\text{La}_{0.7}\text{Sr}_{0.3}\text{MnO}_3$ multiferroic tunnel junctions. *Advanced Electronic Materials*, pages n/a–n/a, 2015. ISSN 2199-160X. doi: 10.1002/aelm.201500183. URL <http://dx.doi.org/10.1002/aelm.201500183><http://onlinelibrary.wiley.com/doi/10.1002/aelm.201500183/abstract>.
- [29] I. Hallsteinsen, J. E. Boschker, M. Nord, S. Lee, M. Rzechowski, P. E. Vullum, J. K. Grepstad, R. Holmestad, C. B. Eom, and T. Tybell. Surface stability of epitaxial $\text{La}_{0.7}\text{Sr}_{0.3}\text{MnO}_3$ thin films on (111)-oriented SrTiO_3 . *Journal of Applied Physics*, 113(18): 183512, 2013. doi: [doi:http://dx.doi.org/10.1063/1.4804312](http://dx.doi.org/10.1063/1.4804312). URL <http://scitation.aip.org/content/aip/journal/jap/113/18/10.1063/1.4804312><http://scitation.aip.org/docserver/fulltext/aip/journal/jap/113/18/1.4804312.pdf?expires=1445245397&id=id&accname=2120809&checksum=18551149C574081DE727235FFAABF181>.
- [30] Ingrid Hallsteinsen, Magnus Nord, Torstein Bolstad, Per-Erik Vullum, Jos Emiel Boschker, Paolo Longo, Ryota Takahashi, Randi Holmestad, Mikk Lippmaa, and Thomas Tybell. The effect of polar (111)-oriented SrTiO_3 on initial perovskite growth. *Crystal Growth & Design*, 2016. ISSN 1528-7483. doi: 10.1021/acs.cgd.6b00143. URL <http://dx.doi.org/10.1021/acs.cgd.6b00143>.
- [31] I. Hallsteinsen, E. Folven, F. K. Olsen, R. V. Chopdekar, M. S. Rzechowski, C. B. Eom, J. K. Grepstad, and T. Tybell. Crystalline symmetry controlled magnetic switching in epitaxial (111) $\text{La}_{0.7}\text{Sr}_{0.3}\text{MnO}_3$ thin films. *APL Materials*, 3(6):062501, 2015. doi: [doi:http://dx.doi.org/10.1063/1.4907877](http://dx.doi.org/10.1063/1.4907877). URL <http://scitation.aip.org/content/aip/journal/aplmater/3/6/10.1063/1.4907877><http://scitation.aip.org/docserver/fulltext/aip/journal/aplmater/>

- 3/6/1.4907877.pdf?expires=1444633035&id=id&accname=guest&checksum=1E4CB18A40F9F9CBACC02A6AD827B9E9.
- [32] Herbert Kroemer. Nobel lecture: Quasi-electric fields and band offsets: Teaching electrons new tricks. *Nobelprize.org*, Nobel Media AB 2014(29 Jun 2016), 2000. URL http://www.nobelprize.org/nobel_prizes/physics/laureates/2000/kroemer-lecture.html.
- [33] Isao H. Inoue and Marcelo J. Rozenberg. Taming the mott transition for a novel mott transistor. *Advanced Functional Materials*, 18(16):2289–2292, 2008. ISSN 1616-3028. doi: 10.1002/adfm.200800558. URL <http://dx.doi.org/10.1002/adfm.200800558>.
- [34] Zheng Yang, Changhyun Ko, and Shriram Ramanathan. Oxide electronics utilizing ultrafast metal-insulator transitions. *Annual Review of Materials Research*, 41(1):337–367, 2011. doi: doi:10.1146/annurev-matsci-062910-100347. URL <http://www.annualreviews.org/doi/abs/10.1146/annurev-matsci-062910-100347>.
- [35] Igor Žutić, Jaroslav Fabian, and S. Das Sarma. Spintronics: Fundamentals and applications. *Reviews of Modern Physics*, 76(2):323–410, 2004. URL <http://link.aps.org/doi/10.1103/RevModPhys.76.323>.
- [36] Supriyo Bandyopadhyay and Marc Cahay. *Introduction to spintronics*. CRC press, Taylor & Francis Group, 2nd edition, 2015. ISBN 148225557X.
- [37] A. Z. Chandler. Everspin releases fastest and most reliable non-volatile storage class memory. Everspin Technologies, 2016. everspin.com, accessed 30 June 2016, 2016. URL <https://www.everspin.com/news/everspin-releases-fastest-and-most-reliable-non-volatile-storage-class-memory>.
- [38] J. G. Alzate, P. K. Amiri, P. Upadhyaya, S. S. Cherepov, J. Zhu, M. Lewis, R. Dorrance, J. A. Katine, J. Langer, K. Galatsis, D. Markovic, I. Krivorotov, and K. L. Wang. Voltage-induced switching of nanoscale magnetic tunnel junctions. In *Electron Devices Meeting (IEDM), 2012 IEEE International*, pages 29.5.1–29.5.4, 2012. ISBN 0163-1918. doi: 10.1109/IEDM.2012.6479130.
- [39] P. Khalili Amiri, J. G. Alzate, X. Q. Cai, F. Ebrahimi, Q. Hu, K. Wong, C. Gr, x00E, zes, H. Lee, G. Yu, X. Li, M. Akyol, Q. Shao, J. A. Katine, J. Langer, B. Ocker, and K. L. Wang. Electric-field-controlled magnetoelectric ram: Progress, challenges, and scaling. *IEEE Transactions on Magnetism*, 51(11):1–7, 2015. ISSN 0018-9464. doi: 10.1109/TMAG.2015.2443124.
- [40] K. L. Wang, H. Lee, and P. Khalili Amiri. Magnetoelectric random access memory-based circuit design by using voltage-controlled magnetic

- anisotropy in magnetic tunnel junctions. *IEEE Transactions on Nanotechnology*, 14(6):992–997, 2015. ISSN 1536-125X. doi: 10.1109/TNANO.2015.2462337.
- [41] Jacob Linder and Jason W. A. Robinson. Superconducting spintronics. *Nat Phys*, 11(4):307–315, 2015. ISSN 1745-2473. doi: 10.1038/nphys3242. URL <http://dx.doi.org/10.1038/nphys3242>.
- [42] Marina S. Leite, Robyn L. Woo, Jeremy N. Munday, William D. Hong, Shoghig Mesropian, Daniel C. Law, and Harry A. Atwater. Towards an optimized all lattice-matched inala/ingaasp/ingaas multijunction solar cell with efficiency >50%. *Applied Physics Letters*, 102(3):033901, 2013. doi: doi:http://dx.doi.org/10.1063/1.4758300. URL <http://scitation.aip.org/content/aip/journal/apl/102/3/10.1063/1.4758300>.
- [43] M. N. Baibich, J. M. Broto, A. Fert, F. Nguyen Van Dau, F. Petroff, P. Etienne, G. Creuzet, A. Friederich, and J. Chazelas. Giant magnetoresistance of (001)fe/(001)cr magnetic superlattices. *Physical Review Letters*, 61(21):2472–2475, 1988. URL <http://link.aps.org/doi/10.1103/PhysRevLett.61.2472><http://journals.aps.org/prl/abstract/10.1103/PhysRevLett.61.2472>.
- [44] IBM Research. The giant magnetoresistive head: A giant leap for ibm research. IBM Research, 1997. research.ibm.com, accessed 1 July 2016, 1997. URL <http://www.research.ibm.com/research/gmr.html>.
- [45] Yuasa Shinji, Fukushima Akio, Nagahama Taro, Ando Koji, and Suzuki Yoshishige. High tunnel magnetoresistance at room temperature in fully epitaxial fe/mgo/fe tunnel junctions due to coherent spin-polarized tunneling. *Japanese Journal of Applied Physics*, 43(4B):L588, 2004. ISSN 1347-4065. URL <http://stacks.iop.org/1347-4065/43/i=4B/a=L588>.
- [46] Shinji Yuasa, Taro Nagahama, Akio Fukushima, Yoshishige Suzuki, and Koji Ando. Giant room-temperature magnetoresistance in single-crystal fe/mgo/fe magnetic tunnel junctions. *Nat Mater*, 3(12):868–871, 2004. ISSN 1476-1122. doi: http://www.nature.com/nmat/journal/v3/n12/supinfo/nmat1257_S1.html. URL <http://dx.doi.org/10.1038/nmat1257><http://www.nature.com/nmat/journal/v3/n12/pdf/nmat1257.pdf>.
- [47] Mao Sining, J. Nowak, Song Dian, P. Kolbo, Wang Lei, E. Linville, D. Saunders, E. Murdock, and P. Ryan. Spin tunneling heads above 20 gb/in². *IEEE Transactions on Magnetics*, 38(1):78–83, 2002. ISSN 0018-9464. doi: 10.1109/TMAG.2002.988915.
- [48] Mao Sining, Chen Yonghua, Liu Feng, Chen Xingfu, Xu Bin, Lu Puling, M. Patwari, Xi Haiwen, Chang Clif, B. Miller, D. Menard, B. Pant,

- J. Loven, K. Duxstad, Li Shaoping, Zhang Zhengyong, A. Johnston, R. Lamberton, M. Gubbins, T. McLaughlin, J. Gadbois, Ding Juren, B. Cross, Xue Song, and P. Ryan. Commercial tmr heads for hard disk drives: characterization and extendibility at 300 gbit/in². *IEEE Transactions on Magnetics*, 42(2):97–102, 2006. ISSN 0018-9464. doi: 10.1109/TMAG.2005.861788.
- [49] J.Z. Sun, L. Krusin-Elbaum, P.R. Duncombe, A. Gupta, and R.B. Laibowitz. Temperature dependent, non-ohmic magnetoresistance in doped perovskite manganate trilayer junctions. *Applied Physics Letters*, 70(13):1769–1771, 1997.
- [50] M. Viret, M. Drouet, J. Nassar, J. P. Contour, C. Fermon, and A. Fert. Low-field colossal magnetoresistance in manganite tunnel spin valves. *EPL (Europhysics Letters)*, 39(5):545, 1997. ISSN 0295-5075. URL <http://stacks.iop.org/0295-5075/39/i=5/a=545>.
- [51] Manuel Bibes, Javier E. Villegas, and Agnès Barthélémy. Ultrathin oxide films and interfaces for electronics and spintronics. *Advances in Physics*, 60(1):5–84, 2011. ISSN 0001-8732. doi: 10.1080/00018732.2010.534865. URL <http://dx.doi.org/10.1080/00018732.2010.534865>.
- [52] Rainer Waser. *Nanoelectronics and information technology*. John Wiley & Sons, 3rd edition, 2012. ISBN 9783527409273.
- [53] Rajesh V. Chopdekar, Elke Arenholz, and Y. Suzuki. Orientation and thickness dependence of magnetization at the interfaces of highly spin-polarized manganite thin films. *Physical Review B*, 79(10):104417, 2009. URL <http://link.aps.org/doi/10.1103/PhysRevB.79.104417>.
- [54] H. Kohlstedt, N. A. Pertsev, J. Rodríguez Contreras, and R. Waser. Theoretical current-voltage characteristics of ferroelectric tunnel junctions. *Physical Review B*, 72(12):125341, 2005. URL <http://link.aps.org/doi/10.1103/PhysRevB.72.125341>.
- [55] T. Tybell, C. H. Ahn, and J.-M. Triscone. Ferroelectricity in thin perovskite films. *Applied Physics Letters*, 75(6):856–858, 1999. doi: [doi:http://dx.doi.org/10.1063/1.124536](http://dx.doi.org/10.1063/1.124536). URL <http://scitation.aip.org/content/aip/journal/apl/75/6/10.1063/1.124536>.
- [56] M. Ye Zhuravlev, R. F. Sabirianov, S. S. Jaswal, and E. Y. Tsymbal. Giant electroresistance in ferroelectric tunnel junctions. *Physical Review Letters*, 94(24):246802, 2005. URL <http://link.aps.org/doi/10.1103/PhysRevLett.94.246802>.
- [57] YS Kim, DH Kim, JD Kim, YJ Chang, TW Noh, JH Kong, K Char, YD Park, SD Bu, and JG Yoon. Critical thickness of ultrathin ferroelectric

- batio3 films. *Applied Physics Letters*, 86(10):102907–103100, 2005. ISSN 0003-6951.
- [58] A. Petraru, H. Kohlstedt, U. Poppe, R. Waser, A. Solbach, U. Klemradt, J. Schubert, W. Zander, and N. A. Pertsev. Wedgelike ultrathin epitaxial batio3 films for studies of scaling effects in ferroelectrics. *Applied Physics Letters*, 93(7):072902, 2008. doi: doi:http://dx.doi.org/10.1063/1.2972135. URL <http://scitation.aip.org/content/aip/journal/apl/93/7/10.1063/1.2972135>.
- [59] Peter Maksymovych, Stephen Jesse, Pu Yu, Ramamoorthy Ramesh, Arthur P. Baddorf, and Sergei V. Kalinin. Polarization control of electron tunneling into ferroelectric surfaces. *Science*, 324(5933):1421–1425, 2009. URL <http://www.sciencemag.org/content/324/5933/1421.abstractN2><http://www.sciencemag.org/content/324/5933/1421.full.pdf>.
- [60] V. Garcia, S. Fusil, K. Bouzouhane, S. Enouz-Vedrenne, N. D. Mathur, A. Barthelemy, and M. Bibes. Giant tunnel electroresistance for non-destructive readout of ferroelectric states. *Nature*, 460(7251):81–84, 2009. ISSN 0028-0836. doi: http://www.nature.com/nature/journal/v460/n7251/supinfo/nature08128_S1.html. URL <http://dx.doi.org/10.1038/nature08128>.
- [61] A. Gruverman, D. Wu, H. Lu, Y. Wang, H. W. Jang, C. M. Folkman, M. Ye Zhuravlev, D. Felker, M. Rzechowski, C. B. Eom, and E. Y. Tsymbal. Tunneling electroresistance effect in ferroelectric tunnel junctions at the nanoscale. *Nano Letters*, 9(10):3539–3543, 2009. ISSN 1530-6984. doi: 10.1021/nl901754t. URL <http://dx.doi.org/10.1021/nl901754t><http://pubs.acs.org/doi/pdfplus/10.1021/nl901754t>.
- [62] Zheng Wen, Chen Li, Di Wu, Aidong Li, and Naiben Ming. Ferroelectric-field-effect-enhanced electroresistance in metal/ferroelectric/semiconductor tunnel junctions. *Nat Mater*, 12(7):617–621, 2013. ISSN 1476-1122. doi: 10.1038/nmat3649<http://www.nature.com/nmat/journal/v12/n7/abs/nmat3649.html#supplementary-information>. URL <http://dx.doi.org/10.1038/nmat3649>.
- [63] Lingfei Wang, Myung Rae Cho, Yeong Jae Shin, Jeong Rae Kim, Saikat Das, Jong-Gul Yoon, Jin-Seok Chung, and Tae Won Noh. Overcoming the fundamental barrier thickness limits of ferroelectric tunnel junctions through batio3/srtio3 composite barriers. *Nano Letters*, 2016. ISSN 1530-6984. doi: 10.1021/acs.nanolett.6b01418. URL <http://dx.doi.org/10.1021/acs.nanolett.6b01418>.
- [64] V. Garcia, M. Bibes, L. Bocher, S. Valencia, F. Kronast, A. Crassous, X. Moya, S. Enouz-Vedrenne, A. Gloter, D. Imhoff,

- C. Deranlot, N. D. Mathur, S. Fusil, K. Bouzehouane, and A. Barthélemy. Ferroelectric control of spin polarization. *Science*, 327(5969):1106–1110, 2010. doi: 10.1126/science.1184028. URL <http://www.sciencemag.org/content/327/5969/1106.abstract><http://www.sciencemag.org/content/327/5969/1106.full.pdf>.
- [65] S. Valencia, A. Crassous, L. Bocher, V. Garcia, X. Moya, R. O. Cherifi, C. Deranlot, K. Bouzehouane, S. Fusil, A. Zobelli, A. Gloter, N. D. Mathur, A. Gaupp, R. Abrudan, F. Radu, A. Barthélemy, and M. Bibes. Interface-induced room-temperature multiferroicity in batio₃. *Nat Mater*, 10(10):753–758, 2011. ISSN 1476-1122. doi: <http://www.nature.com/nmat/journal/v10/n10/abs/nmat3098.html#supplementary-information>. URL <http://dx.doi.org/10.1038/nmat3098>.
- [66] D. Pantel, S. Goetze, D. Hesse, and M. Alexe. Reversible electrical switching of spin polarization in multiferroic tunnel junctions. *Nat Mater*, 11(4):289–293, 2012. ISSN 1476-1122. doi: <http://www.nature.com/nmat/journal/v11/n4/abs/nmat3254.html#supplementary-information>. URL <http://dx.doi.org/10.1038/nmat3254>.
- [67] Y. K. Liu, Y. W. Yin, S. N. Dong, S. W. Yang, T. Jiang, and X. G. Li. Coexistence of four resistance states and exchange bias in la_{0.6}sr_{0.4}mno₃/bifeo₃/la_{0.6}sr_{0.4}mno₃ multiferroic tunnel junction. *Applied Physics Letters*, 104(4):043507, 2014. doi: [doi:http://dx.doi.org/10.1063/1.4863741](http://dx.doi.org/10.1063/1.4863741). URL <http://scitation.aip.org/content/aip/journal/apl/104/4/10.1063/1.4863741>.
- [68] H. M. Yau, Z. B. Yan, N. Y. Chan, K. Au, C. M. Wong, C. W. Leung, F. Y. Zhang, X. S. Gao, and J. Y. Dai. Low-field switching four-state nonvolatile memory based on multiferroic tunnel junctions. *Scientific Reports*, 5:12826, 2015. doi: 10.1038/srep12826<http://www.nature.com/articles/srep12826#supplementary-information>. URL <http://dx.doi.org/10.1038/srep12826><http://www.ncbi.nlm.nih.gov/pmc/articles/PMC4523833/pdf/srep12826.pdf>.
- [69] Andre Chanthbouala, Arnaud Crassous, Vincent Garcia, Karim Bouzehouane, Stephane Fusil, Xavier Moya, Julie Allibe, Bruno Dlubak, Julie Grollier, Stephane Xavier, Cyrile Deranlot, Amir Moshar, Roger Proksch, Neil D. Mathur, Manuel Bibes, and Agnes Barthelemy. Solid-state memories based on ferroelectric tunnel junctions. *Nat Nano*, 7(2):101–104, 2012. ISSN 1748-3387. doi: <http://www.nature.com/nnano/journal/v7/n2/abs/nnano.2011.213.html#supplementary-information>. URL <http://dx.doi.org/10.1038/nnano.2011.213>.
- [70] D. J. Kim, H. Lu, S. Ryu, C. W. Bark, C. B. Eom, E. Y. Tsymbal, and A. Gruverman. Ferroelectric tunnel memristor. *Nano Letters*, 12(11):5697–

- 5702, 2012. ISSN 1530-6984. doi: 10.1021/nl302912t. URL <http://dx.doi.org/10.1021/nl302912t>.
- [71] X. S. Gao, J. M. Liu, K. Au, and J. Y. Dai. Nanoscale ferroelectric tunnel junctions based on ultrathin batio3 film and ag nanoelectrodes. *Applied Physics Letters*, 101(14):142905, 2012. doi: [doi:http://dx.doi.org/10.1063/1.4756918](http://dx.doi.org/10.1063/1.4756918). URL <http://scitation.aip.org/content/aip/journal/apl/101/14/10.1063/1.4756918>.
- [72] Y. W. Yin, J. D. Burton, Y. M. Kim, A. Y. Borisevich, S. J. Pennycook, S. M. Yang, T. W. Noh, A. Gruverman, X. G. Li, E. Y. Tsymbal, and Qi Li. Enhanced tunnelling electroresistance effect due to a ferroelectrically induced phase transition at a magnetic complex oxide interface. *Nat Mater*, 12(5):397–402, 2013. ISSN 1476-1122. doi: 10.1038/nmat3564<http://www.nature.com/nmat/journal/v12/n5/abs/nmat3564.html#supplementary-information>. URL <http://dx.doi.org/10.1038/nmat3564><http://www.nature.com/nmat/journal/v12/n5/pdf/nmat3564.pdf>.
- [73] Weichuan Huang, Yue Lin, Yuewei Yin, Lei Feng, Dalong Zhang, Wenbo Zhao, Qi Li, and Xiaoguang Li. Interfacial ion intermixing effect on four-resistance states in $\text{La}_{0.7}\text{Sr}_{0.3}\text{MnO}_3/\text{BaTiO}_3/\text{La}_{0.7}\text{Sr}_{0.3}\text{MnO}_3$ multiferroic tunnel junctions. *ACS Applied Materials & Interfaces*, 8(16):10422–10429, 2016. ISSN 1944-8244. doi: 10.1021/acsami.6b02150. URL <http://dx.doi.org/10.1021/acsami.6b02150>.
- [74] LD Landau and EM Lifshitz. *Electrodynamics of continuous media*, volume 8 of *Course of theoretical physics*. Pergamon Press Ltd., 1st edition, 1960. ISBN 08-016019-0.
- [75] David Keun Cheng. *Field and wave electromagnetics*, volume 2. Pearson Education Limited, 2nd edition, 2014. ISBN 978-1-292-02656-5.
- [76] J. Clerk Maxwell. A dynamical theory of the electromagnetic field. *Philosophical Transactions of the Royal Society of London*, 155(0):459–512, 1865. ISSN 0261-0523. doi: 10.1098/rstl.1865.0008. URL <http://rstl.royalsocietypublishing.org/content/155/459.shorth><http://rstl.royalsocietypublishing.org/content/155/459.full.pdf>.
- [77] FR Fickett. Standards for measurement of the critical fields of superconductors. *J. Res. Natl. Bur. Stand.*, 90(2):95–113, 1985. ISSN 0022-4332.
- [78] Manfred Fiebig. Revival of the magnetoelectric effect. *Journal of Physics D: Applied Physics*, 38(8):R123, 2005. ISSN 0022-3727. URL <http://stacks.iop.org/0022-3727/38/i=8/a=R01>.

- [79] Hans Schmid. On a magnetoelectric classification of materials. *International Journal of Magnetism*, 4(4):337–361, 1973. ISSN 0020-7365. URL <http://archive-ouverte.unige.ch/unige:32935>.
- [80] Patrick Royce LeClair. *Fundamental Aspects of Spin Polarized Tunneling: magnetic tunnel junctions and spin filters*. Doctoral thesis, Technische Universiteit Eindhoven, 2002.
- [81] D. Pantel and M. Alexe. Electroresistance effects in ferroelectric tunnel barriers. *Physical Review B*, 82(13):134105, 2010. URL <http://link.aps.org/doi/10.1103/PhysRevB.82.134105>.
- [82] Vincent Garcia and Manuel Bibes. Ferroelectric tunnel junctions for information storage and processing. *Nat Commun*, 5, 2014. doi: 10.1038/ncomms5289. URL <http://dx.doi.org/10.1038/ncomms5289>.
- [83] Charles Kittel. *Introduction to solid state physics*. John Wiley & Sons, 8th edition, 2005. ISBN 978-0-471-41526-8.
- [84] Ben G Streetman and Sanjay Kumar Banerjee. *Solid state electronic devices*. Pearson Prentice Hall New Jersey, 6th edition, 2006.
- [85] W. F. Brinkman, R. C. Dynes, and J. M. Rowell. Tunneling conductance of asymmetrical barriers. *Journal of Applied Physics*, 41(5):1915–1921, 1970. doi: [doi:http://dx.doi.org/10.1063/1.1659141](http://dx.doi.org/10.1063/1.1659141). URL <http://scitation.aip.org/content/aip/journal/jap/41/5/10.1063/1.1659141>.
- [86] R. H. Fowler and L. Nordheim. Electron emission in intense electric fields. *Proceedings of the Royal Society of London A: Mathematical, Physical and Engineering Sciences*, 119(781):173–181, 1928. URL <http://rspa.royalsocietypublishing.org/content/119/781/173.abstract>.
- [87] M. Dawber, K. M. Rabe, and J. F. Scott. Physics of thin-film ferroelectric oxides. *Reviews of Modern Physics*, 77(4):1083–1130, 2005. URL <http://link.aps.org/doi/10.1103/RevModPhys.77.1083>.
- [88] Keithley Instruments. An improved method for differential conductance measurements. White paper, Tektronix, 2005. URL http://www.tek.com/sites/tek.com/files/media/document/resources/2610%20Diff%20Conductance_WP.pdf.
- [89] David P. Norton. Synthesis and properties of epitaxial electronic oxide thin-film materials. *Materials Science and Engineering: R: Reports*, 43(5–6): 139–247, 2004. ISSN 0927-796X. doi: <http://dx.doi.org/10.1016/j.mser.2003.12.002>. URL <http://www.sciencedirect.com/science/article/pii/S0927796X03001384>.

- [90] Anthony R West. *Solid state chemistry and its applications*. John Wiley & Sons, 2nd edition, 2014. ISBN 978-1-119-94294-8.
- [91] J. Hemberger, A. Krimmel, T. Kurz, H. A. Krug von Nidda, V. Yu Ivanov, A. A. Mukhin, A. M. Balbashov, and A. Loidl. Structural, magnetic, and electrical properties of single-crystalline $\text{La}_{1-x}\text{Sr}_x\text{MnO}_3$ ($0.4 < x < 0.85$). *Physical Review B*, 66(9):094410, 2002. URL <http://link.aps.org/doi/10.1103/PhysRevB.66.094410>.
- [92] M. Paraskevopoulos, F. Mayr, C. Hartinger, A. Pimenov, J. Hemberger, P. Lunkenheimer, A. Loidl, A. A. Mukhin, V. Yu Ivanov, and A. M. Balbashov. The phase diagram and optical properties of $\text{La}_{1-x}\text{Sr}_x\text{MnO}_3$ for $x \leq 0.2$. *Journal of Magnetism and Magnetic Materials*, 211(1-3):118-127, 2000. ISSN 0304-8853. doi: [http://dx.doi.org/10.1016/S0304-8853\(99\)00722-2](http://dx.doi.org/10.1016/S0304-8853(99)00722-2). URL <http://www.sciencedirect.com/science/article/pii/S0304885399007222>.
- [93] J. H. Van Santen and G. H. Jonker. Electrical conductivity of ferromagnetic compounds of manganese with perovskite structure. *Physica*, 16(7):599-600, 1950. ISSN 0031-8914. doi: [http://dx.doi.org/10.1016/0031-8914\(50\)90104-2](http://dx.doi.org/10.1016/0031-8914(50)90104-2). URL <http://www.sciencedirect.com/science/article/pii/0031891450901042>.
- [94] G. H. Jonker and J. H. Van Santen. Ferromagnetic compounds of manganese with perovskite structure. *Physica*, 16(3):337-349, 1950. ISSN 0031-8914. doi: [http://dx.doi.org/10.1016/0031-8914\(50\)90033-4](http://dx.doi.org/10.1016/0031-8914(50)90033-4). URL <http://www.sciencedirect.com/science/article/pii/0031891450900334>.
- [95] Clarence Zener. Interaction between the d shells in the transition metals. ii. ferromagnetic compounds of manganese with perovskite structure. *Physical Review*, 82(3):403-405, 1951. URL <http://link.aps.org/doi/10.1103/PhysRev.82.403>.
- [96] Richard JD Tilley. *Understanding solids: the science of materials*. John Wiley & Sons, 1st edition, 2004. ISBN 0470852763.
- [97] H. Y. Hwang, S. W. Cheong, N. P. Ong, and B. Batlogg. Spin-polarized intergrain tunneling in $\text{La}_{2/3}\text{Sr}_{1/3}\text{MnO}_3$. *Physical Review Letters*, 77(10):2041-2044, 1996. URL <http://link.aps.org/doi/10.1103/PhysRevLett.77.2041>.
- [98] G. H. Kwei, A. C. Lawson, S. J. L. Billinge, and S. W. Cheong. Structures of the ferroelectric phases of barium titanate. *The Journal of Physical Chemistry*, 97(10):2368-2377, 1993. ISSN 0022-3654. doi: 10.1021/j100112a043. URL <http://dx.doi.org/10.1021/j100112a043><http://pubs.acs.org/doi/pdf/10.1021/j100112a043>.

- [99] L. F. Yin, D. H. Wei, N. Lei, L. H. Zhou, C. S. Tian, G. S. Dong, X. F. Jin, L. P. Guo, Q. J. Jia, and R. Q. Wu. Magnetocrystalline anisotropy in permalloy revisited. *Physical Review Letters*, 97(6):067203, 2006. URL <http://link.aps.org/doi/10.1103/PhysRevLett.97.067203>.
- [100] T. R. McGuire and R. I. Potter. Anisotropic magnetoresistance in ferromagnetic 3d alloys. *Magnetics, IEEE Transactions on*, 11(4):1018–1038, 1975. ISSN 0018-9464. doi: 10.1109/TMAG.1975.1058782. URL <http://ieeexplore.ieee.org/ielx5/20/22814/01058782.pdf?tp=&arnumber=1058782&isnumber=22814>.
- [101] Gesche Nahrwold, Jan M. Scholtyssek, Sandra Motl-Ziegler, Ole Albrecht, Ulrich Merkt, and Guido Meier. Structural, magnetic, and transport properties of permalloy for spintronic experiments. *Journal of Applied Physics*, 108(1):013907, 2010. doi: doi:http://dx.doi.org/10.1063/1.3431384. URL <http://scitation.aip.org/content/aip/journal/jap/108/1/10.1063/1.3431384>.
- [102] P. Yu, X. F. Jin, J. Kudrnovský, D. S. Wang, and P. Bruno. Curie temperatures of fcc and bcc nickel and permalloy: Supercell and green’s function methods. *Physical Review B*, 77(5):054431, 2008. URL <http://link.aps.org/doi/10.1103/PhysRevB.77.054431>.
- [103] Mohammad Abuwasib, Hyungwoo Lee, Alexei Gruverman, Chang-Beom Eom, and Uttam Singisetti. Contact resistance to sr-ro3 and la0.67sr0.33mno3 epitaxial films. *Applied Physics Letters*, 107(24):242905, 2015. doi: doi:http://dx.doi.org/10.1063/1.4938143. URL <http://scitation.aip.org/content/aip/journal/apl/107/24/10.1063/1.4938143>.
- [104] Michael Quirk and Julian Serda. *Semiconductor manufacturing technology*, volume 1. Prentice Hall, Inc., Upper Saddle River, NJ, 2001. ISBN 0-13-081520-9.
- [105] Franz Hickmann. Wire bonding technology. Report, TPT, 1996.
- [106] Quantum Design. Electrical transport option (eto) user’s manual. Report PPMS ETO User’s Manual, 1084-700, Rev. B1, Quantum Design, 2011.
- [107] Keithley Instruments. Low level measurements handbook: Precision dc current, voltage, and resistance measurements. Report, Tektronix, 2016. URL <http://info.tek.com/KI-Low-Level-Measurements-Handbook-LP.html>.
- [108] Stanford Research Systems. About lock-in amplifiers. Report, SRS Stanford Research Systems, 2016. URL <http://www.thinksrs.com/downloads/PDFs/ApplicationNotes/AboutLIAs.pdf>.

- [109] K. J. O' Shea, N. Homonnay, G. Schmidt, and D. A. MacLaren. Investigating the effects of contacting functional oxide films. *Journal of Physics: Conference Series*, 644(1):012001, 2015. ISSN 1742-6596. URL <http://stacks.iop.org/1742-6596/644/i=1/a=012001>.
- [110] Nico Homonnay, Kerry J. ÓShea, Christian Eisenschmidt, Martin Wahler, Donald A. MacLaren, and Georg Schmidt. Interface reactions in lsmo–metal hybrid structures. *ACS Applied Materials & Interfaces*, 7(40):22196–22202, 2015. ISSN 1944-8244. doi: 10.1021/acsami.5b04465. URL <http://dx.doi.org/10.1021/acsami.5b04465>.
- [111] Laurent Mieville, Daniel Worledge, T. H. Geballe, Ramiro Contreras, and K. Char. Transport across conducting ferromagnetic oxide/metal interfaces. *Applied Physics Letters*, 73(12):1736–1738, 1998. doi: [doi:http://dx.doi.org/10.1063/1.122261](http://dx.doi.org/10.1063/1.122261). URL <http://scitation.aip.org/content/aip/journal/apl/73/12/10.1063/1.122261>.
- [112] Kristoffer Skogen Raa. *Electrical Transport Studies of (111)-Oriented BTO/LSMO-Based Heterostructures*. Master thesis, Norwegian University of Science and Technology, 2015. URL <https://daim.idi.ntnu.no/masteroppgave?id=13019>.
- [113] James W. Nilsson and Susan A. Riedel. *Electric Circuits*. Pearson Education, Inc, Prentice Hall, One Lake Street, Upper Saddle River, New Jersey, 07458, 9th edition, 2011. ISBN 978-0-13-705051-2.
- [114] Osamu Nakagawara, Toru Shimuta, Takahiro Makino, Seiichi Arai, Hitoshi Tabata, and Tomoji Kawai. Epitaxial growth and dielectric properties of (111) oriented batio₃/sr tio₃ superlattices by pulsed-laser deposition. *Applied Physics Letters*, 77(20):3257–3259, 2000. doi: [doi:http://dx.doi.org/10.1063/1.1324985](http://dx.doi.org/10.1063/1.1324985). URL <http://scitation.aip.org/content/aip/journal/apl/77/20/10.1063/1.1324985>.
- [115] MicroChem Corporation. Nano pmma and copolymer. Datasheet, MicroChem Corporation, 2001. URL http://microchem.com/pdf/PMMA_Data_Sheet.pdf.
- [116] Shazia Yasin, D. G. Hasko, and H. Ahmed. Comparison of mibk/ipa and water/ipa as pmma developers for electron beam nanolithography. *Microelectronic Engineering*, 61–62:745–753, 2002. ISSN 0167-9317. doi: [http://dx.doi.org/10.1016/S0167-9317\(02\)00468-9](http://dx.doi.org/10.1016/S0167-9317(02)00468-9). URL <http://www.sciencedirect.com/science/article/pii/S0167931702004689>.
- [117] HTE Labs. Physical vapor deposition, magnetron sputter deposition, dc, rf: Metals, alloys, dielectrics. HTE Labs, 2016. [htelabs.com](http://www.htelabs.com), accessed 15 February 2016, 2016. URL http://www.htelabs.com/virtual_fab/pvd_sputter_deposition_physical_vapor_deposition_sputtering.htm.

- [118] J. E. Krzanowski, E. Razon, and A. F. Hmiel. The effect of thin film structure and properties on gold ball bonding. *Journal of Electronic Materials*, 27(11):1211–1215, 1998. ISSN 1543-186X. doi: 10.1007/s11664-998-0071-x. URL <http://dx.doi.org/10.1007/s11664-998-0071-x>.
- [119] I Lum, M Mayer, and Y Zhou. Footprint study of ultrasonic wedge-bonding with aluminum wire on copper substrate. *Journal of electronic materials*, 35(3):433–442, 2006. ISSN 0361-5235.
- [120] AmTECH Microelectronics. Wire bonding guidelines. AmTECH Microelectronics, Inc., 2015. [amtechmicro.com](http://www.amtechmicro.com), accessed 13 May 2016, 2015. URL <http://www.amtechmicro.com/wire-bonding-guidelines/>.
- [121] Rainer Dohle, Tobias Müller, Holger Schulze, and Eugen Milke. Gold wire for room temperature wedge-wedge bonding. In *Proceedings of the 41st international symposium on microelectronics, Providence, Rhode Island*, pages 6–11, 2008.
- [122] J. F. Haag. *A new Explanation for the Degradation of Gold-Aluminium Bonds*, book section 54, pages 381–388. Springer Berlin Heidelberg, 1990. ISBN 978-3-642-45680-0. doi: 10.1007/978-3-642-45678-7_54. URL http://dx.doi.org/10.1007/978-3-642-45678-7_54.
- [123] G. Chen. On the physics of purple-plague formation, and the observation of purple plague in ultrasonically-joined gold-aluminum bonds. *IEEE Transactions on Parts, Materials and Packaging*, 3(4):149–153, 1967. ISSN 0018-9502. doi: 10.1109/TPMP.1967.1135733.
- [124] Elliott Philofsky. Intermetallic formation in gold-aluminum systems. *Solid-State Electronics*, 13(10):1391–1394, 1970. ISSN 0038-1101. doi: [http://dx.doi.org/10.1016/0038-1101\(70\)90172-3](http://dx.doi.org/10.1016/0038-1101(70)90172-3). URL <http://www.sciencedirect.com/science/article/pii/0038110170901723>.
- [125] Masatoshi Imada, Atsushi Fujimori, and Yoshinori Tokura. Metal-insulator transitions. *Reviews of Modern Physics*, 70(4):1039–1263, 1998. URL <http://link.aps.org/doi/10.1103/RevModPhys.70.1039>.
- [126] A. P. Ramirez. Colossal magnetoresistance. *Journal of Physics: Condensed Matter*, 9(39):8171, 1997. ISSN 0953-8984. URL <http://stacks.iop.org/0953-8984/9/i=39/a=005>.
- [127] LJ van der Pauw. A method of measuring specific resistivity and hall effect of discs of arbitrary shape. *Philips Res. Repts*, 13:1–9, 1958.
- [128] LJ van der Pauw. A method of measuring the resistivity and hall coefficient on lamellae of arbitrary shape. *Philips Technical Review*, 20:220–224, 1958.

- [129] Elizabeth A. Dobisz, Susan L. Brandow, Robert Bass, and Jeffrey Mitterender. Effects of molecular properties on nanolithography in polymethyl methacrylate. *Journal of Vacuum Science & Technology B*, 18(1):107–111, 2000. doi: [doi:http://dx.doi.org/10.1116/1.591242](http://dx.doi.org/10.1116/1.591242). URL <http://scitation.aip.org/content/avs/journal/jvstb/18/1/10.1116/1.591242>.
- [130] Maroun Khoury and David K. Ferry. Effect of molecular weight on poly(methyl methacrylate) resolution. *Journal of Vacuum Science & Technology B*, 14(1):75–79, 1996. doi: [doi:http://dx.doi.org/10.1116/1.588437](http://dx.doi.org/10.1116/1.588437). URL <http://scitation.aip.org/content/avs/journal/jvstb/14/1/10.1116/1.588437>.
- [131] Koichi Momma and Fujio Izumi. Vesta 3 for three-dimensional visualization of crystal, volumetric and morphology data. *Journal of Applied Crystallography*, 44(6):1272–1276, 2011. ISSN 0021-8898. doi: [doi:10.1107/S0021889811038970](http://dx.doi.org/10.1107/S0021889811038970). URL <http://dx.doi.org/10.1107/S0021889811038970http://journals.iucr.org/j/issues/2011/06/00/db5098/db5098.pdf>.

Appendix A

Measurements

A.1 Contact Resistance

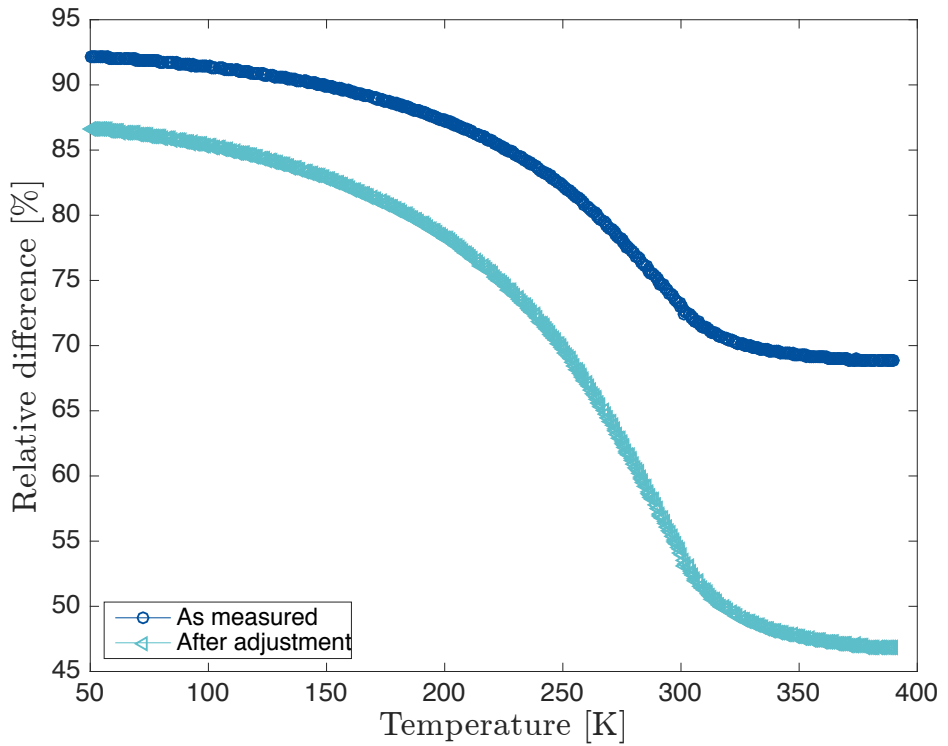


Figure A.1: Relative share of measured resistance ascribed to contact resistance in sample P60212. *As measured* shows the relative difference between improper and proper 4-wire in-plane resistance measurements. *After adjustment* shows the relative difference after multiplying the proper 4-wire resistance with 1.7 to account for the additional LSMO sheet resistance. The improper measurement had 2.42 mm/1.42 mm \approx 1.7 times longer current path in the LSMO than the proper one. The plots are based on the data presented in fig. 7.4

A.2 Current-voltage Curves

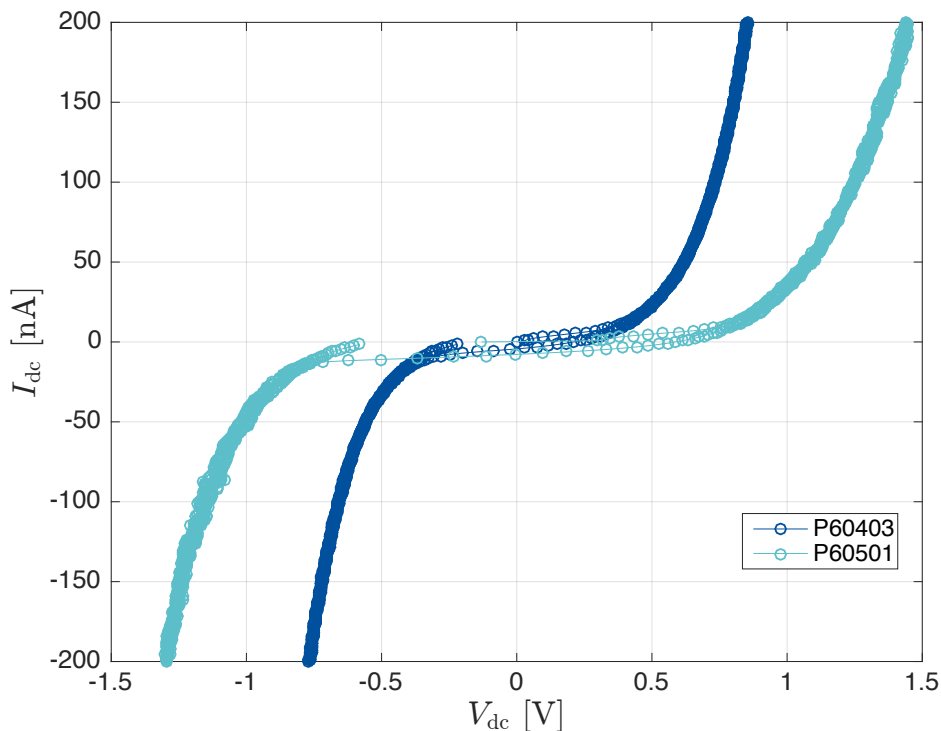


Figure A.2: IV-curves for samples P60403 and P60501 for current excitation $I_{dc} = \pm 200$ nA. Triangular current ramp from zero to positive max to negative max to zero.

A.3 Differential Resistance and Conductance

A.3.1 Calculations for AC lock-in Measurements

First, equation 7.16 is expressed in terms of the capacitance

$$\begin{aligned}
 R &= A(1 + (\omega RC)^2) \\
 \left(\frac{R}{A} - 1\right) \frac{1}{(\omega R)^2} &= C^2 \\
 C &= \pm \frac{1}{\omega R} \sqrt{\frac{R - A}{A}}
 \end{aligned} \tag{A.1}$$

Second, equation A.1 is substituted into 7.17 to express the resistance

$$\begin{aligned}
 \frac{-\omega R^2 \left(\pm \frac{1}{\omega R} \sqrt{\frac{R-A}{A}} \right)}{1 + (\omega R)^2 \left(\left(\frac{R}{A} - 1 \right) \frac{1}{(\omega R)^2} \right)} &= B \\
 \mp \sqrt{\frac{R-A}{A}} \frac{R}{1 + \frac{R}{A} - 1} &= B \\
 \mp \sqrt{\frac{R-A}{A}} &= \frac{B}{A} \\
 \frac{R-A}{A} &= \frac{B^2}{A^2} \\
 R = \frac{B^2}{A} + A &= \frac{A^2 + B^2}{A}
 \end{aligned} \tag{A.2}$$

To express the capacitance, equation A.2 is inserted back into A.1

$$\begin{aligned}
 C &= \pm \frac{1}{\omega \left(\frac{A^2 + B^2}{A} \right)} \sqrt{\frac{\left(\frac{B^2}{A} + A \right) - A}{A}} \\
 C &= \pm \frac{A}{\omega (A^2 + B^2)} \sqrt{\frac{B^2}{A^2}} \\
 C &= \pm \frac{B}{\omega (A^2 + B^2)}
 \end{aligned} \tag{A.3}$$

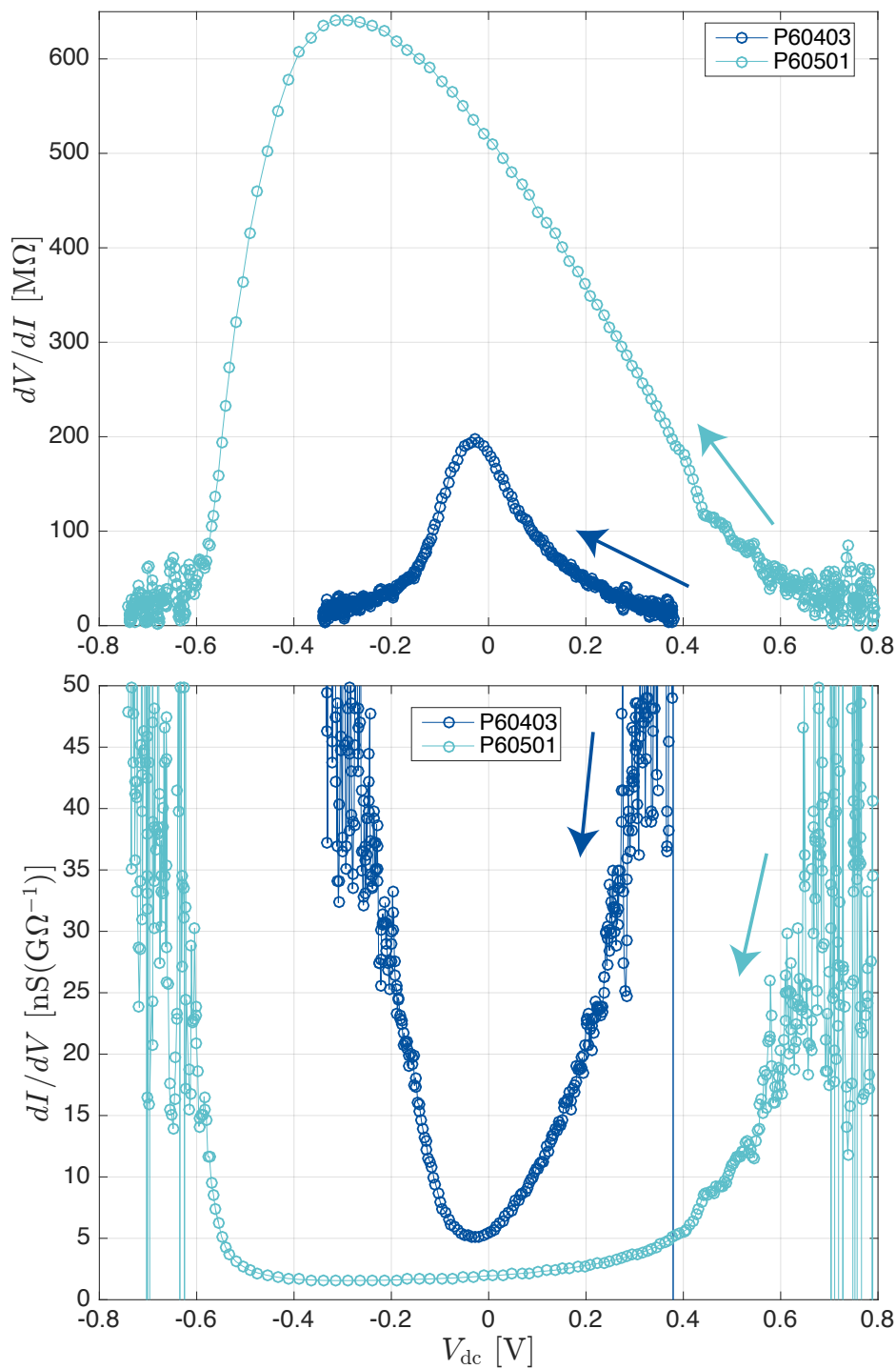


Figure A.3: Differential resistance (upper) and conductance (lower) versus V_{dc} for samples P60403 and P60501. Both plots are based on the continuous current sweeps from $+10$ nA to -10 nA shown in fig. 7.6 (arrows along the sweep direction).

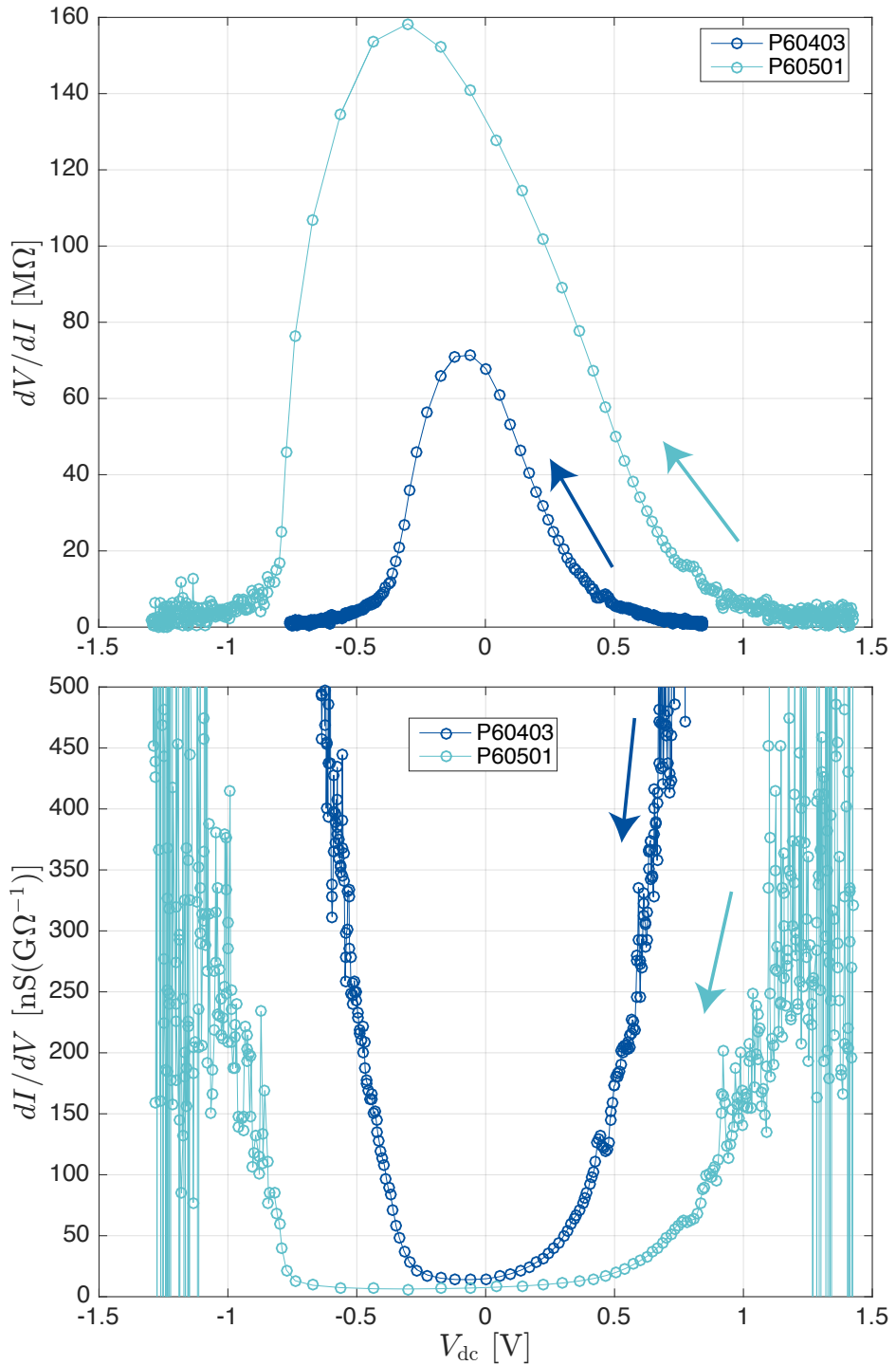


Figure A.4: Differential resistance (upper) and conductance (lower) versus V_{dc} for samples P60403 and P60501. Both plots are based on the continuous current sweeps from +200 nA to -200 nA shown in fig. A.2 (arrows along the sweep direction).

A.4 Magnetic Measurements

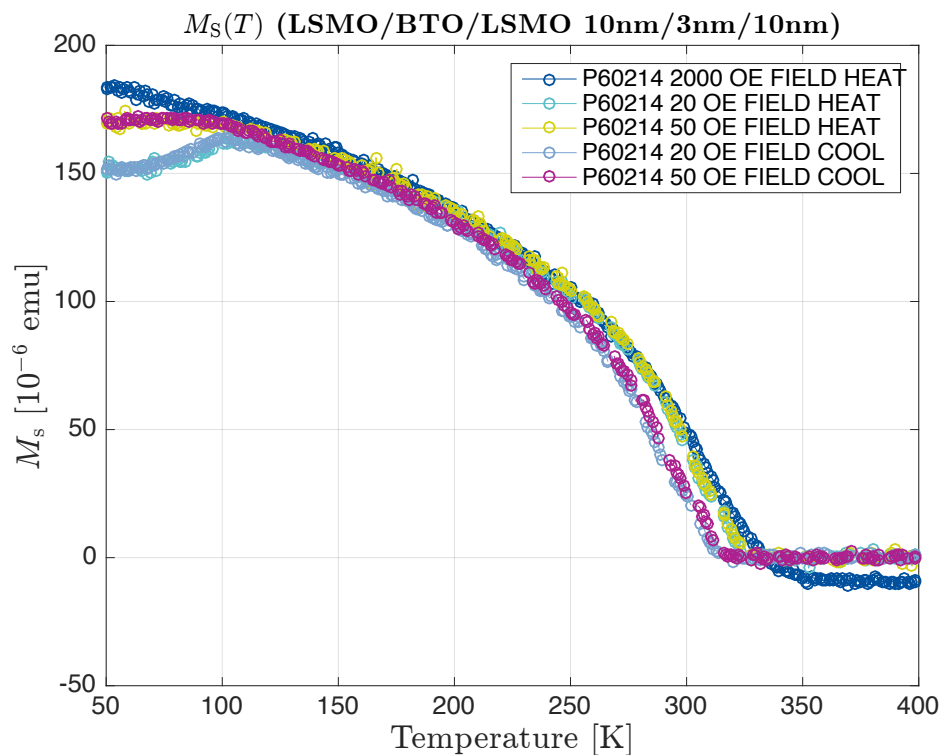


Figure A.5: Saturation magnetization measurements on sample P60214 before any fabrication processing was done.

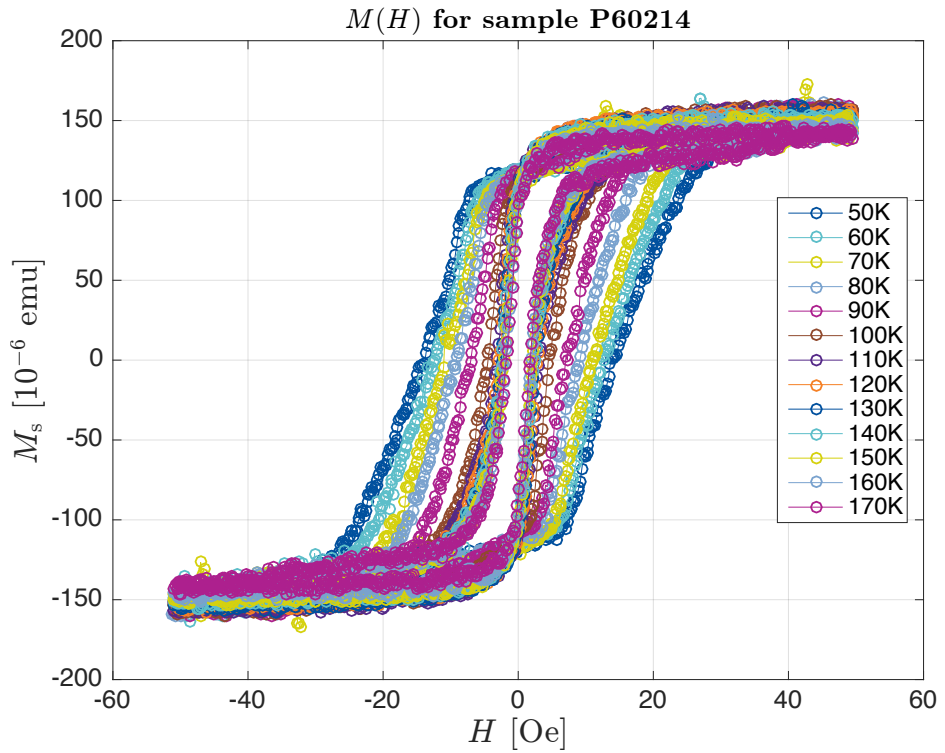


Figure A.6: Magnetization versus magnetic field versus temperature measurements on sample P60214 before any fabrication processing was done.

Appendix B

Fabrication

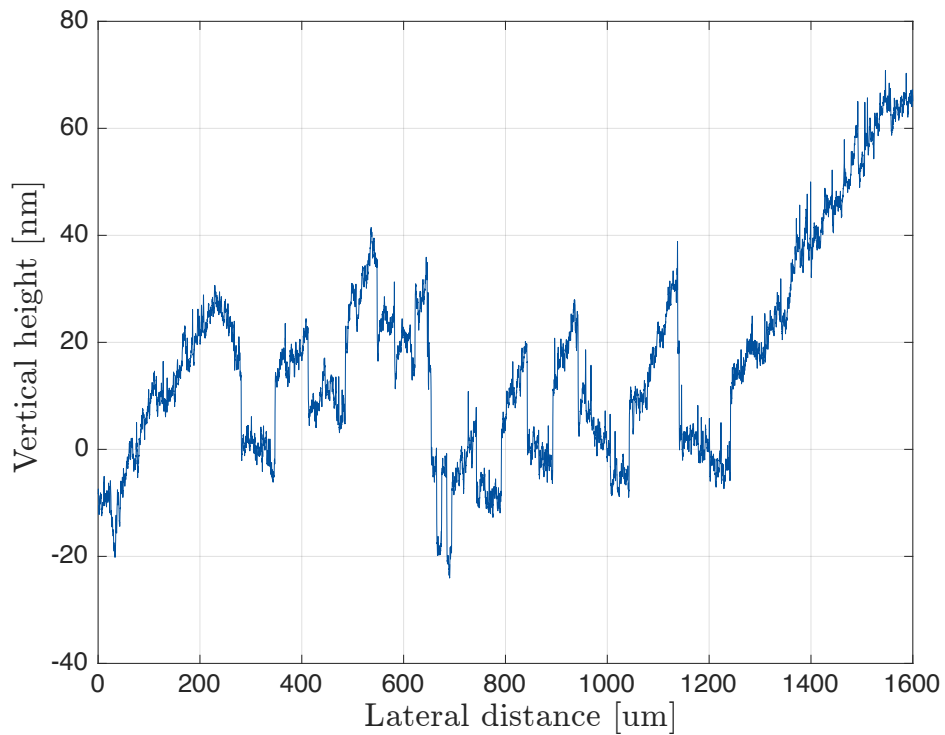


Figure B.1: Titanium step profile after sputter-etching in the AJA system. The etch rate was lower than expected and too close to the profilometer sensitivity to be resolved well. The lines are seen, and the step height is about 15 nm to 20 nm. However, on the right side a step of approximately 30 nm is also visible.

Stage 2; insulation layer deposition and etch

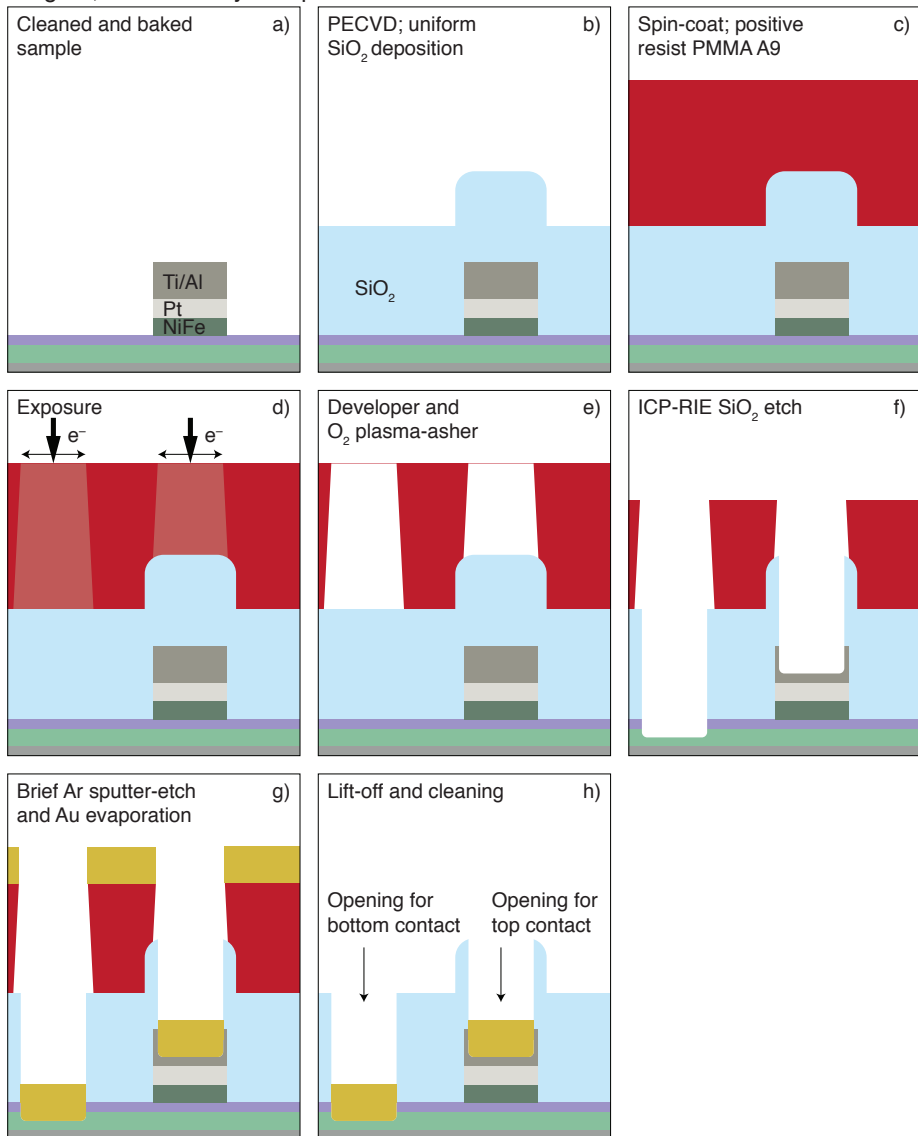


Figure B.2: MFTJ fabrication stage 2 (not to scale). Steps a) to h) show the most important processing steps for insulator deposition by PECVD and dry etching by EBL and ICP-RIE. Alternative termination and masking metals is needed, as gold is prohibited in the PECVD/ICP-RIE systems due to contamination issues.

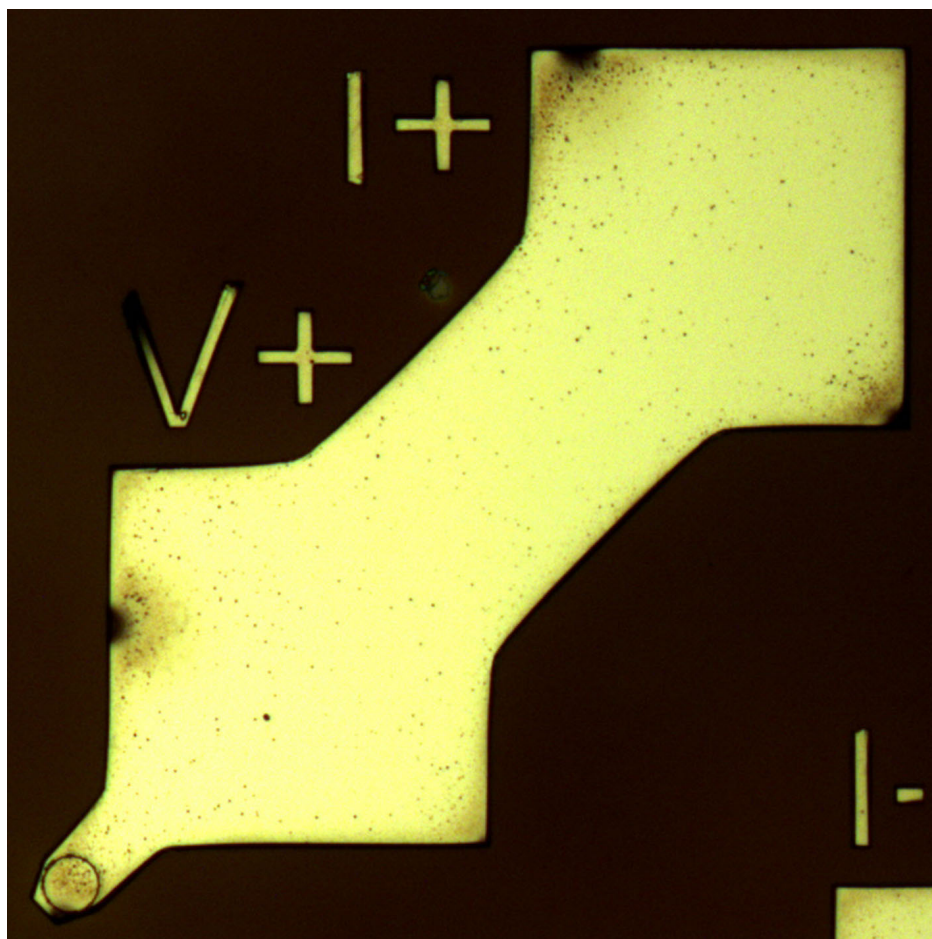


Figure B.3: Signs of boiling or dissolving PMMA during evaporation of titanium (20 nm) and aluminium (1 μm). Relatively low deposition rates were used, 1 \AA s^{-1} to 2 \AA s^{-1} and 5 \AA s^{-1} to 7 \AA s^{-1} for titanium and aluminium, respectively. The partial layout seen here was the first revision and used for sample P60212.

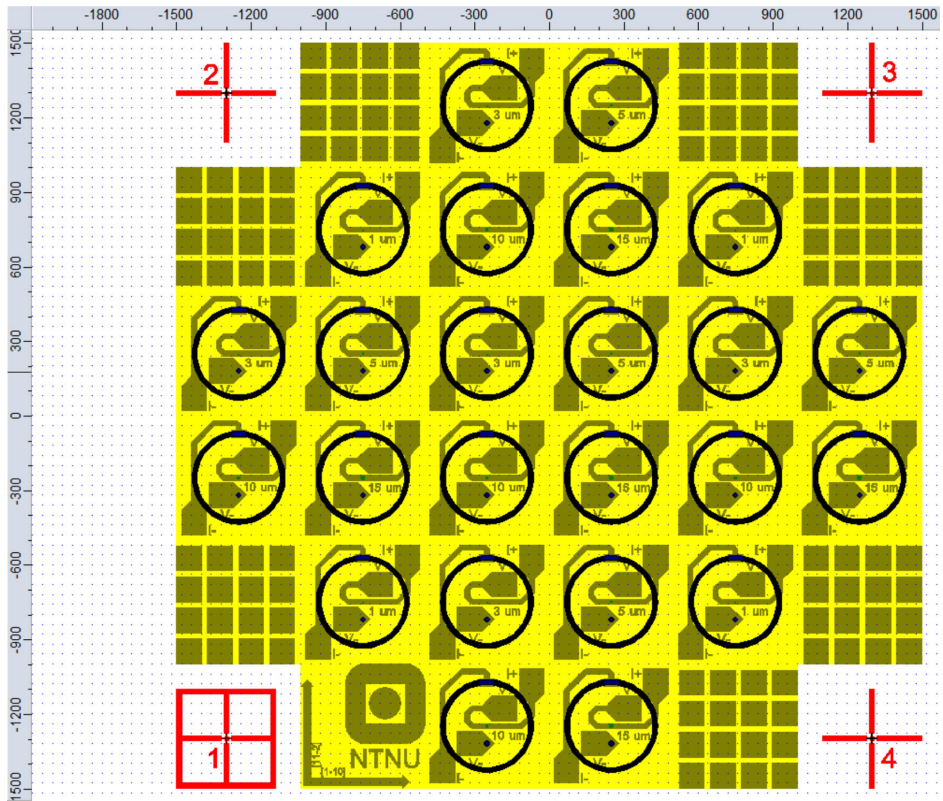


Figure B.4: EBL mask overview, final sample fabrication.

Appendix C

Substrate Symmetries

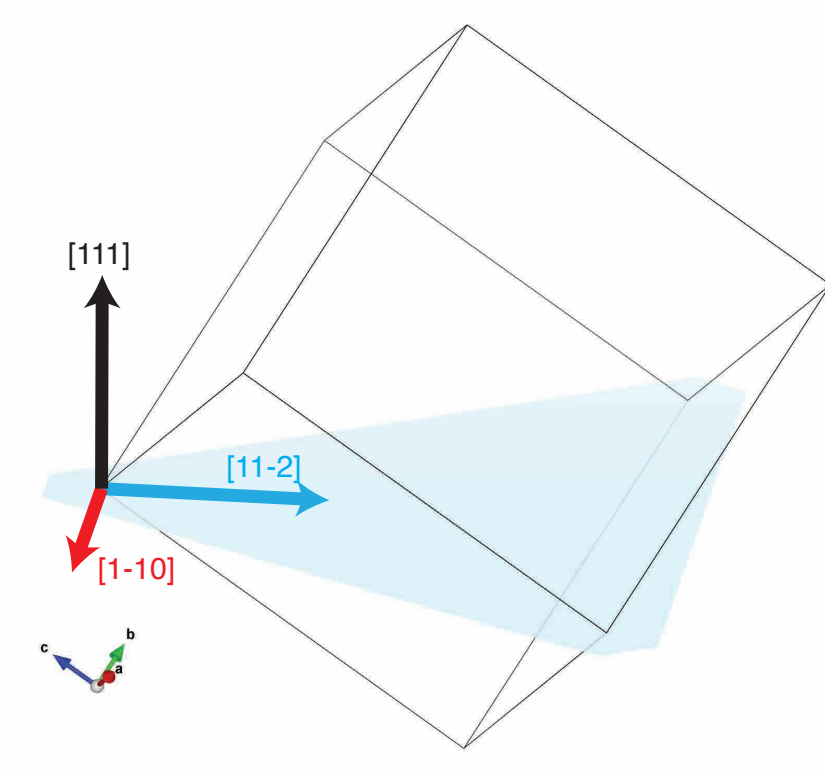


Figure C.1: Sample orientation and important crystal directions.

Appendix D

Program Scripts

D.1 MultiVu Sequence

Listing D.1: sequences/I-V_50K.seq

```
1 !ETODF 'C:\QdVersaLab\Data\Kristoffer\master\P60403+P60501\ETO\IV_50K_ch1+2_
+-IV-Res10nA_3TFC-400K_00000.dat' 0 Untitled
2 !REM Channel1
3 !ETOR 'C:\QdVersaLab\default_ETO.qmap' 0 3 50 0 1E-05 0.4359654 10.00 0 1 0 0
0 0
4 ETOIV 'C:\QdVersaLab\default_ETO.qmap' 0 0 0.0007 0.1525879 0 1 0 1 0 0 2 0 0
5 !ETOR 'C:\QdVersaLab\default_ETO.qmap' 0 3 50 0 1E-05 0.4359654 10.00 0 1 0 0
0 0
6 ETOIV 'C:\QdVersaLab\default_ETO.qmap' 0 0 0.02 0.1525879 0 1 0 1 0 0 3 0 0
7 !ETOR 'C:\QdVersaLab\default_ETO.qmap' 0 3 50 0 1E-05 0.4359654 10.00 0 1 0 0
0 0
8 !REM Channel2
9 !ETOR 'C:\QdVersaLab\default_ETO.qmap' 0 0 3 50 0 1E-05 0.5086263 10.00 0 1 0
0 0
10 ETOIV 'C:\QdVersaLab\default_ETO.qmap' 0 1 0.05 0.1525879 0 1 0 1 0 0 2 0 0
11 !ETOR 'C:\QdVersaLab\default_ETO.qmap' 0 0 3 50 0 1E-05 0.5086263 10.00 0 1 0
0 0
12 ETOIV 'C:\QdVersaLab\default_ETO.qmap' 0 1 0.75 0.1525879 0 1 0 1 0 0 3 0 0
13 !ETOR 'C:\QdVersaLab\default_ETO.qmap' 0 0 3 50 0 1E-05 0.5086263 10.00 0 1 0
0 0
14 !REM I-V curves, 4-wire
15 !REM 130mV range
```

Listing D.2: sequences/RvT_resistivity_50-390K.seq

```
1 REM
2 REM Resistivity measurement; 390K-->50K, 3T field cooling
3 TMP TEMP 390.000000 20.000000 0
4 ETODF 'C:\QdVersaLab\Data\Kristoffer\master\P60212\data\ETO\RvT\incl-cont-res
\RvT_390-50K_3T-cooling.dat' 0 Untitled
5 WAI WAITFOR 0 1 0 0 0 0
6 FLD FIELD 30000.0 300.0 0 0
7 WAI WAITFOR 0 0 1 0 0 0
8 CMB CHAMBER 1
```

```

9  WAI WAITFOR 0 0 0 0 1 0
10 ETOR 'C:\QdVersaLab\default_ET0.qmap' 0 1 0 0.1 9.155273 3.00 1 1 0 0 0 0
11 LPT SCANT 390.000000 50.000000 3.000000 341 0 2
12 ETOR 'C:\QdVersaLab\default_ET0.qmap' 0 6 2 0 0.1 9.155273 3.00 1 1 0 0 0 0
13 ENT EOS
14 ETOR 'C:\QdVersaLab\default_ET0.qmap' 0 4 0
15 ETOR 'C:\QdVersaLab\default_ET0.qmap' 0 5 5
16 REM
17 REM Resistivity measurement; 50K-->390K, 3T field heating
18 ETODF 'C:\QdVersaLab\Data\Kristoffer\master\P60212\data\ET0\RvT\incl-cont-res
  \RvT_50-390K_3T-heating.dat' 0 Untitled
19 FLD FIELD 30000.0 300.0 0 0
20 WAI WAITFOR 0 0 1 0 0 0
21 ETOR 'C:\QdVersaLab\default_ET0.qmap' 0 1 0 0.1 9.155273 3.00 1 1 0 0 0 0
22 LPT SCANT 50.000000 390.000000 3.000000 341 0 2
23 ETOR 'C:\QdVersaLab\default_ET0.qmap' 0 6 2 0 0.1 9.155273 3.00 1 1 0 0 0 0
24 ENT EOS
25 ETOR 'C:\QdVersaLab\default_ET0.qmap' 0 4 0
26 ETOR 'C:\QdVersaLab\default_ET0.qmap' 0 5 5
27 REM
28 REM Resistivity measurement; 390K-->50K, zero field cooling
29 ETODF 'C:\QdVersaLab\Data\Kristoffer\master\P60212\data\ET0\RvT\incl-cont-res
  \RvT_390-50K_ZF-cooling.dat' 0 Untitled
30 FLD FIELD 0.0 300.0 2 0
31 WAI WAITFOR 0 0 1 0 0 0
32 CMB CHAMBER 1
33 WAI WAITFOR 0 0 0 0 1 0
34 ETOR 'C:\QdVersaLab\default_ET0.qmap' 0 1 0 0.1 9.155273 3.00 1 1 0 0 0 0
35 LPT SCANT 390.000000 50.000000 3.000000 341 0 2
36 ETOR 'C:\QdVersaLab\default_ET0.qmap' 0 6 2 0 0.1 9.155273 3.00 1 1 0 0 0 0
37 ENT EOS
38 ETOR 'C:\QdVersaLab\default_ET0.qmap' 0 4 0
39 ETOR 'C:\QdVersaLab\default_ET0.qmap' 0 5 5
40 REM
41 REM Resistivity measurement; 50K-->390K, zero field heating
42 ETODF 'C:\QdVersaLab\Data\Kristoffer\master\P60212\data\ET0\RvT\incl-cont-res
  \RvT_50-390K_ZF-heating.dat' 0 Untitled
43 ETOR 'C:\QdVersaLab\default_ET0.qmap' 0 1 0 0.1 9.155273 3.00 1 1 0 0 0 0
44 LPT SCANT 50.000000 390.000000 3.000000 341 0 2
45 ETOR 'C:\QdVersaLab\default_ET0.qmap' 0 6 2 0 0.1 9.155273 3.00 1 1 0 0 0 0
46 ENT EOS
47 ETOR 'C:\QdVersaLab\default_ET0.qmap' 0 4 0
48 ETOR 'C:\QdVersaLab\default_ET0.qmap' 0 5 5
49 TMP TEMP 300.000000 20.000000 0
50 WAI WAITFOR 600 1 0 0 0 0

```

Listing D.3: sequences/RvHvT_50-390K_20Kstep_50Oe.seq

```

1  LPT SCANT 50.000000 390.000000 10.000000 18 0 0
2  REM R(H) @ +1.0 +/- 0.2 uA
3  ETODF 'C:\QdVersaLab\Data\Kristoffer\P51006\data\eto\TMR\RvHvT_50-390
  K_20Kstep\RVH_500E_+1UA_00000.dat' 0 Untitled
4  FLD FIELD 50.0 50.0 0 0
5  WAI WAITFOR 0 0 1 0 0 0
6  LPB SCANH 50.0 -50.0 1.0 101 0 0 0
7  !ETODVDI 'C:\QdVersaLab\default_ET0.qmap' 0 0 0.0002 1.525879 0 3 0 1 1 0 0
  100 0.001 1 2 1 0
8  ETODVDI 'C:\QdVersaLab\default_ET0.qmap' 0 1 0.0002 1.525879 0 3 0 1 1 0 0
  100 0.001 1 2 1 0
9  ENB EOS
10 LPB SCANH -49.0 50.0 1.0 100 0 0 0
11 !ETODVDI 'C:\QdVersaLab\default_ET0.qmap' 0 0 0.0002 1.525879 0 3 0 1 1 0 0
  100 0.001 1 2 1 0

```

```

12 ETODVDI 'C:\QdVersaLab\default_ET0.qmap' 0 1 0.0002 1.525879 0 3 0 1 1 0 0
    100 0.001 1 2 1 0
13 ENB EOS
14 REM R(H) @ -1.0 +- 0.2 uA
15 ETODF 'C:\QdVersaLab\Data\Kristoffer\P51006\data\eto\TMR\RVHvT_50-390
    K_20Kstep\RVH_500E_-1UA_00000.dat' 0 Untitled
16 FLD FIELD 50.0 50.0 0 0
17 WAI WAITFOR 0 0 1 0 0 0
18 LPB SCANH 50.0 -50.0 1.0 101 0 0 0
19 !ETODVDI 'C:\QdVersaLab\default_ET0.qmap' 0 0 0.0002 1.525879 0 3 0 1 1 0 0
    100 0.001 3 4 1 0
20 ETODVDI 'C:\QdVersaLab\default_ET0.qmap' 0 1 0.0002 1.525879 0 3 0 1 1 0 0
    100 0.001 3 4 1 0
21 ENB EOS
22 LPB SCANH -49.0 50.0 1.0 100 0 0 0
23 !ETODVDI 'C:\QdVersaLab\default_ET0.qmap' 0 0 0.0002 1.525879 0 3 0 1 1 0 0
    100 0.001 3 4 1 0
24 ETODVDI 'C:\QdVersaLab\default_ET0.qmap' 0 1 0.0002 1.525879 0 3 0 1 1 0 0
    100 0.001 3 4 1 0
25 ENB EOS
26 FLD FIELD 0.0 5.0 2 0
27 ENT EOS

```

Listing D.4: sequences/TER_IV-poling_IV-meas+5uA.seq

```

1 REM This script will measure the Tunnel Electroresistance of the device if
  present
2 ETODF 'C:\QdVersaLab\Data\Kristoffer\P51006\data\eto\TER\TER_IV-poling_p-n-
  p_IV+5uA.dat' 0 Untitled
3 REM Polarize with about +2.5 V
4 ETOIV 'C:\QdVersaLab\default_ET0.qmap' 0 1 3.8 0.3051758 0 1 0 1 0 0 2 0 0
5 REM Polarize with about -0.5 V
6 ETOIV 'C:\QdVersaLab\default_ET0.qmap' 0 1 0.465 0.3051758 0 1 0 1 0 0 3 0 0
7 REM Measure IV and differential resistance at about +10 mV
8 ETOIV 'C:\QdVersaLab\default_ET0.qmap' 0 1 0.005 0.3051758 0 1 0 1 1 0 2 0 0
9 ETODVDI 'C:\QdVersaLab\default_ET0.qmap' 0 1 0.001 1.525879 0 4 0 1 1 0 0 500
    0.005 1 3 1 0
10 REM Polarize with about -1.0 V
11 ETOIV 'C:\QdVersaLab\default_ET0.qmap' 0 1 1.25 0.3051758 0 1 0 1 0 0 3 0 0
12 ETOIV 'C:\QdVersaLab\default_ET0.qmap' 0 1 0.005 0.3051758 0 1 0 1 1 0 2 0 0
13 ETODVDI 'C:\QdVersaLab\default_ET0.qmap' 0 1 0.001 1.525879 0 4 0 1 1 0 0 500
    0.005 1 3 1 0
14 REM Polarize with about -1.5 V
15 ETOIV 'C:\QdVersaLab\default_ET0.qmap' 0 1 2.09 0.3051758 0 1 0 1 0 0 3 0 0
16 ETOIV 'C:\QdVersaLab\default_ET0.qmap' 0 1 0.005 0.3051758 0 1 0 1 1 0 2 0 0
17 ETODVDI 'C:\QdVersaLab\default_ET0.qmap' 0 1 0.001 1.525879 0 4 0 1 1 0 0 500
    0.005 1 3 1 0
18 REM Polarize with about -2.0 V
19 ETOIV 'C:\QdVersaLab\default_ET0.qmap' 0 1 3.06 0.3051758 0 1 0 1 0 0 3 0 0
20 ETOIV 'C:\QdVersaLab\default_ET0.qmap' 0 1 0.005 0.3051758 0 1 0 1 1 0 2 0 0
21 ETODVDI 'C:\QdVersaLab\default_ET0.qmap' 0 1 0.001 1.525879 0 4 0 1 1 0 0 500
    0.005 1 3 1 0
22 REM Polarize with about -2.5 V
23 ETOIV 'C:\QdVersaLab\default_ET0.qmap' 0 1 4.2 0.3051758 0 1 0 1 0 0 3 0 0
24 ETOIV 'C:\QdVersaLab\default_ET0.qmap' 0 1 0.005 0.3051758 0 1 0 1 1 0 2 0 0
25 ETODVDI 'C:\QdVersaLab\default_ET0.qmap' 0 1 0.001 1.525879 0 4 0 1 1 0 0 500
    0.005 1 3 1 0
26 REM Polarize with about -2.0 V
27 ETOIV 'C:\QdVersaLab\default_ET0.qmap' 0 1 3.06 0.3051758 0 1 0 1 0 0 3 0 0
28 ETOIV 'C:\QdVersaLab\default_ET0.qmap' 0 1 0.005 0.3051758 0 1 0 1 1 0 2 0 0
29 ETODVDI 'C:\QdVersaLab\default_ET0.qmap' 0 1 0.001 1.525879 0 4 0 1 1 0 0 500
    0.005 1 3 1 0
30 REM Polarize with about -1.5 V

```

```

31 ETOIV 'C:\QdVersaLab\default_ET0.qmap' 0 1 2.09 0.3051758 0 1 0 1 0 0 3 0 0
32 ETOIV 'C:\QdVersaLab\default_ET0.qmap' 0 1 0.005 0.3051758 0 1 0 1 1 0 2 0 0
33 ETODVDI 'C:\QdVersaLab\default_ET0.qmap' 0 1 0.001 1.525879 0 4 0 1 1 0 0 500
   0.005 1 3 1 0
34 REM Polarize with about -1.0 V
35 ETOIV 'C:\QdVersaLab\default_ET0.qmap' 0 1 1.25 0.3051758 0 1 0 1 0 0 3 0 0
36 ETOIV 'C:\QdVersaLab\default_ET0.qmap' 0 1 0.005 0.3051758 0 1 0 1 1 0 2 0 0
37 ETODVDI 'C:\QdVersaLab\default_ET0.qmap' 0 1 0.001 1.525879 0 4 0 1 1 0 0 500
   0.005 1 3 1 0
38 REM Polarize with about -0.5 V
39 ETOIV 'C:\QdVersaLab\default_ET0.qmap' 0 1 0.465 0.3051758 0 1 0 1 0 0 3 0 0
40 ETOIV 'C:\QdVersaLab\default_ET0.qmap' 0 1 0.005 0.3051758 0 1 0 1 1 0 2 0 0
41 ETODVDI 'C:\QdVersaLab\default_ET0.qmap' 0 1 0.001 1.525879 0 4 0 1 1 0 0 500
   0.005 1 3 1 0
42 REM Polarize with about +0.5 V
43 ETOIV 'C:\QdVersaLab\default_ET0.qmap' 0 1 0.42 0.3051758 0 1 0 1 0 0 2 0 0
44 ETOIV 'C:\QdVersaLab\default_ET0.qmap' 0 1 0.005 0.3051758 0 1 0 1 1 0 2 0 0
45 ETODVDI 'C:\QdVersaLab\default_ET0.qmap' 0 1 0.001 1.525879 0 4 0 1 1 0 0 500
   0.005 1 3 1 0
46 REM Polarize with about +1.0 V
47 ETOIV 'C:\QdVersaLab\default_ET0.qmap' 0 1 1.133 0.3051758 0 1 0 1 0 0 2 0 0
48 ETOIV 'C:\QdVersaLab\default_ET0.qmap' 0 1 0.005 0.3051758 0 1 0 1 1 0 2 0 0
49 ETODVDI 'C:\QdVersaLab\default_ET0.qmap' 0 1 0.001 1.525879 0 4 0 1 1 0 0 500
   0.005 1 3 1 0
50 REM Polarize with about +1.5 V
51 ETOIV 'C:\QdVersaLab\default_ET0.qmap' 0 1 1.953 0.3051758 0 1 0 1 0 0 2 0 0
52 ETOIV 'C:\QdVersaLab\default_ET0.qmap' 0 1 0.005 0.3051758 0 1 0 1 1 0 2 0 0
53 ETODVDI 'C:\QdVersaLab\default_ET0.qmap' 0 1 0.001 1.525879 0 4 0 1 1 0 0 500
   0.005 1 3 1 0
54 REM Polarize with about +2.0 V
55 ETOIV 'C:\QdVersaLab\default_ET0.qmap' 0 1 2.8 0.3051758 0 1 0 1 0 0 2 0 0
56 ETOIV 'C:\QdVersaLab\default_ET0.qmap' 0 1 0.005 0.3051758 0 1 0 1 1 0 2 0 0
57 ETODVDI 'C:\QdVersaLab\default_ET0.qmap' 0 1 0.001 1.525879 0 4 0 1 1 0 0 500
   0.005 1 3 1 0
58 REM Polarize with about +2.5 V
59 ETOIV 'C:\QdVersaLab\default_ET0.qmap' 0 1 3.8 0.3051758 0 1 0 1 0 0 2 0 0
60 ETOIV 'C:\QdVersaLab\default_ET0.qmap' 0 1 0.005 0.3051758 0 1 0 1 1 0 2 0 0
61 ETODVDI 'C:\QdVersaLab\default_ET0.qmap' 0 1 0.001 1.525879 0 4 0 1 1 0 0 500
   0.005 1 3 1 0
62 REM Polarize with about +2.0 V
63 ETOIV 'C:\QdVersaLab\default_ET0.qmap' 0 1 2.8 0.3051758 0 1 0 1 0 0 2 0 0
64 ETOIV 'C:\QdVersaLab\default_ET0.qmap' 0 1 0.005 0.3051758 0 1 0 1 1 0 2 0 0
65 ETODVDI 'C:\QdVersaLab\default_ET0.qmap' 0 1 0.001 1.525879 0 4 0 1 1 0 0 500
   0.005 1 3 1 0
66 REM Polarize with about +1.5 V
67 ETOIV 'C:\QdVersaLab\default_ET0.qmap' 0 1 1.953 0.3051758 0 1 0 1 0 0 2 0 0
68 ETOIV 'C:\QdVersaLab\default_ET0.qmap' 0 1 0.005 0.3051758 0 1 0 1 1 0 2 0 0
69 ETODVDI 'C:\QdVersaLab\default_ET0.qmap' 0 1 0.001 1.525879 0 4 0 1 1 0 0 500
   0.005 1 3 1 0
70 REM Polarize with about +1.0 V
71 ETOIV 'C:\QdVersaLab\default_ET0.qmap' 0 1 1.133 0.3051758 0 1 0 1 0 0 2 0 0
72 ETOIV 'C:\QdVersaLab\default_ET0.qmap' 0 1 0.005 0.3051758 0 1 0 1 1 0 2 0 0
73 ETODVDI 'C:\QdVersaLab\default_ET0.qmap' 0 1 0.001 1.525879 0 4 0 1 1 0 0 500
   0.005 1 3 1 0
74 REM Polarize with about +0.5 V
75 ETOIV 'C:\QdVersaLab\default_ET0.qmap' 0 1 0.42 0.3051758 0 1 0 1 0 0 2 0 0
76 ETOIV 'C:\QdVersaLab\default_ET0.qmap' 0 1 0.005 0.3051758 0 1 0 1 1 0 2 0 0
77 ETODVDI 'C:\QdVersaLab\default_ET0.qmap' 0 1 0.001 1.525879 0 4 0 1 1 0 0 500
   0.005 1 3 1 0

```

D.2 WinWrap Basic

Listing D.5: wwb-com/dVdI_all-data.bas

```

1  '#Language "WWB-COM"
2
3  '#Uses ".\SDO\SDO.obm"
4  '#Uses ".\ETO\ETO.obm"
5  '#Uses ".\Utils\Utils.obm"
6  '#Uses ".\MultiVuDataFile\MultiVuDataFile.cls"
7
8  'This script is made for testing and development of specific functionality
   with the ETO-module on a QD Versalab system. It is based on a prototype
   script by QD from the Visual Basic Macro package "
   Macros_QD_Library_Oct_2015", but has been extended and modified by MSC
   student Kristoffer Kjaernes at the Norwegian University of Science and
   Technology, NTNU.
9
10 Option Explicit
11
12 '==== Change the following paths and addresses to your needs
13 'Make sure to have \ on corresponding places. Set ChOne/TwoPath to ""
14 'if you don't want to use separate paths
15 Const Path As String = "C:\QdVersaLab\Data\Kristoffer\master"           'Main
   path to save data
16 Const ChOnePath As String = "\P60501\ETO"                               'Subdirectory for
   Ch1 sample
17 Const ChTwoPath As String = "\P60403\ETO"                               'Subdirectory for
   Ch2 sample
18 Const ChOneName As String = "\RvI\RvI-deviation-harmonics_AC1nA_DC10nA"
   'Ch1 filename
19 Const ChTwoName As String = "\RvI\RvI-deviation-harmonics_AC100pA_DC10nA"
   'Ch2 filename
20 Const ChOneTitle As String = "P60501 R(I_dc) with I_ac = 1nA"          'Ch1 plot
   title
21 Const ChTwoTitle As String = "P60403 R(I_dc) with I_ac = 100pA"        'Ch2
   plot title
22 Const Extension As String = ".dat"                                     'Data file
   extension
23
24 '==== Mechanism for telling the script if there's one or two channels active
   ====
25 Enum ActChan
26     Ch1
27     Ch2
28     Both
29 End Enum
30 'The following variable will be used by the script to run one or both
   channels:
31 Const ActiveChannel As ActChan = Ch1  '***** Change only this declaration to
   your needs
32 'ActiveChannel = Ch1
33
34 '==== Measurement start
35 Sub Main
36     Debug.Clear
37     Dim Run As Byte
38     Dim CurrentChannel As Byte
39     Dim DateTime As String
40     Dim SubPath As String
41     Dim Filename As String
42     Dim Title As String
43     Select Case ActiveChannel

```

```

44     Case 0   'Only run channel 1
45         Run = 1
46         CurrentChannel = 1
47         SubPath = ChOnePath
48         Filename = ChOneName
49         Title = ChOneTitle
50         Debug.Print "Channel 1 selected..."
51     Case 1   'Only run channel 2
52         Run = 1
53         CurrentChannel = 2
54         SubPath = ChTwoPath
55         Filename = ChTwoName
56         Title = ChTwoTitle
57         Debug.Print "Channel 2 selected..."
58     Case 2   'Run both channels in sequence, starting with ch2
59         Run = 2
60         CurrentChannel = 2
61         SubPath = ChTwoPath
62         Filename = ChTwoName
63         Title = ChTwoTitle
64         Debug.Print "Both channels selected..."
65     Case Else 'Something's not right, abandon measurements
66         Run = 0
67         Debug.Print "Something was wrong with the channel initialization.
68             Abandoning measurement..."
69
70 End Select
71
72 While Run
73     Debug.Print "Now running channel ";CurrentChannel; "..."
74
75     'Create data file and write the header.
76     'If the file exists, this will do nothing.
77     'Be sure that all of your columns are the same as the existing file if
78     you are appending!
79     Dim F As New MultiVuDataFile
80     'SetupFile(F) 'Sets up default column headers. Change default plot
81     columns in this function
82     'Assign all the wanted column headers with appropriate names
83     Const TCol As String = "Temperature (K)"
84     Const FCol As String = "Field (Oe)"
85     Const ResCol As String = "Resistance (Ohms)"
86     Const DCCol As String = "Req. DC Offset (mA)"
87     Const ActDCCol As String = "Calculated Actual DC Current (mA)"
88     Const ACCol As String = "Req. AC Excitation (mA)"
89     Const ActACCol As String = "Calculated Actual AC Peak Current (mA)"
90     Const ADCVoltCol As String = "(Peak ADC) Voltage Ampl. (V)"
91     Const InPhCol As String = "In Phase Volt. Ampl. (V)"
92     Const QuadrCol As String = "Quadrature Volt. Ampl. (V)"
93     Const CorrResCol As String = "1-pole Corrected Resistance (Ohms)"
94     Const AcMDACCol As String = "AC MDAC Counts"
95     Const DcMDACCol As String = "DC MDAC Counts"
96     Const AcMDACAmplCol As String = "AC MDAC Ampl"
97     Const DcMDACAmplCol As String = "DC MDAC Ampl"
98     Const PhAnCol As String = "Phase Angle"
99     Const PhDyCol As String = "Phase Delay"
100    Const AvgTmCol As String = "Averaging Time (s)"
101    Const FreqCol As String = "Frequency (Hz)"
102    Const ResStdDevCol As String = "Resistance Std.Dev. (Ohms)"
103    Const SampleVoltCol As String = "Sample Peak Voltage (V)"
104    Const VoltStdDevCol As String = "Voltage Std.Dev. (V)"
105    Const AvgPwrCol As String = "Average Power (W)"
106    Const EtoModeCol As String = "ETO Measurement Mode"
107    Const DspModeCol As String = "DSP Operating Mode"
108    Const IRangeCol As String = "Drive Current Range"
109    Const DriveVoltCol As String = "Voltage of Current Drive (V)"

```

```

106     Const SecHarmCol As String = "2nd Harmonic Amplitude (V)"
107     Const ThirdHarmCol As String = "3rd Harmonic Amplitude (V)"
108     Const AddtlHarmCol As String = "Additional Harmonic Amplitude (V)"
109     Const SecPhaseCol As String = "2nd Harmonic Phase Angle"
110     Const ThirdPhaseCol As String = "3rd Harmonic Phase Angle"
111     Const AddtlPhaseCol As String = "Additional Harmonic Phase Angle"
112     Const AddtlCol As String = "Order of Additional Harmonic"
113
114     'Set up the columns that you would like to write to file
115     'The Label strings are used both as column headers and to access these
116     'columns programmatically (like key-value coding)
117     'You can add axis types if you want a column to be used for multiple
118     'axes:
119     'F.AddColumn(TCol, mvStartupAxisX + mvStartupAxisY1)
120
121     F.AddColumn(TCol, mvStartupAxisNone)
122     F.AddColumn(FCol, mvStartupAxisNone)
123     F.AddColumn(ResCol, mvStartupAxisY1)
124     F.AddColumn(DCCol, mvStartupAxisNone)
125     F.AddColumn(ACCol, mvStartupAxisNone)
126     F.AddColumn(ActDCCol, mvStartupAxisX)
127     F.AddColumn(ActACCol, mvStartupAxisNone)
128     F.AddColumn(ADCVoltCol, mvStartupAxisNone)
129     F.AddColumn(InPhCol, mvStartupAxisNone)
130     F.AddColumn(QuadrCol, mvStartupAxisNone)
131     F.AddColumn(CorrResCol, mvStartupAxisNone)
132     F.AddColumn(ACMDACCol, mvStartupAxisNone)
133     F.AddColumn(DcMDACCol, mvStartupAxisNone)
134     F.AddColumn(ACMDACAmplCol, mvStartupAxisNone)
135     F.AddColumn(DcMDACAmplCol, mvStartupAxisNone)
136     F.AddColumn(PhAnCol, mvStartupAxisY2)
137     F.AddColumn(PhDyCol, mvStartupAxisNone)
138     F.AddColumn(AvgTmCol, mvStartupAxisNone)
139     F.AddColumn(FreqCol, mvStartupAxisNone)
140     F.AddColumn(ResStdDevCol, mvStartupAxisNone)
141     F.AddColumn(SampleVoltCol, mvStartupAxisNone)
142     F.AddColumn(VoltStdDevCol, mvStartupAxisNone)
143     F.AddColumn(AvgPwrCol, mvStartupAxisNone)
144     F.AddColumn(EtoModeCol, mvStartupAxisNone)
145     F.AddColumn(DspModeCol, mvStartupAxisNone)
146     F.AddColumn(IRangeCol, mvStartupAxisNone)
147     F.AddColumn(DriveVoltCol, mvStartupAxisNone)
148     F.AddColumn(SecHarmCol, mvStartupAxisY3)
149     F.AddColumn(ThirdHarmCol, mvStartupAxisY3)
150     F.AddColumn(AddtlHarmCol, mvStartupAxisNone)
151     F.AddColumn(SecPhaseCol, mvStartupAxisNone)
152     F.AddColumn(ThirdPhaseCol, mvStartupAxisNone)
153     F.AddColumn(AddtlPhaseCol, mvStartupAxisNone)
154     F.AddColumn(AddtlCol, mvStartupAxisNone)
155
156     'To prevent overwriting files, the date and time function is used at
157     'the end of filename.
158     DateTime = Utils.DateAndTime()
159     F.CreateFileAndWriteHeader(Join(Array(Path, SubPath, Filename, "-",
160     DateTime, Extension), ""), Title)
161
162     'Open the file for viewing in MultiVu
163     F.OpenInMultiVu()
164
165     Dim I As Double
166     Dim Frequency As Single
167     Dim TotalGain As TGain
168     Dim ACAmplitude As Single
169     Dim StartDCCurrent As Single

```

```

167 Dim EndDCCurrent As Single
168 Dim StepsPerQuadrant As Integer
169 Dim AveragingTime As Single
170 Dim CurrentRange As IRange
171 Dim I_Stepsize As Single
172 Dim MMode As Mode
173 Dim SettlingTime As Single
174 Dim Resistance As Single
175 Dim PeakADCVoltage As Single
176 Dim InPhVoltage As Single
177 Dim QuadrVoltage As Single
178 Dim Temperature As Double
179 Dim Status As Long
180 Dim Field As Double
181 Dim B As Double
182 Dim Sweep As Double
183 Dim FieldRamp As Double
184 Dim StartField As Double
185 Dim EndField As Double
186 Dim Scanfield As Boolean
187 Dim B_stepsize As Double
188 Dim ResStdDev As Single
189 Dim SamplePeakVoltage As Single
190 Dim VoltStdDev As Single
191 Dim AvgPwr As Single
192 Dim DspMode As Integer
193 Dim AcMdacCount As UInteger
194 Dim DcMdacCount As UInteger
195
196 MMode=dVdI 'Resistance, dVdI, IV, Oscilloscope, SpectrumAnalyzer,
           vanderPauw, CriticalCurrent
197 ETO.Set_Mode(MMode)
198
199 '*** USER INPUT NEEDED HERE ***
200 'Define ETO Params
201 Frequency = 1.525879 'Hz. Standard lowest frequencies from QD: IV:
           0.30517578125 dVdI: 1.52587890625 Resistance: 0.43596540178
202 TotalGain = A_1X
203 ACAmplitude = 0.000001 'mA
204 StartDCCurrent = -0.00001 'mA
205 EndDCCurrent = 0.00001 'mA
206 I_Stepsize = 0.00000001 'mA
207 AveragingTime = 10 'sec: averaging time must be larger than 0.5
           sec but less than 1 minute
208 CurrentRange = A_100nA 'the current range must be large enough for the
           DC current + the AC current
209 SettlingTime = 0.5 'sec
210
211 'Make sure the current scan will go the right way
212 If (EndDCCurrent < StartDCCurrent) AndAlso (I_Stepsize > 0) Then
213     I_Stepsize = -I_Stepsize 'Positive value will become negative
214 ElseIf (EndDCCurrent > StartDCCurrent) AndAlso (I_Stepsize < 0) Then
215     I_Stepsize = -I_Stepsize 'Negative value will become positive
216 End If
217
218 '*** USER INPUT NEEDED HERE ***
219 'Define Field Scan params
220 Scanfield = False 'If field sweep is not desired, choose False here.
221 FieldRamp = 100 'Oe/s
222 StartField = -1000
223 EndField = 1000
224 B_stepsize = 50
225
226 'Make sure the field sweep will go the right way

```

```

227     If (EndField < StartField) AndAlso (B_stepsize > 0) AndAlso Scanfield
228         Then
229             B_stepsize = -B_stepsize           'Positive value will become negative
230     ElseIf (EndField > StartField) AndAlso (B_stepsize < 0) AndAlso
231         Scanfield Then
232         B_stepsize = -B_stepsize           'Negative value will become positive
233     End If
234
235 'Initialize Module parameters
236     ETO.Turn_Channel_Off(1)
237     ETO.Turn_Channel_Off(2)
238
239 'Initialize Measurement
240     ETO.Set_Frequency(CurrentChannel, Frequency)
241     ETO.Set_Ave_Time(CurrentChannel, AveragingTime)
242     ETO.Set_I_Range(CurrentChannel, CurrentRange)
243     ETO.Set_Total_Gain(CurrentChannel, TotalGain)
244     ETO.Set_AC_Current(CurrentChannel, ACAmplitude)
245     ETO.Set_DC_Current(CurrentChannel, 0.0)
246     ETO.Set_Addtl_Harm(CurrentChannel, 3)      '3rd...6th harmonic as 3...6
247     ETO.Set_Feedback_Enable(CurrentChannel, 1)
248     ETO.Set_Output_Enable(CurrentChannel, 1)
249 'Ramp to starting current, then initialize a measurement to get settled
250     ETO.Set_DC_Current(CurrentChannel, StartDCCurrent)
251     Wait(SettlingTime)
252     TriggerMeasurement(CurrentChannel)      'Just to "reset" old stuff etc..
253     Wait(AveragingTime+0.5)
254
255 'Start measurement
256     For I = StartDCCurrent To EndDCCurrent Step I_stepsize
257         ETO.Set_DC_Current(CurrentChannel, I)
258         Resistance = MeasureResistance(CurrentChannel, SettlingTime,
259             AveragingTime)
260         MultiVu.GetTemperature(Temperature, Status)
261         MultiVu.GetField(Field, Status)
262         F.SetValue(TCol, Temperature)
263         F.SetValue(ResCol, Resistance)
264         F.SetValue(ADCVoltCol, ETO.Read_ADC_Peak_Volts(CurrentChannel))
265         F.SetValue(InPhCol, ETO.Read_InPh_Volt(CurrentChannel))
266         F.SetValue(QuadrCol, ETO.Read_Quadr_Volt(CurrentChannel))
267         F.SetValue(FCol, Field)
268         F.SetValue(DCCol, ETO.Read_DC_Offset(CurrentChannel))
269         F.SetValue(ACCol, ETO.Read_AC_Amplitude(CurrentChannel))
270         F.SetValue(ActDCCol, ETO.Read_Act_DC_Current(CurrentChannel))
271         F.SetValue(ActACCol, ETO.Read_Act_AC_Peak_Current(CurrentChannel))
272         F.SetValue(CorrResCol, ETO.Read_Corr_Resistance(CurrentChannel))
273         'F.SetValue(AcMDACCol, ETO.Read_AC_MDAC_Counts(CurrentChannel))
274         'F.SetValue(DcMDACCol, ETO.Read_DC_MDAC_Counts(CurrentChannel))
275         AcMdacCount = ETO.Read_AC_MDAC_Counts(CurrentChannel) 'Detour to get
276             the unsigned integer value right
277         DcMdacCount = ETO.Read_DC_MDAC_Counts(CurrentChannel) 'Detour to get
278             the unsigned integer value right
279         F.SetValue(AcMDACCol, AcMdacCount)
280         F.SetValue(DcMDACCol, DcMdacCount)
281         F.SetValue(AcMDACAmplCol, ETO.Read_AC_MDAC_Ampl(CurrentChannel))
282         F.SetValue(DcMDACAmplCol, ETO.Read_DC_MDAC_Ampl(CurrentChannel))
283         F.SetValue(PhAnCol, ETO.Read_Phase_Angle(CurrentChannel))
284         F.SetValue(PhDyCol, ETO.Read_Phase_Delay(CurrentChannel))
285         F.SetValue(AvgTmCol, ETO.Read_Ave_Time(CurrentChannel))
286         F.SetValue(FreqCol, ETO.Read_Frequency(CurrentChannel))
287         F.SetValue(ResStdDevCol, ETO.Read_Resistance_StdDev(CurrentChannel))
288         F.SetValue(SampleVoltCol, ETO.Read_Sample_Peak_Volts(CurrentChannel))
289         F.SetValue(VoltStdDevCol, ETO.Read_Voltage_StdDev(CurrentChannel))
290         F.SetValue(AvgPwrCol, ETO.Read_Average_Power(CurrentChannel))
291         F.SetValue(EtoModeCol, ETO.Read_ET0_Mode(CurrentChannel))

```

```

287     F.SetValue(DspModeCol,ETO.Read_DSP_Mode(CurrentChannel))
288     F.SetValue(IRangeCol,ETO.Read_I_Range(CurrentChannel))
289     F.SetValue(DriveVoltCol,ETO.Read_Current_Drive_Appl_Volts(
        CurrentChannel))
290     F.SetValue(SecHarmCol,ETO.Read_2nd_Harm(CurrentChannel))
291     F.SetValue(ThirdHarmCol,ETO.Read_3rd_Harm(CurrentChannel))
292     F.SetValue(AddtlHarmCol,ETO.Read_Addtl_Harm(CurrentChannel))
293     F.SetValue(SecPhaseCol,ETO.Read_2nd_Harm_Phase(CurrentChannel))
294     F.SetValue(ThirdPhaseCol,ETO.Read_3rd_Harm_Phase(CurrentChannel))
295     F.SetValue(AddtlPhaseCol,ETO.Read_Addtl_Harm_Phase(CurrentChannel))
296     F.SetValue(AddtlCol,ETO.Read_Addtl_Order(CurrentChannel))
297     F.WriteData()
298     Next I
299
300     'Turn off field when done
301     MultiVu.SetField(0,FieldRamp,2,0)           'Oscillate field to zero
302
303     'Always end at zero bias
304     ETO.Set_DC_Current(CurrentChannel, 0.0)
305     ETO.Set_AC_Current(CurrentChannel, 0.0)
306
307     'Turn off Channels when done
308     ETO.Turn_Channel_Off(1)
309     ETO.Turn_Channel_Off(2)
310
311     'Run again with channel 1 if both were selected. If only one channel was
        selected,
312     'or if both channels are completed, while loop will terminate with Run=0
313     Run = Run - 1
314     CurrentChannel = 1
315     SubPath = ChOnePath
316     Filename = ChOneName
317     Title = ChOneTitle
318     If Run = 0 Then Debug.Print "Script finished successfully..."
319     Wend
320 End Sub
321
322 Function TriggerMeasurement(Channel As Integer)
323     If Channel = 1 Then
324         ETO.Trigger1()
325     Else
326         ETO.Trigger2()
327     End If
328 End Function
329
330 Function MeasureResistance(ChNum As Byte, Settle As Single, AveT As Single)
        As Single
331     Wait(Settle)
332     TriggerMeasurement(ChNum)
333     If AveT > 1.0 Then
334         Wait(AveT+0.5)
335     Else
336         Wait(AveT*1.5)
337     End If
338     MeasureResistance=ETO.Read_Resistance(ChNum)
339 End Function

```

Listing D.6: wwb-com/ETO.obm

```

1  VERSION 1.0 OBJECT
2  BEGIN
3      MultiUse = 0   'False
4  END

```

```
5 Attribute VB_PredeclaredId = True
6 Attribute VB_Creatable = True
7 Attribute VB_Exposed = True
8 Attribute VB_GlobalNameSpace = False
9 Attribute VB_Name = "ETO"
10 'ETO.obm
11 'Engineering prototype SAX object for CAN ACT
12
13 'This object file has been extended from the initial version by MSc student
14 'Kristoffer Kjaernes
15 'at the Norwegian University of Science and Technology (NTNU), Norway. It has
16 'been developed for
17 'specific functionality with the ETO module on a VersaLab system. It's been
18 'extended from the
19 'initial version found in "Macros_QD_Library_Oct_2015".
20
21 '#Uses "..\SDO\SDO.obm"
22
23 Option Explicit
24
25 Enum TGain
26     A_1X
27     B_3X
28     C_10X
29     D_30X
30     E_100X
31     F_300X
32     G_900X
33     H_3000X
34     I_9000X
35     J_30000X
36     K_90000X
37 End Enum
38
39 Enum IRange
40     A_100nA
41     B_1uA
42     C_10uA
43     D_100uA
44     E_1mA
45     F_10mA
46     G_100mA
47 End Enum
48
49 'Modes Oscilloscope through CriticalCurrent might not be supported by ETO?
50 Enum Mode
51     Resistance
52     dVdI
53     IV
54     Oscilloscope
55     SpectrumAnalyzer
56     vanderPauw
57     CriticalCurrent
58 End Enum
59
60 Enum Waveform
61     Sine
62     Triangle
63     Ramp_up
64     Ramp_dn
65 End Enum
66
67 Dim ETOID As Long
```

```

67 Private Sub Object_Initialize()
68 'set the default values for the ACT
69     ETOID = 19
70 End Sub
71
72 'Read ETO firmware Value
73 Function ReadFirmwareRev() As String
74     ReadFirmwareRev = SDO.ReadSDO(ETOID,&h100A,0, vbString)
75 End Function
76
77 '''''' Module Controls Start ''''''
78 '''''' Main index 0x6050
79 'Set Module Mode
80 Function Set_Mode(Mode As Byte)
81     Dim Address As Long
82     Address = &h6050
83     SDO.WriteSDO(ETOID, Address, 2, Mode)
84 End Function
85 'Read Module Mode (ETO)
86 Function Read_ETO_Mode(Channel As Integer) As Byte
87     Dim Address As Long
88     Address = &h6050
89     Read_ETO_Mode = SDO.ReadSDO(ETOID, Address, 2, vbByte)
90 End Function
91
92 'Excitation Waveform Select
93 Function Set_Waveform(Waveform As Byte)
94     Dim Address As Long
95     Address = &h6050
96     SDO.WriteSDO(ETOID, Address, 3, Waveform)
97 End Function
98
99 'Trigger to perform a single measurement of the selected mode on Ch1
100 Function Trigger1()
101     Dim Address As Long
102     Address = &h6050
103     SDO.WriteSDO(ETOID, Address, 4, CByte(1))
104 End Function
105
106 'Trigger to perform a single measurement of the selected mode on Ch2
107 Function Trigger2()
108     Dim Address As Long
109     Address = &h6050
110     SDO.WriteSDO(ETOID, Address, 5, CByte(1))
111 End Function
112
113 'Initialize DSP
114 'Write 1 to stop measuring and enter setup mode.
115 'Write 0 to leave setup mode and start measuring.
116 Function InitDSP()
117     Dim Address As Long
118     Address = &h6050
119     SDO.WriteSDO(ETOID, Address, 6, CByte(1))
120 End Function
121 '''''' Module Controls End ''''''
122
123 '''''' IV Sweep Controls Start ''''''
124 '''''' Main index 0x6060
125 'Not yet implemented
126 '''''' Module Controls End ''''''
127
128 '''''' Current Drive Controls Start ''''''
129 '''''' Main index 0x6110 (ch1) 0x6210 (ch2)
130 'Set User Requested Frequency
131 Function Set_Frequency(Channel As Integer, F As Single)

```

```

132   Dim Address As Long
133   Address = &h6010 + Channel*&h100
134   SDO.WriteSDO(ETOID, Address, 1, F)
135 End Function
136 'Read User Requested Frequency
137 Function Read_Req_Frequency(Channel As Integer) As Single
138   Dim Address As Long
139   Address = &h6010 + Channel*&h100
140   Read_Req_Frequency = SDO.ReadSDO(ETOID, Address, 1, vbSingle)
141 End Function
142 'Read Actual DSP Frequency Returned by Module
143 Function Read_Frequency(Channel As Integer) As Single
144   Dim Address As Long
145   Address = &h6010 + Channel*&h100
146   Read_Frequency = SDO.ReadSDO(ETOID, Address, 2, vbSingle)
147 End Function
148
149 'Set Current Range
150 Function Set_I_Range(Channel As Integer, Range As Byte)
151   Dim Address As Long
152   Address = &h6010 + Channel*&h100
153   SDO.WriteSDO(ETOID, Address, 3, Range)
154 End Function
155 'Read Current Range
156 Function Read_I_Range(Channel As Integer) As Byte
157   Dim Address As Long
158   Address = &h6010 + Channel*&h100
159   Read_I_Range = SDO.ReadSDO(ETOID, Address, 3, vbByte)
160 End Function
161
162 'Read AC Multiplying DAC (MDAC) Amplitude (0-1 unit unknown)
163 Function Read_AC_MDAC_Ampl(Channel As Integer) As Single
164   Dim Address As Long
165   Address = &h6010 + Channel*&h100
166   Read_AC_MDAC_Ampl = SDO.ReadSDO(ETOID, Address, 4, vbSingle)
167 End Function
168
169 'Read DC Multiplying DAC (MDAC) Amplitude (0-1 unit unknown)
170 Function Read_DC_MDAC_Ampl(Channel As Integer) As Single
171   Dim Address As Long
172   Address = &h6010 + Channel*&h100
173   Read_DC_MDAC_Ampl = SDO.ReadSDO(ETOID, Address, 5, vbSingle)
174 End Function
175
176 'Set AC current amplitude. Requested AC peak output current in mA: 0-100 mA
177 Function Set_AC_Current(Channel As Integer, F As Single)
178   Dim Address As Long
179   Address = &h6010 + Channel*&h100
180   SDO.WriteSDO(ETOID,Address,6,F)
181 End Function
182 'Read AC current amplitude setpoint (this is the currently requested setpoint
    , see below for actual AC current)
183 Function Read_AC_Amplitude(Channel As Integer) As Single
184   Dim Address As Long
185   Address = &h6010 + Channel*&h100
186   Read_AC_Amplitude = SDO.ReadSDO(ETOID,Address, 6, vbSingle)
187 End Function
188
189 'Set DC Current Offset. Requested DC output current in mA: 0-100 mA
190 Function Set_DC_Current(Channel As Integer, F As Single)
191   Dim Address As Long
192   Address = &h6010 + Channel*&h100
193   SDO.WriteSDO(ETOID,Address, 7, F)
194 End Function
195 'Read DC Current Offset (this is the currently requested setpoint, see below

```

```

    for actual DC current)
196 Function Read_DC_Offset(Channel As Integer) As Single
197     Dim Address As Long
198     Address = &h6010 + Channel*&h100
199     Read_DC_Offset = SDO.ReadSDO(ETOID,Address, 7, vbSingle)
200 End Function
201
202 'Set Current Drive Output Enable
203 Function Set_Output_Enable(Channel As Integer, J As Byte)
204     Dim Address As Long
205     Address = &h6010 + Channel*&h100
206     SDO.WriteSDO(ETOID, Address, 8, J)
207 End Function
208
209 'Set Current Drive High-Z Enable
210 Function Set_Feedback_Enable(Channel As Integer, J As Byte)
211     Dim Address As Long
212     Address = &h6010 + Channel*&h100
213     SDO.WriteSDO(ETOID, Address, 9, J)
214 End Function
215
216 'Read Applied Voltage of Current Drive Dropping Resistors (0-30V)
217 Function Read_Current_Drive_Appl_Volts(Channel As Integer) As Single
218     Dim Address As Long
219     Address = &h6010 + Channel*&h100
220     Read_Current_Drive_Appl_Volts = SDO.ReadSDO(ETOID,Address, 10, vbSingle)
221 End Function
222
223 'Read AC Multiplying DAC Counts (0-65535, unsigned 16bit)
224 Function Read_AC_MDAC_Counts(Channel As Integer) As Integer
225     Dim Address As Long
226     Address = &h6010 + Channel*&h100
227     Read_AC_MDAC_Counts = SDO.ReadSDO(ETOID, Address, 11, vbInteger)
228 End Function
229
230 'Read DC Multiplying DAC Counts (0-65535, unsigned 16bit)
231 Function Read_DC_MDAC_Counts(Channel As Integer) As Integer
232     Dim Address As Long
233     Address = &h6010 + Channel*&h100
234     Read_DC_MDAC_Counts = SDO.ReadSDO(ETOID, Address, 12, vbInteger)
235 End Function
236 '''' Current Drive Controls End ''''
237
238 '''' Current Readback Start ''''
239 '''' Main index 0x6112 (ch1) 0x6212 (ch2)
240 'Read Calculated AC Peak Current Readback: This is the actual AC current
    applied based on the MDAC counts and the low-Z correction if enabled:
    0-100 mA
241 Function Read_Act_AC_Peak_Current(Channel As Integer) As Single
242     Dim Address As Long
243     Address = &h6012 + Channel*&h100
244     Read_Act_AC_Peak_Current = SDO.ReadSDO(ETOID,Address, 1, vbSingle)
245 End Function
246
247 'Read Calculated DC Current Readback: This is the actual DC current applied
    based on the MDAC counts and the low-Z correction if enabled: 0-100 mA
248 Function Read_Act_DC_Current(Channel As Integer) As Single
249     Dim Address As Long
250     Address = &h6012 + Channel*&h100
251     Read_Act_DC_Current = SDO.ReadSDO(ETOID,Address, 2, vbSingle)
252 End Function
253
254 'Set Lead Resistance: The value of the probe lead resistance in Ohms: 0-100
    kOhms
255 Function Set_Lead_Res(Channel As Integer, F As Single)

```

```

256   Dim Address As Long
257   Address = &h6012 + Channel*&h100
258   SDO.WriteSDO(ETOID,Address, 3, F)
259 End Function
260 'Read Lead Resistance: The value of the probe lead resistance in Ohms: 0-100
    kOhms
261 Function Read_Lead_Res(Channel As Integer) As Single
262   Dim Address As Long
263   Address = &h6010 + Channel*&h100
264   Read_Lead_Res = SDO.ReadSDO(ETOID,Address, 3, vbSingle)
265 End Function
266
267 'Read Low-Z Correction factor: Unitless multiplicative factor to calculate
    the corrected output current: 0-10
268 Function Read_LowZ_CF(Channel As Integer) As Single
269   Dim Address As Long
270   Address = &h6012 + Channel*&h100
271   Read_LowZ_CF = SDO.ReadSDO(ETOID,Address, 4, vbSingle)
272 End Function
273
274 'Set low-Z Drive Current Correction: Flag to enable the current correction
    due to low-Z mode:
275 Function Set_LowZ_I_Corr(Channel As Integer, J As Byte)
276   Dim Address As Long
277   Address = &h6012 + Channel*&h100
278   SDO.WriteSDO(ETOID, Address, 5, J)
279 End Function
280 '''' Current Readback End ''''
281
282 '''' DSP Controls Start ''''
283 '''' Main index 0x6160 (ch1) 0x6260 (ch2)
284 'Set Averaging Time
285 Function Set_Ave_Time(Channel As Integer, F As Single)
286   Dim Address As Long
287   Address = &h6060 + Channel*&h100
288   SDO.WriteSDO(ETOID,Address, 1, F)
289 End Function
290 'Read Averaging Time
291 Function Read_Ave_Time(Channel As Integer) As Single
292   Dim Address As Long
293   Address = &h6060 + Channel*&h100
294   Read_Ave_Time = SDO.ReadSDO(ETOID,Address, 2, vbSingle)
295 End Function
296
297 'Read ADC Peak Voltage
298 Function Read_ADC_Peak_Volts(Channel As Integer) As Single
299   Dim Address As Long
300   Address = &h6060 + Channel*&h100
301   Read_ADC_Peak_Volts = SDO.ReadSDO(ETOID,Address, 3, vbSingle)
302 End Function
303
304 'Read In-Phase Voltage Amplitude
305 Function Read_InPh_Volt(ByVal Channel As Integer) As Single
306   Dim Address As Long
307   Address = &h6060 + Channel*&h100
308   Read_InPh_Volt = SDO.ReadSDO(ETOID, Address, 4, vbSingle)
309 End Function
310
311 'Read Quadrature Voltage Amplitude
312 Function Read_Quadr_Volt(ByVal Channel As Integer) As Single
313   Dim Address As Long
314   Address = &h6060 + Channel*&h100
315   Read_Quadr_Volt = SDO.ReadSDO(ETOID, Address, 5, vbSingle)
316 End Function
317

```

```

318 'Read Phase Angle
319 Function Read_Phase_Angle(Channel As Integer) As Single
320     Dim Address As Long
321     Address = &h6060 + Channel*&h100
322     Read_Phase_Angle = SDO.ReadSDO(ETOID, Address, 6, vbSingle)
323 End Function
324
325 'Read Phase Delay
326 Function Read_Phase_Delay(Channel As Integer) As Single
327     Dim Address As Long
328     Address = &h6060 + Channel*&h100
329     Read_Phase_Delay = SDO.ReadSDO(ETOID, Address, 7, vbSingle)
330 End Function
331
332 'Read Resistance
333 Function Read_Resistance(Channel As Integer) As Single
334     Dim Address As Long
335     Address = &h6060 + Channel*&h100
336     Read_Resistance = SDO.ReadSDO(ETOID, Address, 8, vbSingle)
337 End Function
338
339 'Read 1-Pole Model Corrected Resistance
340 Function Read_Corr_Resistance(ByVal Channel As Integer) As Single
341     Dim Address As Long
342     Address = &h6060 + Channel*&h100
343     Read_Corr_Resistance = SDO.ReadSDO(ETOID, Address, 9, vbSingle)
344 End Function
345
346 'Read Sample Peak Voltage 0-5V
347 Function Read_Sample_Peak_Volts(Channel As Integer) As Single
348     Dim Address As Long
349     Address = &h6060 + Channel*&h100
350     Read_Sample_Peak_Volts = SDO.ReadSDO(ETOID, Address, 13, vbSingle)
351 End Function
352
353 'Read Average Power (0-5 W)
354 Function Read_Average_Power(Channel As Integer) As Single
355     Dim Address As Long
356     Address = &h6060 + Channel*&h100
357     Read_Average_Power = SDO.ReadSDO(ETOID, Address, 16, vbSingle)
358 End Function
359
360 'Read Voltage Standard Dev.
361 Function Read_Voltage_StdDev(Channel As Integer) As Single
362     Dim Address As Long
363     Address = &h6060 + Channel*&h100
364     Read_Voltage_StdDev = SDO.ReadSDO(ETOID, Address, 17, vbSingle)
365 End Function
366
367 'Read Resistance Standard Dev.
368 Function Read_Resistance_StdDev(Channel As Integer) As Single
369     Dim Address As Long
370     Address = &h6060 + Channel*&h100
371     Read_Resistance_StdDev = SDO.ReadSDO(ETOID, Address, 18, vbSingle)
372 End Function
373
374 'Read DSP Operating Mode
375 Function Read_DSP_Mode(Channel As Integer) As Integer
376     Dim Address As Long
377     Address = &h6060 + Channel*&h100
378     Read_DSP_Mode = SDO.ReadSDO(ETOID, Address, 19, vbInteger)
379 End Function
380 '''' DSP Controls End ''''
381
382 '''' Measured Harmonics Start ''''

```

```

383  '''' Main index 0x6165 (ch1) 0x6265 (ch2)
384  'Read 2nd Harmonic Amplitude (0-5 V)
385  Function Read_2nd_Harm(Channel As Integer) As Single
386      Dim Address As Long
387      Address = &h6065 + Channel*&h100
388      Read_2nd_Harm = SDO.ReadSDO(ETOID, Address, 1, vbSingle)
389  End Function
390  'Read 2nd Harmonic Phase Angle (0-360)
391  Function Read_2nd_Harm_Phase(Channel As Integer) As Single
392      Dim Address As Long
393      Address = &h6065 + Channel*&h100
394      Read_2nd_Harm_Phase = SDO.ReadSDO(ETOID, Address, 2, vbSingle)
395  End Function
396
397  'Read 3rd Harmonic Amplitude (0-5 V)
398  Function Read_3rd_Harm(Channel As Integer) As Single
399      Dim Address As Long
400      Address = &h6065 + Channel*&h100
401      Read_3rd_Harm = SDO.ReadSDO(ETOID, Address, 4, vbSingle)
402  End Function
403  'Read 3rd Harmonic Phase Angle (0-360)
404  Function Read_3rd_Harm_Phase(Channel As Integer) As Single
405      Dim Address As Long
406      Address = &h6065 + Channel*&h100
407      Read_3rd_Harm_Phase = SDO.ReadSDO(ETOID, Address, 5, vbSingle)
408  End Function
409
410  'Set Additional Harmonic (integer)
411  '3: 3rd Harmonic
412  '4: 4th Harmonic
413  '5: 5th Harmonic
414  '6: 6th Harmonic
415  Function Set_Addtl_Harm(Channel As Integer, J As Byte)
416      Dim Address As Long
417      Address = &h6065 + Channel*&h100
418      SDO.WriteSDO(ETOID, Address, 7, J)
419  End Function
420  'Read Order of selected Additional Harmonic
421  Function Read_Addtl_Order(Channel As Integer) As Byte
422      Dim Address As Long
423      Address = &h6065 + Channel*&h100
424      Read_Addtl_Order = SDO.ReadSDO(ETOID, Address, 7, vbByte)
425  End Function
426  'Read Addtl Harmonic Amplitude (0-5 V)
427  Function Read_Addtl_Harm(Channel As Integer) As Single
428      Dim Address As Long
429      Address = &h6065 + Channel*&h100
430      Read_Addtl_Harm = SDO.ReadSDO(ETOID, Address, 8, vbSingle)
431  End Function
432  'Read Addtl Harmonic Phase Angle (0-360)
433  Function Read_Addtl_Harm_Phase(Channel As Integer) As Single
434      Dim Address As Long
435      Address = &h6065 + Channel*&h100
436      Read_Addtl_Harm_Phase = SDO.ReadSDO(ETOID, Address, 9, vbSingle)
437  End Function
438  '''' Measured Harmonics End ''''
439
440  'Select Preamp
441  Function Set_Preamp(Channel As Integer, J As Byte)
442      Dim Address As Long
443      Address = &h6020 + Channel*&h100
444      SDO.WriteSDO(ETOID,Address, 1, J)
445  End Function
446
447  'Set Preamp Gain

```

```
448 Function Set_PGA_Gain(Channel As Integer, J As Byte)
449     Dim Address As Long
450     Address = &h6020 + Channel*&h100
451     SDO.WriteSDO(ETOID,Address, 2, J)
452 End Function
453
454 'Set Module Gain
455 Function Set_Module_Gain(Channel As Integer, J As Byte)
456     Dim Address As Long
457     Address = &h6020 + Channel*&h100
458     SDO.WriteSDO(ETOID,Address, 3, J)
459 End Function
460
461 'Set Total Gain
462 Function Set_Total_Gain(Channel As Integer, Gain As Integer)
463     Select Case Gain
464     Case 0
465         Set_Preamp(Channel, 1)
466         Set_PGA_Gain(Channel, 0)
467         Set_Module_Gain(Channel, 0)
468     ' Debug.Print 0
469     Case 1
470         Set_Preamp(Channel, 1)
471         Set_PGA_Gain(Channel, 0)
472         Set_Module_Gain(Channel, 1)
473     ' Debug.Print 1
474     Case 2
475         Set_Preamp(Channel, 1)
476         Set_PGA_Gain(Channel, 1)
477         Set_Module_Gain(Channel, 0)
478     ' Debug.Print 2
479     Case 3
480         Set_Preamp(Channel, 1)
481         Set_PGA_Gain(Channel, 1)
482         Set_Module_Gain(Channel, 1)
483     ' Debug.Print 3
484     Case 4
485         Set_Preamp(Channel, 1)
486         Set_PGA_Gain(Channel, 2)
487         Set_Module_Gain(Channel, 0)
488     ' Debug.Print 4
489     Case 5
490         Set_Preamp(Channel, 3)
491         Set_PGA_Gain(Channel, 0)
492         Set_Module_Gain(Channel, 0)
493     ' Debug.Print 5
494     Case 6
495         Set_Preamp(Channel, 3)
496         Set_PGA_Gain(Channel, 0)
497         Set_Module_Gain(Channel, 1)
498     ' Debug.Print 6
499     Case 7
500         Set_Preamp(Channel, 3)
501         Set_PGA_Gain(Channel, 1)
502         Set_Module_Gain(Channel, 0)
503     ' Debug.Print 7
504     Case 8
505         Set_Preamp(Channel, 3)
506         Set_PGA_Gain(Channel, 1)
507         Set_Module_Gain(Channel, 1)
508     ' Debug.Print 8
509     Case 9
510         Set_Preamp(Channel, 3)
511         Set_PGA_Gain(Channel, 2)
512         Set_Module_Gain(Channel, 0)
```

```

513 '     Debug.Print 9
514 Case 10
515     Set_Preamp(Channel, 3)
516     Set_PGA_Gain(Channel, 2)
517     Set_Module_Gain(Channel, 1)
518 '     Debug.Print 10
519 End Select
520
521
522 End Function
523
524 'Send Current Range Corrections
525 Function Send_I_Range_CFs(Channel As Integer, Range As Integer, ACGain_CF As
    Single, Phase_Delay As Single, Freq1 As Single, Freq2 As Single,
    DCGain_CF As Single)
526 Dim Address As Long
527 Address = &h6014 + Channel*&h100
528 SDO.WriteSDO(ETOID,Address, 1, CByte(Range))
529 SDO.WriteSDO(ETOID,Address, 2, ACGain_CF)
530 SDO.WriteSDO(ETOID,Address, 3, Phase_Delay)
531 SDO.WriteSDO(ETOID,Address, 4, Freq1)
532 SDO.WriteSDO(ETOID,Address, 5, Freq2)
533 SDO.WriteSDO(ETOID,Address, 6, DCGain_CF)
534 End Function
535
536 'Send PGA Gain Correction Factor
537 Function Send_PGA_CFs(Channel As Integer, Range As Integer, GainCF As Single,
    Delay As Single)
538 Dim Address As Long
539 Address = &h6021 + Channel*&h100
540 SDO.WriteSDO(ETOID,Address, CLng(Range + 1), GainCF)
541 SDO.WriteSDO(ETOID,Address, CLng(Range + 4), Delay)
542 End Function
543
544
545 'Turn Off Channel
546 Function Turn_Channel_Off(Channel As Integer)
547 Set_AC_Current(Channel,0)
548 Set_DC_Current(Channel,0)
549 Set_Addtl_Harm(Channel, 3) '3rd is the default for ET0, make sure it stays
    that way
550 Set_I_Range(Channel, 6)
551 Set_Feedback_Enable(Channel, 0)
552 Set_Output_Enable(Channel, 0)
553 Set_Preamp(Channel, 0)
554 End Function
555
556 'Send HGA Corrections
557 Function Send_LNA_CFs(Channel As Integer, GainCF As Single, Delay As Single)
558 Dim Address As Long
559 Address = &h6022 + Channel*&h100
560 SDO.WriteSDO(ETOID,Address, 1, GainCF)
561 SDO.WriteSDO(ETOID,Address, 2, Delay)
562 End Function
563
564 'Set module phase delay
565 Function Set_Module_Delay(Channel As Integer, Delay As Single)
566 Dim Address As Long
567 Address = &h6061 + Channel*&h100
568 SDO.WriteSDO(ETOID,Address, 1, Delay)
569 End Function
570
571 'Set AC MDAC Offset
572 Function Set_AC_MDAC_Offset(Channel As Integer, Offset As Integer)
573 Dim Address As Long

```

```

574     Address = &h6013 + Channel*&h100
575     SDO.WriteSDO(ETOID,Address,1,Offset)
576 End Function
577
578 'Set AC MDAC Gain CF
579 Function Set_AC_MDAC_Gain_CF(Channel As Integer, GainCF As Single)
580     Dim Address As Long
581     Address = &h6013 + Channel*&h100
582     SDO.WriteSDO(ETOID,Address, 3, GainCF)
583 End Function
584
585 'Set DC MDAC Offset
586 Function Set_DC_MDAC_Offset(Channel As Integer, Offset As Integer)
587     Dim Address As Long
588     Address = &h6013 + Channel*&h100
589     SDO.WriteSDO(ETOID,Address, 2, Offset)
590 End Function
591
592 'Set DC MDAC Gain CF
593 Function Set_DC_MDAC_Gain_CF(Channel As Integer, GainCF As Single)
594     Dim Address As Long
595     Address = &h6013 + Channel*&h100
596     SDO.WriteSDO(ETOID,Address, 4, GainCF)
597 End Function
598
599 'Set ADC Volts Conversion Correction
600 Function Set_ADC_CF(Channel As Integer, ADCCF As Single)
601     Dim Address As Long
602     Address = &h6061 + Channel*&h100
603     SDO.WriteSDO(ETOID,Address, 4, ADCCF)
604 End Function
605
606 'Set Module 1X Gain CF
607 Function SetModule_1X_Gain_CF(Channel As Integer, GainCF As Single)
608     Dim Address As Long
609     Address = &h6061 + Channel*&h100
610     SDO.WriteSDO(ETOID,Address, 2, GainCF)
611 End Function
612
613 'Set Module 3X Gain CF
614 Function SetModule_3X_Gain_CF(Channel As Integer, GainCF As Single)
615     Dim Address As Long
616     Address = &h6061 + Channel*&h100
617     SDO.WriteSDO(ETOID,Address, 3, GainCF)
618 End Function
619
620 'Send High Z Corrections
621 Function Send_HighZ_CFs(Channel As Integer, GainCF As Single, Delay As Single
622 )
623     Dim Address As Long
624     Address = &h6023 + Channel*&h100
625     SDO.WriteSDO(ETOID,Address, 1, GainCF)
626     SDO.WriteSDO(ETOID,Address, 2, Delay)
627 End Function
628
629 Sub Zero_Head_CFs(ByVal Channel As Integer)
630     Dim II As Integer
631
632     For II = 0 To 1
633         Send_I_Range_CFs(Channel, II, 1, 0, 1, 0, 1)
634         Wait(0.1)
635     Next II
636
637     For II = 2 To 6
638         Send_I_Range_CFs(Channel, II, 1, 0, 0, 1, 1)

```

```

638     Wait(0.1)
639     Next II
640
641     For II = 0 To 2
642         Send_PGA_CFs(Channel, II, 1, 0)
643     Next II
644
645     Send_LNA_CFs(Channel, 1, 0)
646
647     Send_HighZ_CFs(Channel, 1, 0)
648
649 End Sub
650
651 Private Sub Object_Terminate()
652
653 End Sub

```

D.3 Matlab

Listing D.7: matlab/afmAnalyze.m

```

1  %% Choose file(s) to read in with a user interface
2  [filename, pathname] = uigetfile(...
3      '/Users/kristoffer/Dropbox/Studier/5.klasse/measurements/*.txt',...
4      'Pick file(s)', 'MultiSelect', 'on');
5
6  %% Check if the user cancels. If so, terminate session
7  if isequal(filename,0) || isequal(pathname,0)
8      disp('You cancelled the program.')
```

```

9      clearvars filename pathname;
10     return;
11 end
12
13 %% Check if user chose one or more files, then convert to same format in any
14 %% case.
15 if ischar(filename) % If one file was selected, uigetfile returns string.
16     NumI = 1; % Number of input files
17     filename = cellstr(filename); % Convert to cell with single string.
18 else
19     NumI = length(filename); % Number of input files
20     % filename variable is already a cell array of strings in this case.
21 end
22
23 %% Open file(s), extract data, close file(s) properly.
24 %% Read all raw VSM data into a multilevel cell array with the function
25 %% vsmImport.
26 rawData = cell(1, NumI);
27 for i = 1:NumI
28     rawData{i} = afmImport(strcat(pathname, filename{i}));
29 end
30
31 %% Analyze and plot relevant data
32 if NumI > 1
33     mode = menu('All in one plot or separate plots? ', 'All together!', '
34         Separate!');
```

```

35 else
36     mode = 0;
37 end
38 if mode == 1

```

```

39     fh = figure;
40     hold on
41     box on
42     grid on
43 end
44
45 adjData = rawData;
46 for i = 1:NumI
47     %Autolevel all to zero
48     minimum = min(rawData{1,i}(1:end,2));
49     adjData{1,i}(1:end,2) = adjData{1,i}(1:end,2) - minimum;
50     %Autocenter all to zero
51     width = rawData{1,i}(end,1);
52     adjData{1,i}(1:end,1) = adjData{1,i}(1:end,1) - width/2;
53     %Autoadjust scale if units in meters
54     maxy = max(adjData{1,i}(1:end,2));
55     maxx = max(adjData{1,i}(1:end,1));
56     if maxy < 1e-6 && maxx < 1e-3
57         adjData{1,i}(1:end,2) = adjData{1,i}(1:end,2) * 1e9;
58         adjData{1,i}(1:end,1) = adjData{1,i}(1:end,1) * 1e6;
59     end
60 end
61
62 Legend = cell(NumI,1);
63 for i = 1:NumI
64     if mode == 2
65         fh(i) = figure;
66         box on
67         grid on
68         xlabel('Lateral distance [um]')
69         ylabel('Vertical height [nm]')
70     end
71     plot(adjData{1,i}(1:end,1),adjData{1,i}(1:end,2))
72     if mode < 2
73         Legend{i} = filename{i};
74     end
75 end
76
77 if mode < 2
78     xlabel('Lateral distance [um]')
79     ylabel('Vertical height [nm]')
80     legend(Legend,'location','best');
81 end

```

Listing D.8: matlab/etoAnalyze.m

```

1  % Script for importing, analyzing and plotting ET0 data
2
3  %close all
4  %clear all
5
6  %% Choose file(s) to read in with a user interface
7  [filename, pathname] = uigetfile(...
8      '/Users/kristoffer/Dropbox/Studier/5.klasse/measurements/*.DAT',...
9      'Pick file(s)', 'MultiSelect', 'on');
10
11 % Check if the user cancels. If so, terminate session
12 if isequal(filename,0) || isequal(pathname,0)
13     disp('You cancelled the program.')
14     clearvars filename pathname;
15     return;
16 end
17

```

```

18 % Find sample name
19 sampleName = vsmSample(pathname);
20
21 % Check if user chose one or more files, then convert to same format in any
22 % case.
23 if ischar(filename) % If one file was selected, uigetfile returns string.
24     NumI = 1; % Number of input files
25     filename = cellstr(filename); % Convert to cell with single string.
26 else
27     NumI = length(filename); % Number of input files
28     % filename variable is already a cell array of strings in this case.
29 end
30
31 %% Open file(s), extract data, close file(s) properly.
32 % Read all raw VSM data into a multilevel cell array with the function
33 % vsmImport.
34 rawData = cell(1,NumI);
35 for i = 1:NumI
36     rawData{i} = vsmImport(strcat(pathname,filename{i}));
37 end

```

Listing D.9: matlab/etoMacroExtract.m

```

1 function etoData = etoMacroExtract(rawData)
2
3 % Find index of data start
4 idx = find(strcmp(rawData(1:end,1), '[Data]')) + 2;
5 % index of [Data] + 2 rows to jump over header row.
6
7 % Temperature
8 T = cellfun(@str2double, rawData(idx:end,3));
9 % Resistance vs magnetic field
10 R = cellfun(@str2double, rawData(idx:end,5));
11 Rstdev = cellfun(@str2double, rawData(idx:end,22));
12 ScndHrm = cellfun(@str2double, rawData(idx:end,30)); %2nd harm
13 ThrdHrm = cellfun(@str2double, rawData(idx:end,31)); %3rd harm
14 Phase = cellfun(@str2double, rawData(idx:end,18));
15 PeakVolt = cellfun(@str2double, rawData(idx:end,10));
16 InPhVolt = cellfun(@str2double, rawData(idx:end,11));
17 QuadVolt = cellfun(@str2double, rawData(idx:end,12));
18 Freq = cellfun(@str2double, rawData(idx:end,21));
19 % Magnetic field
20 H = cellfun(@str2double, rawData(idx:end,4));
21
22 % Differential resistance measurement data
23 dR = R; % unit Ohms
24 I_dc = cellfun(@str2double, rawData(idx:end,6)); % unit mA
25 I_ac = cellfun(@str2double, rawData(idx:end,7)); % unit mA
26 V_dc = dR.*I_dc./10^3; % unit V
27 dG = 1./dR; % unit S
28
29 % IV-curve measurement data
30 I = cellfun(@str2double, rawData(idx:end,10:20:30)); % unit mA
31 V = cellfun(@str2double, rawData(idx:end,11:20:31)); % unit V
32 R_iv = V./I./10^3; % unit Ohms
33
34 etoData = {I_dc, V_dc, dR, dG, I, V, R_iv, H, R, T, ScndHrm, ThrdHrm, Phase, ...
35     PeakVolt, InPhVolt, QuadVolt, Freq, Rstdev, I_ac};
36 end

```

Listing D.10: matlab/dVdI_P60403_P60501.m

```

1  % Analyze dVdI data for samples P60403 and P60501
2  % First import data with etoAnalyze
3
4  %Extract data
5  etoData = cell(NumI,1);
6  for i = 1:NumI
7      etoData{i} = etoMacroExtract(rawData{1,i});
8  end
9  close all
10
11 % Plot RvI data
12 figure
13 grid on
14 hold on
15 Legend = cell(NumI,1);
16 for i = 1:NumI
17     plot(etoData{i}{1,1}*1e6,etoData{i}{1,9}*1e-6,'-o')
18     Legend{i} = filename{1,i};
19 end
20 xlabel('$I_{\rm dc}$ [nA]')
21 ylabel('$dV/dI$ [M$\Omega$]')
22 ylim([0 220])
23 legend(Legend,'location','best');
24
25 % Plot derived dG/dV vs V_dc data
26 figure
27 grid on
28 Legend = cell(NumI,1);
29 for i = 1:NumI
30     semilogy(etoData{i}{1,2},etoData{i}{1,4}*1e6,'-o')
31     hold on
32     Legend{i} = filename{1,i};
33 end
34 xlabel('$V_{\rm dc}$ [V]')
35 ylabel('$dI/dV$ [ $\mu$S (M$\Omega^{-1}$) ]')
36 %xlim([-0.2 0.2])
37 ylim([0.004 0.1])
38 legend(Legend,'location','best');
39
40 % Analyze in-phase and quadrature components
41 fh(1) = figure;
42 box on;grid on;
43 fh(2) = figure;
44 box on;grid on;
45 fh(3) = figure;
46 box on;grid on;
47 fh(4) = figure;
48 box on;grid on;
49 LegendCap = cell(NumI*2,1);
50 for i = 1:NumI
51     %phase = etoData{i}{1,13};
52     %peakV = etoData{i}{1,14};
53     inphV = etoData{i}{1,15};
54     quadV = etoData{i}{1,16};
55     freq = etoData{i}{1,17};
56     %Restdv = etoData{i}{1,18};
57     Idc = etoData{i}{1,1}*1e-3; %mA-->A
58     Iac = etoData{i}{1,19}*1e-3; %mA-->A
59     A = inphV./Iac;%Real(Z)
60     B = quadV./Iac;%Imag(Z)
61     Res = B.^2./A + A;%Ohm
62     Con = 1./Res;
63     Cap = abs(B)./(2*pi*freq.*(A.^2 + B.^2));%Farad

```

```

64     Vdc = Idc.*Res; %V
65     %plot resistance
66     figure(fh(1))
67     plot(etoData{i}{1,1}*1e6,Res*1e-6,'-o')
68     hold on
69     %plot capacitance
70     figure(fh(2))
71     plot(etoData{i}{1,1}*1e6,Cap*1e12,'-o',etoData{i}{1,1}*1e6,Cap*1e12-380,'
->')
72     hold on
73     %plot conductance
74     figure(fh(3))%vs I
75     semilogy(etoData{i}{1,1}*1e6,Con*1e6,'-o')
76     hold on
77     figure(fh(4))%vs V
78     semilogy(Vdc,Con*1e6,'-o')
79     hold on
80     Legend{i} = filename{1,i};
81     LegendCap{2*i-1} = filename{1,i};
82     LegendCap{2*i} = '-380pF';
83 end
84 figure(fh(1))
85 xlabel('$I_{\rm dc}$ [nA]')
86 ylabel('$dV/dI$ [M$\Omega$]')
87 ylim([0 220])
88 legend(Legend,'location','best');
89 figure(fh(2))
90 xlabel('$I_{\rm dc}$ [nA]')
91 ylabel('$C$ [pF]')
92 ylim([0 1000])
93 legend(LegendCap,'location','best');
94 figure(fh(3))
95 xlabel('$I_{\rm dc}$ [nA]')
96 ylabel('$dI/dV$ [ $\mu$S (M$\Omega)^{-1}$]')
97 %ylim([0 200])
98 legend(Legend,'location','best');
99 figure(fh(4))
100 xlabel('$V_{\rm dc}$ [V]')
101 ylabel('$dI/dV$ [ $\mu$S (M$\Omega)^{-1}$]')
102 xlim([-0.5 0.5])
103 ylim([0.0005 0.1])
104 legend(Legend,'location','best');

```

Listing D.11: matlab/IV_P60403_P60501.m

```

1  % Analyze IV data for samples P60403 and P60501
2  % First import data with etoAnalyze
3
4  close all
5  %Extract data
6  etoData = cell(NumI,1);
7  for i = 1:NumI
8      etoData{i} = etoExtract(rawData{1,i});
9  end
10
11 %Analyze and plot
12 sweep = 1023;
13 count = 0;
14 for h = 3:4
15     add = 0 + (h-1)*1023;%3069;%2046;%1023;
16 % Plot IV data
17 figure
18 box on

```

```

19 grid on
20 hold on
21 Legend = cell(NumI,1);
22 for i = 1:NumI
23     plot(etoData{i}{1,6}(add+1:add+sweep,3-i),etoData{i}{1,5}(add+1:add+sweep
24         ,3-i)*1e6,'-o')
25     Legend{i} = filename{1,i};
26 end
27 xlabel('$V_{\rm dc}$ [V]')
28 ylabel('$I_{\rm dc}$ [nA]')
29 %ylim([-100 100])
30 legend(Legend,'location','best');
31
32 % Plot dI/dV vs V
33 figure
34 box on
35 grid on
36 hold on
37 %Legend = cell(NumI,1);
38 for i = 1:NumI
39     len = length(etoData{i}{1,6}(1:end,3-i));
40     dI = diff(etoData{i}{1,5}(1:end,3-i));
41     dV = diff(etoData{i}{1,6}(1:end,3-i));
42     dR = smooth(dV)./smooth(dI);
43     avgV = zeros(1,len-1);
44     for j = 1:len-1
45         avgV(1,j) = (etoData{i}{1,6}(j,3-i)+etoData{i}{1,6}(j+1,3-i))/2;
46     end
47     %plot(etoData{i}{1,6}(256:767,3-i),dG(256:767))
48     plot(avgV(add+272:add+750),dR(add+272:add+750)*1e-3,'-o')
49     %plot(avgV,dR*1e-3,'-o')
50     Legend{i} = filename{1,i};
51 end
52 xlabel('$V_{\rm dc}$ [V]')
53 ylabel('$dV/dI$ [M$\Omega$]')
54 %xlim([-1 1])
55 %ylim([0 ])
56 legend(Legend,'location','best');
57
58 % Plot dI/dV vs V
59 figure
60 box on
61 grid on
62 hold on
63 %Legend = cell(NumI,1);
64 for i = 1:NumI
65     len = length(etoData{i}{1,6}(1:end,3-i));
66     dI = diff(etoData{i}{1,5}(1:end,3-i));
67     dV = diff(etoData{i}{1,6}(1:end,3-i));
68     dG = smooth(dI)./smooth(dV);
69     avgV = zeros(1,len-1);
70     for j = 1:len-1
71         avgV(1,j) = (etoData{i}{1,6}(j,3-i)+etoData{i}{1,6}(j+1,3-i))/2;
72     end
73     %plot(etoData{i}{1,6}(256:767,3-i),dG(256:767))
74     plot(avgV(add+272:add+750),dG(add+272:add+750)*1e6,'-o')
75     %plot(avgV,dG,'-o')
76     Legend{i} = filename{1,i};
77 end
78 xlabel('$V_{\rm dc}$ [V]')
79 ylabel('$dI/dV$ [nS(G$\Omega^{-1}$)']')
80 %xlim([-1 1])
81 ylim([0 500])
82 legend(Legend,'location','best');

```

```
83
84 end
```

Listing D.12: matlab/Plotfix.m

```
1 classdef Plotfix < handle
2     % Plotfix is a figure handle class which takes an input figure handle
3     % and applies specific changes on it. Moreover, it eases the production
4     % of standardized pdf figures with the print function. Other functions
5     % should be self-explanatory; see below. The NTNU palette has been used
6     % to change all line colors to NTNU's default colors. Standard LaTeX
7     % interpretation is used to modify the labels with text and math
8     % environment fonts.
9
10    % Thanks to my good friend Erlend Fasting for sending the first version
11    % of this class over in the autumn 2015. It's been modified according
12    % to my needs later. The class needs further development in order to
13    % work with more advanced figures having multiple axes for example.
14
15    properties
16        fighandle;
17        axeshandle;
18
19        stems;
20        lines;
21
22        % CONFIGURATION PARAMETERS
23        titleconfig = '\fontsize{11}{0}\selectfont\textbf{';
24        labelconfig = '\fontsize{12}{0}\selectfont ';
25        legendconfig = '\fontsize{10}{0}\selectfont ';
26
27        stemLineWidth = 1;
28        stemMarkerSize = 10;
29
30        lineLineWidth = 0.5;
31        lineMarkerSize = 6;
32
33        % Assign correct RGB values based on NTNU's palette. For more info
34        % see http://www.ntnu.no/grafisksenter/ntnu-farger#fargene
35        colorsNTNU = {
36            [0, 80, 158]/255; %ntnu0 blue MAIN
37            %[241, 210, 130]/255;%ntnu1 yellow
38            [92, 190, 201]/255;%ntnu2 cyan
39            [213, 209, 14]/255;%ntnu3 greenyellow
40            %[223, 216, 197]/255;%ntnu4 grey
41            [121, 162, 206]/255;%ntnu5 heavenblue
42            %[201, 212, 178]/255;%ntnu6 lightgreen
43            %[204, 189, 143]/255;%ntnu7 khaki
44            [173, 32, 142]/255;%ntnu8 pink
45            %[221, 231, 238]/255;%ntnu9 lightblue
46            [144, 73, 45]/255; %ntnu10 brown
47            [85, 41, 136]/255; %ntnu11 purple
48            [245, 128, 37]/255 %ntnu12 orange
49        };
50        colNum = 8; % 13 colors in all, but only these give good contrast
51
52        printconfig = '-dpdf';%-depsc';%-dpsc';
53        printfolder = '/Users/kristoffer/Dropbox/Studier/5.klasse/master/
54            illustrator/matlab/';
55        %printfolder = '~/Desktop/';
56    end
57
58    methods
```

```

58     function self = Plotfix(fighandle)
59     % Takes a figure handle and modifies the figure according to setup
60     % constants.
61
62         self.fighandle = fighandle;
63         self.axeshandle = findobj(fighandle,'type','axes');
64         %self.legendhandle = findobj(fighandle,'type','legend');
65
66         % Preserve previous content
67         self.axeshandle.Title.String;
68         self.title(self.axeshandle.Title.String);
69         self.xlabel(self.axeshandle.XLabel.String);
70         self.ylabel(self.axeshandle.YLabel.String);
71
72         % Set up properties
73         self.axeshandle.FontName = 'Helvetica';
74         self.axeshandle.FontSize = 14;
75         self.axeshandle.TitleFontSizeMultiplier = 1;
76         %self.axeshandle.XLabel.Position = self.axeshandle.XLabel.
77             Position - [0 .05 0];
78         %self.axeshandle.YLabel.Position = self.axeshandle.YLabel.
79             Position - [.2 0 0];
80         self.axeshandle.Box = 'on';
81
82         self.stems = findobj(self.axeshandle, 'type', 'stem');
83         self.lines = findobj(self.axeshandle, 'type', 'line');
84
85         self.setupStem();
86         self.setupLines();
87     end
88
89     %__ End constructor. User methods below.
90
91     function title(self,string)
92     % Sets the title to string
93         newstring = [self.titleconfig string ''];
94         title(self.axeshandle,newstring, 'interpreter', 'latex');
95     end
96
97     function xlabel(self,string)
98     % Sets xlabel to string
99         newstring = [self.labelconfig string];
100         xlabel(self.axeshandle, newstring, 'interpreter', 'latex');
101     end
102
103     function ylabel(self,string)
104     % Sets ylabel to string
105         newstring = [self.labelconfig string];
106         ylabel(self.axeshandle, newstring, 'interpreter', 'latex');
107     end
108
109     function print(self, name) % http://se.mathworks.com/help/matlab/ref/print.html
110     % Prints the current figure to file
111         print(self.fighandle, [self.printfolder name], self.printconfig);
112         %, '-cmk');
113
114     end
115
116
117 end
118

```

```
119
120     methods (Access = private)
121
122         function setupStem(self)
123             if ~isempty(self.stems)
124                 for i = 1:length(self.stems)
125                     self.stems(i).LineWidth = self.stemLineWidth;
126                     self.stems(i).MarkerSize = self.stemMarkerSize;
127                     self.stems(i).MarkerFaceColor = self.stems(i).
128                         MarkerEdgeColor;
129                 end
130             end
131
132         function setupLines(self)
133             if ~isempty(self.lines);
134                 j = length(self.lines); % number of lines
135                 mul = floor(j/self.colNum); % multiplier (lowest int)
136                 rem = mod(j,self.colNum); % remainder
137                 order = []; % allocate an empty matrix
138                 while mul % reuse colors if needed
139                     order = [order 1:self.colNum];
140                     mul = mul-1;
141                 end
142                 order = [order 1:rem]; % assign remaining colors
143                 for i = 1:length(self.lines)
144                     self.lines(i).LineWidth = self.lineLineWidth;
145                     self.lines(i).MarkerSize = self.lineMarkerSize;
146                     self.lines(i).Color = self.colorsNTNU{order(j)};
147                     j = j-1; % Lines are counted from the last one added.
148                         % Hence, so must the order vector.
149                 end
150             end
151         end
152     end
153 end
```